Efficient Swimming in Dense Schools: Effect of Formation and Synchronization on Hydrodynamic Interactions

---

A

Dissertation

Presented to

the faculty of the School of Engineering and Applied Science

University of Virginia

---

in partial fulfillment

of the requirements for the degree

Doctor of Philosophy

by

Yu Pan

December 2022

APPROVAL SHEET

This

Dissertation

is submitted in partial fulfillment of the requirements
for the degree of

Doctor of Philosophy

Author: Yu Pan

This Dissertation has been read and approved by the examing committee:

Advisor: Haibo Dong

Advisor:

Committee Member: Daniel B. Quinn

Committee Member: Ye (Sarah) Sun

Committee Member: Matthew A. Reidenbach

Committee Member: George V. Lauder

Committee Member:

Committee Member:

Accepted for the School of Engineering and Applied Science:

Jennifer L. West, School of Engineering and Applied Science

December 2022

Abstract

Fish schools, as one of the most prevalent collective systems in nature, have been thought to provide hydrodynamic benefits to individual fish, supported by many laboratory experiments and field observations. However, accurate measurement and quantitative analysis of hydrodynamic interactions in a fish school are challenging and limited by experimental and numerical techniques, especially for a three-dimensional biological fish school. The underlying physical mechanisms are thus unclear, and no widely accepted theory has been put forward for decades. The lack of understanding of hydrodynamic interactions impedes the research of fish behavior and the design and control of bio-inspired underwater robotic swarms.

Motivated by this deficiency, we first develop a narrow-band level-set-based immersed boundary (NBLS-IB) reconstruction method and a tree-topological local mesh refinement (TLMR) method coupled with parallel computing on Cartesian grids to enable fast and high-fidelity simulations. Using these advanced numerical methods, two-dimensional (2D) and three-dimensional (3D) flow simulations are performed in an incompressible Navier-Stokes in-house solver to investigate hydrodynamic interactions in fish schools.

In the case of 2D studies, a NACA foil imposed on a traveling wave kinematics is employed to mimic 2D fish-like swimming. Simulations of 2D flow past dense diamond-shaped schools suggest that body–body and vortex–body interactions significantly enhance the hydrodynamic performance of individual fish. As the lateral fish diagonally positioned in a school approach the trailing fish, their thrust and efficiency increase. This results from the wall effect elucidated by 2P vortex wakes and angled momentum jets behind the lateral fish. The fluid drained by the leading fish is obstructed by the trailing fish, improving the performance of the leading fish. In the meantime, the trailing fish captures energy from the vortex flow generated by the lateral fish and

produces a high suction thrust at the head through the body–body interaction with the lateral fish. Optimal thrust production and swimming efficiency can be achieved by adjusting the phase or tail-beat frequency. Flow visualizations suggest that the wake pattern strongly depends on the phase offset and the tail-beat frequency, which bridges the gap between the wake pattern and the performance of a dense school.

Thrust enhancement, power-saving, drag reduction and their combinations have been identified through 3D simulations of flow past biological fish bodies arranged in the horizontal and vertical planes. The block effect in an in-line school increases the thrust of the leading fish and is dependent on the streamwise distance. Caudal fin power is greatly saved in an in-phase side-by-side school through flow separation on the fin surface induced by the low-speed flow between the fins. In the anti-phase side-by-side school, thrust enhancement happens because of the virtual wall effect and passive-energy-capturing mechanisms. The small gap between two in-phase fish arranged in the vertical plane speeds up the cross-stream flow between the caudal fins and strengthens and stabilizes the leading-edge vortices (LEV), increasing thrust production. However, the constructive interaction can easily be deteriorated by the out-of-phase motion. In a staggered school, vortex rings with high momentum shed by the leading fish can enhance the leading-edge vortices on the caudal fin of the following fish and significantly increase its thrust by setting the streamwise distance or phase offset at the appropriate values. In the meantime, the drag of the following fish can be significantly reduced through the interaction between its body and vortex rings shed by the leading fish. Flow analyses reveal that the vortex rings reduce the drag by decreasing the streamwise velocity around the body of the following fish, which strongly depends on the evolution and advection of these vortex rings.

Acknowledgements

First, I would like to thank my advisor, Prof. Haibo Dong, for his invaluable guidance and continuous support throughout my Ph.D. study. He provoked my interest in bio-flow physics and taught me to be a careful researcher to tackle tough questions strategically and to discover physics in nature. Haibo also taught me to be a good teacher by providing me with an opportunity to co-teach with him. Haibo stood by me through every challenge and choice, and I consider him a friend as much as a mentor.

I would like to express my heartfelt gratitude to my committee members, Prof. Dan Quinn, George Lauder, Sarah Sun, and Matthew Reidenbach, for their inspiring guidance, constructive criticism and warm encouragement. Many thanks to my past and current teammates, Dr. Pan Han, Junshi Wang, Wei Zhang, Mr. Yuchen Gong, John Kelly, Jiacheng Guo and Alec Menzer, for their support, generosity and discussion.

Finally, and foremost, I would like to express my deepest gratitude and sincere to my family. To my dear parents, Xiliang Pan and Xinfeng Ruan, thank you for your unconditional love and support, which keeps me brave and strong when facing challenges. To my brother, Zhenxi Pan, the first college student in my family, inspired me to be curious and hard-working.

The work presented in this thesis was supported by the Office of Naval Research under MURI grant number N00014-1-0533, the National Science Foundation under grant number CNS-1931929 and the Mechanical and Aerospace Engineering Department at the University of Virginia Distinguished Fellowship.

Table of Contents

List of Figures

List of Tables

1 Introduction

1.1 Motivation and Goals

Schooling, as one of the most spectacular and striking collective behavior possessed by fish, is prevalent in nature. About 25% of all fish species (approximately 20,000) school for their entire life, and approximately 50% live in schools as juveniles [1]. Why do fish school? Fish have been thought to achieve many benefits by swimming in schools, including avoidance of predators [2], better reproductive opportunities [3], and higher foraging efficiency [4]. Of specific interest is that fish can gain hydrodynamic benefits by schooling [1, 5].

The outstanding hydrodynamic performance in nature is of particular inspiration to the design of underwater robotics. Over the past decades, with significant effort in fish swimming research, the understanding of how fish gain high performance has been advanced and applied to the design of unmanned underwater vehicles [6-8], as shown in Figs. 1-1 (a) and (b). Compared to directly replicating fish features, like morphology and locomotion, the gap between engineered robotic systems and fish swimming ability has significantly been closed by applying the knowledge of the biological systems to robotics.

However, the design of underwater swarm robotics is still at a very early stage. Several underwater swarm systems were designed for the growing demand for environmental monitoring, fast-searching and rescue missions in the sea [9-11]. Recently, a fish-inspired robot swarm, Blueswarm in Fig. 1-1(c), was designed to bypass the inherent challenges of underwater coordination [12]. Nevertheless, hydrodynamics is not fully involved in the design and control, and the system is not as efficient as fish schools in nature. The fish interplaying with the flow environment, shown in Fig. 1-2, implies that hydrodynamics is essential for the efficient swimming

of a solitary fish and critical to a fish school. The findings of flow physics in fish schooling will contribute to the design of the next generation of high-efficiency underwater swarm platforms.

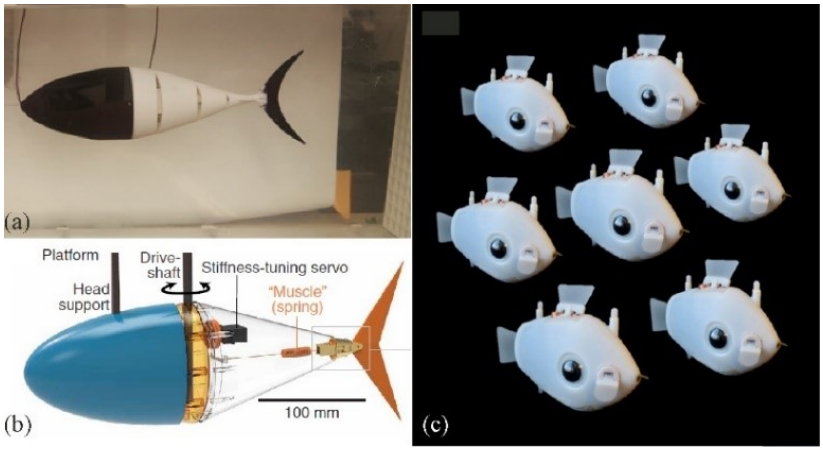

Figure 1-1. Various underwater vehicles and underwater robotic swarms. (a) Tunabot Flex, University of Virginia [6], (b) Tunabot with a stiffness-tunable tail, University of Virginia [8], (c) Blueswarm, Harvard University [12].

The hydrodynamic interactions are complicated, and the flow physics is rich in a fish school. First, owning to the oscillatory/undulatory motion and complex morphologies of bodies and fins, the flow generated by fish is highly unsteady. Second, to a certain degree, fish can freely alter their swimming kinematics and relative positions in a school, introducing more complexities into body-body and wake-body hydrodynamic interactions at spatial and temporal scales. Thus, to achieve high performance, the hydrodynamic interactions between swimmers should be considered both in space and time.

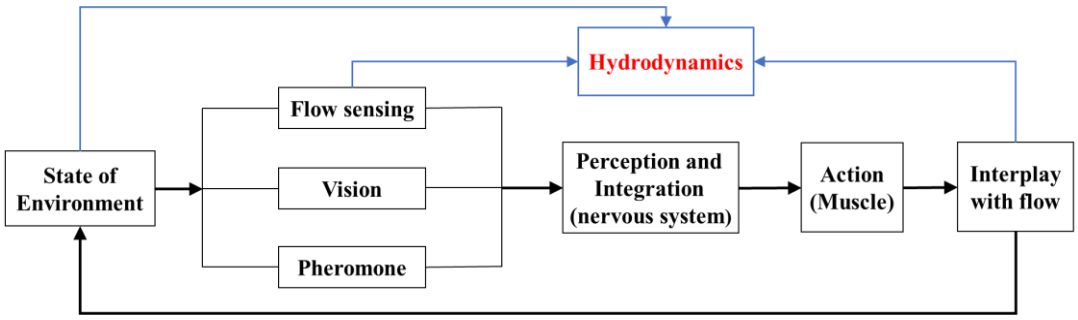

Figure 1-2. Fish behavior. Fishes sense flow and control their body and fins, interplaying with the flow environment.

This work aims to discover the fundamental flow physics by examining the effects of formation and synchronization on hydrodynamic interactions in a fish school. Specifically, the effects of spatial arrangements, tail-beat phase difference, and tail-beat frequency variation on the hydrodynamic performance of individual swimmers will be explored in fish schools composed of two-dimensional (2D) canonical fish and three-dimensional (3D) biological fish imposed on traveling wave kinematics, respectively, through comprehensive numerical simulations. The simulations are conducted in a high-fidelity immersed-boundary-based (IB) direct numerical simulation (DNS) flow solver. The hydrodynamic performance and associated flow dynamics are analyzed to reveal the underlying performance enhancement mechanisms. The general goals are to advance understanding of the hydrodynamic interactions in fish schools and provide novel physical insights into designing and controlling bio-inspired underwater swarm robots.

1.2 Unsteady Hydrodynamics of Single Fish

The study of fish swimming hydrodynamics originated from Leonardo da Vinci, who argued that with a streamlined shape, fish could move through water experiencing little drag. Recently, with the development of bionic technology, the hydrodynamics of swimming fish has stimulated the

interest of engineers and biologists, deepened the understanding of the evolution of swimming fish, and inspired the innovative design of underwater robotics.

As a simplified model for bio-inspired propulsion, oscillating foils have been widely used to measure the hydrodynamic performance in experiments and to unveil the underlying physics mechanisms in swimming [13-21]. In the oscillating foil experiments, Godoy-Diana et al. [20] identified the transition from the Bénard–von Kármán (BvK) vortex wake to the reverse BvK vortex wake proceeding the drag-thrust transition. The classical BvK and rBvK wake patterns and the associated mean flows are shown in Fig. 1-3. Another important finding is that the reverse BvK vortex wake pattern corresponds to the maximum amplification for the perturbation waves and the most efficient swimming mode [18]. Two key parameters characterize the hydrodynamic performance and wake structure of an oscillating foil: the Reynolds number (Re) and Stouhal number (St). The Reynolds number, Re, is defined as $Re = UL/v$, where U is the forward speed, L denotes the chord length of the foil and v is the kinematic viscosity of the fluid, to describe the steady motion of the foil through the water[22]. The Strouhal is wrriten as $St = fA/U$, where f is the oscillating frequency and A indicates the tip-to-tip oscillating amplitude, to describe the oscillating motion relavtive to the forward speed.

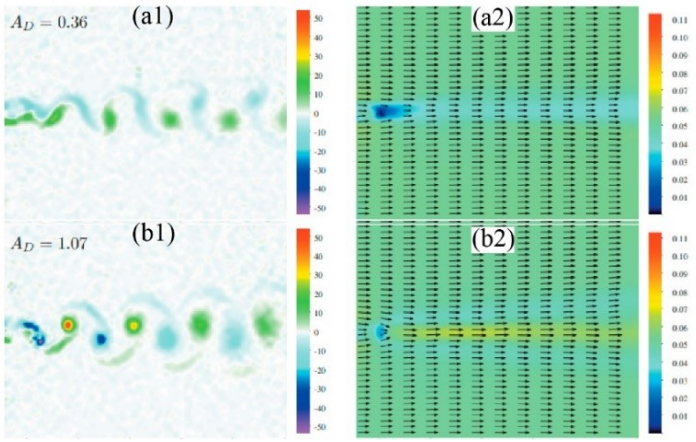

Figure 1-3. (a1) Bénard–von Kármán (BvK) vortex wake, (b1) reverse Bénard–von Kármán (BvK) vortex wake, and (a2, b2) their associated mean flows. Adapted from the Ref. [20].

The flow pattern is frequently taken as the "footprint" of swimming fish [23] and can be an indicator of efficient swimming. However, there is no strict one-to-one connection between the wake structure and the swimming performance because the flow wake is a consequence of a swimming mode [24]. Some flow information has already been lost when the vortices are advected downstream, especially for complex swimming.

In nature, fish swimming with the body and caudal fin (BCF) can be divided into four kinds, including anguilliform, subcarangifrom, carangiform, and thunniform, based on the ratio of the body-wave length to the body length [25-27]. Among these fishes, many carangiform fishes have been reported to swim in schools [28, 29] and to generate three-dimensional linked vortex rings in steady swimming through experimental measurements [30] and numerical simulations [31], as shown in Fig. 1-4. In addition, for BCF fishes, the trunk is traditionally taken as a bluff body suffering drag, whereas the caudal fin generates the most thrust. Experiments have demonstrated that the undulating fish-like body experiences a lower drag than the towed straight body with the necessary condition that the forward speed is smaller than the phase speed of the body wave [32].

Also, the thrust production of the caudal fin can be greatly enhanced through fin-body interaction in fish swimming [33].

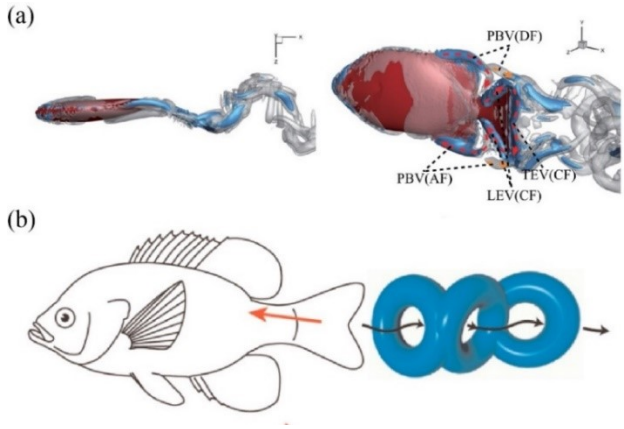

Figure 1-4. (a) Three-dimension linked vortex ring generated by a bluegill sunfish. Adapted from the Ref. [31]. (b) Schematics of a chain of linked vortex rings. Adapted from the Ref. [30].

1.3 Spatial Effect on Hydrodynamic Interactions in a Fish School

The spatial arrangement of the fish, which determines the density and shape of a school, is thought to be one of the most important factors influencing hydrodynamic interactions in the school swimming process [5, 34]. Nevertheless, past research on the effect of the spatial arrangement on fish performance has been limited to sparse fish schools with a streamwise spacing of at least one body length [34, 35], although in nature, the snout of a fish is frequently ahead of the tail of the fish it is following [36].

Experimental and computational studies on the effect of streamwise spacing [37-40] and lateral spacing [41-43] have been conducted for in-line configurations and side-by-side configurations, respectively. Boschitsch et al. [37] conducted an experimental study on two in-line pitching foils and suggested that for in-phase motion, the thrust production and propulsive efficiency of the downstream foil can be enhanced by 50% when the streamwise spacing is around

1.2 chord lengths. By combining remeshed vortex methods and a deep reinforcement learning algorithm, Novati et al. [39] found that the "smart-follower" prefers to position itself 0.7 body lengths behind the leading fish, no matter where the initial position is, to achieve a 19.4% increase in average swimming efficiency. Dewey et al. [42] experimentally studied the performance of two oscillating foils in a side-by-side configuration and reported that when the lateral spacing is 0.5 chord lengths, the efficiency of the system can be enhanced by 35% with in-phase motion. This finding is consistent with the numerical study of Dong and Lu [41] on side-by-side undulating foils. Staggered formations have also received attention [44-46]. Using a three-dimensional overset-grid-based finite-volume method, Li et al. [44] built a full map of the hydrodynamic characteristics of fish swimming in pairs as functions of lateral spacing and streamwise spacing. They reported that the pair could save up to 3% of the cost of transport (CoT) with in-phase motion in a staggered formation. In an experimental study, Kurt et al. [45] reported that the following pitching foil can achieve a 63–81% increase in thrust and efficiency when swimming in a staggered formation. All the aforementioned research demonstrates the significant effect of the spatial arrangement of the fish on the hydrodynamic interactions and energy efficiency of a fish school.

The performance of fish schools involving more than two fish has also been studied [34, 35, 47, 48]. Using an analytical model, Weihs [5] studied a two-dimensional school of four fish constrained to a single plane. His findings suggested that a diamond configuration is optimal for maximizing energy efficiency. Weihs [5] also proposed two possible mechanisms to explain the connection between the hydrodynamic interaction and spatial arrangement of a school: the vortex hypothesis describes the constructive interaction between oncoming vortices and the following fish [5, 49], and the channeling effect states that laterally neighboring fish swimming in close proximity can save energy by enhancing the flow between them [5, 35]. However, the model was

highly simplified and did not include the viscous effect of the flow. In recent years, using a multi-particle collision dynamics model, Hemelrijk et al. [34] numerically studied the hydrodynamic performance of various school configurations, including diamond, rectangular, phalanx, and in-line patterns. Their results confirmed that a fish swimming in a diamond-configuration school could achieve higher efficiency than solitary swimming but argued that the optimal lateral spacing is 1.6 BL rather than the 0.4 BL suggested by Weihs [5]. In addition, Daghooghi and Borazjana [35] investigated the hydrodynamics of a mackerel school in a rectangular configuration using three-dimensional flow simulations under periodical boundary conditions. It was found that the power efficiency of individual fish increased by 8.8% when the lateral distance was 0.4 BL. Nevertheless, there is a lack of comprehensive investigation of the hydrodynamic performance and associated wake structures of dense fish schools, in which fish are in close proximity to each other, using high-fidelity computational fluid dynamics (CFD) flow simulations.

1.4 Synchronization Effects on Hydrodynamic Interactions in a Fish School

For fish swimming, the tail-beat frequency and phase work together to influence the pose and velocity of a fish body at a certain time and the releasing time and advection velocity of shedding vortices, which thus can determine hydrodynamic interactions in a fish school. The tail-beat frequency and phase differences intrinsically represent the synchronization of motion between swimmers and influence the hydrodynamic interactions on the temporal scale. Hence, they are classified as the synchronization effects in this work.

Biological experiments demonstrated that fish could alternate their tail-beat phase to capture energy from the vortex flow through vortex–body interaction [50, 51]. To further elucidate the interaction, computational [38, 52] and experimental studies [37, 53] have been conducted using two in-line pitching foils. It is found that the performance of the trailing foil strongly depends

on the phase difference between the leading and trailing foils because the phase difference affects the timing when the vortices shed by the leading foil arrive at the leading edge (LE) of the trailing foil and influence the formation of the leading-edge vortex (LEV) [38, 52]. For instance, Boschitsch et al. reported that the thrust and the propulsive efficiency of the trailing foil could be enhanced by 60% more than that of an isolated foil when the phase difference is about 300° in the experiment of two in-line pitching foils at a spacing of 0.25 times the chord length [37]. Similar results were obtained in three-dimensional experiments using in-line foils conducted by Kurt and Moored [53]. Furthermore, flow visualizations reveal that the relative orientation of the tailing foil influences the vortex evolution and its hydrodynamic performance after the shedding vortices reach the leading edge of the trailing foil [37]. However, the means whereby the vortex–body interaction affects the distributions of surface pressure and power consumption on a foil have barely been mentioned. Also, due to being limited to the oscillating rigid foil, how a fish, an undulating body, captures energy from the vortex flow has not been fully addressed.

Some research has found that the hydrodynamic performance of swimmers in a side-by-side configuration is dependent on the tail-beat phase and is related to the wake-wake interactions [41-43, 54]. In the experiments of a pair of side-by-side pitching foils, Dewey et al. [42] found that the swimming power is reduced in the in-phase case, and thrust enhancement occurs in the anti-phase case, which results from the associated interaction of vortex pairs produced by the foils. Similar results were obtained in the two-dimensional numerical simulations using undulating foils [41]. Besides, the effects of phase difference on the hydrodynamic interactions in a staggered school, a more common configuration in nature, have received limited attention [45, 55]. Through two-pitching foil experiments, Kurt et al.[45] found that the follower in the staggered configuration with a streamwise spacing of 0.75 chord length and lateral distance of 0.4 chord length achieves

the highest thrust, 67% higher than that of a single foil, at $\varphi = 90°$. However, the body–body interaction occurring in dense schools or compact configurations directly influences hydrodynamic performance and has not received enough attention in previous research.

Trantafyllou et al. [18] suggested that fish swim in a certain range of Strouhal numbers to achieve optimal swimming efficiency. It has been observed that fish tend to increase their tail-beat frequency instead of the amplitude of motion to increase the speed [15, 56]. According to the definition of the Strouhal number, we thus can derive that a single fish adjusts its tail-beat frequency within a certain range to obtain optimal efficiency. Nevertheless, the optimal tail-beat frequency for a fish school is still not known. Additionally, numerous experiments have concluded that fish can get hydrodynamic benefits when swimming in a school by showing a reduction in oxygen consumption and tail-beat frequency [57, 58]. However, how the fish benefit from the hydrodynamic interactions by varying the tail-beat frequency has not been explored yet.

The hydrodynamic performance of fish schools with complex arrangements and containing more individuals has been investigated [34, 35, 48, 59-65] using self-propelled particles [59, 60, 63] and numerical simulations based on the Navier–Stokes equations [34, 35, 61, 64, 65]. These studies confirmed that individual fish swim more efficiently in a school than being solitary [34]. Nevertheless, the frequency and phase difference effects were not considered, and quantitative analyses of the interactions were not presented due to the limitations of the numerical methods.

1.5 Effect of Three-Dimensional Fish Body and School Configuration

The morphologies of real fish and the wake structures are complex and highly three-dimensional. The real fish with undulating locomotion mode usually shed linked or discrete vortex rings downstream during steady swimming. Unlike point vortices, vortex rings have complicated shapes and structures and may evolve and develop in a complicated way when being advected downstream

due to self-induction or influence from other objects. Consequently, except on the spatial scale, the interactions between vortex rings and 3D fish bodies are also complex on the temporal scale. Although two-dimensional (2D) studies provide significant insight into performance enhancement mechanisms and vortex dynamics in fish schools, they cannot fully reveal the mechanisms of the hydrodynamic interactions between three-dimensional fish bodies and vortex structures. Several innovative three-dimensional studies have been conducted to overtake the problem by using fish or fish-like bodies in numerical simulations and experiments.

The first three-dimensional simulation of a fish school was conducted by Daghooghi and Borazjana[35]. They found that fish in a rectangular school swim faster than solitary fish by benefiting from the channeling effect. Yet no coherent three-dimensional vortex structures were observed, and vortex-body interactions were thus not investigated. On the contrary, Verma et al. [61] reported that the following fish synchronizes the undulating motion to capture energy from the vortex wake of the leading fish via 3D simulations combined with the reinforcement learning method. Later, Li et al. [55] measured the energy consumption of two bio-inspired fish-like robots swimming in a staggered configuration and suggested that when the tailbeat phase difference between the leader and the follower varies linearly with streamwise distance, the follower can always obtain hydrodynamic benefits; however, the mechanism proposed in this work is based on 2D theory and is not completed. Recently, through 3D direct numerical simulations and an advanced data-driven method, Seo and Mittal [66] suggested that the trailing fish can improve the LEV and thrust production of the caudal fin by interacting with the vortex rings shed by the leading fish, but the drag reduction mechanism was not deeply explored.

Although the above studies greatly improve our understanding of the hydrodynamic interactions in a fish school, the three-dimensional hydrodynamic mechanisms remain to be

completed. Because of the limitation of the numerical methods or experimental techniques, most research cannot illustrate whether the performance enhancement is due to drag reduction, thrust enhancement or saving power. In addition, it has been reported that the fish school structures in nature are highly three-dimensional [29, 67, 68]. Nevertheless, in most previous research, fish schools were limited to the horizontal plane. The hydrodynamic interactions in the vertical plane and the associated effects on the performance have seldom been explored.

1.6 Current Objectives

To deepen our understanding of hydrodynamics in fish schooling, some fundamental questions are needed to be addressed. This thesis aims to systematically examine the basic hydrodynamic interactions in a fish school and their effects on hydrodynamic performance. Thus, the current study will set out to answer the following questions:

1. What are the spatial effects on hydrodynamic interactions and performance in a fish school? In particular, what are the performance enhancement mechanisms in dense schools where fish are in close proximity to each other?
2. How will the tail-beat phase and frequency differences influence the hydrodynamic interactions and performance of high-density schools? Could we build a relationship between the performance and wake structure for a school?
3. What are the effects of three-dimensionality on hydrodynamic interactions in a fish school? Specifically, what are the fundamental hydrodynamic interactions in a fish school composed of 3D biological fish models? How will the spatial arrangement and phase difference effects influence the interactions and performance?

4. What are basic hydrodynamic interactions in a fish school arranged in three-dimensional space? Will the interactions enhance the hydrodynamic performance? If so, what are the underlying mechanisms?

The above questions will be explored in fish schools with varied spatial arrangements, tail-beat phase differences and tail-beat frequencies through comprehensive 2D and 3D direct numerical simulations. The 2D fish is modeled on a standard NACA foil, the 3D fish model is reconstructed from a live trout, and both are controlled by traveling wave kinematics. Numerical simulations are performed in a high-fidelity immersed-boundary-method-based in-house flow solver. The hydrodynamic performance and flow fields of these 2D and 3D schools will be compared and analyzed in detail to unveil the underlying physical mechanisms.

Objective 1: 2D fish schools: Study the effects of spatial arrangement on hydrodynamic interactions

Numerical simulations are employed to study hydrodynamic interactions between two-dimensional fish-like bodies under a traveling wavy lateral motion in high-density diamond-shaped fish schools. This study compares two different kinds of schools: a dense school with 0.4 BL streamwise spacing and a sparse school with 2.0 BL streamwise spacing. The lateral spacing is changed for each kind of school from 0.4BL to 1.0BL. An immersed-boundary-method-based incompressible Navier–Strokes flow solver is then employed to simulate the flow over these schools. The performance of these two kinds of schools is compared to quantify the effects of spatial arrangement. Also, the wakes of these schools are analyzed and categorized to reveal the corresponding physical mechanisms.

Objective 2: 2D fish schools: Investigate the effects of synchronization on hydrodynamic interactions in a dense school

First, the effects of tail-beat phase differences between the trailing fish and its neighboring fish on hydrodynamic interactions in a high-density school are examined by changing the phase difference from 0° to 360°. A sharp-interface immersed boundary method is used to simulate flows over the fish-like bodies and provide quantitative analysis of the hydrodynamic performance and wakes of the schools. According to the position of the trailing fish in the schools, the body of the fish has been divided into two parts, and for each part, the performance and the associated flow physics are separately presented and analyzed. Also, the characteristics of the vortex wakes are quantified, and the wake patterns are categorized and linked with the hydrodynamic performance.

Second, to explore the effects of tail-beat frequency on the hydrodynamic interactions, two kinds of high-density schools are studied: the synchronized schools, where all individuals vary the tail-beat frequency simultaneously, and the asynchronized schools in which the frequencies of three front fish are fixed while the frequency of the trailing fish changes over a wide range. To explore the relationship between tail-beat frequency and efficient swimming, the vortex wakes of these schools are quantitatively investigated by calculating the relative streamwise momentum and the momentum entrainment ratio.

Objective 3: 3D fish schools: Examine the performance and hydrodynamic interactions of fish schools arranged in the horizontal plane

A biologically realistic trout model is used to compose the two-fish in-line, side-by-side and staggered fish schools. To mimic the real fish swimming, the fish model is driven by traveling wave kinematics whose controlling parameters are drawn from the laboratory experiments. Simulations of the three-dimensional flow past the fish schools are performed in a high-fidelity DNS flow solver. By comparing the hydrodynamic performance of individual fish in the schools with that of a single fish in steady swimming, the effects of spatial arrangement on the performance

are quantified for these schools. Detailed flow analyses are conducted by providing three-dimensional structures and contour plots of vorticity, velocity and pressure on certain slices. Moreover, the phase difference effects on hydrodynamic interactions in each kind of school with a fixed spatial configuration are explored by analyzing the performance and vortex dynamics.

Objective 4: 3D fish schools: Explore the performance and hydrodynamic interactions in a fish school arranged in the vertical plane

This work uses numerical simulations to study hydrodynamic interactions between two three-dimensional trout-like fish bodies arranged in the vertical plane. The fish body is modeled on a live trout and is imposed on a traveling wave kinematics to mimic fish-like swimming. The simulations of flow past the schools are performed using an in-house immersed-boundary-method-based flow solver. The effects of spatial arrangement on hydrodynamic performance and wake dynamics in the tip-to-tip fish schools are investigated by changing the vertical distance (H) from 0.25BL to 0.65BL. Also, the effects of phase differences are examined by comparing the performance and wake structures of schools with varied phase differences.

1.7 Outline of Thesis

The layout of the remainder of the thesis is as follows:

Chapter 2 is the methodology part, which describes details of the computational fluid dynamics techniques employed in the current study. First, section 2.2 develops a fast and robust immersed boundary reconstruction method, the narrow band level-set method, for complex fish geometries. Section 2.3 introduces an efficient tree-topological local mesh refinement technique to speed up the simulations of fish school swimming, and section 2.4 provides detailed validation cases for the new algorithms. The results of Chapter 2 formed the basis of the following publications:

- Pan, Y., Dong, H., & Zhang, W. (2021, August). An Improved Level-Set-Based Immersed Boundary Reconstruction Method for Computing Bio-Inspired Underwater Propulsion. In Fluids Engineering Division Summer Meeting (Vol. 85284, p. V001T02A023). American Society of Mechanical Engineers.
- Zhang, W., Pan, Y., Gong, Y., Dong, H., & Xi, J. (2021, August). A versatile IBM-based AMR method for studying human snoring. In Fluids Engineering Division Summer Meeting (Vol. 85284, p. V001T02A039). American Society of Mechanical Engineers.
- Zhang, W., Pan, Y., Wang, J., Di Santo, V., Lauder, G. V., & Dong, H. An Efficient Tree-Topological Local Mesh Refinement on Cartesian Grids for Multiple Moving Objects in Incompressible Flow. Available at SSRN 4169528. (Submitted to Journal of Computational Physics)

Chapter 3 presents the computation results of hydrodynamic performance and wake topology of sparse and dense 2D diamond-shaped fish schools. A summary of the fish-like kinematics and the diamond-shaped school configuration is given in section 3.1. Section 3.2 presents the definitions of performance parameters, simulation setup and validation cases. The numerical results and hydrodynamic mechanisms are discussed in section 3.3. Sections 3.3.1 and 3.3.2 describes the hydrodynamic performance of a single fish and schools, respectively. The wall effect in dense schools is discussed in section 3.3.3, and the block effect is illustrated in section 3.3.4. A brief chapter summary is given in section 3.4. The results of Chapter 3 formed the basis of the following publications:

- Pan, Y., Han, P., Huang, J., & Dong, H. (2020, July). Effect of Formation Pattern on Schooling Energetics in Fish-Like Swimming. In Fluids Engineering Division Summer Meeting (Vol. 83730, p. V003T05A046). American Society of Mechanical Engineers.

- Pan, Y., & Dong, H. (2020). Computational analysis of hydrodynamic interactions in a high-density fish school. Physics of Fluids, 32(12), 121901.

Chapter 4 discusses the phase difference effects on hydrodynamic interactions in 2D diamond-shaped dense schools. The chapter begins with swimming kinematics and school configuration (section 4.1), then describes the simulation setup (section 4.2). Section 4.3 presents the hydrodynamic performance of a single fish and schools with varied phase differences and discusses the associated hydrodynamic mechanisms. In particular, section 4.3.1 presents the spatiotemporal distributions of force generation and power consumption for a single fish, and section 4.3.2 provides the hydrodynamic performance of individual fish in the schools. Sections 4.3.4 and 4.3.5 explore the vortex capture and body-body matching mechanisms, respectively. The wake patterns are categorized and linked with the performance in section 4.3.6. A summary is given in section 4.4. The results of this chapter formed the basis of the following publication:

- Pan, Y., & Dong, H. (2022). Effects of phase difference on hydrodynamic interactions and wake patterns in high-density fish schools. Physics of Fluids, 34(11), 111902.

Chapter 5 investigates the effects of tail-beat frequency on hydrodynamic interactions in 2D diamond-shaped dense schools. Sections 5.1 and 5.2 describe the swimming kinematic, school configuration and simulation setup. The hydrodynamic performance and corresponding flow analyses are presented in section 5.3. Specifically, section 5.3.1 displays the wake patterns of a single fish varying with the tail-beat frequency, section 5.3.2 studies the effects of frequency on the swimming efficiency of synchronized schools, and section 5.3.3 analyzes the relationship between frequency and efficient swimming of asynchronized schools. A summary is provided in section 5.4. The results of this chapter formed the basis of the following publication:

- Pan, Y., Wray, J., Kelly, J., & Dong, H. On the varying tail-beat frequency in a high-density fish school. *Physical Review E*, under preparation.

Chapter 6 studies the hydrodynamic interactions between two three-dimensional fish arranged in the horizontal plane. Sections 6.1 and 6.2 presents the trout-like fish model, undulating motion kinematics, school arrangements and simulation setup. The hydrodynamic performance and flow analyses are discussed in section 6.3. First, sections 6.3.1 and 6.3.2 investigate the effects of streamwise distance and phase difference on hydrodynamic interactions in an in-line school. Then sections 6.3.3 and 6.3.4 examined the effects of lateral distance and phase difference on the performance and wake of side-by-side schools. Finally, sections 6.3.5 and 6.3.6 study the effects of streamwise distance and phase difference on staggered schools. A summary is presented in section 6.4. The results of Chapter 6 formed the basis of the following publications:

- Pan, Y., Zhang, W., & Dong, H. (2022, August). Computational Modeling and Hydrodynamic Analysis of Fish Schools in Three-Dimensional Arrangements. In Fluids Engineering Division Summer Meeting (Vol. 85840, p. V002T05A024). American Society of Mechanical Engineers.
- Pan, Y., Zhang, W., & Dong, H. (2023, March) Hydrodynamic Performance and Wake Topology of Schooling Fish in Three-Dimensional Formations. *Journal of Fluids Engineering*, invited.
- Pan, Y., & Dong, H. Drag reduction and thrust enhancement mechanisms in a staggered fish school. *Journal of Fluid Mechanics*, under preparation.

Chapter 7 presents the hydrodynamic performance and wake topologies of tip-to-tip fish schools and two pitching-heaving panels in a tip-to-tip formation, respectively. First, sections 7.1 and 7.2 describe models, kinematics, tip-to-tip arrangements, and simulation setup for fish and

panel. Then section 7.3 presents the simulation results, including performance and wake structures. In particular, sections 7.3.1 and 7.3.2 study the effects of vertical distance and phase difference on hydrodynamics in a tip-to-tip fish school. Sections 7.3.3 and 7.3.4 discuss the effects of vertical distance and phase difference on hydrodynamic interactions between the two panels. Section 7.4 briefly summarizes this chapter. The results of Chapter 7 form the basis of the following publications:

- Pan, Y., Zhang, W., & Dong, H. (2023, March) Hydrodynamic Performance and Wake Topology of Schooling Fish in Three-Dimensional Formations. *Journal of Fluids Engineering*, invited.
- Pan, Y., Dong, H. Propulsive performance of unsteady tandem bio-inspired panels in a tip-to-tip configuration. *Physics of Fluids*, under preparation.

Chapter 8 summarizes the conclusions of the current computational studies and points toward future work.

2 Methodology

2.1 Numerical Method

The governing equations of the flow problems solved in this work are the 2D or 3D incompressible viscous Navier-Stokes equations, written in the indicial form as

$$\frac{\partial u_i}{\partial x_i} = 0, \qquad \frac{\partial u_i}{\partial t} + \frac{\partial u_i u_j}{\partial x_j} = -\frac{\partial p}{\partial x_i} + \frac{1}{Re}\frac{\partial^2 u_i}{\partial x_i \partial x_j} \tag{2-1}$$

where $i, j = 1,2$ or 3, and u_i are the velocity components in the x-, y-, and z-directions, p is the pressure, and Re is the Reynold number.

The incompressible flow is solved using a finite-difference-based immersed boundary method (IBM) [69]. Specifically, the equations are discretized in space using a cell-centered, collocated arrangement of the primitive variables, u_i and p, and integrated in time using a fractional step method [70, 71]. A second-order Adams-Bashforth scheme is used to discretize the convection terms, and an implicit Crank-Nicolson scheme is employed for the viscous terms to eliminate the viscous stability constraint. The flow is simulated on non-conformal Cartesian grids, and boundary conditions are precisely imposed on the immersed boundary through a multi-dimensional ghost-cell technique. This numerical method has been successfully applied in many simulations of applied to simulate biological fish swimming [33, 72], fish-like swimming [31, 64, 73-75] and other flapping propulsions [76-80]. More details about this method are provided in Ref. [69], and the validation cases can be found in section 2.4.

2.2 Narrow-Band Level-Set-Based IB Reconstruction

Immersed boundary (IB) methods have been widely used to study bio-inspired flows, including insect flight, fish swimming, and biomedical problems, often involving complex body

morphologies and moving boundaries. For such flows, the unstructured surface mesh is employed to present the body shape, and the interface between the solid body and the fluid at each time step is detected by the immersed boundary reconstruction process, which directly determines the efficiency and quality of the simulations [69]. For some bio-inspired underwater propulsion problems, the geometries of the immersed bodies can be complex, with sharp concave and convex parts. Identifying the interior and exterior nodes for complex body morphologies is challenging, and incorrectly labeling the fluid and solid nodes can ruin the simulation. Besides, in real fish swimming simulations, the Reynolds number can reach $O(10^6)$ or above, which requires dense body mesh and fine-enough Cartesian mesh. The computation domain can also be extremely large when involving multiple swimmers. Hence, the computational cost for IB reconstruction at each step is expensive. A fast, accurate and versatile IB reconstruction method is necessary for studying bio-inspired underwater propulsion.

Mittal et al. [69] employed a direct searching method to determine fluid and solid nodes, reconstructing the interface by sweeping through all the triangular body meshes and finding all Cartesian points near the boundary. The exterior (fluid) and interior (solid) points can be separated according to the sign of the dot-product of the vector extending from the centroid of a triangular element to its closest node with the surface normal of the element. The computational cost of this method is in the order of $O((L_D/\Delta x)^5)$ [81], where L_D is the characteristic length and Δx is the minimum mesh size. The computational consumption will be very high when the Cartesian mesh is dense or the computation domain is large. In addition, Senocak et al. [82] found that the method may fail when the differences in the size of triangular surface elements are large. To improve the robustness and efficiency of detecting immersed boundaries, Deng et al. [81] proposed a level-set-based fast reconstruction method for complex moving boundaries with the 3D finite-difference

sharp-interface immersed boundary method, which we call LS-IBM in the thesis. In their work, the immersed boundary is identified by calculating the signed distance value, stored in the level set function, of grid points near the solid boundaries and propagating the values to the surrounding domain. The computational cost is reduced from $O((L_D/\Delta x)^5)$ to $O((L_D/\Delta x)^3)$ comparing with the standard IB method.

In this work, we further improve the efficiency of immersed boundary reconstruction by developing a narrow-band level-set-based immersed boundary method (NBLS-IBM) and then apply the new method to some underwater propulsion problems. In the previous LS-IBM [81], the level set values of other grid points in the computational domain are obtained by propagating the signed distance values of points in the immediate vicinity of the immersed boundary. The computational cost of this operation is $O((L_D/\Delta x)^3)$, and the operation is required at every time step in a simulation. However, to identify the solid and fluid nodes, we only need to update the level set values near the immersed boundary at the current time step and directly use the level set values passed on from the precious time step for other grid points. Thus, we employ the narrow-band technique[83] to speed up the boundary reconstruction process. By building a thin band around the zero-level set, the computations are only performed on the points in this band, which reduces the computation cost from $O((L_D/\Delta x)^3)$ to $O(k(L_D/\Delta x)^2)$ [84], where k is the number of cells in the narrow band. In the meantime, the NBLS-IBM inherits the accuracy and robustness of LS-IBM demonstrated in Ref. [81]. Next, we present the NBLS-IBM in detail and apply it to the boundary reconstruction for some underwater propulsion problems with complex moving boundaries, like dolphin-like and shark-like body reconstructions.

2.2.1 Numerical Algorithm

In the LS-IB reconstruction method, the level set values are updated for each grid point in the computation domain after calculating the signed distance values of grid points in the immediate vicinity of the solid boundary. The central idea of the narrow-band method is to build a thin band around the zero-level set and to update the level-set values of the Cartesian grids located in this band, which reduces the computational complexity of propagating level-set values to $O(k(L_D/\Delta x)^2)$.

The level set function is smooth [85] and is denoted as φ, recording the signed distance values of any grid point to the interface between the solid body and the fluid. $\varphi = 0$ is the interface, $\varphi < 0$ denotes the fluid, and $\varphi > 0$ represents the solid body. The LS-IBM described in the previous study [81] contains four steps. The difference between the current method and the previous LS-IBM is mainly in the third step. For the completeness of the paper, we still list all four steps here and highlight the changes.

- **Step 1**: Go through all the elements of the immersed boundary, and determine their positions by checking their coordinates along the *x*, *y* and *z* grid lines of the Cartesian mesh. In the above process, the neighbor grid points near the solid boundary have been searched and recorded with the corresponding elements. In Fig. 2-1, the circles and squares represent the fluid and solid points, respectively. And the neighbor points are labeled by solid red circles and squares. The computational cost of this step is $O((L_D/\Delta x)^3)$.
- **Step 2**: For each neighbor point, find the closest element and calculate the signed distance value (level-set value) to the element. The signed distance values of other Cartesian points within the researching area in Fig. 2-1 are also calculated. Figure 2-1 marked the searching area by the dashed lines and the searching points with hollowed red circles and squares. In

this step, the updated level-set values may be incorrect, which can jeopardize the reconstruction of the interface and crash the simulation. In case of that, we check the level-set values one by one and fix the failed point by averaging the level-set values around the point.

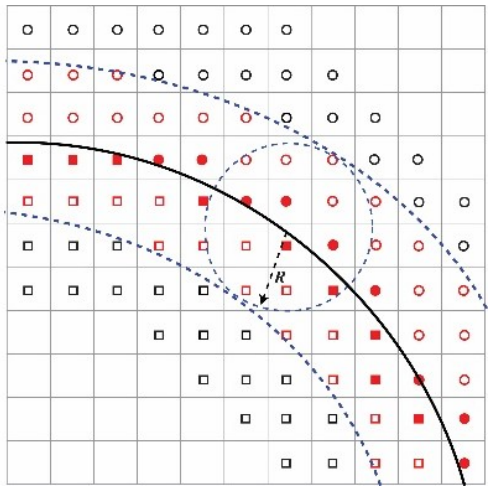

Figure 2-1. Schematic of searching the neighbor points. The dark solid line denotes the immersed boundary, and the blue dashed lines border the searching area. The circles and squares represent the fluid and solid points, respectively.

- **Step 3**: Use the labeled neighbor points to build a narrow band and propagate level-set values to other points in this band. In this work, we set the width of the band as four; that is, the level set values propagate forward and backward for two grids in each direction, respectively. The dashed blue line borders the narrow band in Fig. 2-2. For other points in the narrow band, the calculation of level-set values is as follows,

$$\begin{cases} \varphi^{n}_{I,J,K} = \dfrac{sum\varphi^{u}}{m} + sgn(sum\varphi^{u}) \times dist\varphi \\ sum\varphi^{u} = \displaystyle\sum_{i=I-1}^{I+1} \sum_{j=J-1}^{J+1} \sum_{k=K-1}^{K+1} \varphi^{u}_{i,j,k} \\ dist\varphi = \sqrt{\left(\overline{x^{u}} - x_{I,J,K}\right)^{2} + \left(\overline{x^{u}} - x_{I,J,K}\right)^{2} + \left(\overline{x^{u}} - x_{I,J,K}\right)^{2}} \\ max\{|I - I_0|, |J - J_0|, |K - K_0|\} \leq 2 \end{cases} \tag{2-2}$$

Here $\varphi^{n}_{I,J,K}$ is the level-set value at the gird (I, J, K) that is to be updated by the neighboring grids with the updated level set value $\varphi^{u}_{i,j,k}$, m is the number of cells in the summation. $\overline{(\cdot)}$ denotes the averaged center of the updated grids around the new point. (I_0, J_0, K_0) is the neighbor point in the immediate vicinity of the solid boundary, and $max\{|I - I_0|, |J - J_0|, |K - K_0|\} \leq 2$ represents that the bandwidth is four.

- **Step 4**: Use the level-set value to decide the status of each grid point. As mentioned before, $\varphi > 0$ represents the solid points, and $\varphi < 0$ denotes the fluid points.

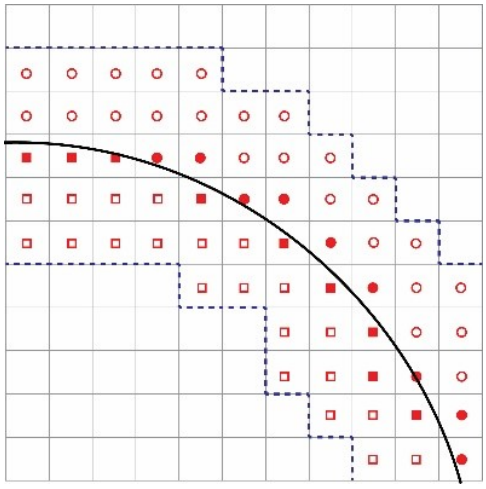

Figure 2-2. Schematic of propagating the level-set values to all points in the narrow band.

In the initial time step of a simulation, the IB reconstruction is conducted by directly calculating the level-set values of grid points in the whole domain. The initialized level-set function stores accurate level-set values for all grid points. After that, by building a narrow band

around the IB, the level-set values are only updated for the points in this band at each time step. The level-set values of grid points outside the narrow band can be directly passed on from the previous time step to the current time step. In this way, the computational cost of the third step is reduced to $O(k(L_D/\Delta x)^2)$. Finally, the fluid/solid grid status can be determined from the sign of the level-set value.

2.2.2 Dolphin-Like Body and Shark-Like Body Reconstructions

A. Dolphin-Like Body Reconstruction

The reconstruction of a dolphin-like body in steady swimming is applied to demonstrate the higher efficiency and reliability of the NBLS-IBM. A comparison of reconstruction time for the dolphin-like body reconstruction has been conducted by applying LS-IBM and NBLS-IBM to different Cartesian meshes. The total number of surface elements of the dolphin body is 59,968, and the unstructured surface mesh is shown in Fig. 2-3(a). The Cartesian grids are 16.6 million, 48.7 million, and 146.2 million, respectively, and the corresponding smallest Cartesian mesh dimensions are 0.028, 0.021, and 0.015.

The time for reconstructing the immersed boundary at one time step for each case is listed in Table 2-1. We use the Δt to denote the time saved by the NBLS-IBM compared to the LS-IBM and use the ratio of Δt to the time for IB reconstruction by using LS-IBM to represent to what extent the IB reconstruction efficiency has been improved.

Table 2-1 shows that the time saved by the NBLS-IBM changes from 48.1% to 63.7% for different Cartesian meshes. It demonstrates the narrow-band level-set method is much more efficient than the original LS-IBM. Next, we present the unstructured mesh on a dolphin-like body, the calculated zero-level-set body shape, and the reconstructed immersed boundary of the case

with 146.2 million Cartesian mesh in Fig. 2-3. Figure 2-4 shows three slices of the level-set contour around the dolphin-like body at the front, middle and tail of the body. Figures 2-3 and 2-4 demonstrate that the immersed boundary can be precisely detected using the NBLS-IBM.

TABLE 2-1. IB construction time for each case in dolphin swimming.

Cartesian grids (million)		16.6	48.7	146.2
Time(sec) for IB reconstruction	LS-IBM	7.99	21.45	97.76
	NBLS-IBM	3.90	11.13	35.49
Time-saving		51.19%	48.11%	63.70%

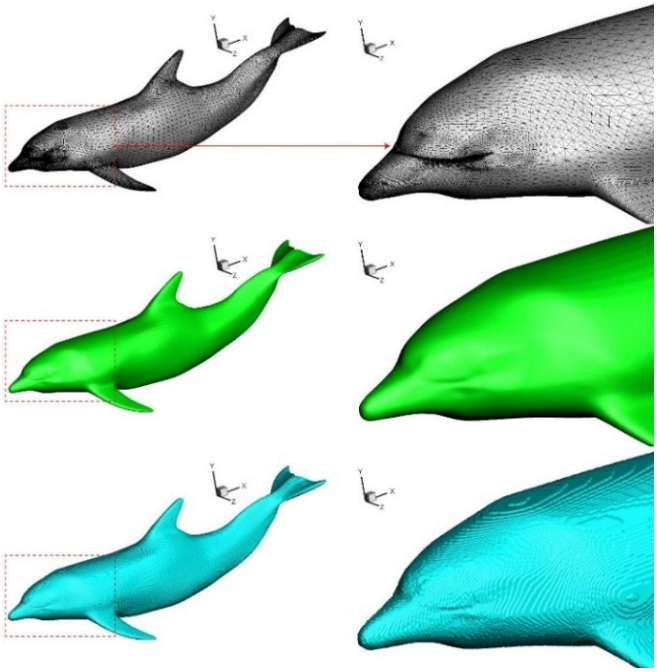

Figure 2-3. IB reconstruction process of a dolphin-like body, (a) unstructured mesh on a dolphin-like body, (b) the calculated zero-level-set body shape, and (c) the reconstructed immersed boundary built on the Cartesian mesh.

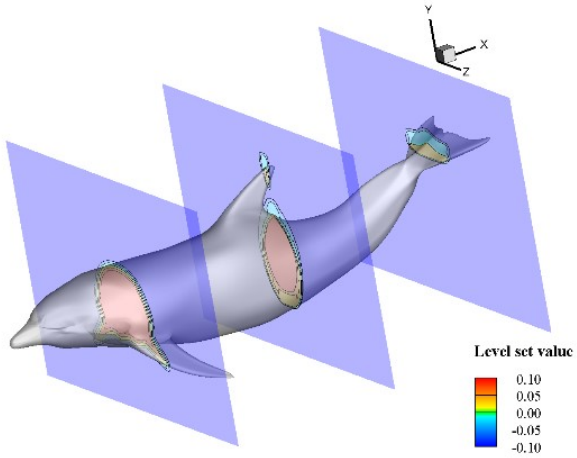

Figure 2-4. Level-set contour slices are at the front, middle and tail of a dolphin-like body.

B. Shark-Like Body Reconstruction

In this part, we tested the boundary reconstruction time for a shark-like body with 107K triangular surface elements, as shown in Fig. 2-5(a), immersed in the Cartesian meshes with 24.8 million, 48 million, 97.6 million and 196.4 million computational grids, respectively. The smallest Cartesian mesh dimensions for each case are 0.021, 0.016, 0.013, and 0.010.

The results are listed in Table 2. The maximum time-saving is 64.6% and is reached when the Cartesian grids are 48 million, showing the higher efficiency of the NBLS-IBM compared to the original LS-IBM. It also implies that the matching between the body and Cartesian mesh may affect the reconstruction speed, which will be explored in the future. Similar to the reconstruction of the dolphin-like body, we present the IB reconstruction process for the shark-like body in Fig. 2-5, including the unstructured mesh on the body surface, the zero-level-set body shape and the reconstructed immersed boundary built on the Cartesian mesh. Besides, the three slices at the front, middle and tail of the shark-like body of the level set contour around the body are shown in Fig. 2-6.

TABLE 2-2. IB construction time for each case in shark swimming.

Cartesian grids (Million)		24.8	48	97.6	196.4
Time(sec) for IB reconstruction	LS-IBM	8.71	9.52	32.47	42.94
	NBLS-IBM	3.08	5.45	12.74	29.37
Time-saving		64.64%	42.75%	60.76%	31.60%

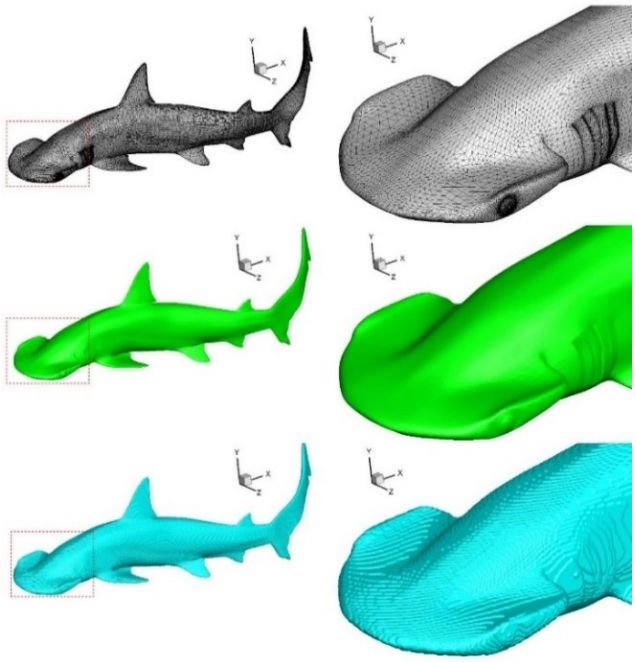

Figure 2-5. IB reconstruction process of a shark-like body, (a) the unstructured mesh on a shark-like body, (b) the calculated zero-level-set body shape, and (c) the reconstructed immersed boundary built on the Cartesian mesh.

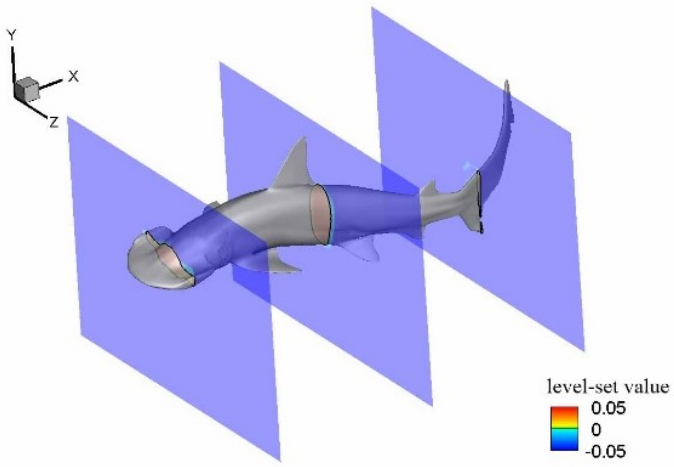

Figure 2-6. Level-set contour slices are at the front, middle and tail of a shark-like body.

2.3 Tree-Topological Local Mesh Refinement Method

We develop a tree-topological block-based mesh refinement method (TLMR) on Cartesian grids to simulate biofluid flow with multiple moving objects. The discretized equations are solved iteratively on the refinement mesh with ghost-cell communication between blocks, enabling parallel computation on a distributed memory system. For better accuracy and faster convergence, the momentum equation is solved on non-overlapped refinement meshes, while the Poisson equation is solved on overlapped meshes, recursively from the coarsest block to the finest ones, or parallelly using a Schwarz method if child blocks of the same tree node are connected. Convergence studies show that the algorithm is second-order accurate in space for both velocity and pressure. TLMR enables a fast solution to an incompressible flow problem with complex boundaries or multiple moving objects.

2.3.1 Meshes for TLMR

The tree-topological block refinement mesh can be introduced using the example in Fig. 2-7(a), where a fish school is swimming. Instead of having a uniform mesh for the computational domain, we can gradually refine the mesh around the fish with refined blocks. In Fig. 2-7(a), one block

with the background Cartesian grids covers the whole computational domain. Then another block covers the school with an additional refinement block around each adult swimmer for better resolution. To better resolve the body-body/fin interaction of the baby and adult swimmers, one more refinement block can be placed around the baby swimmer. If the wake is of interest, an additional refinement block is placed in the far wake region.

The above mesh refinement has nested the fine blocks inside a coarse one. This approach balances the need for desired resolution around solid boundaries and the simplicity of communication between refinement blocks. The parent and child hierarchy of refinement blocks resembles a tree topology, which can be employed to describe the connectivity between these blocks. In this description, as referenced in Fig. 2-7(b), each refinement block is a tree node, and its refinement block is its child node. We may further require that each node can have only one parent block, meaning that a refinement block is located inside a coarse one. This restriction may degrade slightly the flexibility of adding refinement blocks but can greatly simplify information communication between the blocks because of the simplified connection. The child blocks under the same parental node may also be connected, such as B1-B2 on Level 1 or B3-B4 on Level 2 in Fig. 2-7(b). An additional dash line is added for such intralayer-connected blocks. The boundary-induced mesh refinement for biofluid simulation often adopts a fixed hierarchical mesh refinement and does not need to be changed during the simulation. These predetermined meshes can avoid the overhead of dynamic allocation and deallocation of grids in a standard AMR technique.

Meshes in the refined block are obtained by subdividing that of the coarse block in each direction by a factor of two. Hence, a three-dimensional cell will have eight subcells or four for a two-dimensional case. By adjusting the resolution of background meshes and the total levels of

refinements, the local refinement approach can provide the necessary grid resolution without significantly increasing the overall grid size.

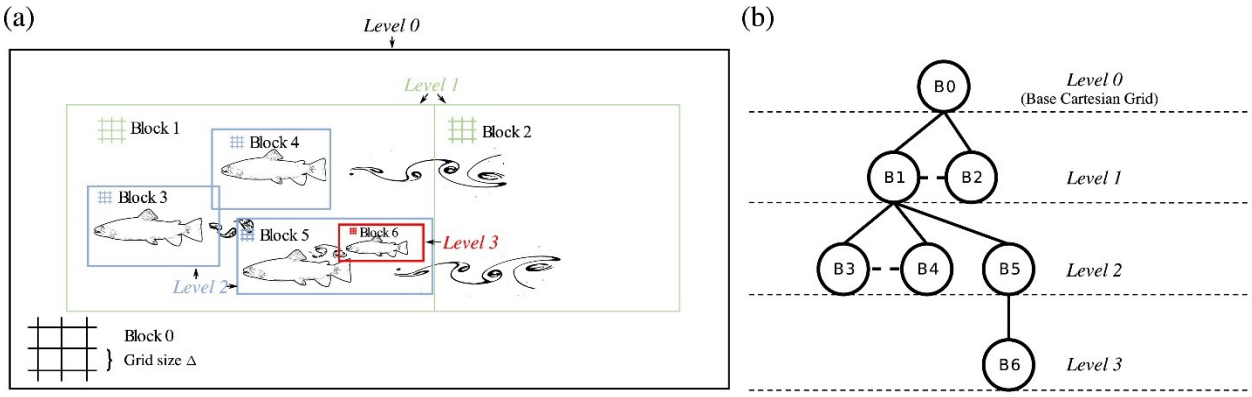

Figure 2-7. Schematic of a tree-topological block-based mesh refinement for flow with multiple moving objects: (a) a biofluid flow problem with local block refinement and (b) a tree topology for the refinement blocks, with solid lines denoting interlayer connections and dash lines for intralayer connections.

2.3.2 Discretization on TLMR Meshes

The discretized momentum and Poisson equations on the Cartesian grids can be reformulated to the following form

$$a_W\psi_W + a_E\psi_E + a_C\psi_C + a_N\psi_N + a_S\psi_S = RHS, \tag{2-3}$$

where $\psi_{(\cdot)}$ is the discretized value for velocity or pressure and $a_{(\cdot)}$ is the corresponding coefficient in the discretized equations. The discretization scheme requires a ghost cell when performed at the boundary of each block. Similar to a domain decomposition approach in parallel computing, a layer of ghost cells is arranged at the block interface, as illustrated in Fig. 2-8(b). A block may have an outer ghost cell layer if it resides in a coarse block and multiple inner ghost cell layers if it contains refined blocks.

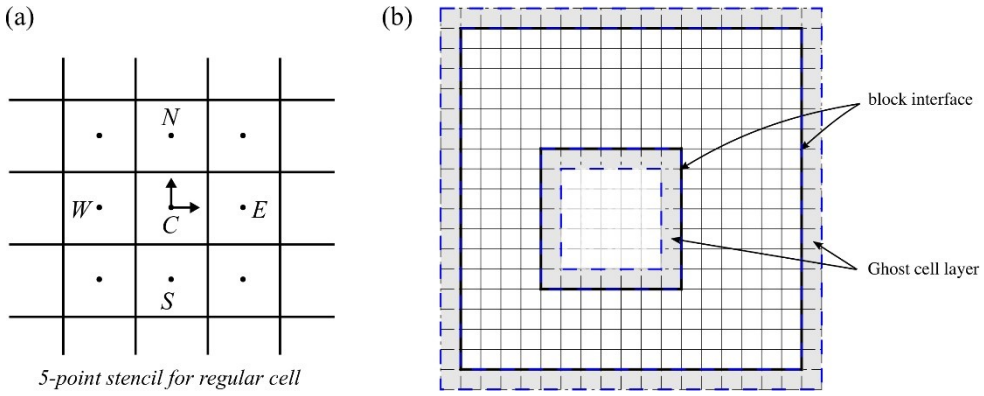

Figure 2-8. Illustration of discretization stencil and the ghost cell arrangement for a refined block: (a) a 5-point discretization stencil for a fluid cell and (b) the arrangement of ghost cell layers (shaded) around the block interfaces.

The discretized equation (2-3) can be solved using an iterative algorithm to achieve a convergent solution on all blocks. Some iterative methods, such as Jacobi or successive over-relaxation (SOR), can be adopted, or one can use the popular Krylov subspace methods, such as the generalized minimal residual method (GMRES) [86] and the biconjugate gradient stabilized method (BiCGSTAB) [87]. In this study, an incomplete LU factorization method, modified strongly implicit procedure (MSIP) [88-90], is adopted for its simple implementation and fast convergence. The MSIP algorithm is threaded for a multi-core computer system to further improve computation speed.

To proceed with the iterative procedures on the block refinement meshes, ghost cell values need to be synchronized among the distributed memories. Two types of block connections, shown in Fig. 2-7(b), are considered for the communication between blocks. The first is the interlayer connection of two blocks between two different refinement levels, and the second is the intralayer connection of two blocks in the same refinement level.

2.3.3 Efficient Poisson Solver on the TLMR Meshes

For fast convergence, a multigrid method [91, 92] is employed on block refinement meshes on a shared memory system. The main idea of multigrid to accelerate the convergence of an iterative method is to improve the fine grid solution by a global correction obtained on a coarse grid.

For the interlayer-connected blocks, the Poisson equation is solved recursively from the coarse block to the fine ones. The Poisson equation is first solved on the coarsest block and then the finer blocks, where the latter proceeds as its boundary values are interpolated from the former. For computation efficiency, the boundary value is synchronized at every iteration instead of waiting for the convergence of its parent block. When intralayer-connected blocks appear, the Schwarz approach [93] almost leverages the full power of a multigrid algorithm and converges much faster than a domain decomposition approach. The two-interfacial exchanging approach allows much more efficient information exchange across the overlapped refinement blocks during the multigrid sweeps.

The procedures for efficiently solving the discretized Poisson equation on the TLMR meshes are summarized as follows:

Procedure 1 Procedures to solve the Poisson equation on the TLMR meshes

---

1. Initialize the Pressure by guessed ϕ^0
2. Compute the divergence rate $\nabla \cdot \boldsymbol{u}^*$ by the Poisson equation on each block with values in the refined regions synchronized from fine blocks.
3. Enforce boundary conditions around the computational domain.
4. Continue following iterations.

(a) For each refined block, synchronize values ghost cell layer from the coarse parental block. If an intralayer connection exists, replace values of the ghost cell layer of the connected region from the connected block.

(b) Enforce boundary conditions around the immersed solid via an IBM method.

(c) For each refinement block, solve the Poisson equation on the Cartesian grids using a multigrid method and accelerate the computation with multithreading if needed.

(d) Check the convergence of the Poisson equation: if yes, exit iteration; otherwise, return to step 4a.

2.4 Validation Study

In this section, 2D and 3D canonical flow problems with moving boundaries are simulated and compared with experimental results to validate the current solver.

2.4.1 Two-Dimensional Flow Past Flapping Foil

To validate the current flow solver, we simulated flow past solitary foil and two side-by-side foils in pitching at $Re = 4700$ and compared the results with previously reported experimental data[42]. Figure 2-9(a) compares the thrust coefficients of the solitary pitching foil between the experiments and simulations at different St, and Fig. 2-9(b) presents the normalized cycle-averaged thrust of the bottom foil (Foil 1 in Ref. [42]) in a two side-by-side foil configuration with phase difference φ varying from 0°to 360° at a lateral distance of $D^* = 0.25$ and a Strouhal number of $St = 0.25$. Figure 2-9(c) compares the wake structures of side-by-sdie pitching foils at $\varphi = 0°$, obtained from the simulations (Left) and experiments (Right). The comparisons suggest that the simulation

results are good agreement with the experiment data both for performance calculation and vortex structure visualization, and validate the accuracy and reliability of the current solver.

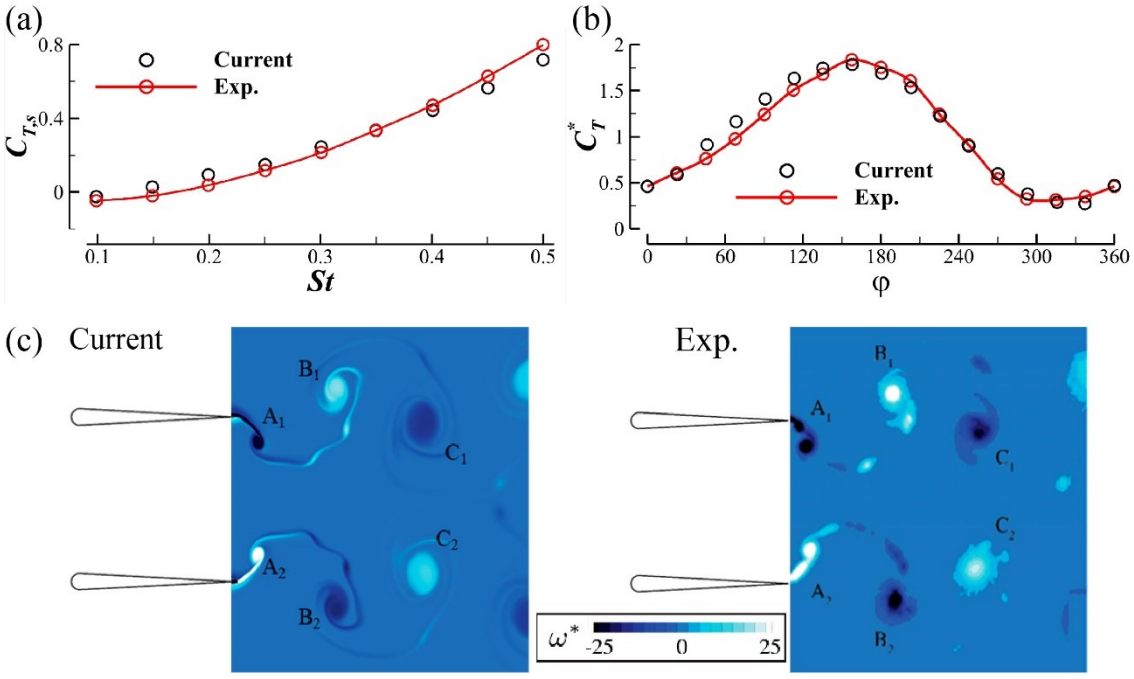

Figure 2-9. (a) Thrust coefficient $(C_{T,s})$ of solitary foil pitching at different St, (b) normalized cycle-averaged thrust coefficient (C_T^*) of bottom foil (Foil 1) in a two side-by-side foil configuration pitching at $St = 0.25$, $Re = 4700$ from current flow solver and experimental measurements [42] and (c) vorticity contours of two side-by-side foils pitching at a lateral distance of $D^* = 0.25$ and a phase difference of $\varphi = 0°$ obtained from the current flow solver (Left) and the experiments (Right).

2.4.2 Three-Dimensional Flow Past Pitching Panel

In this section, we simulate three-dimensional flow past a trapezoidal pitching panel. For a fair comparison, the panel geometry and kinematics are the same as the experiments conducted by King et al. [94]. The geometry of the panel is shown in Fig. 2-10(a), and the associated parameters are listed in Table 2-3. c is the cord length of the panel and is chosen as the reference length. All

dimensions are scaled respectively. The panel pitches around the leading edge following a sine wave at a frequency of $f = 1Hz$ and a peak-to-peak amplitude of 15°. The Strouhal number, St, and Reynolds number, Re, are defined as $St = fA/U$ and $Re = Uc/\upsilon$, respectively, where A denotes the peak-to-peak trailing edge amplitude, U is the incoming flow velocity, and υ indicates the kinematic viscosity of the fluid. Three cases with different Strouhal numbers, 0.27, 0.37, and 0.46, are chosen from the experiments and repeated here for validation. In the simulations, the variation of the Strouhal number is accomplished by changing the incoming flow velocity, and the corresponding Reynolds numbers are $Re = 10200$, 7400, and 5800, respectively.

TABLE 2-3. Summary of the nondimensional geometry parameters in simulations.

Chord length, c	Span, b	Sweep angle	Aspect ratio, AR
1.0	2.51	45°	4.17

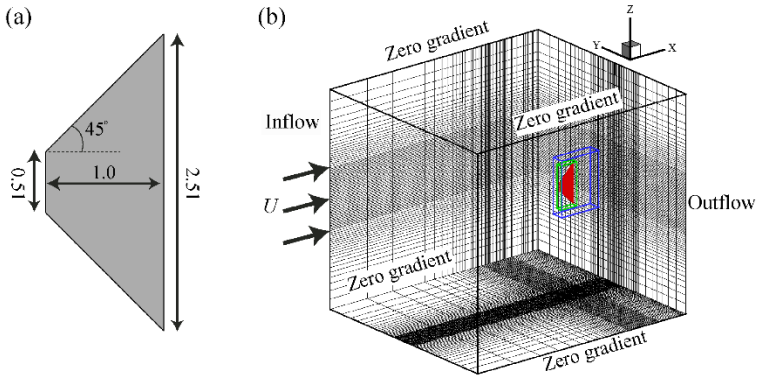

Figure 2-10. Schematic of the 3D pitching panel simulation: (a) panel geometry and (b) case setup.

The configuration for the numerical simulation, including the block refinement meshes and the boundary conditions, are displayed in Fig. 2-10(b). The domain size is $16.0c \times 14.0c \times 14.0c$ with total grid nodes around 5.68 million ($176 \times 144 \times 224$). Two layers of refined meshes are employed to resolve the flow structures at a high Reynolds number, and the resolution reaches 0.0052 around the thin plate. The total number of meshes is around 15.4 million. In contrast, the

grid number can easily go up to 1 billion ($15.4\text{M} \times 8 \times 8$) without the TLMR method. The details of the refinement blocks are summarized in Table 2-4. A constant inflow velocity boundary condition is assigned at the left-hand boundary, and an outflow boundary is imposed at the right-hand boundary. The zero-gradient boundary condition is set at all other lateral boundaries. For the pressure condition, a homogeneous Neumann boundary is applied at all boundaries.

TABLE 2-4. Summary of the nondimensional geometry parameters in simulations.

Block	Block size	Grid resolution	Grid size ($\times 10^6$)
0	$16.0c \times 14.0c \times 14.0c$	$0.0208c$	5.68
1	$2.8c \times 0.8c \times 3.6c$	$0.0104c$	4.13
2	$1.18c \times 0.4c \times 2.8c$	$0.0052c$	5.63

Figure 2-11 presents the vortex wake structures under three Strouhal numbers at two different time instances, $t = 0$ and $t = 0.25T$. Figure 2-11(a1-f1) are the experimentally observed wakes by King et al. [94] (courtesy of King et al.) using isosurfaces of Q-criterion [95]. Figure 2-11(a2-f2) shows the numerically observed wakes, which are visualized at a value of 1% of Q_{max}, and Q isosurfaces are colored by the value of the spanwise vorticity ω_z to be consistent with the experiments. The plot shows that the numerical simulation captures the main flow features of the unsteady flow observed in the experiments. For example, the spanwise vortices are shed from the trailing edge of the panel alternatively and form the reverse vortex Kármán street. The vortex street shrinks in the spanwise direction and gradually becomes disorganized as it convects downstream. At the same time, tip vortices are generated at the ends of the panel, connecting the neighboring spanwise vortices. Furthermore, the numerical simulations correctly reveal the dominant role of St in the development of wake structures. With increased St, the wakes are compressed heavier in

the spanwise direction, and the onset of wake breakdown moves upstream. For instance, at $St = 0.27$, the Q isosurface exhibits between $z/b \approx \pm 0.45$ at $x/c \approx 0.5$, and the wake breaks at $x/c \approx 1.75$ near the midspan plane [Fig. 2-11(a2)]; while at a higher St of 0.46, the Q isosurface extents from $z/b \approx \pm 0.375$ at $x/c \approx 0.5$. In addition, the vortex tube at $x/c \approx 0.75$ become twisted and weak, and the wake breakdown begins at $x/c \approx 1.2$ where the ω_z is around zero near the midspan plane, as shown in Fig. 2-11(c2).

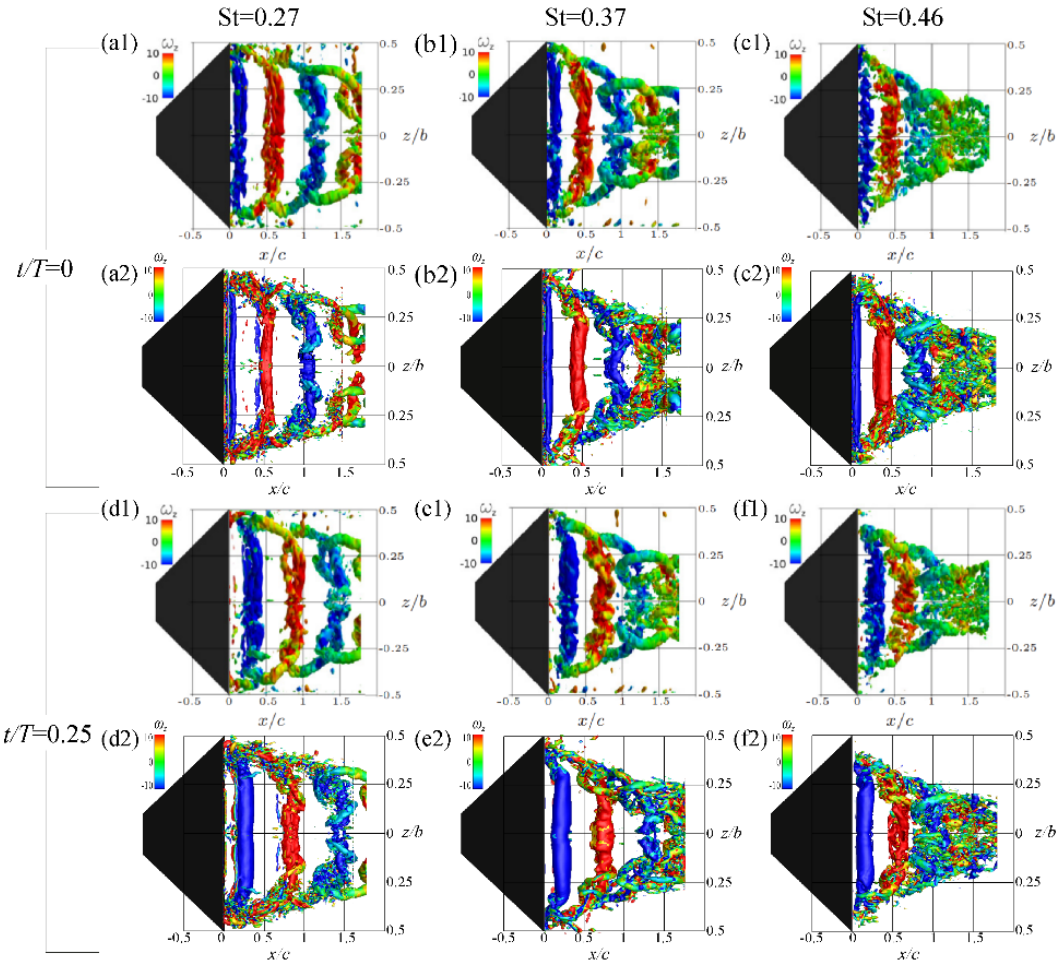

Figure 2-11. Snapshots of wake structures of the pitching panel with (a, d) $St = 0.27$, (b, e) $St = 0.37$ and (c, f) $St = 0.46$ at (a-c) $t = 0$ and (d-f) $t = 0.25$, respectively. The figures (a1-f1) are from experiments in Ref. [94], and (a2-f2) are from simulations.

In addition to the well-captured wake structures, the block-based mesh refinement technique could provide sufficient resolution to a three-dimensional high Reynolds number problem. Such as, in the aforementioned case of $St = 0.27$, the Reynold number is at the magnitude of 10^4. The forces on the pitching panels are well-resolved and plotted in Fig. 2-12. The simulation clearly shows that at higher pitching frequency (or lower St), thrust ($-C_X$) and transversal forces (C_Y) are bigger.

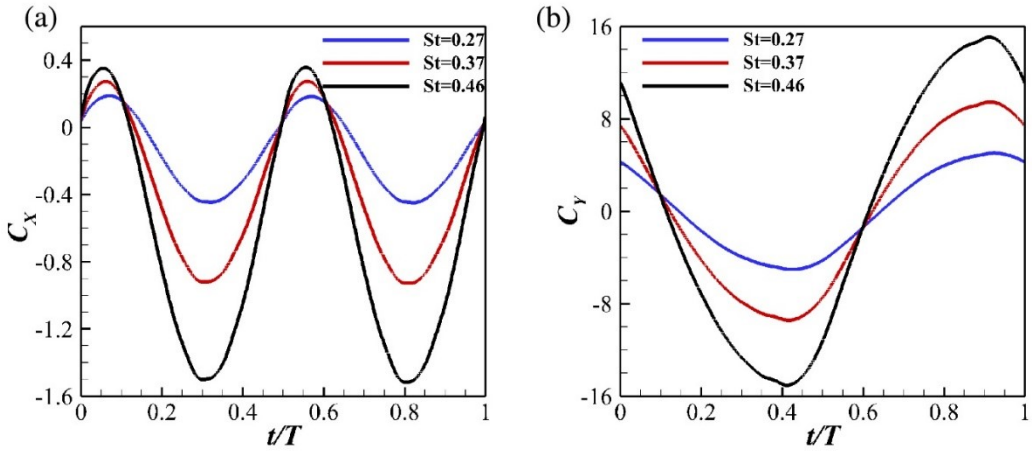

Figure 2-12. Forces on the pitching panel: (a) streamwise force C_X and (b) transversal force C_Y.

3 Effects of Spatial Arrangement on Hydroyanmic Interactions in a Fish School

Numerical simulations are employed to study hydrodynamic interactions between two-dimensional fish-like bodies under a traveling wavy lateral motion in high-density diamond-shaped fish schools. The study focuses on two different streamwise spacings: a dense school with 0.4 body length (BL) spacing and a sparse school with 2.0 BL spacing. An immersed-boundary-method-based incompressible Navier-Strokes flow solver is then employed to quantitatively simulate the resulting flow patterns and associated propulsive performance of the schools. The results suggest that a fish in the dense school achieves higher thrust production and higher propulsive efficiency than the sparse school due to a strong wall effect from neighboring fishes. Besides, results from changing the lateral spacing in the dense school have shown that the wall effect is enhanced as the lateral spacing decreases. Flow analyses have shown that the wake pattern of the fish swimming diagonally behind the leading fish in a dense diamond-shaped school transfers from 2S to 2P when the lateral spacing is smaller than 0.6 BL. As a result, an angled jet is produced behind the school and brings more momentum downstream. At the same time, the appearance of the trailing fish results in a stronger pressure region behind the leading fish and leads to a higher hydrodynamic performance of the leading fish in the dense school. The insights revealed from this study will contribute to understanding physical mechanisms in fish schools and provide a new swimming strategy for bio-inspired underwater swarm robots.

3.1 Fish-Like Kinematics and School Configuration

In this study, a NACA0012 foil is employed to represent a two-dimensional swimming body at an equilibrium state of undulating motion. To mimic fish-like swimming, traveling wave kinematics

is imposed on the foil, similar to previous work [41]. For convenience, "fish" or "swimmers" are used to refer to foils in this paper. Considering that many sorts of carangiform fish have been reported to swim in schools [28, 29], we model carangiform undulating motion in this work, and the traveling equation is:

$$y(x,t) = A(x) \cdot sin\left(\frac{2\pi}{\lambda}x - \frac{2\pi}{T}t + \varphi\right), \tag{3-1}$$

where the position variables, x and y, are normalized by the body length L, so that $x = 0$ denotes the leading edge of a fish body and the trailing edge is at $x = 1$. The chord of the original foil is regarded as the fish spine, represented by $y = 0$ at rest, and $y(x,t)$ represents the lateral deviation for any point on the midline of the fish body at time t. $\lambda = 1$ denotes the wavelength of the traveling wave over an undulating body, T is the wave period, and φ is the tail-beat phase and is set as 0° for all fish in a school in this section. $A(x)$ represents the amplitude envelope of lateral motion and is expressed as a quadratic polynomial function:

$$A(x) = a_2x^2 + a_1x + a_0 \tag{3-2}$$

Based on the experimental data [96], when the coefficients $a_0 = 0.02$, $a_1 = -0.08$, and $a_2 = 0.16$, the undulating motion can be defined as carangiform motion. Figure 3-1 presents the amplitude envelope of a carangiform motion and a sequence of midlines during one tail-beat period.

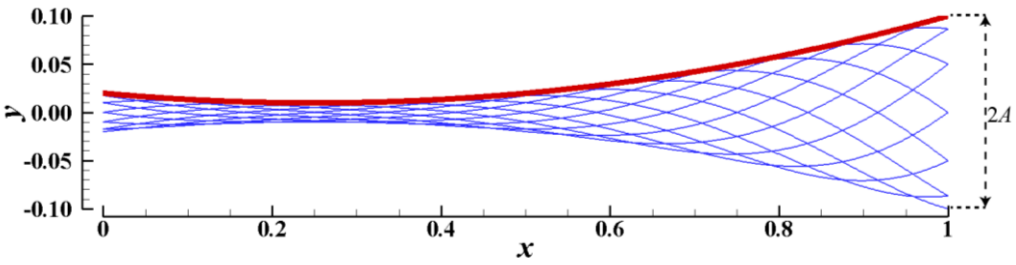

Figure 3-1. Traveling wave amplitude of a carangiform motion (red line) and the motion of the fish-body midline during one tail-beat period (blue lines). A denotes the amplitude at the tail tip.

Figure 3-2 shows the profiles of individual swimmers in a diamond-shaped school, where L is the body length and U_∞ is the swimming speed. The streamwise spacing S is defined as the distance between the tail of the leading fish (fish 1) and the head of the trailing fish (fish 4), and the lateral spacing D is defined as the spacing between the centers of fish 2 and 3, which are on the lateral sides of the school. The whole school is symmetric both in the streamwise and lateral directions. For example, the distance between the tail of the leading fish and the black point o in Fig. 3-2 (the center of the school) is $S/2$, which is half the total streamwise spacing.

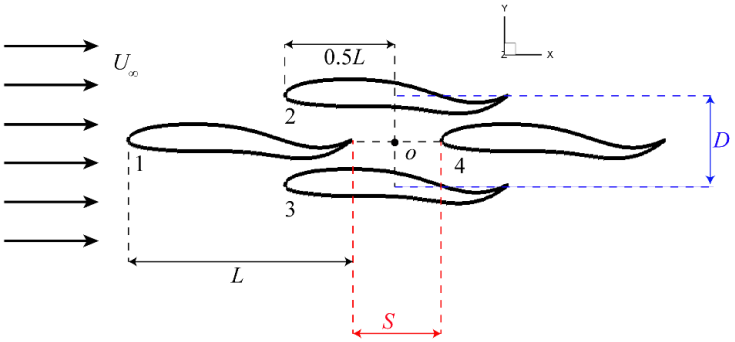

Figure 3-2. Schematic of a diamond-shaped fish school and definitions of quantities describing its spatial arrangement.

3.2 Simulation Setup and Validation Study

In this work, two key parameters characterizing fish-like swimming, the Reynolds number Re and the Strouhal number St, are defined as follows:

$$Re = \frac{U_\infty L}{v}, \tag{3-3}$$

$$St = \frac{2fA}{U_\infty}, \tag{3-4}$$

where U_∞, L, and v have the same meaning as stated above, f is the tail-beat frequency and A is the amplitude of lateral motion at the tail tip. We set the tail-beat frequency f as 1.0 and the amplitude at the tail tip A as 0.1 (shown in Fig. 3-1). The Reynolds number Re is set as 1000, a value relevant to fish swimming. In the present study, steady swimming is simulated to form a stable school formation by applying an incoming flow with constant velocity over fixed traveling wavy foils. The Strouhal number is thus obtained through Eq. (3-4) by changing the incoming flow speed U_∞ to meet the steady-swimming condition.

The definitions of the hydrodynamic forces, power consumption and propulsive efficiency are stated in the following. In our solver, the instantaneous forces are calculated by directly integrating the computed pressure and viscous stress on the surface of a fish and can be expressed as follows:

$$F_X = \int_S (-pn_x + \tau_{xi}n_i)dS\,, \tag{3-5}$$

$$F_Y = \int_S \left(-pn_y + \tau_{yi}n_i\right)dS\,, \tag{3-6}$$

where p is the pressure, the indices $i = 1,2$ denote the *x*- and *y*-direction, respectively (repeated indices imply summation), n_i represents the *i*-th component of the unit normal vector on an element dS, and τ_{ij} is the viscous stress tensor.

In Eq. (3-5), F_X is the instantaneous net force in the *x*-direction on a fish body, which is the sum of the drag F_D and the thrust F_T that are calculated by the sign of the pressure and viscous stress acting on the surface [97] with respect to the swimming direction. In this paper, considering the coordinate system and the swimming direction, when $F_X < 0$, the fish produces a net thrust. Doing integral over the surface of the fish body, the thrust F_T can be computed as follows:

$$F_T = \frac{1}{2}\left(-\int_S -pn_x dS + \left|\int_S pn_x dS\right|\right) + \frac{1}{2}\left(-\int_S \tau_{xi}n_i dS + \left|\int_S \tau_{xi}n_i dS\right|\right), \tag{3-7}$$

The power required for the undulating motion can be defined as

$$P_u = \int_S \left(-pn_i + \tau_{ij}n_j\right)\Delta u_i dS, \tag{3-8}$$

where Δu_i is the relative velocity of an element *dS* to its surrounding fluid in the *i*-th direction. The forces and power, then, can be normalized by the swimming speed and the body length:

$$C_{X,Y} = \frac{F_{X,Y}}{\frac{1}{2}\rho U_\infty^2 L}, C_T = \frac{F_T}{\frac{1}{2}\rho U_\infty^2 L}, C_{PW} = \frac{P_u}{\frac{1}{2}\rho U_\infty^3 L}, \tag{3-9}$$

The definition of propulsion efficiency of undulating swimming is still controversial and varies depending on the assumptions and conditions utilized in different studies [97-99]. In this study, a modified form of Froude efficiency η is defined to measure the ratio of useful power to the total power [100]:

$$\eta = \frac{\overline{F_T} U_\infty}{\overline{F_T} U_\infty + \overline{P_u}} = \frac{\overline{C_T}}{\overline{C_T} + \overline{C_{PW}}} \tag{3-10}$$

where the overline represents the time-averaged value during one tail-beat cycle. Here, the thrust $\overline{F_T}$ is used to calculate the propulsive efficiency of the swimming body, instead of the net force: as for steady swimming or quasi-steady swimming, the net-force-based propulsive efficiency is zero or close to zero, which results in the measurement of efficiency becoming too small and meaningless [98].

The computational domain and Cartesian computational grid for simulating flow over traveling foils are presented in Fig. 3(a). In this study, fish swim in the negative *x*-direction. The computational domain size is $20L \times 20L$, with 2337×897 grid nodes (about 2.10 million). A high-resolution uniform grid is used in a region of size $6.0L \times 3.0L$ to solve the flow field near the swimmers. The minimum grid spacing is set as $\Delta_{min} = 3.50 \times 10^{-3} L$ in this study, which is sufficiently fine at the relevant Reynolds number [101]. The left-hand boundary is the inflow boundary with a constant incoming flow velocity U_∞. At the right-hand boundary, the outflow boundary condition allows the vortices to move out of the domain without reflection. The upper and lower boundaries are set as zero-gradient boundaries with constant velocity U_∞ to represent free-stream conditions. A homogeneous Neumann boundary condition is applied for the pressure at all boundaries. In addition, a convergence study has been conducted to ensure that the results are grid-independent. Figure 3-3(b) presents the instantaneous net force coefficient in the *x*-direction for an isolated fish with three different grids. The minimum grid spacings of the coarse, medium and fine meshes are $7.04 \times 10^{-3} L$, $3.50 \times 10^{-3} L$, and $2.04 \times 10^{-3} L$, respectively. This shows that the mean force difference between the medium grid case and the fine grid case is less than 1%, which demonstrates that the simulation results are grid-independent in this study.

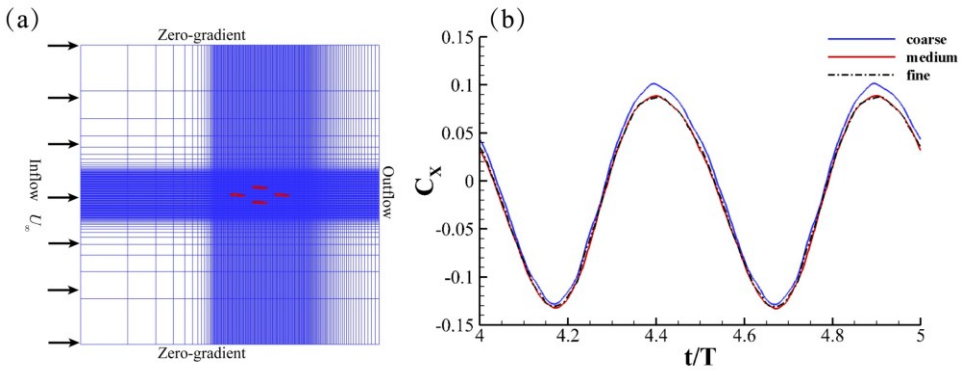

Figure 3-3. (a) Schematic of the computational domain, Cartesian grids, and boundary conditions. (b) Comparison of the instantaneous net force coefficient in the *x*-direction of an isolated fish using coarse, medium and fine meshes.

3.3 Results and Discussions

3.3.1 Steady Swimming of a Single Fish

To conveniently measure the hydrodynamic interactions, the initial condition is set as steady swimming; that is, the net force on each individual is zero at the beginning. The Reynolds number $Re = 1000$ is chosen for the following reasons: (1) the flow at this Reynolds number in two dimensions is similar to that at a much higher Re in three dimensions [34]; (2) this Reynolds number makes the viscous effect small enough but also able to contribute to maintaining a coherent vortex structure [39]. For a given Re, the time-averaged net force on a fish in the swimming direction is a function of the Strouhal number [102], so the correct Strouhal number St can be obtained by measuring the net force on an isolated fish. The Strouhal number varies from 0.3 to 0.6, as shown in Table 3-1. Figure 3-4(a) presents the time-averaged net force coefficient in the streamwise direction $\overline{C_X}$ for different Strouhal numbers. The shaded area below the dashed line denotes the increasing magnitude of the net thrust acting on the fish body. By interpolation, it is found that $St = 0.43$ satisfies the steady-swimming condition. It is also found that, for a given

Reynolds number, $\overline{C_X}$ decreases with increasing Strouhal number from 0.3 to 0.6 [see in Fig. 3-4(a)].

TABLE 3-1. Strouhal numbers tested in this study.

Re	A	f	L	St
1000	0.1	1.0	1.0	0.3, 0.35, 0.4, 0.45, 0.5, 0.55, 0.6

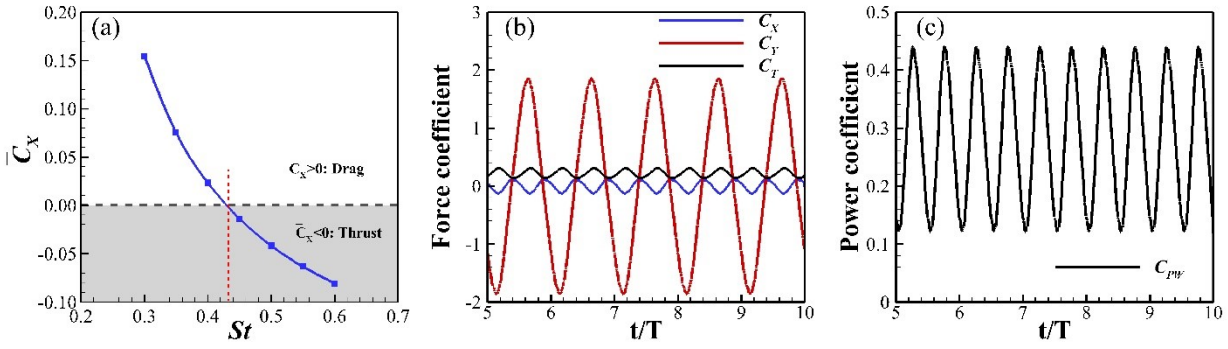

Figure 3-4. (a) Time-averaged net force coefficient in the x-direction of an isolated fish at different St, where the shaded area below the dashed line denotes the increasing magnitude of the net thrust. Time histories of (b) the net force coefficient in the x- and y-directions and the thrust coefficient, and (c) the undulating power coefficient at $St = 0.43$.

To elucidate the variation in the hydrodynamic performance of an isolated fish at $St = 0.43$, we present the time histories of the net force coefficients in the x- and y-directions, the thrust coefficient and the undulating power coefficient during five cycles in Figs. 3-4(b) and 3-4(c). The time-averaged net force coefficients can be obtained as $\overline{C_X} = -3.16 \times 10^{-4}$ and $\overline{C_Y} = -3.90 \times 10^{-4}$, which are close to zero, proving that the steady-swimming state has been reached. Figure 3-5 presents the vortex structure and the time-averaged streamwise velocity field of an isolated fish

at $St = 0.43$. For the parameters considered in this work, the vortices shed by an undulating foil form a reverse von Kármán street [Fig. 3-5(a)].

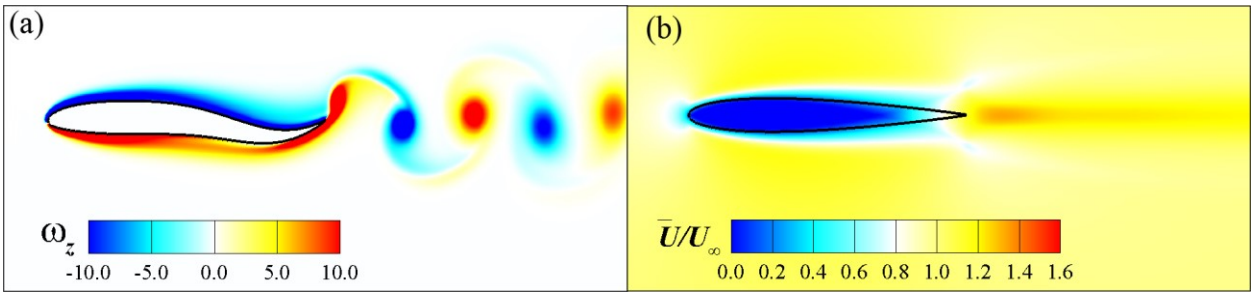

Figure 3-5. (a) Vortex wake and (b) time-averaged streamwise velocity field for an isolated fish at $St = 0.43$.

3.3.2 Dense and Sparse Diamond-Shaped Schools

When the leading fish (fish 1) and the trailing fish (fish 4) are located in the channel formed by fish 2 and fish 3 in a diamond-shaped school (see Fig.3-2), strong nonlinear body-body interactions between lateral neighbors occur, which have not yet been studied in depth. Therefore, two kinds of typical diamond-shaped schools are designed here to study the body-body interactions in a fish school. In the dense school, the streamwise spacing *S* is equal to 0.4BL, and fish 1 and fish 4 are located in the channel formed by fish 2 and fish 3. For comparison, the streamwise spacing is set as 2.0BL in the sparse school, where fish 1 and 4 are both 0.5BL away from the channel. The effect of lateral spacing on the hydrodynamic performance in a diamond-shaped school is also studied.

Figure 3-6(a) presents the time-averaged net force in the *x*-direction $\overline{C_X}$ on each fish, and Fig. 3-6(b) shows the average value of $\overline{C_X}$ of the whole school. Due to symmetry and synchronization, fish 2 and 3 have the same hydrodynamic performance, so only the results for fish 2 are presented, while the average value for the whole system is computed from the performances of all four fishes.

As illustrated in Fig. 3-6(a), in the dense school, $\overline{C_X}$ for fish 1 changes from a net thrust to a net drag when the lateral spacing D goes above 0.65, while in the sparse school, $\overline{C_X}$ for fish 1 remains almost constant at around -0.025. In the dense school, fish 2 experiences a net thrust ($\overline{C_X} < 0$) when the lateral spacing $D < 0.6$, while a net drag ($\overline{C_X} > 0$) is applied to fish 2 in the sparse school when $D < 0.55$. In both schools, $\overline{C_X}$ for fish 2 tends to zero when the lateral spacing increases. In the dense school, $\overline{C_X}$ for fish 4 is much less than zero at around -0.09, and the absolute value decreases slowly with increasing lateral distance. Fish 4 in the sparse school experiences a net thrust when $D < 0.45$ and $D > 0.8$, while it suffers a net drag when $0.45 \leq D \leq 0.8$. In Fig. 3-6(b), the average net force on the dense school is less than zero, and the absolute value decreases when the lateral spacing increases. In the sparse school, the average net force is a net drag when $0.4 < D \leq 0.7$, and becomes a net thrust when $D > 0.7$.

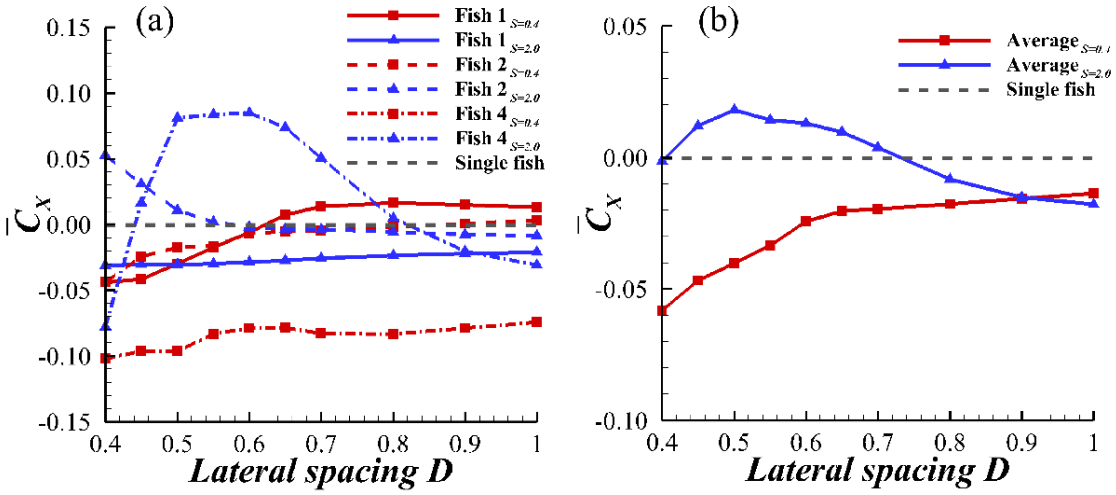

Figure 3-6. Time-averaged net force in the x-direction on each fish as a function of lateral spacing in the dense school ($S = 0.4$) and the sparse school ($S = 2.0$): (a) fish 1, fish 2, and fish 4, and (b) the average net force on the whole school. The gray dashed line denotes the time-averaged net force on an isolated fish swimming steadily.

Figure 3-7 shows the time-averaged thrust coefficient $\overline{C_T}$ for individuals in different schools as a function of lateral spacing. It is found that in both the dense and the sparse schools, $\overline{C_T}$ for each fish, and the average value over the whole school, is higher than that of an isolated fish; that is, individuals in a school can always obtain a greater thrust production regardless of their position. In addition, as shown in Figs. 3-7(a) and 3-7(b), $\overline{C_T}$ values for individuals in the dense school ($S = 0.4$) monotonically rise with decreasing lateral spacing, as opposed to those of individuals (except fish 4) in the sparse school, which only vary slightly. From Fig. 3-7(a), when the lateral spacing is less than 0.65, $\overline{C_T}$ for fish 1 in the dense school is higher than that for fish 1 in the sparse school, while this is reversed when $D > 0.65$. When $D = 0.4$, the thrust on fish 1 in the dense school is 41.3% higher than that in the sparse school. $\overline{C_T}$ for fish 1 increases by 53.2% in the dense school when the lateral spacing changes from 1.0 to 0.4, while in the sparse school, $\overline{C_T}$ for fish 1 remains at around 0.25 at all lateral spacings. Similar results are observed for fish 2, although here $\overline{C_T}$ is slightly larger than that for fish 1 at different lateral spacings in the dense school. $\overline{C_T}$ for fish 2 in the dense school increases by 56%, from 0.25 to 0.39, when the lateral spacing decreases from 1.0 to 0.4. As a comparison, the thrust on fish 2 in the sparse school shows a slight growth when the lateral spacing decreases [see Fig. 3-7(a)]. Furthermore, the difference in $\overline{C_T}$ for fish 2 between the dense school and the sparse increases with decreasing lateral spacing; when $D = 0.4$, $\overline{C_T}$ for fish 2 in the dense school is 45.8% higher than that in the sparse school.

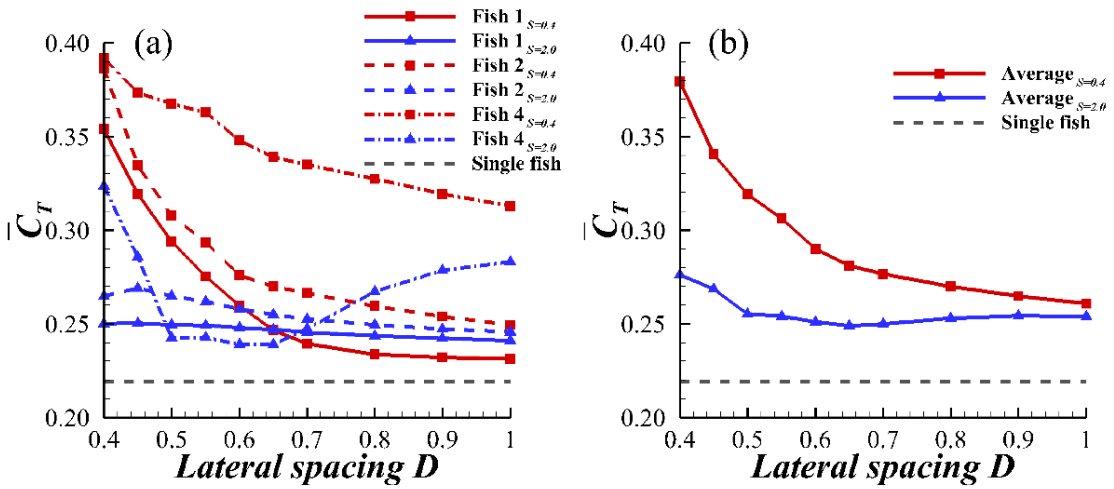

Figure 3-7. Time-averaged thrust coefficient for each fish as a function of lateral spacing in different schools ($S = 0.4$ and $S = 2.0$): (a) fish 1, fish 2, and fish 4, and (b) the average thrust on the whole school. The gray dashed line denotes the time-averaged thrust coefficient of an isolated fish swimming steadily.

In the dense school, even though $\overline{C_T}$ of fish 4 monotonically increases with decreasing lateral spacing, the rate of increase is lower than that for fish 1 and fish 2 when $D < 0.7$. In the sparse school, however, $\overline{C_T}$ for fish 4 decreases with increasing lateral spacing at lower values ($0.4 \leq D < 0.5$), reaches a plateau from 0.5 to 0.65 and shows a concave rise with the increasing lateral spacing when $D \geq 0.65$ [see Fig. 3-7(a)]. Moreover, in Fig. 3-7(b), the averaged $\overline{C_T}$ for the dense school rises monotonically, from 0.26 to 0.38, when the lateral spacing decreases from 1.0 to 0.4. Figure 3-7(b) also shows that the average thrust on the sparse school follows a similar variation to that on the dense school, although the rate of change and range of variation is much lower. When $D = 0.4$, the average $\overline{C_T}$ of the dense school is 37.4% higher than that of the sparse school, and the difference in the average $\overline{C_T}$ between the two schools reaches its maximum value.

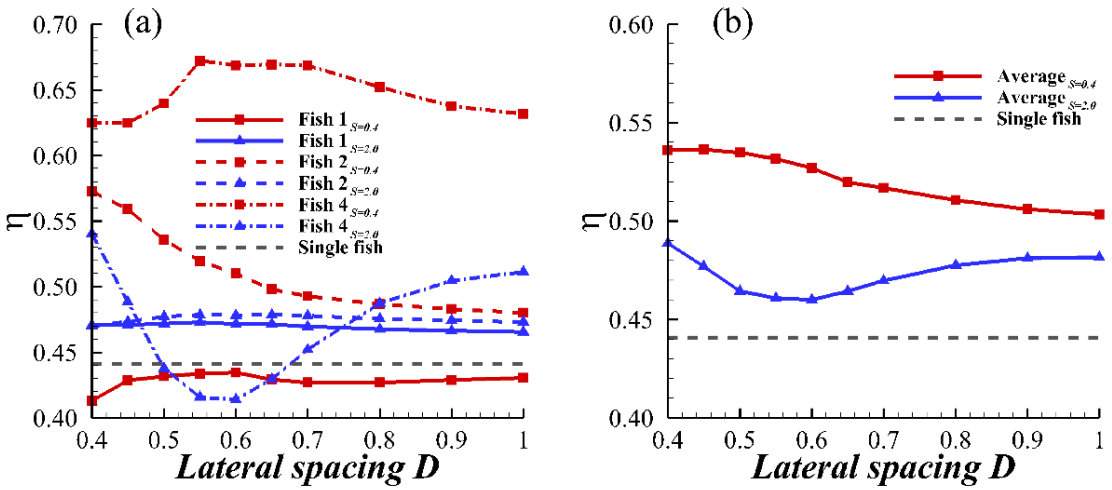

Figure 3-8. Propulsive efficiency of each fish as a function of the lateral spacing in different schools ($S = 0.4$ and $S = 2.0$): (a) fish 1, fish 2, and fish 4, and (b) the average propulsive efficiency of the whole school. The gray dashed line denotes the time-averaged propulsive efficiency of an isolated fish swimming steadily.

Figure 3-8 shows the propulsive efficiency η of each fish, and the average value of the whole school, in the two schools as a function of lateral spacing. Here, for convenience, we use the first subscript to denote the school type and the second subscript to denote the fish; the dense school has subscript 1, and the sparse school has subscript 2. For example, the propulsive efficiency of fish 1 in the dense school is denoted by η_{11}. Firstly, it can be seen that η_{11} is lower than that of an isolated fish ($\eta_{single} = 0.44$), while η_{21} is higher than η_{single} and remains at around 0.47 when the lateral spacing changes from 0.4 to 1.0 [see Fig. 3-8(a)]. When $D < 0.6$, η_{11} increases with increasing lateral spacing and then decreases slowly from $D = 0.6$ to around 0.43 when $D \geq 0.7$. Secondly, η_{12} increases by 18.8%, from 0.48 to 0.57, when the lateral spacing decreases from 1.0 to 0.4, while η_{22} remains at around 0.47. Thirdly, the propulsive efficiencies of Fish 4 show opposite trends in the dense and sparse schools [see Fig. 3-8(a)]. When $D < 0.55$,

η_{14} rises, but η_{24} falls with increasing lateral spacing. When $D = 0.55$, η_{14} reaches its maximum value $\eta_{14\_max} = 0.67$, and η_{24} reaches its minimum value $\eta_{24\_min} = 0.42$. When D increases further, both η_{14} and η_{24} reach a plateau where the propulsive efficiencies remain almost unchanged. Then η_{14} decreases when $D > 0.7$, and η_{24} rises when $D > 0.6$. In the sparse school, due to the wider streamwise spacing, Fish 4 is barely influenced by the body-body interaction imposed by its lateral neighbors but is mainly affected by the vortex wake shed by the fish in front. Thus, the opposite trends suggest that the vortex wake can impose an opposing effect on the propulsive efficiency when involving body-body interactions. Finally, the average propulsive efficiency of the dense school is at least 4.5% higher than that of the sparse school, and they are both higher than η_{single} [see Fig. 3-8(b)]. The average propulsive efficiency of the dense school η_{1a} increases by 8.0%, from 0.50 to 0.54, when the lateral spacing decreases from 1.0 to 0.4, while η_{2a} shows a similar trend to η_{24} but within a smaller range.

From Firs. 3-6(a), 3-7(a) and 3-8(a), compared with the other fish, C_X, C_T and η for fish 4 vary in a more complicated way in both the dense school and the sparse school. Being located at the rear of the school, fish 4 occupies a more chaotic flow environment and is influenced by various hydrodynamic interactions, including the lateral body-body interaction and the vortex wake interaction, which will be explored in further research.

3.3.3 Wall Effect in a Dense School

From Figs. 3-7(a) and 3-8(a), the hydrodynamic performance of fish 2 in the dense school is much better than that in the sparse school, and the difference increases with decreasing lateral spacing. In particular, when $D = 1.0$, $\overline{C_T}$ and η for fish 2 in the dense school are both 1.5% higher than in the sparse school; when $D = 0.4$, $\overline{C_T}$ for Fish 2 in the dense school is 37.4% higher, and η is 21.9%

higher. This significant improvement in hydrodynamic performance suggests a strong hydrodynamic effect acting on fish 2 in the dense school.

An experimental study by Quinn et al. [103] found that, for an oscillating foil near a solid boundary, the thrust can be enhanced by 40%, consuming little extra power when the foil is 0.4 chord lengths from the ground. Quinn et al. [104] also reported that a flexible propulsor could obtain hydrodynamic benefits when swimming near the ground. In previous research [41], it has been shown that the thrust is mainly produced at the tail for an isolated undulating foil. Thus, based on our results and those of previous studies, we assume that, in a dense diamond-shaped school, when fish 2 is close to fish 4 in the lateral direction, the body of fish 4 acts like a wavy wall to fish 2 (see Fig. 3-2). The wall effect is applied to the body-body interaction produced by lateral neighbors in a dense school and investigated in this subsection by analyzing flow fields.

It is found that the time-averaged thrust coefficient and propulsive efficiency of fish 2 in the dense school monotonically increase with decreasing lateral spacing D. In particular, when the lateral spacing reduces from 0.6 to 0.4, $\overline{C_T}$ for fish 2 in the dense school increases by 39%, from 0.28 to 0.39, and the propulsive efficiency η increases by 12%, from 0.51 to 0.57. They vary slowly when $D > 0.6$ [see Figs. 3-7(a) and 3-8(a)]. A comparison indicates that the wall effect on fish 2 in the dense school weakens with increasing lateral spacing. Thus, according to the behavior at different lateral spacings, the wall effect can be divided into two regimes: $0.4 \leq D \leq 0.6$ and $D > 0.6$. We identify a typical dense school in each regime: school A ($D = 0.4, S = 0.4$) and school B ($D = 1.0, S = 0.4$), and compare and analyze their flow characteristics.

Figure 3-9 shows the vortex fields of school A and school B at $t = 10T$. Vortices shed by an isolated undulating foil form an archetypal reverse von Kármán street (2S wake) for the parameters considered in the present study [see Fig. 3-5(a)], which can also be found in the wakes

of school A and school B (see Fig. 3-9). However, owing to the close proximity in the lateral direction, the stability has been broken, and vortex pairs are formed in the wake of school A, as shown in Fig. 3-9. A similar pairing was reported by Quinn et al. [103] when they studied a rigid pitching foil near the ground. By checking the vortex wake of all dense schools in this study, we find that the vortex wake of fish 2 and fish 3 transfer from 2S to 2P when $D \leq 0.6$, that is, the spatial arrangement can significantly change the wake pattern of a school. In addition, Fig. 3-9 shows that vortices shed by fish 2 in school A are stronger than those in school B, which means that the shedding vortices of fish 2 are enhanced when the lateral spacing is small.

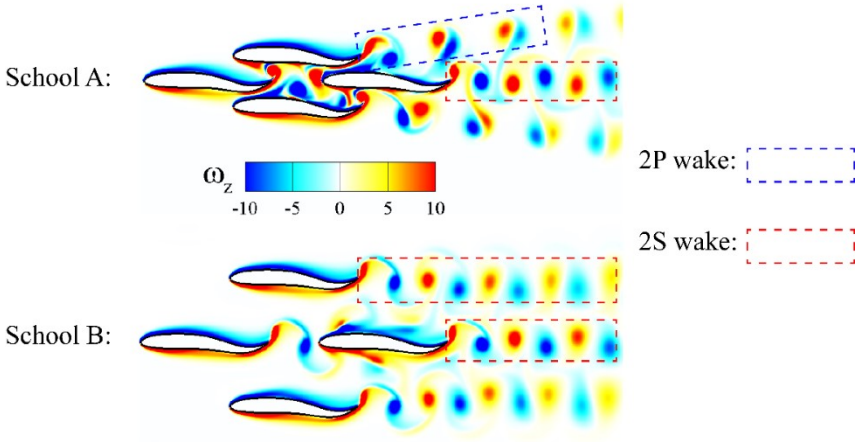

Figure 3-9. Vortex wake of school A (top, $D = 0.4, S = 0.4$) and school B (bottom, $D = 1.0, S = 0.4$) at $t = 10T$. A 2P wake is marked by a blue dashed square, and a 2S wake is marked by a red dashed square.

Two distinct phenomena relating to the vortex wake of school A are identified during the pairing process [see Figs. 3-10(a-d)]. In this study, we define the direction of a vortex pair as perpendicular to the line connecting the cores of two vortices and parallel to the advection direction, denoted by gray arrows in Fig. 3-10. Initially, from Figs. 3-10(a-d), the angle between the direction of a vortex pair shed by fish 2, and the flow direction gradually increases while the pair advects

downstream. Then, Fig. 3-10 shows that the negative (blue) vortex decays faster than the positive (red) vortex in a vortex pair, and the negative vortex has been stretched during the advection [see vortex 2 in Figs. 3-10(c) and 3-10(d)]. The method of images [103] and vortex induction theory can be applied to explain these phenomena. Figure 3-11 illustrates the formation of a vortex pair using the method of images. For each vortex shed by fish 2, there is an opposite-sign image vortex beneath the boundary (the top surface of fish 4) to satisfy the no-flux boundary condition. According to the Biot–Savart law, vortex 2 (negative) is slowed by the opposite-sign image (vortex 2′), while vortex 1 speeds up due to the induction from its image vortex. Then a vortex pair is formed because of the advection-velocity difference between vortex 1 and vortex 2. The mutual induction between vortex 1 and vortex 2 also contributes to the formation of the vortex pair. However, this mutual induction only occurs after the pairing process initiates and is thus assumed to take a secondary role. Thereafter, the mutual induction leads the vortex pair to move away from the boundary while advecting downstream.

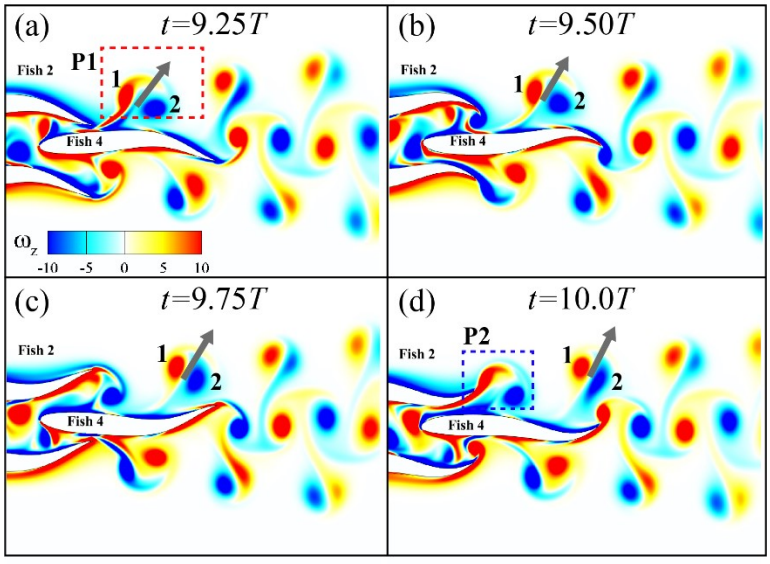

Figure 3-10. Process of vortex pairing and advection during the tenth cycle (a–d). The gray arrows denote the direction of a vortex pair. The positive vortex (red) is denoted as vortex 1, and the

negative vortex (blue) is vortex 2. P1 is the first vortex pair shed by fish 2, marked by a red dashed square in (a), and P2 is the second vortex pair, marked by a blue dashed square in (d).

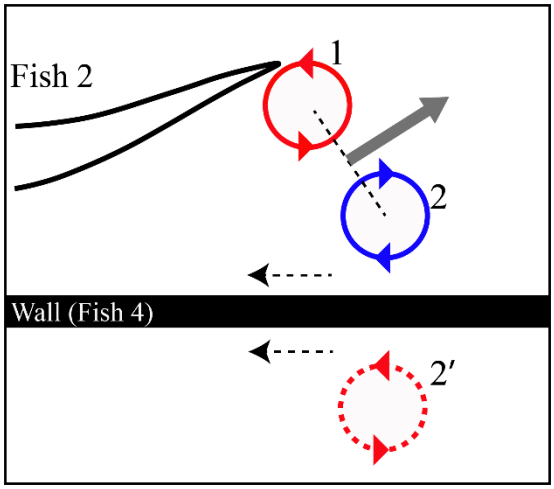

Figure 3-11. Use the method of images and vortex induction theory to explain the formation of a vortex pair. The gray arrow denotes the direction of the vortex pair, and the dashed circle is the opposite-sign image vortex. The dashed arrows denote the direction of induced velocity.

The negative vortex shed by fish 2 is stretched when moving downstream due to the mutual induction with the boundary-layer vortex of fish 4, shown by the variation of vortex 2 in Figs. 3-10(c) and 3-10(d). The boundary-layer vortex can also slow the motion of vortex 2 by induction. Furthermore, the stretching results in a decay of vortex 2, as shown in Figs. 3-10(d) and 3-12. The strength of vortex 2 thus gradually reduces while vortex 1 almost maintains its vortex strength while advecting downstream. The discrepancy in strength causes the vortex pair to rotate in an anticlockwise direction, shown in Fig. 3-12(b), which results in the advection direction of the vortex pair moving closer to the vertical. While fish 3 follows similar behavior to fish 2 because of symmetry, the signs of its shedding vortices are opposite.

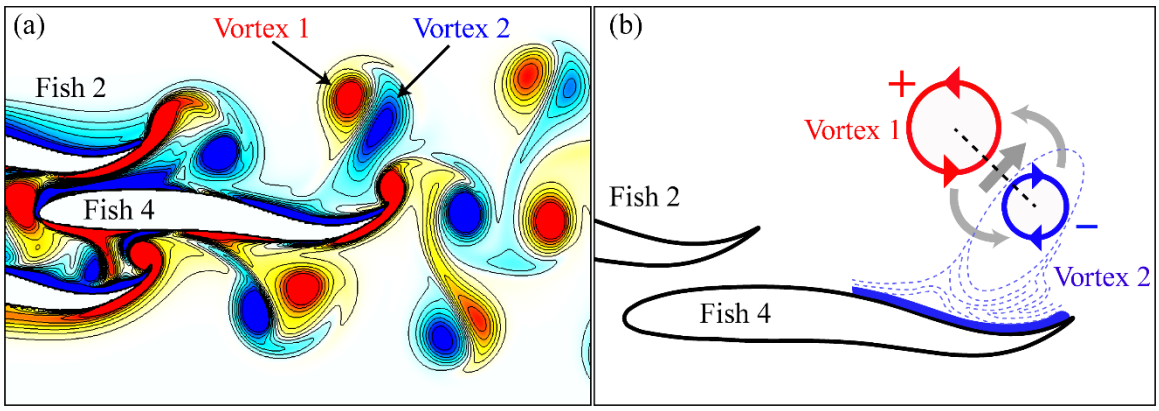

Figure 3-12. The mutual induction and the stretching of vortices illustrate the decay of the negative vortex (vortex 2) in a vortex pair and the rotation of the vortex pair. (a) A vortex pair composed of vortex 1 and 2 in the vorticity field; (b) a schematic of vortex stretching and vortex-pair rotating. The straight gray arrow denotes the direction of the vortex pair, and the curved gray arrows denote the rotating direction of the vortex pair.

The motion of the vortices delivers momentum downstream, and locomotive forces are produced. Figure 3-13 displays the time-averaged streamwise velocity field of school A and B. An angled high-density velocity jet has formed behind fish 2 and 3 in school A, which is expected when angled shedding vortices of fish 2 move downstream (see Fig. 3-10). The stronger jet indicates more streamwise momentum [105] has been transported downstream. Fish 2 in School A, therefore, has a higher thrust production.

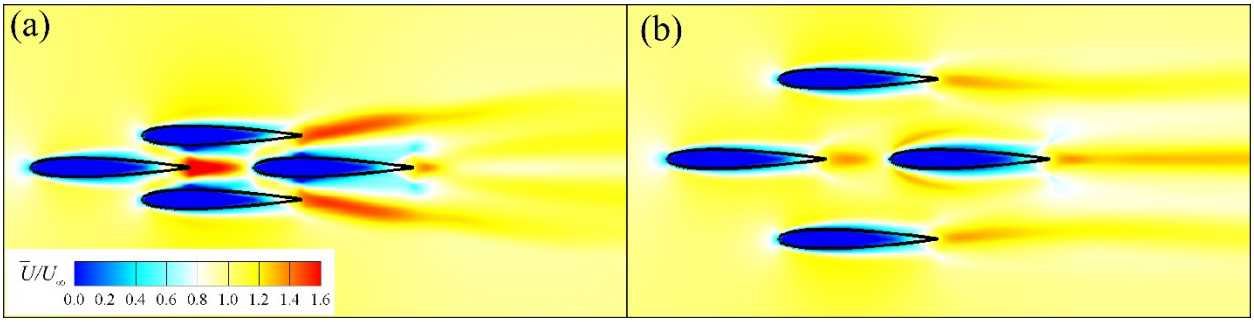

Figure 3-13. Time-averaged streamwise velocity field of (a) school A and (b) school B.

3.3.4 Block Effect in a Dense School

In a finite fish school, a fish can experience the wall effect, as fish 2 does in a dense diamond-shaped school. In an infinite school, however, many fish may be located in the channel formed by laterally neighboring fish in a staggered manner, like the leading fish (fish 1) in the dense school. The channeling effect is quite different from the wall effect described in the previous section. Besides, in a dense diamond-shaped school, fish 1 is also influenced by fish 4. Further research on the hydrodynamic performance of fish 1 in a dense diamond-shaped school is needed.

Owing to the wall effect, fish 2 in a dense school has a higher thrust production and a higher propulsive efficiency than in a sparse school. On the other hand, it is found that fish 1 in a dense school has a higher thrust [Fig. 3-7(a)] but a lower propulsive efficiency [Fig. 3-8(a)]. These differences in the variation of propulsive efficiency of fish 1 and fish 2 represent one of the differences between the channeling effect and the wall effect. It can be shown that while the thrust of fish 1 in the dense school increases with decreasing lateral distance, the lateral force substantially increases, meaning more power is consumed to produce the lateral undulating motion. The propulsive efficiency can therefore be even lower than that of a single fish [Fig. 3-8(a)]. Considering the higher efficiency of the other members, this implies that the leading fish sacrifices its propulsive efficiency to benefit other members in a dense school. The above analysis also makes clear that it may not be sufficient only to consider the effect of neighboring swimmers preventing the wake of a swimmer from freely expanding in the lateral direction to illustrate the hydrodynamic benefits of the channeling effect in a fish school.

What, then, is the role of fish 4 in the hydrodynamic performance of fish 1 in a dense school? To answer this question, we compare the hydrodynamic performance of a dense diamond-shaped

school ($S = 0.4$) and the corresponding triangular school in which fish 1, fish 2, and fish 3 are located in the same positions as in the diamond-shaped school.

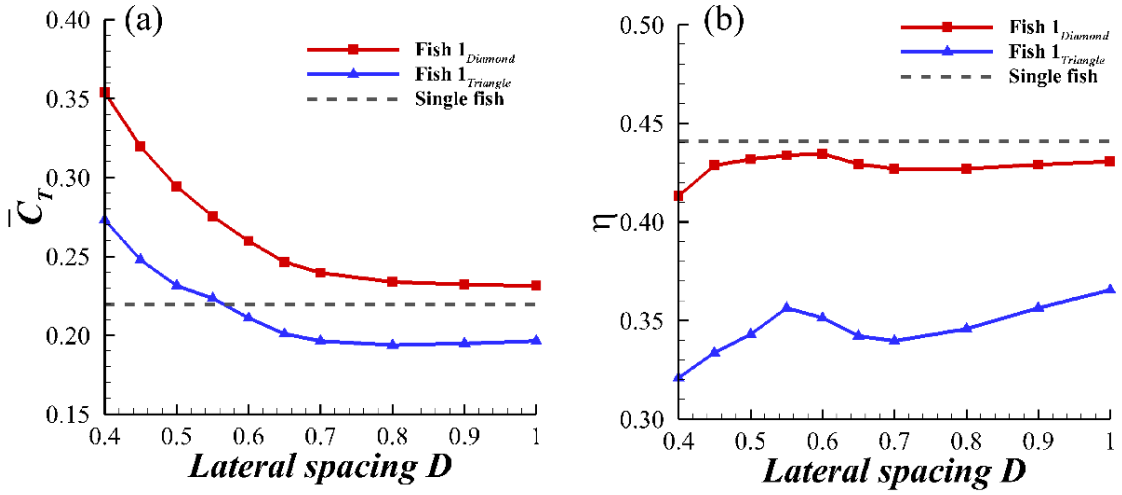

Figure 3-14. Time-averaged thrust coefficient and propulsive efficiency of fish 1 as a function of lateral spacing in dense diamond-shaped schools ($S = 0.4$) and triangular schools. The gray dashed line denotes the corresponding values for an isolated fish swimming steadily.

Figure 3-14 shows the time-averaged thrust coefficient and propulsive efficiency of fish 1 as a function of the lateral spacing in dense diamond-shaped and triangular schools. In Fig. 3-14(a), with decreasing lateral spacing, the thrust coefficient rises, both in the diamond-shaped and triangular schools. $\overline{C_T}$ for fish 1 in the diamond-shaped school is at least 17.8% higher than that for fish 1 in the triangular school, and the difference in thrust production between the two schools increases with decreasing lateral spacing [see Fig. 3-14(a)]. In addition, when $D > 0.55$, $\overline{C_T}$ for fish 1 in a triangular school is even less than that for an isolated fish. In Fig. 3-14(b), the propulsive efficiency of fish 1 in both schools is lower than that of an isolated fish. However, it is found that the propulsive efficiency of fish 1 in the diamond-shaped school is at least 17.8% higher than that

of fish 1 in the triangular school. In short, fish 1 in the dense diamond-shaped school has a higher thrust production and propulsive efficiency than that in the triangular school.

Sometimes, destructive hydrodynamic interactions are unavoidable for certain fish in a school. For example, as stated above, fish 1 needs to consume more energy as a sacrifice for other members in a dense school. However, the results suggest that the loss of the propulsive efficiency of fish 1 can be reduced by placing fish 4 at the rear of the channel formed by fish 2 and 3. Flow comparisons between a diamond-shaped and a triangular school provide insight into how fish 1 obtains a better hydrodynamic performance in a dense diamond-shaped school. Figure 15 presents the vorticity fields at $t = 10.0T$, the time-averaged streamwise velocity fields and the time-averaged pressure fields of a dense diamond-shaped school ($D = 0.4, S = 0.4$) and the corresponding triangular school.

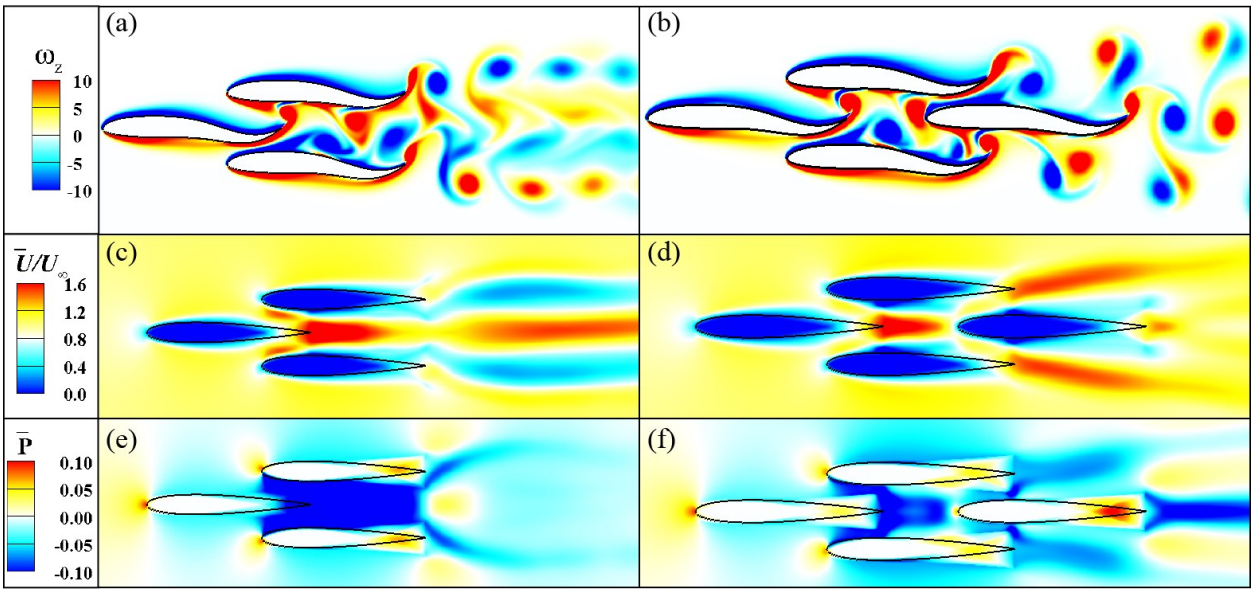

Figure 3-15. Vorticity fields (a, b) at $t = 10.0T$, time-averaged streamwise velocity fields (c, d) and time-averaged pressure fields (e, f) over one tail-beat period of a triangular school (a, c, e), and a diamond-shaped school ($D = 0.4, S = 0.4$) (b, d, f).

From Fig. 3-15, the flow fields of the triangular school are quite different from those of the diamond-shaped school. Behind the triangular school, the vortex wake in the middle is weaker and more chaotic [Fig. 3-15(a)], due to the vortices shed by fish 1 interacting with the vortices shed by fish 2 and 3 separately. Negative vortices are left behind fish 2, and positive vortices behind fish 3, and both are arranged on a line when advecting downstream instead of generating 2S or 2P wakes. In comparison, in the diamond-shaped school, the presence of fish 4 impedes the interactions between the vortex wakes of fish 1 and 2, and an angled 2P wake is generated behind fish 2; this also happens to fish 3. Correspondingly, a straight jet is produced behind the triangular school, while two separate angled jets are produced behind the diamond-shaped school. Moreover, there are two small jets in front of the tail of fish 1 in the triangular school [see Fig. 3-15(c)], indicating that some momentum has been transported upstream, which is detrimental to the efficiency of the system.

Because fish 4 prevents the interactions between the vortex wakes and redirects the flow in the channel formed by fish 2 and 3, the pressure around the tail of fish 1 in the diamond-shaped school is much higher than in the triangular school [see Figs. 3-15(e) and 3-15(f)]. Therefore, considering that the thrust is mainly produced at the tail of a fish and that pressure is the dominant part of the thrust, the different pressure fields mean that fish 1 produces a higher thrust in the diamond-shaped school than in the triangular school. Moreover, the pressure behind fish 1 is higher in the diamond-shaped school, while the pressure distributions in front of fish 1 in the two schools are almost the same. It can therefore be derived that fish 1 in the triangular school has a higher form drag than in the diamond-shaped school, which illustrates that the difference in net force ($\Delta\overline{C_X} = 0.20$) on fish 1 between the two schools is higher than the difference in thrust ($\Delta\overline{C_T} = 0.08$). It is thus safe to conclude that the presence of fish 4, which works like a block preventing

the interaction between the vortex wakes and enhancing the pressure field between fish 1 and fish 4 in the channel, essentially improves the thrust production and the propulsive efficiency of fish 1 in a dense diamond-shaped school. It appears that fish 1 is propelled by fish 4 in a dense diamond-shaped school, and we call this effect the block effect.

3.4 Chapter Summary

In this work, an immersed-boundary-method-based flow solver is employed to investigate the effects of the spatial arrangement of the fish on the hydrodynamic performance and wake structures of a diamond-shaped fish school in low Reynolds number ($Re = 1000$) flows. Firstly, the results suggest that in a dense school, in which the streamwise spacing is 0.4BL, the thrust production and the propulsive efficiency of the lateral fish, which are diagonally located in the school, are substantially enhanced due to a wall effect imposed by the trailing fish. This wall effect is enhanced when the lateral spacing decreases. Flow analysis shows that when the lateral spacing is less than 0.6BL, the vortices shed by the lateral fish start pairing, and the wake expands in the lateral direction. Correspondingly, an angled jet is generated behind the lateral fish, which results in a high thrust production by the fish. This change in the wake patterns has commonly been ignored in past analytical models for studying dense fish schools.

Secondly, in dense schools, the block effect imposed by the trailing fish on the performance of the leading fish is substantial. When the lateral spacing reaches 0.4BL, the thrust produced by the leading fish in the diamond-shaped school is 29.6% higher than that in a triangular school without the trailing fish, and its hydrodynamic efficiency is 28.7% higher. Wake analysis reveals that, in a dense diamond-shaped school, the trailing fish redirects the flow in the channel formed by the lateral fish and prevents interactions between the wakes shed by the leading fish and the lateral fish. This creates a stable high-pressure zone between the leading fish and the trailing fish

in the channel and consequently enhances the thrust production of the leading fish. These findings provide new insight into the channeling effect and reveal the positive influence of the trailing fish on the performance of the leading fish in dense schools.

4 Effects of Phase Difference on Hydrodynamic Interactions in a High-Density Fish School

In this study, we numerically investigate the effects of the tail-beat phase differences between the trailing fish and its neighboring fish on the hydrodynamic performance and wake dynamics in a two-dimensional high-density school. Foils undulating with a wavy-like motion are employed to mimic swimming fish, and the phase difference varies from 0° to 360°. A sharp-interface immersed boundary method is used to simulate flows over the fish-like bodies and provide quantitative analysis of the hydrodynamic performance and wakes of the school. It is found that the highest net thrust and swimming efficiency can be reached at the same time in the fish school with a phase difference of 180°. In particular, when the phase difference is 90°, the trailing fish achieves the highest efficiency, 58% enhancement compared with a single fish, while it has the highest thrust production, increased by 108% over a single fish, at a phase difference of 0°. The performance and flow visualization results suggest that the phase of the trailing fish in the dense school can be controlled to improve thrust and propulsive efficiency, and these improvements occur through the hydrodynamic interactions with the vortices shed by the neighboring fish and the channel formed by the side fish. Besides, the investigation of the phase difference effects on the wake dynamics of schools performed in this work represents the first study in which the wake patterns for systems consisting of multiple undulating bodies are categorized. In particular, a reversed Bénard-von Kármán vortex (rBvK) wake is generated by the trailing fish in the school with a phase difference of 90°, while a Bénard-von Kármán vortex (BvK) wake is produced when the phase difference is 0°. Results have revealed that the wake patterns are critical to predicting the hydrodynamic performance of a fish school and are highly dependent on the phase difference.

4.1 Fish-Like Kinematics and School Configuration

In this section, fish-like swimming is obtained by imposing a traveling wave on a 2D NACA0012 foil shape. Similar to the previous section, the carangiform undulating motion is employed, and the equations are the same as Eqs. (3-1) and (3-2). All the parameters are the same except for the tail-beat phase φ, which changes from 0° to 360° in this section. More details about the fish model and the locomotion can be found in the previous section. Figure 4-1(a) shows the amplitude envelope $A(x)$ of the carangiform motion (red dashed lines) and the resulting sequenced midlines in a tail-beat period (blue lines).

To ensure the problem complexity remains manageable, we vary the undulating phase of the trailing fish (fish 4) from 0° to 360°, at intervals of 30°, while keeping the phase of the other fish at zero in a high-density school with a lateral spacing of $D = 0.4L$ and a streamwise spacing of $S = 0.4L$, as shown in Fig. 4-1(b). The phase difference of the school is thus defined as the difference between the phase of fish 4 (φ) and that of the other fish (0°), i.e., φ. In these schools, fish 4 starts the undulating motion from different positions, marked with different colors in Fig. 4-1(b), compared with the other fish because of the phase difference. Figure 4-1(c) presents the lateral motion of the tail-tip point of fish 4 at the different phases.

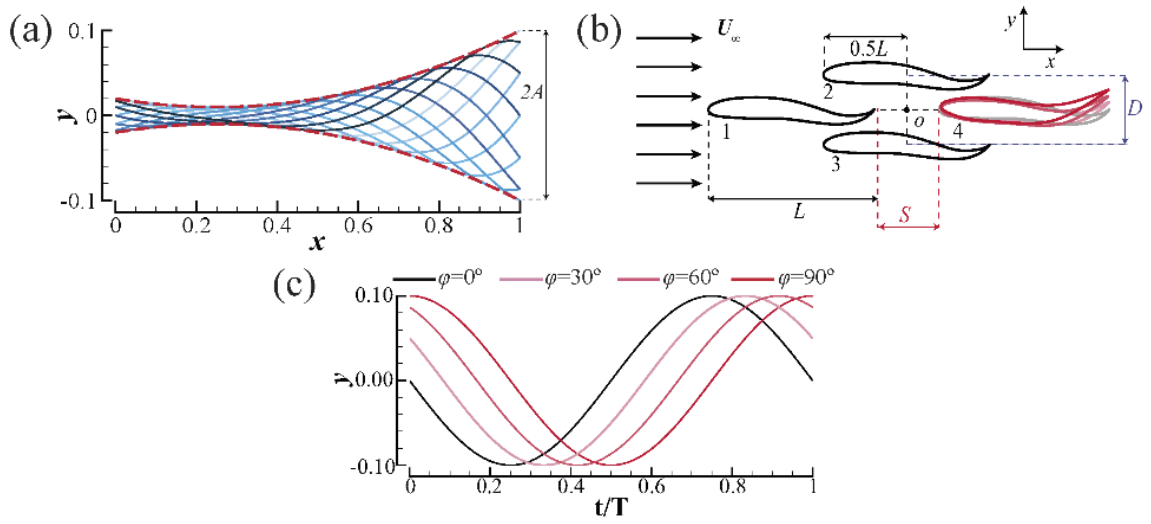

Figure 4-1. (a) Amplitude envelopes of a carangiform motion (red dashed lines) and the sequenced midlines of the fish body during one tail-beat period (blue lines). A is the lateral motion amplitude at the tail-tip. (b) Schematic of high-density diamond-like fish school with varied phase differences. Fish 4 in different schools is indicated by different colors. (c) Tail-tip motion of fish 4 with varied phases.

4.2 Computational Setup and Validation Study

Similarly, two dimensionless parameters, the Reynolds number *Re* and the Strouhal number *St* are used to examine the hydrodynamics and flow characteristics of fish-like swimming. Following previous work [64], the Reynolds number and the Strouhal number are set to $Re = 1000$ and $St = 0.43$, which satisfy the steady swimming condition. All the performance parameters, including forces, powers and efficiencies, are calculated using the same definitions as in Chapter 3.

Figure 4-2(a) presents a schematic of the non-uniform Cartesian computational grids employed in the simulations, with a domain size of $12L \times 8L$. There are approximately 1.03 million (1601×641) grid points in total, with a minimum grid spacing of $\Delta_{min} = 2.94 \times 10^{-3}L$. The fish swim in the negative *x*-direction, and an incoming flow with a constant velocity of U_∞ is

applied as the boundary condition at the left-hand boundary. The right-hand boundary is assigned the outflow boundary condition, and the zero-gradient boundary condition is employed at lateral boundaries. As for the pressure, a homogeneous Neumann boundary condition is imposed on all boundaries.

A grid-independence study was conducted to prove that the current grid setup is fine enough to obtain accurate results. Figure 4-2(b) compares the instantaneous net force coefficient C_X (along the swimming direction) of a solitary fish calculated using the coarse, medium, fine, and dense meshes. As the grid spacing decreases, C_X converges. The percentage difference between the peak values of the fine grid and the dense grid is less than 2%. Therefore, the fine grid is employed for all simulations described below.

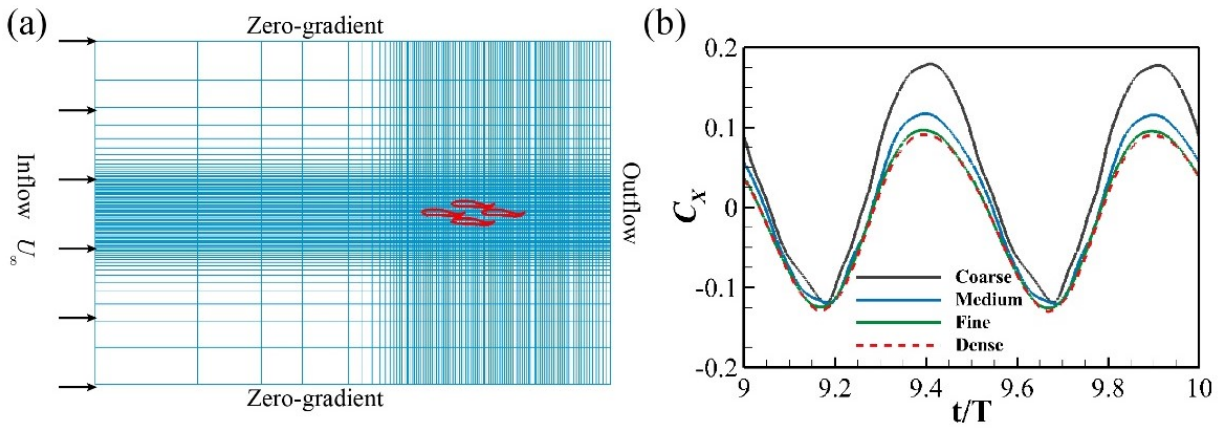

Figure 4-2. (a) Schematic of the computational mesh and boundary conditions employed in this study, where U_∞ is the incoming flow velocity. The fish school is marked in red. (b) Grid independence study on C_X for a solitary fish with a coarse mesh ($\Delta_{min} = 0.011L$), medium mesh ($\Delta_{min} = 5.88 \times 10^{-3}L$), fine mesh ($\Delta_{min} = 2.94 \times 10^{-3}L$) and dense mesh ($\Delta_{min} = 1.92 \times 10^{-3}L$).

4.3 Results and Discussions

4.3.1 Performance of a Single Fish in Steady Swimming

In a previous study, we examined the hydrodynamic performance, vortex wake, and time-averaged velocity field of a single fish in steady swimming [64]. Here, a more comprehensive analysis of the hydrodynamic performance of a single fish is performed by identifying the spatiotemporal distribution of the force generation in the *x*-direction and power consumption required for deformation during one cycle (see Fig. 4-3). In each panel of Fig. 4-3, the *x*-axis indicates the position along the body, and the y-axis denotes the time in one period. Blue represents suffering drag or the capture of energy from vortex flow, and red indicates producing thrust or consuming power.

The force generation and power consumption patterns of a solitary 2D swimmer, shown in Figs. 4-3(a) and 4-3(b), are similar to those of a three-dimensional mackerel [106], which is also a carangiform swimmer. Unsurprisingly, the fish snout always suffers drag, while the tail generates most of the thrust, as shown in Fig. 4-3(a). The high-thrust-production region extends from roughly 0.65L to 0.95L on the body, and two thrust peaks appear near 0.82L. Due to the smaller undulation amplitude, the force at the middle part of the body is close to zero.

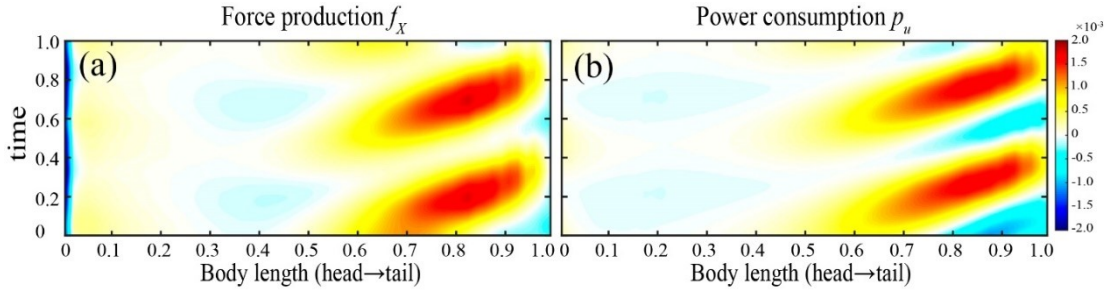

Figure 4-3. Spatiotemporal distribution of (a) force production in the *x*-direction $f_X = -(-pn_x + \tau_{xi}n_i)$ and (b) power consumption for undulating motion $p_u = -(\bar{\bar{\boldsymbol{\sigma}}} \cdot \boldsymbol{n}) \cdot \boldsymbol{u}$ along the

fish body during one period. Positive values, marked in red, denote thrust [in (a)] or output power [in (b)], while negative values indicate drag [in (a)] or input power [in (b)].

The power consumption shows a similar traveling wave pattern as the force generation, whereas the high-power-consumption regions are longer and narrower than the high-thrust regions. Two large areas of negative power consumption appear on the posterior part of the body. Negative power consumption indicates that the body extracts energy from the fluid environment, which implies a potential to improve propulsive efficiency.

4.3.2 Hydrodynamic Performance of Individuals in a School

Due to the strong body–body interaction in the high-density diamond-shaped school, the performance of individuals can be significantly influenced by the phase difference. Figure 4-4 presents the time-averaged hydrodynamic performance of individuals in schools varying with the phase difference. A school's performance is calculated by averaging that of the four swimmers; the results are also shown in Fig. 4-4. Due to symmetry, fish 3 has the same propulsive performance as fish 2, and the results shown for fish 2 are representative of both fish 2 and fish 3.

Figure 4-4(a) shows the relationship between the time-averaged net force in the *x*-direction $\overline{C_X}$ and the phase difference. First, for all the fish in these schools, $\overline{C_X}$ is greater than zero and is a net thrust. It implies that fish in a high-density school can always gain a net thrust, regardless of position or phase difference. Both $\overline{C_X^1}$ and $\overline{C_X^4}$ are more sensitive to phase variation than $\overline{C_X^2}$. (Here, the superscript denotes different fish in a school.) $\overline{C_X^1}$ exhibits an approximate cosinusoidal shape, while $\overline{C_X^4}$ displays the opposite trend as φ increases. $\overline{C_X^2}$ has a bell shape and is symmetric about the φ =180°. Remarkably, fish 4 obtains the highest net thrust in the school in most situations. When φ =30°, $\overline{C_X^4}$ reaches its maximum value of $\overline{C_X^4}_{max} = 0.111$, 15.6% larger than $\overline{C_X^1}_{max}$ =

0.096 and 33.7% higher than $\overline{C_{X}^{2}}_{max} = 0.083$. The minimum value of $\overline{C_X^4}$ is 0.057 at φ =210°, and this value is larger than $\overline{C_{X}^{1}}_{min}$and $\overline{C_{X}^{2}}_{min}$.

Figure 4-4(b) presents the time-averaged power consumption coefficient for undulating motion $\overline{C_{PW}}$ with respect to the phase difference. The gray dashed line denotes $\overline{C_{PW}}$ for a solitary fish, $\overline{C_{PW}^{s}} = 0.278$. $\overline{C_{PW}^{1}}$, $\overline{C_{PW}^{2}}$, and $\overline{C_{PW}^{ave}}$ display sinusoidal waveforms, whereas $\overline{C_{PW}^{4}}$ exhibits the opposite trend. By comparison, fish 1 consumes the most energy in a school regardless of phase difference. It can be explained by the block effect [64]. At φ =60°, $\overline{C_{PW}^{1}}$ reaches its maximum value of $\overline{C_{PW}^{1}}_{max} = 0.501$, which is 80.2% higher than that of a solitary fish. Surprisingly, fish 4 consumes less energy than a solitary fish and the other fish in the school at all phases. The maximum occurs at φ =300°, where $\overline{C_{PW}^{4}}_{max} = 0.256$, which is less than $\overline{C_{PW}^{s}}$. At φ =120°, $\overline{C_{PW}^{4}}$ reaches its minimum of 0.159, which is 42.8% less than $\overline{C_{PW}^{s}}$. The variation of $\overline{C_{PW}^{4}}$ implies that the trailing fish can save more energy by changing its phase in a high-density school.

Figure 4-4(c) displays the variation of the time-averaged total thrust coefficient $\overline{C_T}$ of each fish in the high-density schools. For a single fish, $\overline{C_T}$ is around 0.219 [64]. First, from Fig. 4-4(c), it can be seen that $\overline{C_T}$ for each fish in the schools is much larger than that of a single fish ($\overline{C_T^s}$). $\overline{C_{T}^{4}}_{max}$ is 107.8% higher than $\overline{C_T^s}$ ($\overline{C_{T}^{4}}_{max} = 0.455$, which occurs at φ =0°.), and $\overline{C_{T}^{4}}_{min}$ is 63.5% higher than $\overline{C_T^s}$ ($\overline{C_{T}^{4}}_{min} = 0.358$, which occurs at φ =120°.). The curves of $\overline{C_T}$ for each fish are approximately W-shaped, although they are somewhat different. Fish 2 and 4 attain their maximum values at φ =0° ($\overline{C_{T}^{2}}_{max} = 0.440$), while fish 1 gains its largest thrust of $\overline{C_{T}^{1}}_{max} = 0.422$ at φ =180°. Compared with the other fish, $\overline{C_T^4}$ is more dependent on the phase difference. The difference between $\overline{C_{T}^{4}}_{max}$ and $\overline{C_{T}^{4}}_{min}$ is 0.097, 44.3% of $\overline{C_T^s}$, and is much larger than that of the

other fish. According to the definitions of thrust and drag, we can obtain $\overline{C_D}$ by subtracting $\overline{C_X}$ from $\overline{C_T}$. The results show that, at any φ, the relationship among $\overline{C_D^1}$, $\overline{C_D^2}$, and $\overline{C_D^4}$ is that $\overline{C_D^4} < \overline{C_D^1} < \overline{C_D^2}$, which implies that fish 4 experiences the smallest drag in a high-density school.

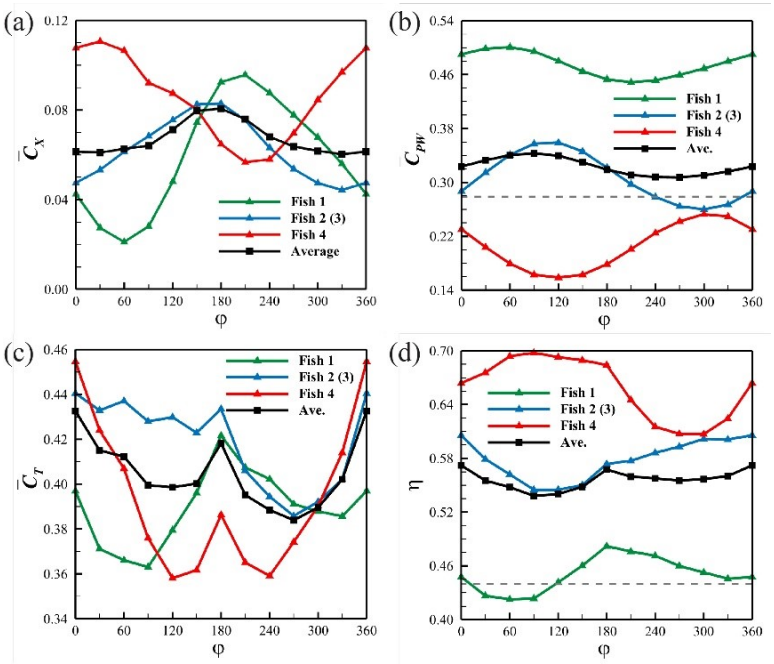

Figure 4-4. Hydrodynamic performance of each fish as a function of phase difference φ in high-density fish schools: (a) time-averaged net force coefficient in the x-direction $\overline{C_X}$, (b) time-averaged power consumption coefficient $\overline{C_{PW}}$, (c) time-averaged total thrust coefficient $\overline{C_T}$, (d) hydrodynamic efficiency η. The gray dashed lines in (b) and (d) denote $\overline{C_{PW}}$ and η for a solitary fish in steady swimming, respectively.

Figure 4-4(d) plots the variation of the propulsive efficiency versus the phase difference. The gray dashed line denotes the swimming efficiency of a single fish ($\eta^s = 0.441$). First, there exists an approximately sinusoidal relationship between η^4 and the phase φ, while η^1 exhibits an opposite trend. η^2 and η^{ave} present W-shaped profiles. When φ =90°, η^4 reaches its maximum of $\eta^4_{max} = 0.698$, which is 58.3% higher than that of a solitary fish. However, η^1, η^2 and η^{ave} reach

their minimum at this phase difference: $\eta_{min}^{1} = 0.423$, $\eta_{min}^{2} = 0.545$ and $\eta_{min}^{ave} = 0.538$. It has been observed that fish 4 gains higher swimming efficiency than other fish in a school and a solitary fish, regardless of phase difference. In particular, the minimum η^4 ($\eta_{min}^{4} = 0.607$ at φ =270°) is 37.6% higher than η^s and is also larger than $\eta_{max}^{1} = 0.482$ and $\eta_{max}^{2} = 0.605$.

Based on the above discussion, we conclude that the trailing fish, fish 4, can save the most energy for undulating motion, suffer the lowest drag and achieve the highest swimming efficiency by maintaining an appropriate phase difference in a high-density school. Two associated assumptions explain this: (1) the phase difference affects the interaction between the vortices shed by fish 2 and fish 3 and the undulating body of fish 4, (2) the phase difference alters the flow environment around the anterior part of fish 4 in the channel formed by fish 2 and fish 3. The hydrodynamic performance of fish 4 is thoroughly investigated in the following section.

4.3.3 Trailing Fish in a Dense School

To reveal the underlying mechanisms, four typical schools are considered: school 1 (φ =0°), school 2 (φ =90°), school 3 (φ =180°) and school 4 (φ =270°). Figure 5 presents the time history of the hydrodynamic performance of fish 4 in each school, including the total thrust coefficient C_T, power coefficient C_{PW}, and x-direction net force coefficient C_X. We denote the thrust coefficient of fish 4 in school i as C_{iT}. A similar definition is used for other coefficients. For comparison, the timelines of schools 2, 3, and 4 are shifted, so that fish 4 has the same undulation motion in all four schools.

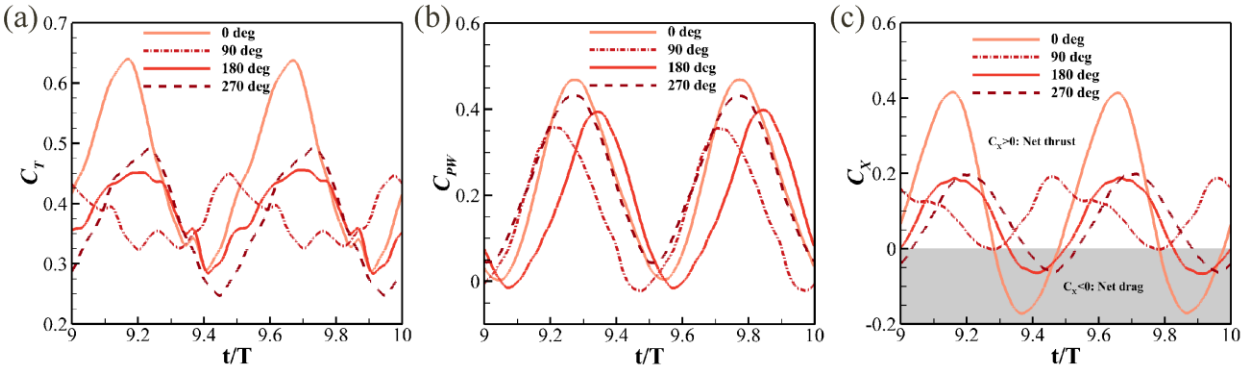

Figure 4-5. Time history of hydrodynamic performance of fish 4 in the schools with φ =0°, 90°, 180°, and 270°: (a) total thrust coefficient C_T, (b) power consumption coefficient C_{PW}, (c) net force coefficient in the x-direction C_X.

Figure 4-5 shows a more detailed influence of the phase difference on hydrodynamic interactions by presenting the time history of the performance of fish 4. First, the peaks of C_T, C_{PW} and C_X are incredibly varied in the different schools. The highest peak of C_T is $C_{1T\_peak} = 0.642$ at $t = 9.17T$ in school 1. This value is 42% higher than the peak in school 2 ($C_{2T\_peak} = 0.452$ at $t = 9.48T$). Correspondingly, fish 4 has the highest peak of C_{PW} in school 1 ($C_{1PW\_peak} = 0.469$ at $t = 9.78T$), and this is 31.7% higher than $C_{2PW\_peak} = 0.356$ at $t = 9.78T$, the lowest peak. For C_X, the highest peak still occurs in school 1 ($C_{1X\_peak} = 0.417$ at $t = 9.16T$), which is 113% higher than $C_{4X\_peak} = 0.196$ at $t = 9.20T$. In addition, the times of the peaks are shifted. For instance, in Fig. 5(a), the peaks of C_{1T} are at $t = 9.17$ and $t = 9.67T$, while the peaks of C_{2T} are at $t = 9.48T$ and $t = 9.98T$, respectively. Besides, the C_T curves, except for school 1 ($\varphi = 0°$), present a higher level of fluctuation than the C_X and C_{PW} curves. It is because the C_T implies more specific information about force generation along the swimming direction and is more sensitive to the flow variation, which can be derived from their definitions. The differences in performance suggest that the time and extent of constructive interactions for fish 4 can be dramatically altered

by the flow environment, which depends on the phase difference. This implies that the trailing fish can further improve thrust production and reduce power consumption by varying its phase.

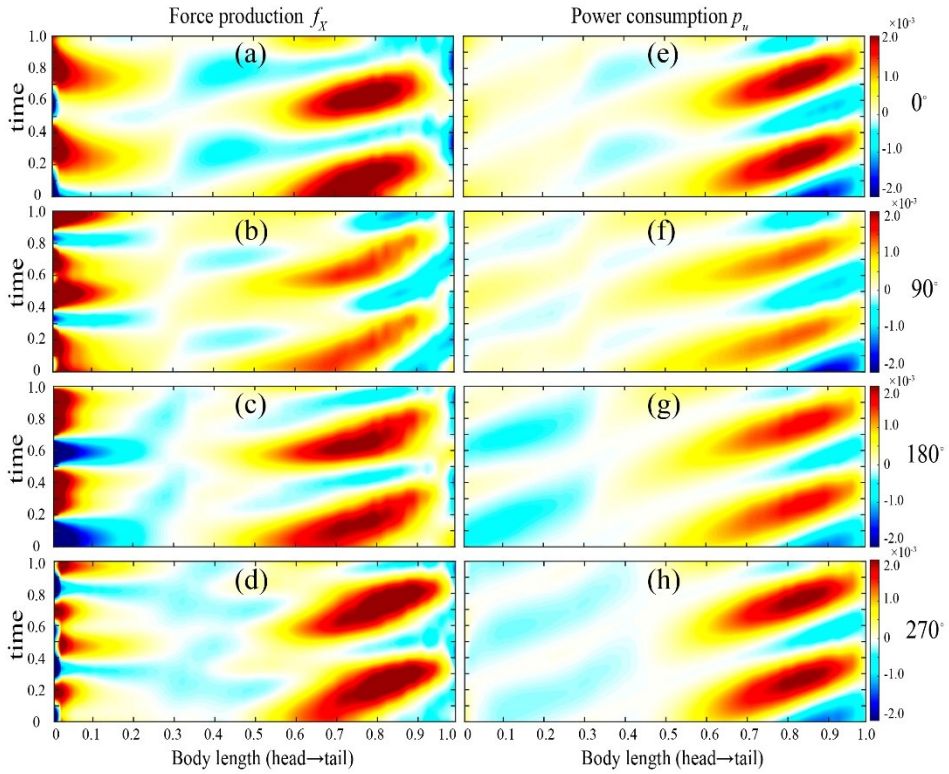

Figure 4-6. Spatiotemporal distribution of force production f_x (a)–(d) and power consumption p_u (e)–(h) of fish 4 in the four different schools. Positive values, marked in red, denote thrust or output power, while negative values indicate drag or input power.

To clearly show the phase difference effect on hydrodynamic interactions, Fig. 4-6 presents the spatiotemporal distribution of force generation and power consumption along the body of fish 4 during one cycle in these four schools. Dark red regions in Figs. 4-6(a-d) indicate areas of high thrust produced by fish 4. By comparison, fish 4 generates much more thrust than a solitary fish at the tail. The anterior part of fish 4 produces high thrust during most of a cycle instead of only suffering drag [Fig. 4-3(a)]. However, when and how much thrust can be generated depend on the phase difference at the head and tail of fish 4. Compared with the rear part of fish 4 in school 1

[Fig. 4-6(a)], the corresponding high-thrust regions in school 2 [Fig. 4-6(b)] are stretched, but the strength decreases and the times of the centers are shifted upward. Additionally, the anterior part of fish 4 generates high thrust in school 2 from $t = 0$ to $t = 0.1T$ [Fig. 4-6(b)], whereas it suffers drag in school 3 [Fig. 4-6(c)]. Similar phenomena are found for the power consumption in Figs. 4-6(e-h). Remarkably, when φ =90°, the strength of the high-power regions becomes much weaker than in other schools, which implies that less energy is consumed by fish 4 for undulation in school 2. The blue regions in Fig. 4-6(f) suggest that fish 4 extracts energy from the flow. This results in the highest swimming efficiency of fish 4 occurring in school 2 ($\eta^4_{max} = 0.698$). According to the force generation and power consumption patterns shown in Fig. 6, we can quickly determine which part of the body affects the hydrodynamic performance and the extent to which the phase difference influences this.

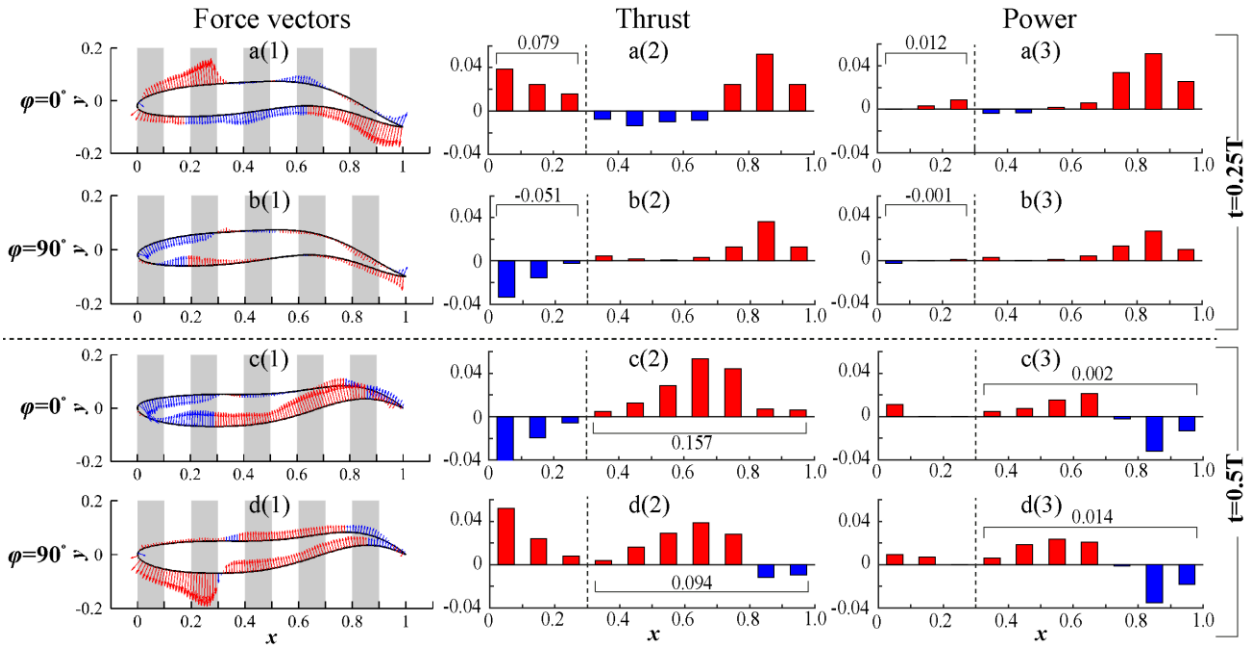

Figure 4-7. Force vectors along fish 4 (a1)–(d1), thrust production (a2)–(d2), and power consumption for undulation (a3)–(d3) of each segment on fish 4 in the two schools, φ =0° and

φ =90°, at $t = 0.25T$ and $t = 0.5T$. Blue denotes drag or capturing energy, and red represents generating thrust or exhausting energy.

Furthermore, to quantitatively clarify the performance variations, the body of fish 4 is evenly divided into ten segments, and the hydrodynamic performance of each segment is calculated separately and illustrated. Figure 4-7 shows the flow-induced force vectors on the body of fish 4, the thrust production and power consumption of each segment of fish 4 in the two schools, school 1 and school 2, at two times, $t = 0.25T$ and $t = 0.50T$. Based on the position of fish 4 in the high-density schools, it can be divided into two essential parts: (1) the anterior part, $0{\sim}0.3L$, located in the channel formed by fish 2 and fish 3, (2) the posterior part, $0.3{\sim}1.0L$, out of the channel. The phase difference effects on these two parts can be separately and quantitively investigated. First, when $t = 0.25T$, the anterior part of fish 4 generates high net thrust ($C_{1X}^{a} = 0.079$) in school 1 [see Fig. 4-7(a2)], and consumes power of $C_{1PW}^{a} = 0.012$ for undulating motion [see Fig. 4-7(a3)], while in school 2, it suffers drag ($C_{2X}^{a} = -0.051$) [Fig. 4-7(b2)], and captures energy from the flow ($C_{2PW}^{a} < 0$) [Fig. 4-7(b3)]. For the posterior part, at $t = 0.50T$, fish 4 generates a large thrust ($C_{1X}^{p} = 0.157$) in school 1 with a small power consumption of $C_{1PW}^{p} = 0.002$. For comparison, fish 4 produces a much lower thrust ($C_{2X}^{p} = 0.094$) in school 2 and consumes much more power ($C_{4PW}^{p} = 0.014$) in school 4.

The differences in performance shown in Figs. 4-6 and 4-7 suggest the mutual interaction between the vortical flow and the posterior part (vortex–body interaction) and the interaction between the anterior part and the channel (body–body interaction) affect the hydrodynamic performance of fish 4 as the phase difference varies. Based on these findings, the fundamental flow physics of the phase difference effects in a high-density school are discussed in the following subsections.

4.3.4 Vortex Capture Mechanism between Neighboring Fish

The flow fields of schools 1 and 2 are now analyzed and compared to explore the phase difference effects on the vortex-undulating body interaction. Figure 4-8 presents the undulating velocity along fish 4, the vortex wake and the pressure field around fish 4 in schools 1 and 2 at $t = 0.25T$ and $0.75T$. Because of the symmetry of the schools, only the interaction between the shedding vortices of fish 2 and the upper surface of fish 4 is analyzed. To quantify the variation in the interactions, we display the hydrodynamic performance of the upper surface of fish 4 in schools 1 and 2 at $t = 0.25T$ and $0.75T$ in Fig. 4-9.

In these high-density schools, vortex pairs are formed due to the wall effect [64] and shed downstream at different positions with respect to fish 4 at a specific time. When $t = 0.25T$, the vortex pair $V_{11}V_{12}$ is located at around $x = 9.5$ in school 1, as shown in Fig. 4-8(a2), whereas the vortex pair $V_{11}'V_{12}'$ is located at $x = 9.7$ in school 2 [Fig. 4-8(c2)]. This difference results in the pressure field around the upper surface of fish 4 changing from negative-dominant [in school 1, Fig. 4-8(a3)] to positive-dominant [in school 2, Fig. 4-8(c3)]. Considering the undulating motion of fish 4 at $t = 0.25T$, it can be deduced that fish 4 produces higher thrust but consumes more power in school 2 than in school 1, which is verified by the quantitative results in Figs. 4-9(a1-a2) and 4-9(c1-c2). Similar phenomena can be observed at other times. For instance, when $t = 0.75T$, the difference in the positions of the vortex pair $V_{11}V_{12}$ [around $x = 9.8$, Fig. 4-8(b2)] and $V_{11}'V_{12}'$ [around $x = 10.0$, Fig. 4-8(d2)] leads to that the pressure magnitude around the tail of fish 4 is much larger in school 1 than in school 2. Thus, a higher suction thrust is generated in school 1, corresponding to more energy consumed by the upper surface to overcome the higher suction force. The quantitative differences are shown in Figs. 4-9(b1-b2) and 4-9(d1-d2).

In Figs. 4-8(a2) and 4-8(b2), it can be observed that a secondary vortex iV_1 is induced and advected downstream along the undulating body. The induced secondary vortex attaches to the upper surface of fish 4, and its rotation direction is opposite to that of the vortex attached to the boundary. However, in Figs. 4-8(c2) and 4-8(d2), the induced secondary vortex iV_1' decays rapidly and does not move downstream. Thus, the secondary vortex is induced at the anterior part of fish 4 regardless of phase difference, but whether it becomes fully developed and moves downstream depends on the phase difference.

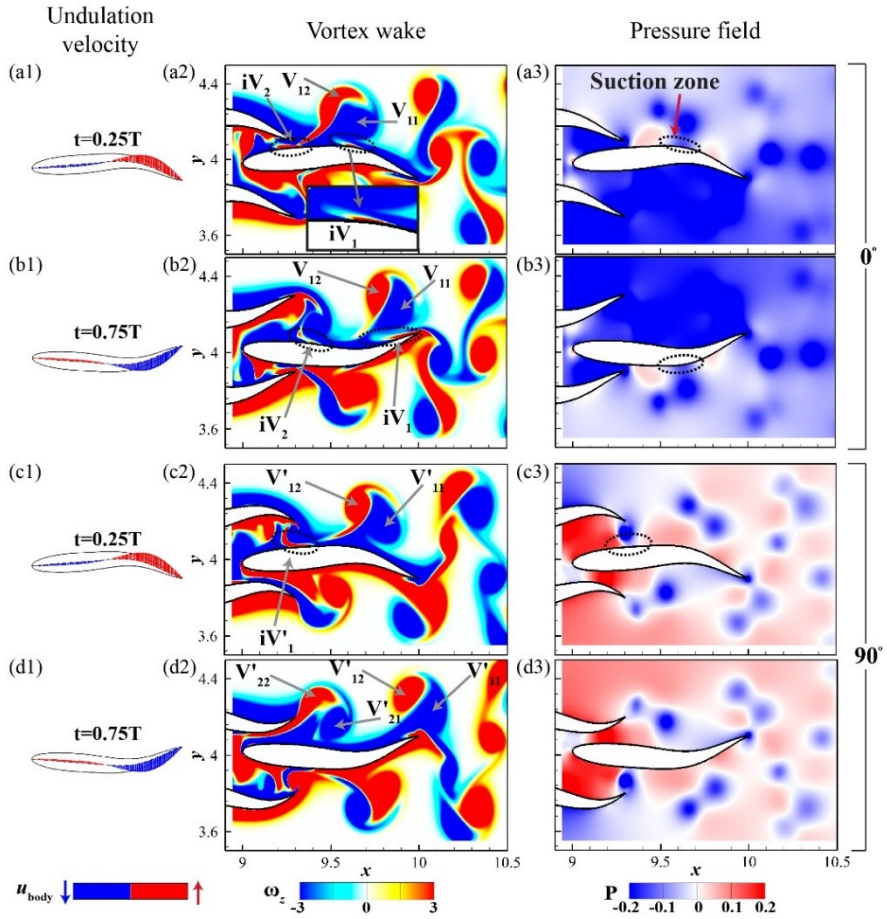

Figure 4-8. Undulation velocity along fish 4 (a1)–(d1), vortex wake (a2)–(d2), and pressure field (a3)–(d3) around fish 4 in schools 1 and 2 at $t = 0.25T$ and $0.75T$.

Additionally, the induced vortex moving along the body can modify the local pressure on the body to be negative or augment the magnitude of the negative pressure. The local curvature and the lateral motion should also be considered to determine whether the induced vortex is beneficial or detrimental to hydrodynamic performance. When $t = 0.25T$, the induced vortex iV_1 is located at $x = 9.5\sim9.7$ in school 1 [Fig. 4-8(a2)], and the local pressure on this part becomes negative [Fig. 4-8(a3)], unlike in school 2 [Fig. 4-8(c3)]. Considering the local curvature and the lateral motion [Fig. 4-8(a1)], it can be deduced that drag is produced and energy is captured from the flow by the associated part of the body. The quantitative results are shown in Figs. 4-9(a1) and 4-9(a2). In addition, when $t = 0.75T$, the induced vortex iV_1 moves to $x = 9.8\sim1.0L$ [see Fig. 4-8(b2)], and the pressure amplitude increases at the corresponding location in school 1. Therefore, much more thrust is generated, and more power is consumed by the upper surface of fish 4 in school 1, as shown in Figs. 4-9(b1) and 4-9(b2).

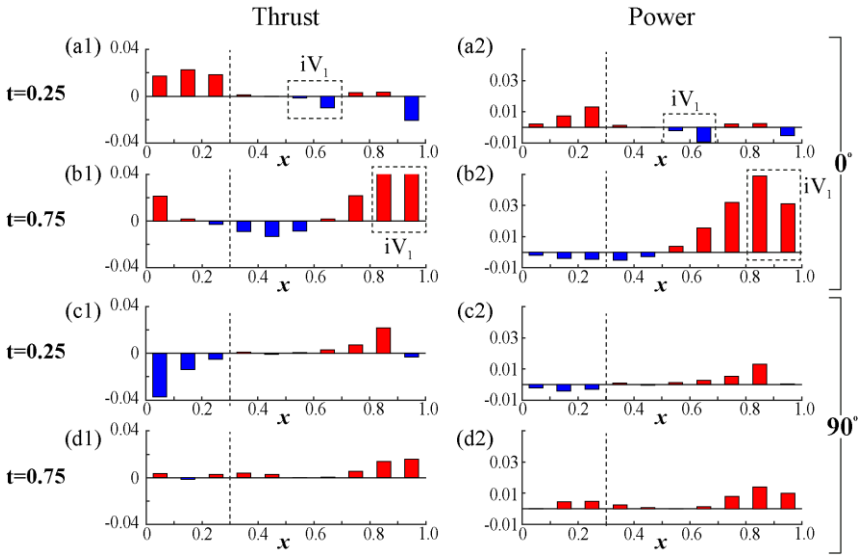

Figure 4-9. Thrust (a1)–(d1) and power consumption for undulation motion (a2)–(d2) of each segment on the upper surface of fish 4 in schools 1 and 2 at $t = 0.25T$ and $0.75T$.

Two aspects of the vortex capture mechanism for an undulating swimmer have been revealed: (1) the interaction between vortex pairs and the undulating body and (2) the induction and convection of a secondary vortex. To concisely illustrate the two mechanisms, the associated schematics are displayed in Fig. 4-10. Figure 4-10(a) defines the location o, advection velocity u_p and rotation angle β for a vortex pair. The location of a vortex pair is defined as the midpoint of the cores of the two vortices, and the vortex cores are located at the local extremum of vortices [14]; for the definitions of the advection velocity and rotation angle, see Refs. [14] and [64], respectively. Figures 4-10(b) and 4-10(c) are based on the plots in Figs. 4-8(b2) and 4-8(d2), respectively, showing the vortex field around the upper surface of fish 4 in schools with various phases. First, in Figs. 4-10(b) and 4-10(c), the vortex pairs are at different locations because of the phase difference, influencing the interaction between the vortex pair and fish 4. These figures suggest that the trailing fish can achieve optimal hydrodynamic performance in a high-density school by adjusting the phase. The mechanism also explains how trout save energy in the vortex wake of a D-section cylinder [50]. Second, there is a secondary vortex (iV_1), the red vortex attached to the body surface in Fig. 4-10(b), transported downstream; however, this is not observed in the other school [Fig. 4-10(c)]. The attached vortex alters the surrounding pressure, dramatically influencing the thrust production and power consumption at the corresponding position on the body. The advection of the secondary vortex depends on the phase difference. From our observations, when $0° \leq \varphi < 90°$ or $270° < \varphi \leq 360°$, the secondary vortex can be advected downstream. Moreover, the secondary induced vortex is viscosity-dominated [107]. These results imply that the viscous effect should not be neglected when studying hydrodynamic interactions in a high-density fish school. A similar conclusion was mentioned in a previous study on three-dimensional fish swimming [61].

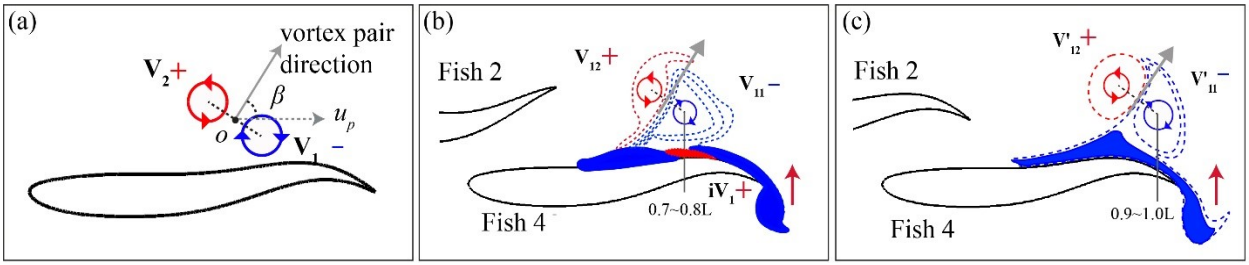

Figure 4-10. (a) Definitions of the location o, advection velocity u_p and rotation angle β for a vortex pair, (b) schematic of vortex–body interaction in school 1, and (c) schematic of vortex–body interaction in school 2.

4.3.5 Suction Thrust and The Body–Body Matching Mechanism

In Fig. 4-3(a), the anterior part ($0.0\sim0.3L$) of a single fish mainly generates drag, while in Figs. 4-6(a-d), the same part of fish 4 produces thrust in a high-density school. It can also be observed that the magnitude of the force generation and power consumption of the anterior part of fish 4 depend strongly on the phase difference of the fish school. For instance, compared with the thrust region at the anterior part of fish 4 in school 4, the corresponding thrust region is much larger in school 1. Next, we compare the performance of the anterior part of fish 4 in schools 1 and 4 to measure the phase difference effect.

Figure 4-11 shows the time history of the net force coefficient C_X^a and power consumption coefficient C_{PW}^a for the anterior part of fish 4 in schools 1 and 4. The superscript a denotes the anterior part. First, $\overline{C_{1X}^a} = 0.048$ and $\overline{C_{4X}^a} = 0.023$, implying a net thrust generated at the anterior part of fish 4 in both schools during one tail-beat cycle. In Fig. 4-11(a), compared with C_{1X}^a, the peaks and troughs of C_{4X}^a have shifted to the left by 0.25T, which indicates the flow environment around the anterior part, determined by the phase difference, controls the force generation. Second,

in Fig. 4-11(b), $C_{1PW}^{a} > 0$ and $C_{4PW}^{a} < 0$ during the whole cycle. This suggests that the anterior part of fish 4 consumes power in school 1, while it extracts energy from the flow in school 4.

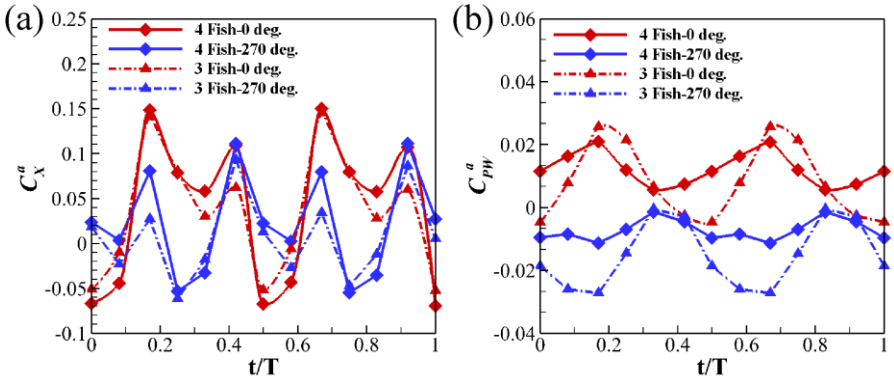

Figure 4-11. Time history of (a) net force coefficient in the x-direction C_X^a and (b) power consumption coefficient C_{PW}^a of the anterior part of fish 4 in schools 1 and 4.

The anterior part of fish 4 can improve its performance by generating more thrust or capturing energy from the flow in a high-density school. However, the extent to which the improvement can be achieved depends on the phase difference. The phase difference effect stems from two aspects: (1) the interaction between shedding vortices of fish 1 and the anterior part of fish 4, and (2) the body–body interactions between the channel formed by fish 2 and fish 3 and the anterior part of fish 4. First, due to the phase difference, the vortices shed by fish 1 may impinge on the anterior part of fish 4 at different locations. Second, the body–body interaction between the undulating channel and the anterior part of fish 4, controlled by the phase difference, may change the flow rate of the channel, which modifies the flow environment around the anterior part.

The vortex–body interaction has been studied by many researchers [37, 65, 108-110]. In contrast, the body–body interaction between an undulating channel and a fish body is unique to high-density diamond-shaped schools and has not yet been reported. To measure the influences of these two aspects, we remove the leading fish, fish 1, and simulate the hydrodynamics of triangular

fish schools at φ =0° and φ =270°. The hydrodynamic performance of the anterior part of the trailing fish in triangular schools is also presented in Fig. 4-11. The cycle-averaged values are summarized in Table 4-1. The variation of C_X^a is large when the phase changes, for both diamond-shaped and triangular fish schools, whereas it is very small between the two kinds of schools with the same phase, as shown in Fig. 4-11(a). This suggests that, except for the vortex-body interaction, the matching between the channel and fish 4 also plays an important role in force generation. Additionally, the difference in C_{PW}^a between the two diamond-shaped school is much larger than that between a diamond-shaped school and the same phase triangular school. This highlights the critical role of the body–body matching mechanism in power consumption.

TABLE 4-1. Summary of $\overline{C_X^a}$ and $\overline{C_{PW}^a}$ of fish 4 in four schools.

	$\overline{C_X^a}$	$\overline{C_{PW}^a}$
4 fish-0°	0.038	0.012
4 fish-270°	0.022	-0.007
3 fish-0°	0.035	0.008
3 fish-270°	0.007	-0.015

The natural timeline is now considered to investigate further the body–body matching mechanism, whereby the leading fish starts undulating at the same pose in different schools. The pressure fields of diamond-shaped and triangular schools with varied phases at $t = 0.25T$ are shown in Fig. 4-12. Compared with school 1 [Fig. 4-12(a)], school 4 exhibits higher pressure around the anterior part of fish 4 [Fig. 4-12(b)], while the triangular school at φ =0° has a similar pressure field [Fig. 4-12(c)], demonstrating that the body–body matching mechanism is essential to the hydrodynamics of the anterior part of fish 4 once again.

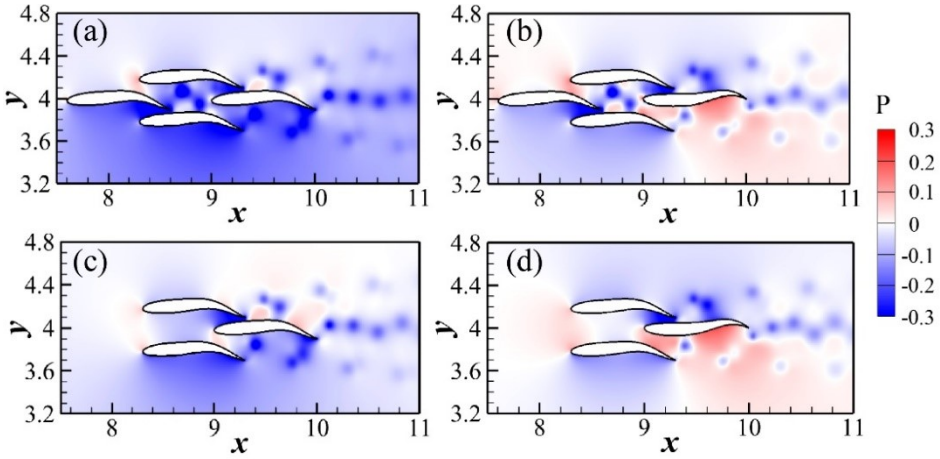

Figure 4-12. Pressure field of (a) school 1 (φ =0°), (b) school 4 (φ =270°), (c) triangular school with φ =0°, and (d) triangular school with φ =270° at $t = 0.25T$.

The instantaneous pressure around the anterior part of fish 4 depends on the lateral spacing and the relative motion between fish 4 and the channel, which changes dynamically with the phase difference. In Fig. 4-12(a), because of the difference in lateral spacing and relative motion, a negative pressure appears around the anterior part of fish 4 in school 1, and a high suction thrust is generated. In contrast, positive pressure can be found at the same position on fish 4 in school 4, and drag is produced. From a fluid dynamics standpoint, this phenomenon can be explained by momentum conservation law. In a high-density school, the phase difference determines the momentum flux passing by the anterior part of fish 4, thus controlling the net momentum transported downstream through the channel. According to Newton's second and third laws, the force generated by a fish is related to the momentum that the fish transfers to the downstream fluid [111]. That is, the matching between the channel and the anterior part of fish 4 governs its hydrodynamic performance. The phase difference effect on the hydrodynamics can be revealed by comparing the momentum passing by the anterior part of fish 4 in schools 1 and 4.

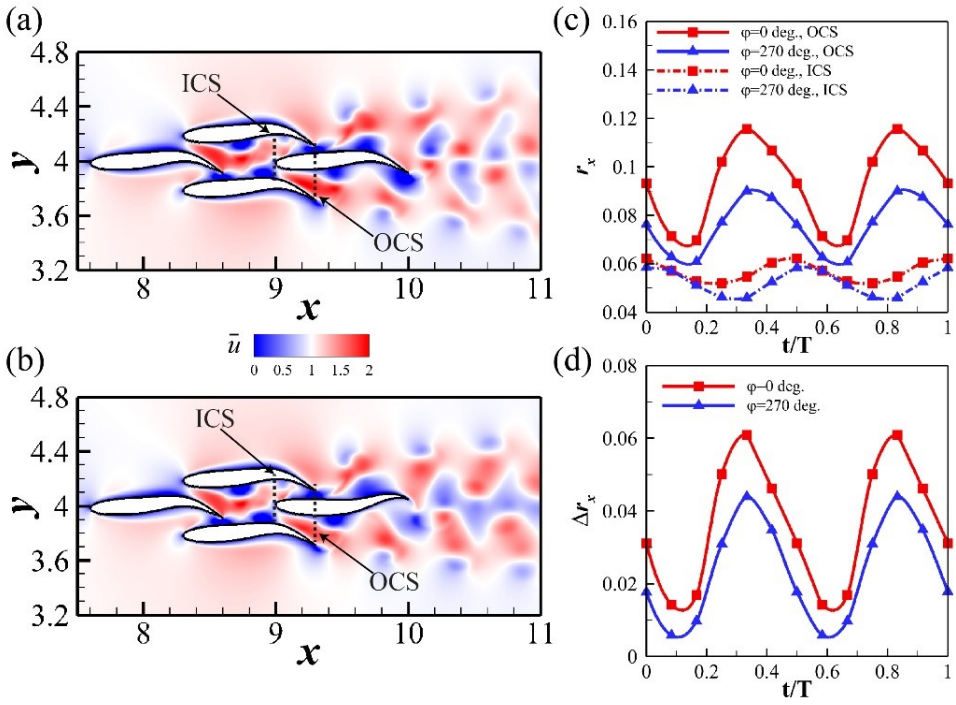

Figure 4-13. (a), (b) Streamwise velocity field, (c) momentum flux at ICS and OCS, and (d) net momentum flux of the channel for schools 1 and 4.

Figure 4-13 presents the instantaneous streamwise momentum flux r_x at the inlet control surface (ICS) and outlet control surface (OCS) during one period for schools 1 and 4. The ICS is at the snout of fish 4, and the OCS is at the tail of fish 2 and 3, as shown in Figs. 4-13(a) and 13(b). In Fig. 4-13(c), the momentum flux at the ICSs is very similar in schools 1 and 4, with time-averaged values of 0.057 and 0.052, respectively. It proves that other factors have only minor effects on the hydrodynamics of the channel. The momentum flux at the OCS r_{x_out} becomes much greater because of the energy output from fish 4 and the channel. We can see that r_{x_out} in school 1 is larger than that in school 4 over the whole period, and the time-averaged values are 0.093 and 0.076, respectively. Compared with $r^1_{x\_out}$, $r^4_{x\_out}$ is 18.7% lower. Figure 4-13(d) presents the net streamwise momentum flux over the volume bordered by the ICS and OCS, showing that Δr^1_x is larger than Δr^4_x during the whole period, and $\overline{\Delta r^1_x} = 0.037$ is 54.2% larger

than $\overline{\Delta r_x^4} = 0.024$. The results indicate that when changing the phase difference, Δr_x through the clearance between fish 4 and the channel may significantly increase because of the matching between fish 4 and the channel, leading to higher thrust production or lower energy consumption (or even the harvesting of energy from the flow) at the anterior part of fish 4. This effect of the phase difference is thus called the body–body matching mechanism.

4.3.6 Wake Dynamics

The phase difference strongly influences the wake of a high-density diamond-shaped school. Figure 4-14 shows the representative vortex structures at $t = 10T$ and the mean flows of high-density fish schools with various phase differences. In Fig. 4-14, the rear fish in each school separately produces the three rows of vortex wakes. The 2P wakes [64] are produced by fish 2 and 3 on the upper and bottom rows, respectively, circled by blue dashed squares in Figs. 4-14(a1) and 4-15(a1). Due to symmetry, the upper and lower wake variations are similar, so only the upper wake is discussed below.

Although the wake pattern is maintained behind fish 2, the vortex strength, rotation angle, and advection velocity [14] of the vortex pairs change with the phase difference through the mutual interactions with the central wake produced by fish 4. In Figs. 4-14(a1-f1), the fourth vortex pairs shed by fish 2, marked by P_{i4} in each figure ($i = a\sim f$ denotes the figure number), are stable and have interacted with the central wake over a period of time. Thus, we present the position, the rotation angle β, and the normalized circulation Γ^* of the fourth vortex pair P_4 in schools with varied phase differences at $t = 10T$ in Figs. 4-15(b-d), respectively, to investigate the phase difference effects on the wake-wake interaction. The circulation is calculated by integrating the vorticity over an area A bounded by a predefined vorticity threshold ($\omega_z = 1$ for the positive vortex and $\omega_z = -1$ for the negative vortex), as shown in Fig. 4-15(a), and is normalized by the

product of the incoming flow velocity U_∞ and the body length L [14, 80, 112]. The calculation of Γ^* can be expressed as follows:

$$\Gamma^* = \left|\frac{\Gamma}{U_\infty L}\right| = \left|\frac{1}{U_\infty L}\iint_A \omega_z \cdot dA\right|, \tag{4-1}$$

where ω_z is the vorticity, and A is the region enclosing vorticity above or below the threshold value.

Figure 4-16(b) shows the variation in the lateral spacing Δy between neighboring positive and negative vortices shed by fish 4, $\Delta y = y_{red} - y_{blue}$, where y_{red} and y_{blue} are located at the cores [14] of positive and negative vortices, respectively. For accuracy, we average the lateral spacings of three successive vortex pairs, circled by black dashed squares in Figs. 4-14(a1-f1), to calculate Δy. The associated schematic of the calculation is shown in Fig. 4-16(a). The value of Δy indicates the patterns of the central wake produced by fish 4: when $\Delta y = 0$, it is a 2S aligned wake [see Fig. 4-14(c1)]; when $\Delta y > 0$, it is a 2S reversed Bénard-von Kármán (rBvK) vortex wake, as shown in Fig. 4-14(b1); when $\Delta y < 0$, it is a 2S Bénard-von Kármán (BvK) wake, as shown in Figs. 4-14(a1) and 4-14(f1) [21]. The central wake produced by fish 4 could be in a transitional state, such as the parallel wake shown in Fig. 4-14(e1).

When $0° \leq \varphi < 90°$, the vortex pairs rotate clockwise, and the vortex wake strengthens with the increasing phase difference, as shown in Figs. 4-14(a1) and 4-14(b1). The variations are quantitively shown in Fig. 4-15. Because the vortex pairs are shed at the same time and in the same position in different schools, the larger coordinates in Fig. 4-15(b) imply a faster advection velocity for a vortex pair. It can be seen that the fourth vortex pair (P_4) in the school with a larger phase difference moves faster in streamwise and lateral directions. Additionally, Fig. 4-15(c) indicates

that the vortex pair angle of P_4 reaches a minimum (β_{min} =5.05°) at φ =90°. The enhancement in the circulation and advection velocity of vortex pairs results in the augmentation of the mean flow behind fish 2. Simultaneously, the positive vortices in the central wake move upward, and the negative vortices move downward. Thus, the central wake transfers from the BvK pattern to the rBvK pattern, and the mean flow at the center is strengthened. Correspondingly, the mean flow of the school alters from a two-short-jet (2SJ) wake [Fig. 4-14(a2)] to a stronger three-long-jet (3LJ) wake [Fig. 4-14(b2)].

When increasing φ to 120°, the strength of the vortex pair P_4 is enhanced and reaches a maximum at φ =120°, as shown in Fig. 4-15(d). When 120°≤ φ <150°, Δy decreases as φ increases, indicating that the central wake becomes narrower. This results in a weaker rBvK wake in the center and stronger interaction between the negative vortices in the upper wake and the central wake. The negative vortices in the upper wake thus become weaker and are stretched, as shown in Fig. 4-14(c1). Driven by the mutual induction between V_{41} and V_{42}, the vortex pair rotates counterclockwise, and β increases [Fig. 4-15(c)]. When φ = 150°, $\Delta y \approx 0$ and a 2S aligned wake is generated in the central region. Accordingly, the mean flow transfers to a two-long-jet (2LJ) wake [Fig. 4-14(c2)]. When 150°≤ φ <210°, the vortices produced by fish 4 cross the central line and move in the opposite spanwise directions. The central wake is transitional, changing from the rBvK type to the BvK type, and is unstable. The wake is of the BvK pattern at φ =180°, while it has changed to a "parallel" wake at φ =210°, as shown in Fig. 4-14(e1). Increasing the phase difference further, the center wake becomes a stable BvK type [Fig. 4-14(f1)]. Moreover, the lateral jet moves closer to the streamwise direction, but its strength decreases.

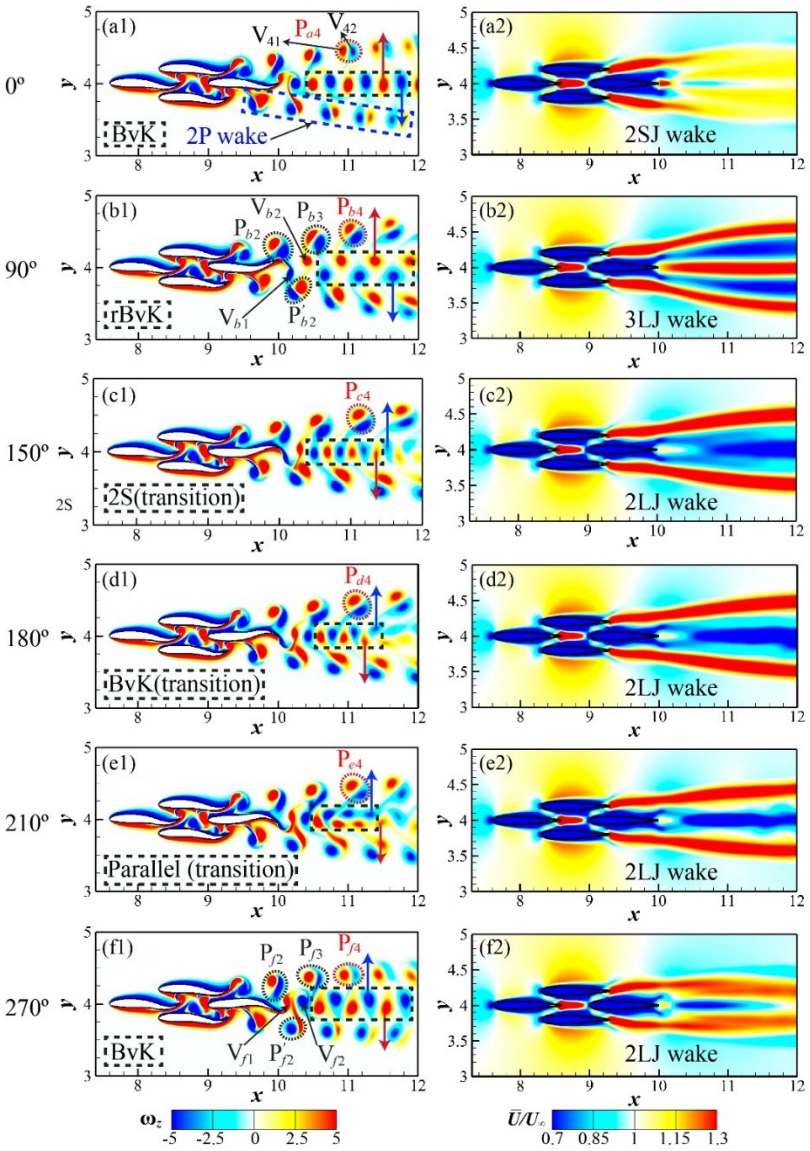

Figure 4-14. Vortex wakes at $t = 10T$ (a1)–(f1) and the mean flow fields (a2)–(f2) of high-density schools at varied phase differences.

The above discussion suggests that phase difference greatly influences the wake pattern and the corresponding mean flow pattern of a high-density school. The associated mechanism is as follows. First, following the vortex pairing mechanism proposed in Ref. [64], vortex pairs are generated by fish 2 and 3 in a high-density school. When being advected downstream, the vortex pairs firstly interact with the undulating body of fish 4 (vortex–body interaction) and then are

influenced by the shedding vortices of fish 4 (wake–wake interaction). In Fig. 4-14(b1), the vortices in vortex pair P_{b2} are strong and coherent, while in Fig. 4-14(f1), at the same position, the negative vortex in the vortex pair P_{f2} is stretched and weakened due to the interaction with the body of fish 4, resulting in P_{f2} rotating counterclockwise. Next, the interaction between the vortex pairs and the shedding vortices of fish 4, the wake–wake interaction, takes effect. The variation of vortex pair P_4 with respect to the phase difference shown in Figs. 4-15(b–d) suggests that the wake–wake interaction can further influence the lateral wakes. In addition, the shedding vortices of fish 4 are also influenced by the wake–wake interaction. In the synchronized school (φ =0°), a 2S BvK wake is produced behind fish 4. Then, when increasing the phase difference, the negative vortex V_{b1} is moving downward, attracted by vortex pair P'_{b2} at the bottom, while the positive vortex V_{b2} is moving upward, attracted by vortex pair P_{b3} at the upper layer, as shown in Fig. 4-14(b1). An rBvK wake is thus formed. Continuing to increase the phase difference, the situation is reversed, and a BvK wake is then formed, as shown in Fig. 4-14(f1). The lateral motion of the shedding vortices of fish 4 depends on the relative distance to the vortex pairs, determined by the phase difference. The mechanism controlling the vortex dynamics indicates that the phase difference determines the wake pattern of a school.

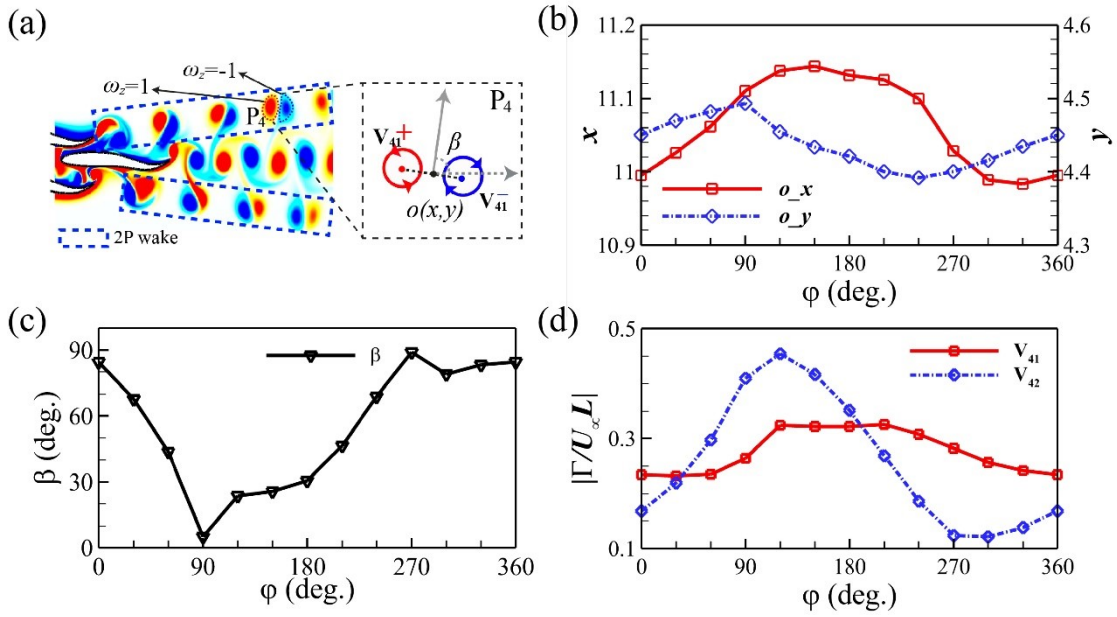

Figure 4-15. (a) Schematic of the location o, rotation angle β and circulation calculation for a vortex pair, (b) relationship between the coordinates of vortex pair P_4 and the phase difference, (c) rotation angle of the vortex pair P_4 with respect to phase difference, (d) absolute circulation of vortex 1 (V_{41}) and vortex 2 (V_{42}) in the pair P_4 varying with the phase difference.

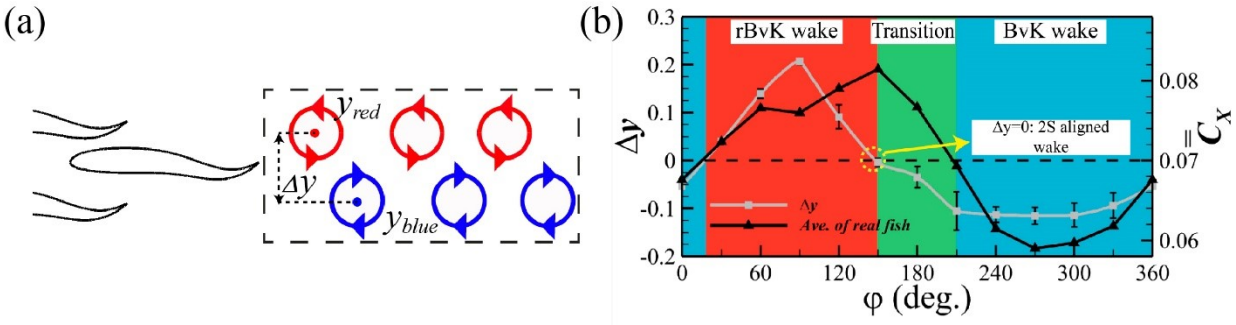

Figure 4-16. (a) Schematic of the calculation of lateral spacing Δy between neighboring positive and negative vortices. (b) central vortex wake and hydrodynamic performance of rear fish varying with the phase difference.

In addition, the wake structures can indicate the hydrodynamic performance of a school. Based on the previous analysis, the swimming performance and vortex structure strongly depend

on the phase difference. Thus, the phase difference can determine the relationship between vortex wake and performance. To help understand this relationship, we show the averaged $\overline{C_X}$ of the three-rear fish, which are directly related to the wake pattern in a school, $\overline{\overline{C_X}} = \sum_{i=2}^{4} \overline{C_X^i}/3$ where i denotes the fish number, as a function of phase difference in Fig. 4-16(b). Like the variation of Δy, the function has an approximately sinusoidal shape. When increasing φ (<150°), Δy increases, and an rBvK (thrust-producing) wake is formed. Accordingly, a 2SJ mean flow wake gradually becomes a 3LJ wake [Fig. 4-14(b2)], implying more net thrust has been produced. Then, Δy starts to decline with increasing φ above 90°, and the thrust-producing wake becomes weaker. In contrast, due to the vortex induction and merging, more of the flow in the low-energy zone (the central wake) is transported to the high-energy wake (the 2P wake), and the lateral mean flow wake is strengthened. Thus, the $\overline{\overline{C_X}}$ continues to increase and reaches a maximum at $\varphi = 150°$, $\overline{\overline{C_X}}_{max} = 0.081$. Then the central wake transforms from thrust-producing (rBvK wake) to drag-producing (BvK wake), and the flow is transported from the high-energy zone to the low-energy zone. Although the lateral jets are gradually deflected to the center, they have less strength and the $\overline{\overline{C_X}}$ drops. The subsequent development of the BvK wake and the force changes in a similar way as that of the rBvK wake with increasing φ. In summary, this study proves that the thrust–drag wake theory still provides an indication of the performance of multiple undulating body systems, and wake–wake interactions in the system can be elucidated by the flow transportation between low- and high-energy zones.

4.4 Chapter Summary

In this work, the sharp interface immersed boundary method has been applied to study the phase difference effects on the hydrodynamic interactions in high-density schools, including vortex–body, body–body, and wake–wake interactions. It has been found that the highest net thrust

$\overline{C_{X\_max}^{ave.}} = 0.08$, and the highest swimming efficiency, $\eta_{max}^{ave.} = 0.57$, of the whole school can be achieved when the phase difference is 180°. The highest propulsive efficiency of fish 4 can be reached at φ =90°, where $\eta_{max}^{4} = 0.698$, an improvement of 58.3% over a single fish. At the same time, $\overline{C_T^4} = 0.376$ is 71.7% higher than $\overline{C_T}$ of a single fish. In addition, for fish 4, there exists a cosinusoidal relationship between $\overline{C_{PW}^4}$ and the phase difference, and an approximately sinusoidal relationship between the swimming efficiency and the phase difference.

Based on its position in a school, the body of fish 4 was divided into two parts: (1) the anterior part, which lies in the channel formed by fish 2 and 3, and (2) the posterior part, which is outside of this channel. The associated mechanisms have been explored separately. For the posterior part of fish 4, the hydrodynamic performance in school 1 (φ =0°) and school 2 (φ =90°) were studied in detail. The vortex-capturing mechanism for an undulating body operates by choosing the appropriate phase, whereby the undulating body can produce more thrust and capture the energy from the vortex flow. Additionally, when vortices interact with the undulating body, the secondary vortex might attach to the body and advect downstream, thus enhancing thrust production or reducing power consumption by altering the pressure around the body. For the anterior part, the hydrodynamic performance in schools 1 and 4 (φ =270°) was compared to clarify the associated mechanisms. C_X and C_{PW} of the anterior part were calculated and quantitatively analyzed. The results suggest that the anterior part of fish 4 in school 1 can produce 56.3% more thrust than in school 4, while the anterior part in school 4 harvests energy from the flow instead of consuming power. By calculating the net streamwise momentum flux, we uncovered the body–body matching mechanism between the anterior part and the channel: by altering the phase, the anterior part can actively control the momentum flux that passes through the channel, resulting in improved thrust production or reduced energy consumption. The vortex-capturing mechanism and body–body

matching mechanism of the trailing fish in a high-density school will offer new insight into possible control strategies for efficient bio-inspired underwater robotic swarms and contribute to understanding the underlying physical mechanisms in fish schools.

Finally, the wake patterns of multiple undulating swimmer systems have been categorized and analyzed for the first time. A study of the vortex dynamics shows that the wake pattern of a school is strongly dependent on the phase difference. When increasing the phase difference from 0° to 360°, the vortex wake of fish 4 changes from the rBvK pattern to the BvK pattern due to the wake–wake interaction with the lateral wakes. Meanwhile, the vortex strength, rotation angle, and advection velocity of vortex pairs behind fish 2 and 3 vary with the phase difference because of the associated vortex–body and wake–wake interactions. Also, the relationship between the generated wake pattern and the performance of a high-density fish school has been built through the phase difference. This increased understanding of the wake dynamics of dense fish schools can inspire the accurate wake detection of multiple swimmers.

5 On the Varying Tail-Beat Frequency in a High-Density Fish School

It has been observed that fish swimming in the vortex wake shed by cylinders synchronize the tail-beat frequency to capture energy from vortices[50]. In experiments with real fish, the trailing fish attain hydrodynamic benefits in a school by utilizing a lower tail-beat frequency [57]. However, the effects of the tail-beat frequency on the hydrodynamic performance and interactions in a high-density school are still ambiguous. To fill the gap, we simulate the flow past synchronized and asynchronized high-density diamond-shaped schools using the immersed-boundary-method-based in-house solver in this section. Specifically, the synchronized school denotes all swimmers performing the same tail-beat frequency in the school, while the asynchronized school indicates only the frequency of the trailing fish is changed. Also, the performance and wake patterns of single fish with varying tail-beat frequencies are presented as baseline cases. Then, a comprehensive comparison and analysis of the hydrodynamic performance and vortex dynamic have been provided for each kind of school to identify the fundamental flow mechanisms associated with efficient swimming in synchronized and asynchronized schools.

5.1 Problem Statement

The swimming kinematics of individual swimmers is set up similarly to the previous sections: a traveling wave kinematics imposed on a NACA0012 foil shape is employed to represent two-dimensional swimming bodies. The carangiform undulating motion is used and the equations are the same as those in previous sections except for the tail-beat frequency f, which covers a wide range in this section. Fig. 5-1(a) shows the corresponding midlines and amplitude envelope. The school configuration is a diamond-shaped formation with the streamwise (S) and lateral (D)

spacings of both 0.4 body length (BL), as shown in Fig. 5-1(d). The schematics of the synchronized and asynchronized schools are shown in Figs. 5-1(c) and 5-1(d), respectively, in which different colors denote individual swimmers with different frequencies. The frequency is varied by changing the undulating period T. The time histories of the tail-tip motion for fish with different frequencies are compared in Fig. 5-1(b).

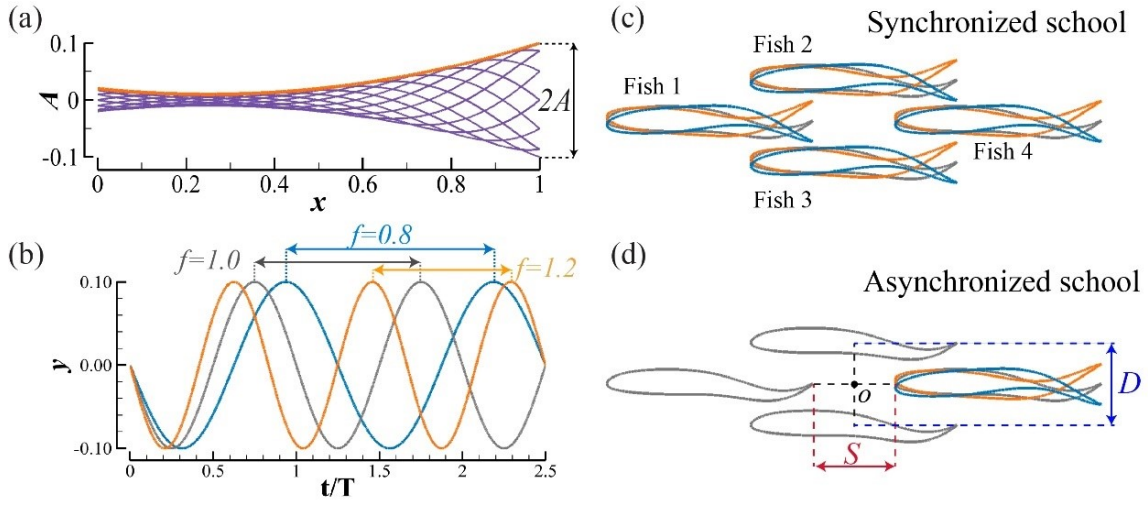

Figure 5-1. (a) Motion of fish model midline during one tail-beat cycle and amplitude envelope of the undulating motion, (b) time history for the tail-tip motion of fish with different tail-beat frequencies, (c) schematic of the synchronized schools with varied frequencies, and (d) schematic of the asynchronized schools with various frequencies. Orange, gray and blue colors indicate individual swimmers with high, medium and low tail-beat frequencies, respectively.

5.2 Simulation Setup and Validation Study

Two key dimensionless parameters associated with the flow simulation of fish swimming are the Reynolds number Re and the Strouhal number St defined as $Re = U_\infty L/\upsilon$ and $St = fA/U_\infty$, where ν denotes the kinematic viscosity. In this section, the Reynold number is set as $Re = 1000$, the frequency f changes from 0.46 to 1.2 and the corresponding Strouhal number is at the range

of $0.20\sim0.52$ which covers the range of real fish swimming [26]. All the performance parameters, including forces, powers and efficiencies, are calculated using the same definitions as in Chapter 3.

The computational domain, Cartesian grid and boundary conditions employed in the simulations are the same as the set-up in Chapter 4 and shown in Fig. 5-2(a). The same grid size is employed as in Chapter 4, in which the simulation results have been proved to be grid-independent, i.e. $\Delta_{min} = 2.94 \times 10^{-3}L$ with a total grid point of 1.03 million (1601×641). A time-independent study is added here to demonstrate that the current time-step size is fine enough to obtain accurate results. Figure 5-2(b) compares the instantaneous net force coefficient C_X (along the swimming direction) of a solitary fish over one period calculated with the time-step size of $\Delta t = 1/400$, $1/800$ and $1/1000$. As the time-step size decrease, C_X converges. The percentage difference between the peak values of the cases with $\Delta t = 1/800$ and $\Delta t = 1/1000$ is less than 1%. Therefore, $\Delta t \leq 1/800$ is used in this section.

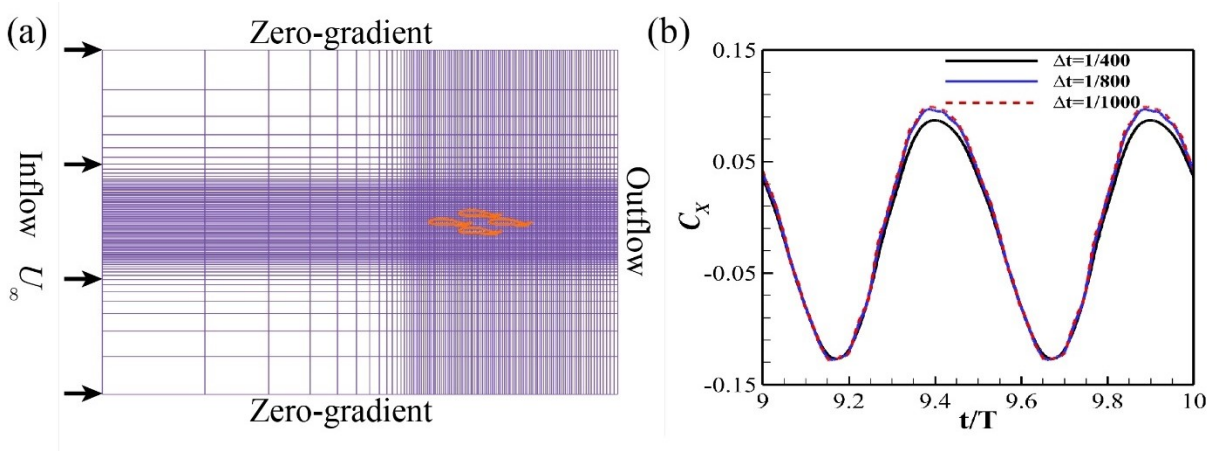

Figure 5-2. (a) Schematic of the computational domain, Cartesian grids, and boundary conditions. (b) Comparison of the instantaneous net force coefficients in the x-direction C_X of a single fish calculated with the time-step size of $\Delta t = 1/400$, $1/800$ and $1/1000$.

5.3 Results and Discussions

We first present the hydrodynamic performance, vortex wakes, mean flows and the corresponding streamwise velocity profiles for single fish with varied tail-beat frequencies in section 5.3.1. It is found that as the frequency increases, the thrust production is monotonically improved and the associated vortex wake changes from the Bénard-von Kármán (BvK) wake to the reverse Bénard-von Kármán (rBvK) wake. Then, the hydrodynamic performance of individuals and vortex dynamics analysis for synchronized schools are provided. In the synchronized schools, when $f = 0.81$, the school reaches a steady swimming state and when $f = 0.83$, the swimming efficiency of the school gets to its peak, $\eta_{max} = 0.55$, which is improved by 31% over a single fish. At $f = 0.83$, two stable 2P wakes are generated on the lateral sides of the school, and a 2S-aligned wake forms behind fish 4. It shows that the peak of the swimming efficiency occurs close to the peak of the momentum entrainment ratio, which implies that the efficient swimming of fish schools is related to the wake resonance theory. Finally, the performance of fish 4 and the associated vortex wakes of asynchronized schools are presented. At $f = 0.71$, the efficiency of fish 4 achieves its optimal, $\eta_4 = 0.66$ improved by 78% over a single fish. Correspondingly, a stable 2S wake is generated behind fish 4.

5.3.1 Performance and Wake Patterns of a Single Fish Varying with Frequency

The time-averaged net force $\overline{C_X}$ (along the swimming direction), the time-averaged thrust $\overline{C_T}$, the time-averaged output power for undulation $\overline{C_{PW}}$, and the associated swimming efficiency η of a solitary fish are presented in Fig. 5-5 as functions of the varied tail-beat frequency. The net force $\overline{C_X}$ monotonically increases with the increasing tail-beat frequency f. When $f < 1.0$, $\overline{C_X} < 0$ denotes the fish suffering net drag; as $f > 1.0$, $\overline{C_X} > 0$ is a net thrust. The total thrust $\overline{C_T}$ and power for undulation $\overline{C_{PW}}$ of the single fish both follow the same trend as the $\overline{C_X}$.The swimming

efficiency increases when $f < 1.05$, then reaches the optimal $\eta_{max} = 0.446$ around $f = 1.05$, and decreases when $f > 1.05$. High swimming efficiency for a single fish can be obtained when $1.0 \leq f \leq 1.11$ [Zone 1 in Fig. 5-5(d)], and the corresponding Strouhal number changes from 0.43 to 0.48. The performance of a single fish is presented to help measure the variation of performance of individuals in synchronized and asynchronized fish schools.

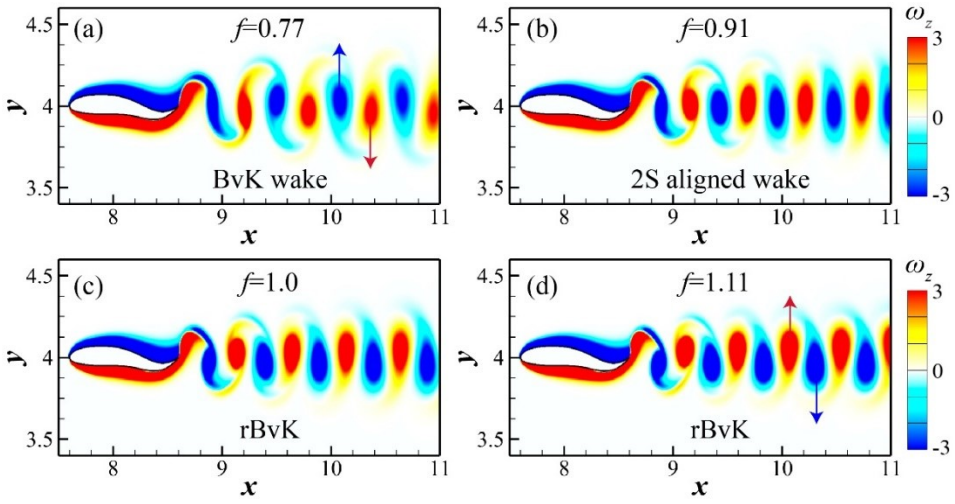

Figure 5-3. Vortex wake of a single fish swimming at (a) $f = 0.77$, (b) $f = 0.91$, (c) $f = 1.0$, and (d) $f = 1.11$ at $t = 10.0T$.

Meanwhile, the wake structures and mean flows are presented in Figs. 5-3 and 5-4, respectively. Figure 5-3 displays the vortex wake of a single fish swimming at a low frequency ($f = 0.77$), medium frequencies ($f = 0.91$ and $f = 1.0$) and a high frequency ($f = 1.11$) at $t = 10.0T$. When increasing frequency, the lateral distance between the neighboring negative (blue) and position (red) vortices decreases, and the wake pattern transfers from a BvK wake [Fig. 5-3(a)] to a 2S aligned wake [Fig. 5-3(b)][14]. Then, the positive vortices are at a higher position than the negative vortices when increasing the frequency. Finally, an rBvK wake is formed [Fig. 5-3(d)]. Correspondingly, the mean flow changes from a drag wake [113] [Fig. 5-4(a)] to a jet wake [the

high momentum jet in Fig.5-4(c)]. The rBvK wake induces a flow between the negative and positive vortices and imparts more streamwise momentum to the fluid, implied by the symmetric high-momentum jet in Fig. 5-4(c). The velocity profiles at $x = 8.7$ (P1 position), $x = 9.0$ (P2 position) and $x = 9.3$ (P3 position) are also presented in Fig. 5-4. The tail-tip of the fish is at $x = 8.6$. In comparison, with a high tail-beat frequency, the time-averaged velocity at the wake's centerline is high and maintained for a long way downstream. With a low frequency, the time-averaged velocity profiles behind the fish body are drag wake, i.e., the velocity at the center of the wake is less than the incoming flow velocity, as shown in Fig. 5-4(f). Besides, the widths of the jets of the fish with varied frequencies are very close [Fig. 5-4(e-f)]. The observations will help to measure the effects of tail-beat frequency on the wakes of fish schools.

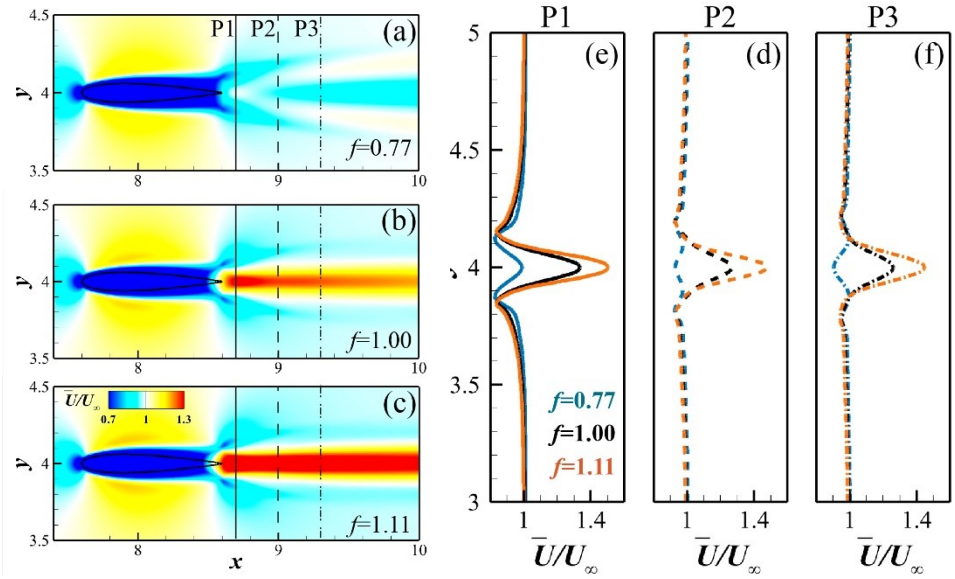

Figure 5-4. Time-averaged streamwise velocity field of the single fish swimming at (a) $f = 0.77$, (b) $f = 1.0$, and (c) $f = 1.11$. Comparisons of velocity profiles among these three cases at (e) $x = 8.7$ (P1 position), (d) $x = 9.0$ (P2 position) and (f) $x = 9.3$ (P3 position). The tail-tip of the fish is at $x = 8.6$.

5.3.2 Performance and Wake structures of Synchronized Schools

The hydrodynamic performance and vortex dynamics are presented in this section to study the effects of tail-beat frequencies on the hydrodynamic interactions in a synchronized school. Figure 5-5 illustrates the time-averaged total thrust coefficient $\overline{C_T}$, time-averaged power for undulation $\overline{C_{PW}}$, the time-averaged net force in the swimming direction $\overline{C_X}$ and the associated swimming efficiency η for individual swimmers in the fish schools varying with the tail-beat frequency. The averaged hydrodynamic performance of the schools is also displayed in Fig. 5-5. In Fig.5-5(a), the $\overline{C_T}$s of all individuals in the schools follow the same trend as the $\overline{C_T}$ of single fish: monotonically rise as the frequency increases. Meanwhile, due to benefiting from the schools, the $\overline{C_T}$s of the individuals grow faster than that of a single fish. Among all the fish, fish 4 has the most significant growth rate for $\overline{C_T}$ because of the vortex-capturing mechanism and body-matching suction studied in section 4. When $f = 1.2$, $\overline{C_{T\_4}} = 0.577$ is 62.5% higher than that of the single fish. For $\overline{C_{PW}}$, it shares the same trend as the $\overline{C_T}$ as the frequency increases. Fish 4 consumes less power than a single fish at different frequencies, and $\overline{C_{PW\_2}}$ and the averaged $\overline{C_{PW}}$ of a school is close to $\overline{C_{PW\_S}}$, where $\overline{C_{PW\_2}}$ denotes $\overline{C_{PW}}$ of fish 2 and $\overline{C_{PW\_S}}$ is the $\overline{C_{PW}}$ of a single fish, while fish 1 outputs more power than a single fish because it needs to overcome the high pressure created by the channel.

In Fig. 5-5(c), the $\overline{C_X}$ of all fish in the schools monotonically increases with increasing frequency, and fish 4 has the highest $\overline{C_X}$. Besides, all individuals reach the steady-swimming condition at lower frequencies than a single fish and then experience a net thrust. For instance, when $f = 0.7$, $\overline{C_{X\_4}} = 0.003$ and fish 4 is at the steady-swimming state. In real fish swimming, the net thrust can be converted into a higher speed or energy savings. The results imply that fish swimming in a high-density school can gain a higher speed without increasing the tail-beat frequency or saving energy by reducing the frequency.

The swimming efficiencies of fish 2, fish 4 and the whole school (the averaged efficiency) show a bell-shaped function of the tail-beat frequency in Fig. 5-5(d). It is similar to that of a single fish. However, the peaks are shifted left with a higher magnitude. The peak efficiencies of fish 2, fish 4 and the school are located at Zone 2, the narrow gray zone around $f = 0.83$ in Fig. 5-5(d). Among all fish in a school, fish 4 has the highest swimming efficiency no matter what the frequency of the school is. This observation is consistent with the finding in section 3. The peak efficiency of fish 4 is 0.637 around $f = 0.83$, improved by 52.4% over a single fish at the same frequency ($\eta_s = 0.418$). The highest efficiency for the whole school is 0.551 at $f = 0.83$, 31.8% higher than that of a single fish. Besides, at $f = 0.83$, the averaged net force coefficient of the school is a net thrust, $\overline{C_X} = 0.006 > 0$. Thus, from the view of efficient swimming, the synchronized school is optimal at $f = 0.83$. The evolution of vortex structures and the wake patterns of schools at different tail-beat frequencies will be investigated in the following to explore the physical mechanisms behind efficient swimming in synchronized schools.

It has long been believed that the flow field contains evidence of efficient swimming [18, 23, 114-117], and considerable effort has been devoted to establishing the relationship between the characteristics of the wake and efficient propulsion. Through a linear stability analysis of the mean flow behind an oscillating foil, Triantafyllou et al. [18] found that the peak in swimming efficiency can be obtained at the frequency of maximum amplification. Based on this finding, Moored et al. [116] developed the wake resonance theory by performing linear spatial stability analysis on the time-averaged flow field of a three-dimensional flexible flapping fin and suggested that when the driving frequency of motion is close to the jet resonant frequency, the optima in swimming efficiency achieve. Inspired by these researches, the highly efficient swimming in fish

schools is investigated by characterizing the vortex wake and time-averaged streamwise velocity field.

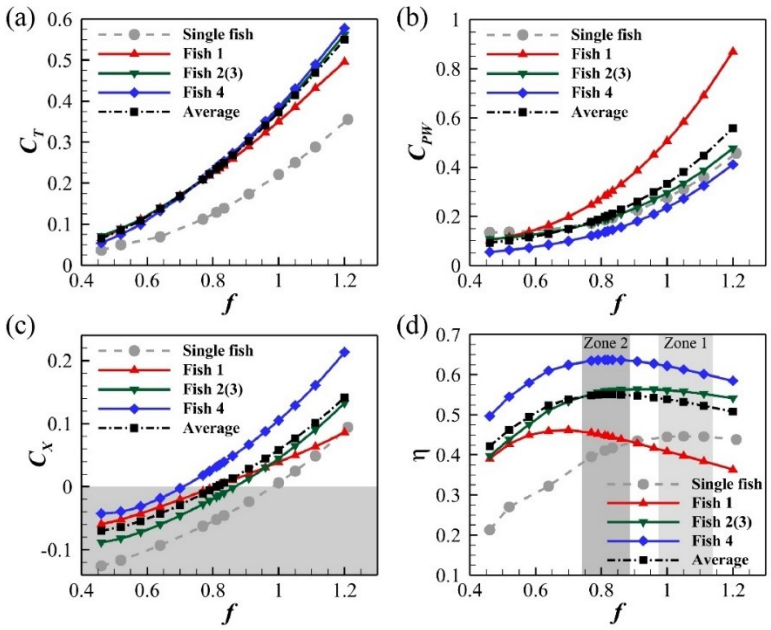

Figure 5-5. (a) Time-averaged thrust $\overline{C_T}$, (b) time-averaged power for undulation $\overline{C_{PW}}$, (c) time-averaged net force in the swimming direction $\overline{C_X}$, and (d) the corresponding swimming efficiency η for single fish, individual swimmers in the schools and the averaged value for the schools varying with the tail-beat frequency.

Figure 5-6 shows the snapshots of the vortex wakes for three synchronized fish schools at $t = 0.25T$ [Figs. 5-6(a1-c1)], $t = 0.50T$ [Figs. 5-6(a2-c2)], $t = 0.75T$ [Figs. 5-6(a3-c3)]. Low frequency ($f = 0.64$), optimal frequency ($f = 0.83$) and high frequency ($f = 1.11$) schools are compared to examine the influence of tail-beat frequency on the vortex wakes. In the low-frequency school, vortex pairs shed by fish 2 rotate clockwise to the center of the wake while advecting downstream [see Fig. 5-6(a1-a3)], the vortices shed by fish 2 will merge with those shed by fish 4, and the wake of the whole school finally becomes a BvK wake [see far wake in Fig. 5-6(a3)]. In comparison, at the optimal frequency ($f = 0.83$), the direction of vortex pairs shed by

fish 2 is maintained while being transported downstream. Hence, stable 2P wakes are formed behind fish 2 and 3, respectively, and a 2S-aligned wake is produced behind fish 4. These three stable wakes are beneficial to converting output energy to the streamwise momentum jet. At high frequency ($f = 0.83$), the vortex pairs shed by fish 2 rotate counterclockwise when advecting downstream, as shown in Fig. 5-6(c1-c3). Due to the wake-wake interaction, a BvK wake is produced behind fish 4, which is usually less efficient than the 2S-aligned and rBvK wake. Also, the counterclockwise rotation reduces the advection velocity of the vortex pairs, resulting in the loss of the momentum jet.

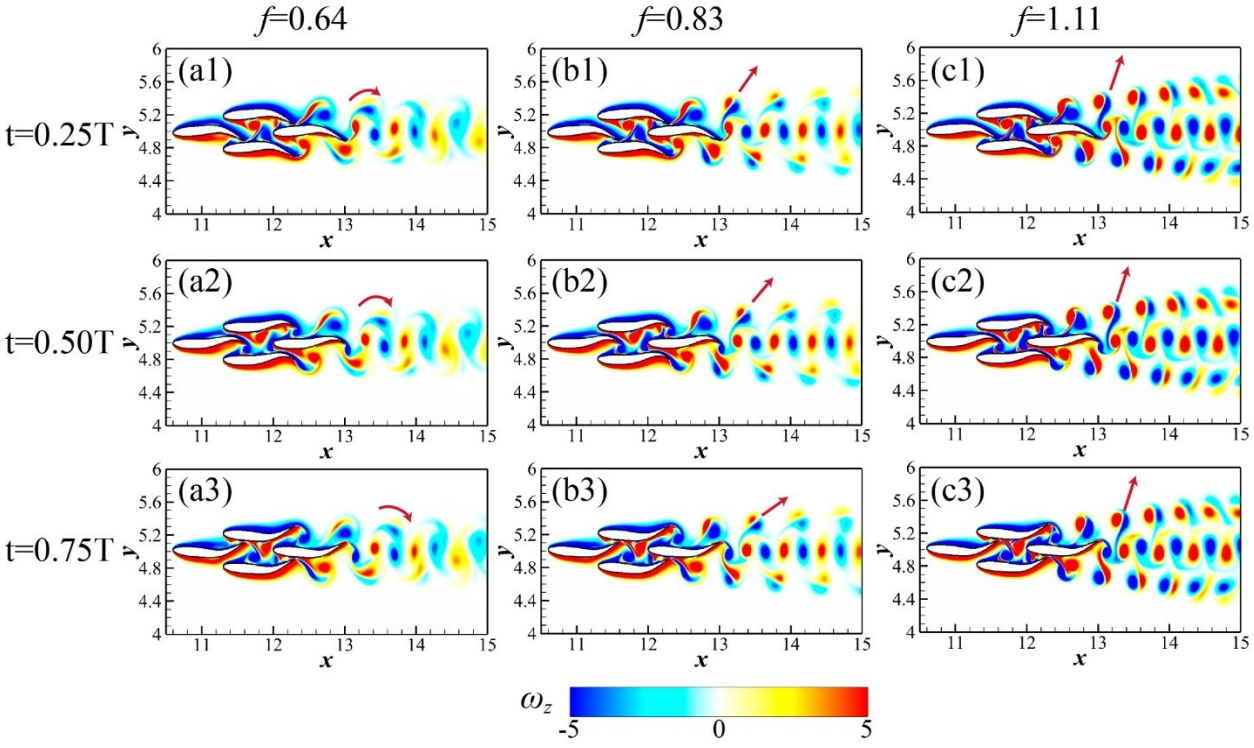

Figure 5-6. Instantaneous vortex wakes of the low-frequency ($f = 0.64$) (a1-a3), optimal frequency ($f = 0.83$) (b1-b3), and high frequency ($f = 1.11$) (c1-c3) schools at $t = 0.25T$ (a1-c1), $t = 0.50T$ (a2-c2), $t = 0.75T$ (a3-c3).

Specifically, the interactions between vortices shed by fish 2 and the body of fish 4 are first influenced by the varied frequencies. Then, the vortex pairs passing by the tail-tip of fish 4 may rotate in different directions with varied angular velocities and interact with the vortices shed by fish 4. Different kinds of wake patterns are thus formed, implying the varying swimming efficiency of the schools. Schematic plots are presented in Fig. 5-7 to help elucidate the vortex-body interaction and vortex pair rotation processes. In the low-frequency school ($f = 0.64$), the negative vortex shed by fish 2 interacts with the boundary layer vortex sheet of fish 4 and is strengthed. Due to the difference in vorticity, the mutual induction between the negative and positive vortices results in the vortex pair rotating clockwise, as shown in Fig. 5-7(a). In the optimal frequency school, the vorticities of negative and positive vortices are comparable, and the direction of the vortex pair can be maintained when advecting downstream. In the high-frequency school, although the vorticity of the negative vortex shed by fish 2 is enhanced when passing by the body of fish 4, it interacts with the vortices shed by fish 4 and is weakened [Fig. 5-6(c1-c3)]. The variation of the negative vortex makes the vortex pair rotate in the counterclockwise direction, as shown in Fig. 5-7(c).

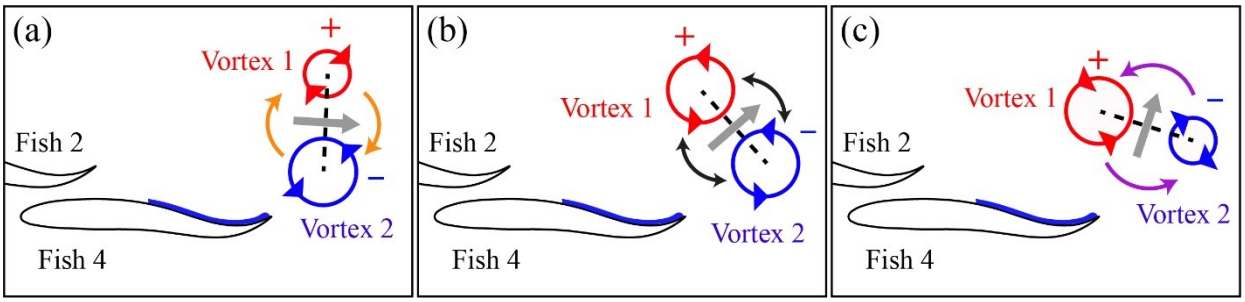

Figure 5-7. Schematics of vortex-body interaction and vortex pair rotation in the (a) low-frequency, (2) optimal-frequency, and (c) high-frequency schools.

Figure 5-8 presents the typical instantaneous vortex wakes at $t = 10.0T$ and time-averaged streamwise velocity fields of schools at low, medium, and high frequencies. At the lowest frequency ($f = 0.46$), the vortices shed by fish 2 merge to the boundary layer vortex sheet of fish 4, and only a BvK wake is formed behind the school. Correspondingly, the time-averaged velocity field is a drag wake. Then, with the frequency increasing to $f = 0.58$, although the vortices shed by fish 2 can 'escape' from the boundary layer vortex sheet of fish 4, the stronger negative vortex results in the vortex pair rotating to the central wake and merging with it. Consequently, an rBvK wake is generated in the far wake of the school. At $f = 0.79$, the net force of the whole school in the swimming direction starts being larger than zero, i.e., being a net thrust, the vortex pairs induced by fish 2 can parallelly advect downstream for a short distance, and 2P wake is formed in the near wake of fish 2 and fish 3. Hence, two short jets (2SJ) are generated behind the school, although the strength of the jets is weak[see Fig. 5-8(c2)]. At the optimal frequency, the vortex pairs generated by fish 2 maintain the direction when advecting downstream, stabilizing the vortex wake, and the school produces two stronger short jets (2SJ).

Meanwhile, a 2S-aligned wake is formed behind fish 4. Continuing increasing the tail-beat frequency, the vortex pairs rotate counterclockwise, and due to the variation of the wake-wake interaction, a 2S BvK wake is developed at the center. Two long jet wake appears at $f = 1.11$. In summary, as the tail-beat frequency increases, the wake at the center changes from an rBvK to a Bvk wake, and the school with optimal efficiency is accompanied by the stable 2P wakes at the upper and bottom sides and 2S aligned wake at the center. Hence, the 2S aligned wake at $f = 0.83$ is at the transition stage.

To further investigate the wakes, Fig. 5-9 presents the velocity profiles extracted at 0.1BL, 0.4BL and 0.7BL behind the schools at different tail-beat frequencies. In Fig. 5-9(a), W-shaped

velocity profiles are formed. The central velocity peaks occur at the position right behind fish 4, and the side velocity peaks happen at the position higher than fish 2 or lower than fish 3. The velocity peaks increase as the tail-beat frequency increases. Besides, in Fig. 5-9(a), when $f = 0.83$ (the optimal frequency), the velocity at the position that is right behind fish 2 and fish 3 is close to the velocity right behind fish 4. When $f < 0.83$, the velocity right behind fish 2(and 3) is larger than that right behind fish 4; when $f > 0.83$, vice versa.

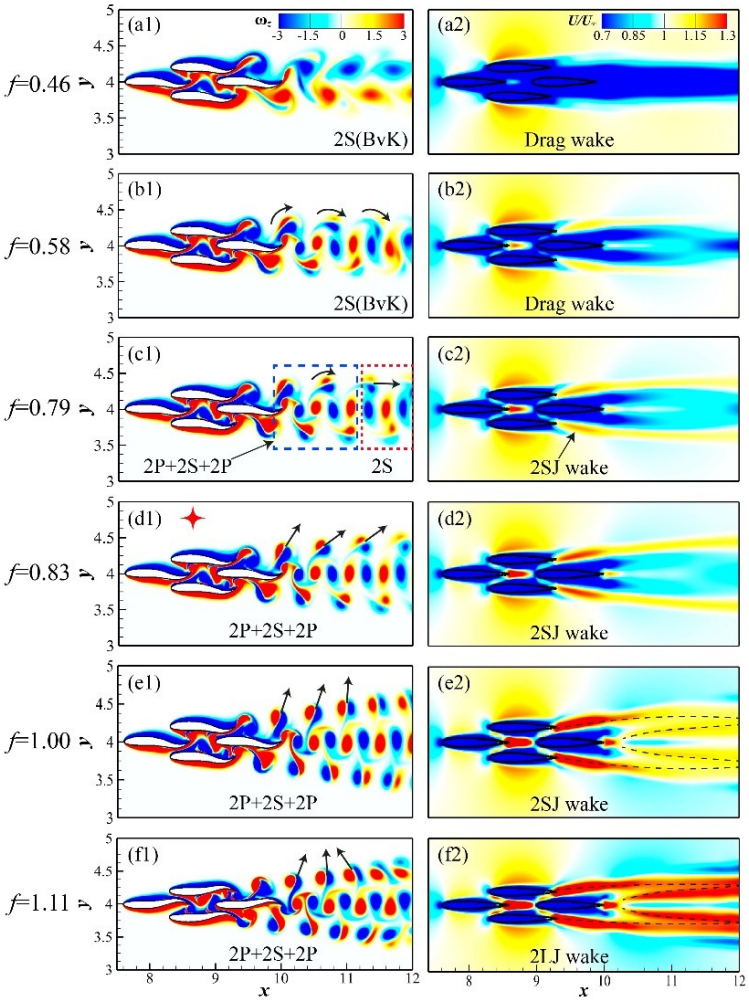

Figure 5-8. Vortex wakes at $t = 10T$ (a1-f1) and time-averaged velocity fields (a2-f2) of schools at different tail-beat frequencies.

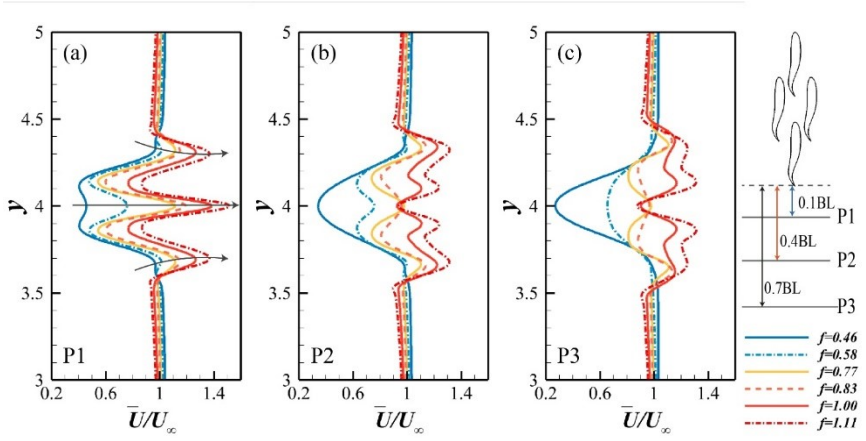

Figure 5-9. Velocity profiles behind the schools at varied tail-beat frequencies at a distance of (a) 0.1BL, (b) 0.4BL and (c) 0.7BL.

With a farther distance (0.4BL), the velocity profile of the school at $f = 0.46$ becomes the classical drag wake velocity profile, while the shapes of other profiles are complex, as shown in Fig. 5-9(b). The shape of the velocity profiles extracted at 0.7BL behind the schools is comparably stable. Then, the relative streamwise momentum with respect to the incoming flow is calculated for each school to categorize the wakes. The relative streamwise momentum is defined as follows

$$\Delta p_x = \int_{y_1}^{y_2} (\bar{U}^2 - U_\infty^2)\, dy, \tag{5-1}$$

where $y_1 = 3.5$ and $y_2 = 4.5$ in this study. The y-values are chosen based on the velocity profiles in Fig. 5-9(c), from which we can see that when $y > 3.5$ and $y < 4.5$, the streamwise velocity becomes steady and is close to the incoming flow velocity. Figure 5-10(a) shows that Δp_x has an approximately linear relationship with the tail-beat frequency. In Fig. 5-10(a), the Δp_x monotonically increases as the tail-beat frequency increases. In Fig. 5-5(c), when $f \leq 0.70$, all the individuals in a school suffer drag; as increasing f, fish 4 first reaches to the steady swimming state at $f \approx 0.71$, and fish 1 secondly satisfies the steady swimming condition at $f \approx 0.80$. When

$f = 0.86$, $\overline{C_X}$ of fish 2 and fish 3 is -0.002, almost reaching the steady swimming state, and other individuals generate a net thrust. According to Newton's second law, the school delivers net momentum downstream at $f = 0.86$. After this point, each member in the schools experiences an increasing net thrust when the tail-beat frequency increases, which implies more momentum is delivered downstream at a higher tail-beat frequency. In the meantime, when $f = 0.86$, the relative streamwise momentum $\Delta p_x = -1.6 \times 10^{-5} \approx 0$. When $f < 0.86$, $\Delta p_x < 0$ and when $f > 0.86$, $\Delta p_x > 0$. The strong correlation between the $\overline{C_X}$ and the Δp_x suggests that the Δp_x can be a representative parameter to describe the wake of a school and help establish the relationship between the tail-beat frequency and the wake of the school. Hence, based on the definitions of the wakes of self-propelled bodies [118], when $f = 0.86$, the wake of the school is defined as the momentumless wake. When $f < 0.86$, $\Delta p_x < 0$ and the corresponding wakes are classified as the drag wake; when $f > 0.86$, $\Delta p_x > 0$ and the wakes are the jet wakes. The velocity profiles behind the schools of $f = 0.70$, 0.86 and 1.11 at a distance of 0.7BL are shown in Fig. 5-10(b) to represent the drag wake, momentumless wake and the jet wake of the fish schools. Although the variation of the velocity profiles of fish schools is more complicated than that of a single fish, the differences among these three kinds of wakes are evident.

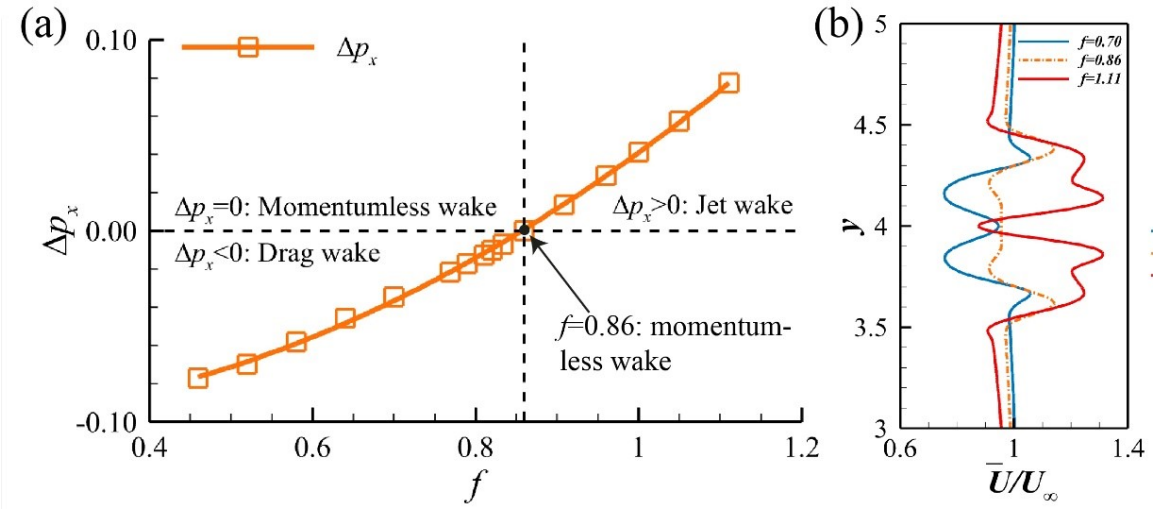

Figure 5-10. (a) Relative streamwise momentum Δp_x varying with the tail-beat frequency and (b) velocity profiles behind the schools of $f = 0.70$, 0.86 and 1.11 at a distance of 0.7BL. The wakes are the drag wake, momentumless wake and jet wake, respectively.

Next, with further analysis of the momentum of the wake, the connections among the wake dynamics, swimming kinematics and swimming efficiency in the fish schools are established. Moored et al. [116] developed the hydrodynamic wake resonance theory for a single flapping fin through a linear spatial stability analysis. They stated that the optimal propulsive efficiency is obtained when the driving frequency of the flapping fin matches the resonant frequency of the wake. However, the theory has not been examined for multiple moving objects. Here, the momentum entrainment [117] from the lateral sides of the wake is calculated to help measure the variation of the swimming efficiency. Within a finite region behind the school, if the time-averaged cross-stream velocity directs to the center and the lateral momentum entrains into the region, the stream-wise vorticity will be compressed and concentrated and a stronger streamwise velocity jet will be generated. The advection of the streamwise momentum is thus enhanced.

We use a control volume, as shown in Fig. 5-11(a), to measure the momentum entrainment. The inlet is located right behind the school, and the outlet is at a distance of 0.7BL behind the school where the velocity profile is pretty stable (see Fig. 5-9). The sides of the CV are centered symmetrically around the center of the school and are fixed at a location where the streamwise velocity is steady. Specifically, the sides are located at $y = 3.5$ and $y = 4.5$. The momentum flux at the sides is calculated by $-\int_{sides} \rho u(\boldsymbol{n} \cdot \boldsymbol{u}) dx$. Then, the momentum entrainment ratio, the ratio of the momentum entrainment from the sides of the CV to the momentum flux at the inlet, is defined as follows,

$$\gamma = \frac{\int_{sides} uvdx}{\int_{inlet} u^2 dy}, \tag{5-2}$$

The results are shown in Fig. 5-11(b) as a function of the tail-beat frequency. In Fig. 5-11(b), a single peak of the momentum entrainment ratio is at $f = 0.68$ where the swimming efficiency of the school is comparatively high, although the peak is earlier than the peak efficiency of the schools ($f = 0.83$) denoted by the red dashed line. Besides, the swimming efficiency of the school is high when the tail-beat frequency is within the range of $0.68 < f < 0.83$. The variation of the entrainment ratio qualitatively shows that the around the wake resonant frequency, more momentum entrains from the sides into the time-averaged velocity jet, contributing to a high swimming efficiency of the schools.

The unmatch between the peak of the entrainment ratio and the peak efficiency might stem from two reasons. First, according to the study of Arbie et al. [119], the instability analysis of the momentum wake of the swimming animal is different from that of the propulsors. The physical interpretations of swimming efficiency based on the wake instability analysis thus cannot be

directly applied to a self-propelled body, no matter for a fish school. Second, the current theory did not consider the interactions between the vortex wakes generated by the lateral fish and the trailing fish. More work is needed to establish the wake resonance theory for fish schools.

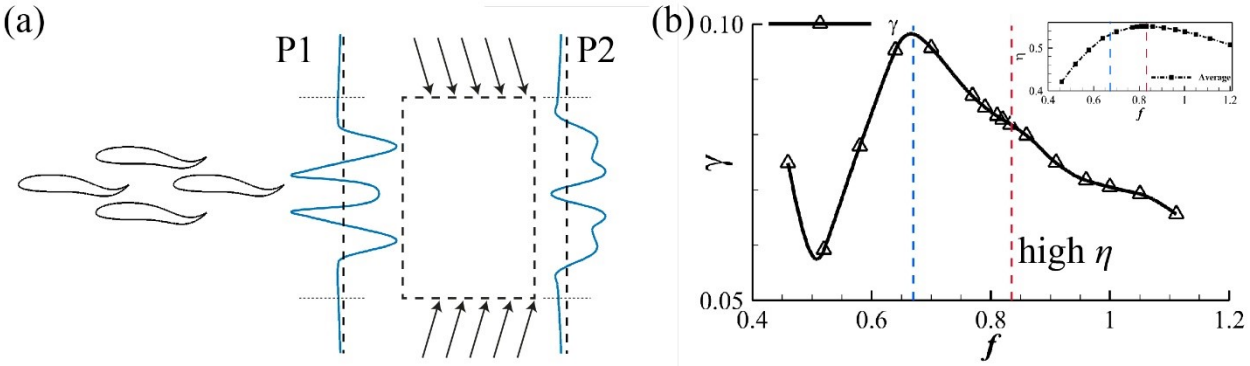

Figure 5-11. (a) Schematic of calculation of the momentum entrainment from the sides of the control volume (CV) with the inlet and outlet velocity profiles. (b) Momentum entrainment ratio varies with the tail-beat frequency. The blue dashed line denotes the peak of the entrainment ratio and the red dashed line indicates the peak of school swimming efficiency. The subplot shows the swimming efficiency of the schools varying with the tail-beat frequency.

5.3.3 Performance and Wake Structures of Asynchronized Schools

In nature, fish at the back of a school prefers to swim at a lower frequency [57] by obtaining the hydrodynamic benefits from the flow generated by fish in the front. It has been reported that fish can extract energy from the vortex flow generated by a stationary object or moving object by alternating the locomotion mode [51, 120]. However, the flow in dense schools is exceptionally complex, and how the trailing fish capture energy in the dense school by adjusting the tail-beat frequency has not ever been studied. This section investigates the effects of tail-beat frequencies on the hydrodynamic interactions in asynchronized schools in which the tail-beat frequency of fish 4, the trailing fish, varies. In particular, the hydrodynamic performance of fish 4 and the wake

dynamics are analyzed. The schematic of asynchronized schools is presented in Fig. 5-1(d), in which all individuals except for fish 4 swim at $f = 0.83$ where the optimal efficiency occurs for the synchronized schools, while the tail-beat frequency of fish 4 changes from $f = 0.46$ to $f = 1.25$.

Figure 5-12 compares the hydrodynamic performance between fish 4 in the asynchronized schools and the single fish as the tail-beat frequency increases. When increasing the tail-beat frequency, the thrust and power consumption monotonically increase both for fish 4 and the single fish, as shown in Figs. 5-11(a) and 5-11(b). However, fish 4 generates more thrust than a single fish with a lower power consumption. In Fig.5-11(c), fish 4 reaches a steady swimming state around $f = 0.71$. The lower frequency implies that fish 4 can obtain hydrodynamic benefits from the fish school. Besides, fish 4 achieves the highest swimming efficiency ($\eta_{max} = 0.66$), 74% higher than that of a single fish at the same frequency, at $f = 0.71$, which is smaller than the efficiency peak of fish 4 in the synchronized schools. Then, as the frequency increases, the η of fish 4 declines. The results suggest the trailing fish in a dense school can reduce its tail-beat frequency to save energy and achieve a higher swimming efficiency without losing thrust production.

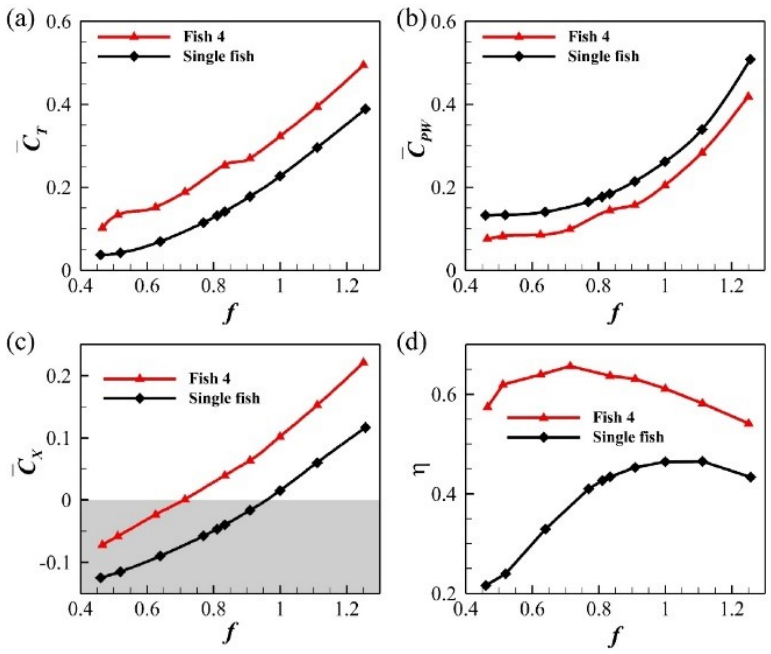

Figure 5-12. Hydrodynamic performance of fish 4 in the asynchronized schools and single fish varying with the tail-beat frequencies, including (a) total time-averages thrust coefficient $\overline{C_T}$, (b) time-averaged power coefficient $\overline{C_{PW}}$, (c) time-averaged net force in the swimming direction $\overline{C_X}$ and (d) the swimming efficiency η.

In all of the asynchronized schools, the tail-beat frequencies of fish 1, 2 and 3 are 0.83 and the corresponding period is defined as T_0. Figure 5-13 shows the vortex wakes of schools at the frequencies of (a) $f_4 = 0.63$, (b) $f_4 = 0.71$, (c) $f_4 = 0.83$ and (d) $f_4 = 1.11$ at $t = 10T_0$. First, it can be observed that the flow environments around fish 4 are very similar in schools at different frequencies at the same time. However, at $t = 10T_0$, fish 4 undulates with different poses and velocities in these schools. The difference in frequency is thus transferred into the phase difference between the flow environment and the undulation of the bodies, which partially results in differences in swimming efficiency in different schools. From a different perspective, if fish 4 undulates to the same pose in different schools, the flow environments around fish 4 are varied, which can be observed by comparing Figs. 5-15(a), 5-16(a) and 5-17(a), and the hydrodynamic

performance thus varies. To directly show the performance variation, the force distribution along the fish body has been presented in Figs. 5-15(a-c) for fish 4 undulating to the same pose in the fish schools of $f_4 = 0.63$, $f_4 = 0.71$ and $f_4 = 1.11$. The pressure profiles of the upper surface of fish 4 are shown in Fig. 5-15(d). The school of $f_4 = 0.63$ shares a similar flow environment as the school of $f_4 = 0.71$. Thus fish 4 has similar force distribution and pressure profiles in these two schools. However, due to the difference in the flow environment, the pressure profile of fish 4 in the high-frequency school has the opposite trend compared to the other two schools.

In comparison, in the low-frequency schools, the negative vortices shed by fish 2 get enhanced through interactions with the boundary layer vortex sheet of fish 4 and become stronger than in the high-frequency schools. For example, the negative vortex in Fig. 5-13(a), V_{a1}, is stronger than the vortex V_{d1}, which is shed at the same time as V_{a1}, in Fig. 5-13(d). Also, in the schools both at high and low frequency, the vortex wake generated by fish 2 strongly interacts with the wake generated by fish 4 in the far wake [see Fig. 5-13(a)] or near wake [see Fig. 5-13(d)]. That is, the wake of the whole school is not stable when fish 4 swims at high and low tail-beat frequencies. However, when the frequency of fish 4 is close to the optimal frequency ($f_4 = 0.71$), the vortex wakes are stable and give rise to the reverse Benard-von Karman (rBvK) vortex street that characterizes the highly efficient fish swimming. Figure 5-13(b) displays an rBvK vortex wake behind fish 4, and at $f_4 = 0.71$, fish 4 has the optimal efficiency. Meanwhile, stable 2P wakes behind fish 2 and 3 are generated, as shown in Figs. 5-13(b) and 5-13(c).

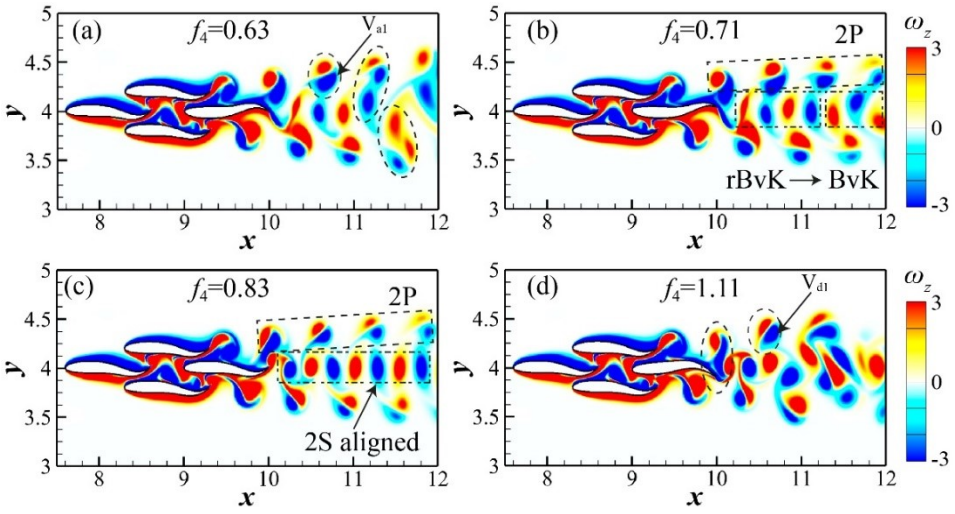

Figure 5-13. Vortex wakes at $t = 10T_0$ of schools at (a) $f_4 = 0.63$, (b) $f_4 = 0.71$, (c) $f_4 = 0.83$ and (d) $f_4 = 1.11$.

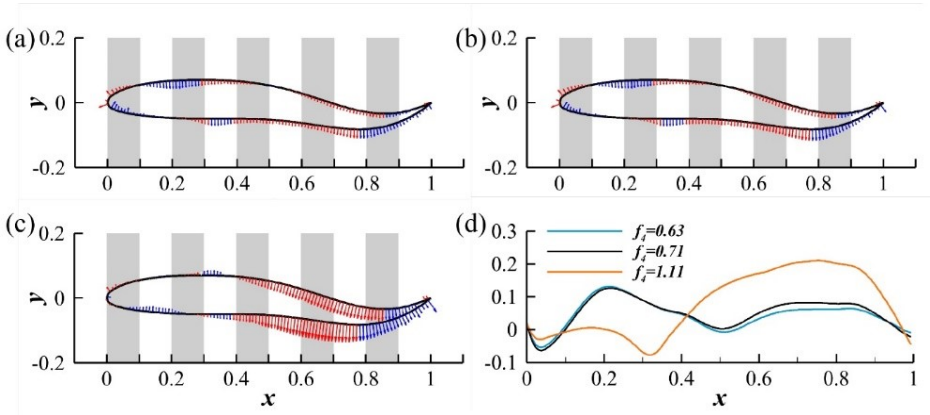

Figure 5-14. Snapshots of force vectors along the body of fish 4 undulating to the same position in the schools of (a) $f_4 = 0.63$, (b) $f_4 = 0.71$ and (c) $f_4 = 1.11$. (d) Pressure profiles on the upper surface of fish 4 in different schools.

Next, to further investigate the influence of the frequency on the wake, the vortex wake evolution of low frequency ($f_4 = 0.63$), optimal frequency ($f_4 = 0.71$) and high frequency ($f_4 = 1.11$) asynchronized schools is presented in Figs. 5-15, 5-16 and 5-17, respectively. Here, the period of each frequency is represented as T_l, T_m and T_h, respectively. In the low-frequency school,

the vortex pairs generated by fish 2 are stronger and move faster before being advected to far wake, compared to the vortices generated by fish 4. Due to the difference in transportation speed between the vortex pairs shed by fish 2 and the vortices shed by fish 4, the wake-wake interaction is influenced. In Fig. 5-15(a), the vortex V_2 interacts with the negative vortex of P_1 and its vorticity is enhanced. Then, when P_2 moves close to the vortex V_2, its negative vortex merges into V_2. The vorticity of V_2 is thus further enhanced. In the meantime, the vortex V_2 moves upwards due to the interactions. Hence, 2P wakes are broken, and a Bénard–von Kármán (BvK) vortex wake is formed behind fish 4.

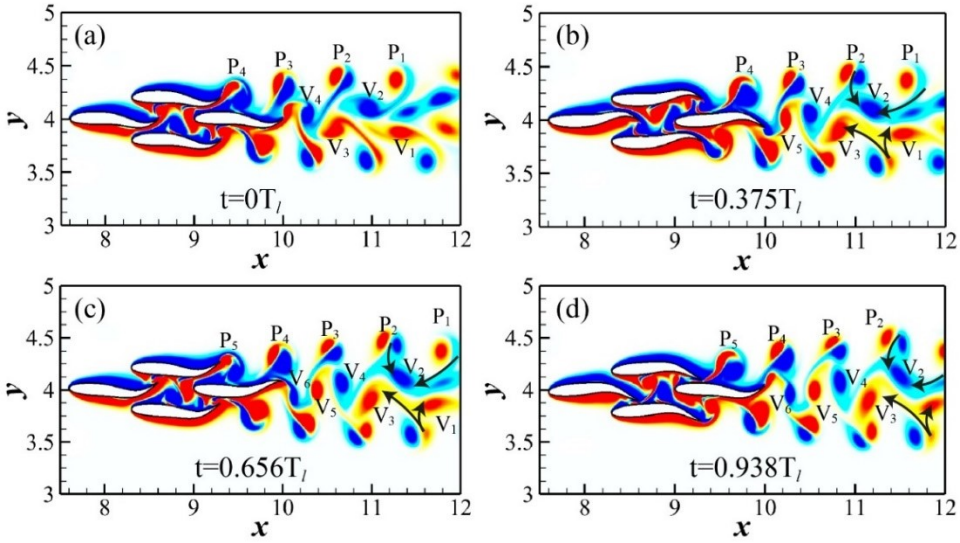

Figure 5-15. Vortex wakes of the school at $f_4 = 0.63$ at (a) $t = 0T_l$, (b) $t = 0.375T_l$, (c) $t = 0.656T_l$ and (d) $t = 0.938T_l$.

In Fig.5-16, the vortex V_3 first interacts with the pairs P_1 and P_2, and then after a certain time, the interaction between V_3 and P_1 is interrupted by a far distance. During the whole process of vortex advection in the optimal frequency school, one vortex generated by fish 4 only interacts with one vortex pair generated by fish 2 or fish 3 most time, which results in the vortices shed by

fish 4 coherent and the distance between the neighboring negative and positive vortices small in the far wake. This results in a higher swimming efficiency for fish 4 in the school at $f_4 = 0.71$.

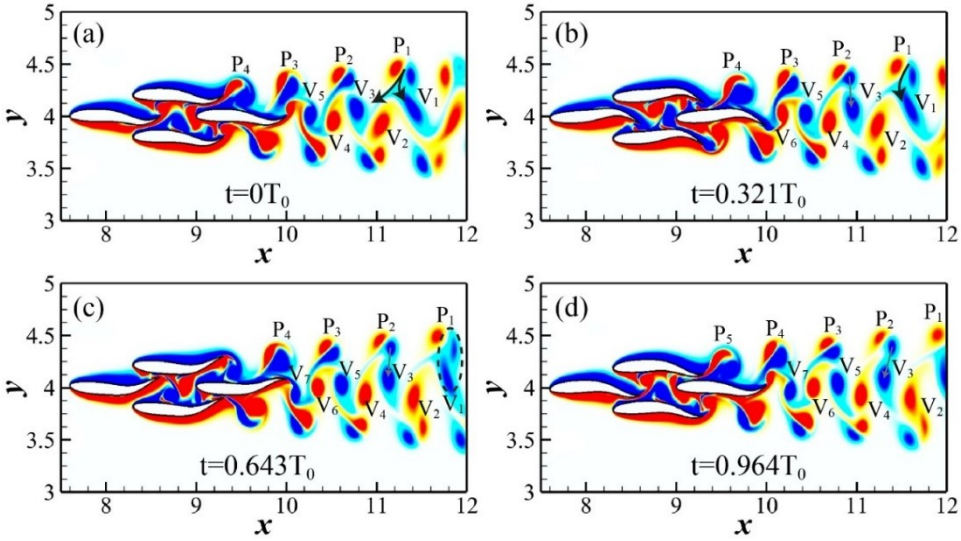

Figure 5-16. Vortex wakes of the school at $f_4 = 0.71$ at (a) $t = 0T_m$, (b) $t = 0.321T_m$, (c) $t = 0.643T_m$ and (d) $t = 0.964T_m$.

Finally, in the high-frequency school, the vortex pairs produced by fish 2 interact with the boundary layer vortex sheet of fish 4 and are weakened. For instance, the negative vortex in P_4 is very weak at $t = 0.667T_h$ due to the interaction with fish 4. On the contrary, the vortices shed by fish 4 are more coherent and stronger. The variation results in strong wake-wake interactions and the vortex wake at the center is unstable. Besides, 2P vortex wakes are not formed at the lateral sides of the wake. The unstable wake contributes to the reduction of the swimming efficiency of fish 4 in the high-frequency school.

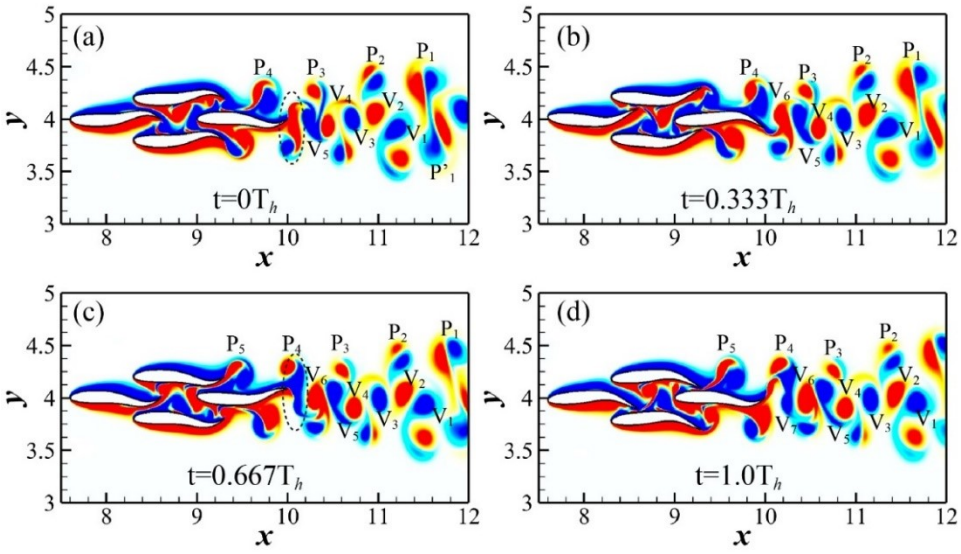

Figure 5-17. Vortex wakes of the school at $f_4 = 1.11$ at (a) $t = 0T_h$, (b) $t = 0.333T_h$, (c) $t = 0.667T_h$ and (d) $t = 1.0T_h$.

5.4 Chapter Summary

In this section, efficient swimming in high-density fish schools has been comprehensively investigated by changing the tail-beat frequency. First, the single fish achieves the optimal swimming efficiency around $f = 1.0$ at which the corresponding Strouhal number is 0.43. As the tail-beat frequency increases, the vortex wake of the single fish changes from the BvK wake to the rBvK wake. Then, two kinds of high-density schools are studied: the synchronized schools, where the frequencies of all individuals vary simultaneously, and the asynchronized schools, where the frequency of three front fish maintains while that of the trailing fish changes.

In synchronized schools, the tail-beat frequency varies from 0.46 to 1.20. It is found that when $f = 0.77$, the school achieves a steady swimming state and the efficiency of the school is 0.55, improved by 37.5% over a single fish at the same frequency. Around $f = 0.83$, fish 4 and the school both obtain the optimal swimming efficiency, $\eta_4 = 0.64$ and $\eta_{ave.} = 0.55$. In the meantime, stable 2P wakes are generated behind fish 2 and fish 3 and stable 2S wake is formed

behind fish 4. We also present the variation of the relative streamwise momentum Δp_x with respect to the incoming flow as a function of the tail-beat frequency and according to the value of Δp_x, the wakes of the fish schools are categorized as the drag wake ($\Delta p_x < 0$), the momentumless wake ($\Delta p_x = 0$), and the jet wake ($\Delta p_x > 0$). Besides, the momentum entrainment ratio γ of each school has been calculated. Even though the peak of γ and the peak of swimming efficiency are not perfectly matched, the variation of γ suggests that the efficient swimming of dense schools is related to the stability of the momentum wake.

In the asynchronized schools, the tail-beat frequency of the three front fish is 0.83, while the frequency of the trailing fish changes from 0.46 to 1.25. The hydrodynamic performance of fish 4 in the asynchronized schools is compared with that of a single fish. The results show that the trailing fish can consume less power and generate higher thrust than a single fish. Also, the trailing fish can save energy in the school by swimming at a lower frequency without losing thrust production. When $f_4 = 0.71$, fish 4 reaches the steady swimming state and achieves the highest swimming efficiency. Correspondingly, stable 2P wakes are generated behind fish 2 and 3 and stable 2S wake is produced behind fish 4.

6 Hydrodynamic Interactions in Planar Fish Schools

A key objective of this section is to investigate the hydrodynamic interactions between two three-dimensional fish bodies arranged in the horizontal plane. As a simplification of complex schooling behavior, the independently controlled three-dimensional fish-like bodies modeled on a juvenile rainbow trout (*Oncorhynchus mykiss*) are placed in in-line, side-by-side and staggered configurations, respectively. The schools in this section thus can also be called planar schools. Hydrodynamic performance and flow information of the schools are obtained through high-fidelity flow simulations. The spatial and phase difference effects on the hydrodynamic interactions in the planar fish schools are comprehensively and systematically examined by comparing the hydrodynamic performance of individuals with that of a single fish and analyzing the wake structures.

6.1 Fish Model, Undulating Motion Kinematics and School Arrangements

As a typical schooling fish, the rainbow trout (*Oncorhynchus mykiss*), which performs a carangiform locomotion mode during steady swimming [27], was chosen to study the hydrodynamic interactions in planar fish schools. Live juvenile trout experiments were conducted in a laboratory water tunnel. The swimming kinematics was recorded with an orthogonally arranged high-speed photogrammetry system from three views, including ventral, lateral and posterior views [121, 122]. The 3D trout-like fish model is reconstructed based on the video sequences in Autodesk Maya (Autodesk Inc.) [122]. More details about the image-guided 3D reconstruction method are presented in Ref. [123]. To keep the problem complexity manageable, we maintain the trunk (TK) and the caudal fin (CF) of the fish but remove other fins on the body, such as the pelvic, dorsal, and pectoral fins, as shown in Fig. 6-1(a). The red dashed line on the

body represents the fish's spine and is straight at rest. In the experiments, the body length of the trout is around 7cm and is normalized as $L = 1.0$.

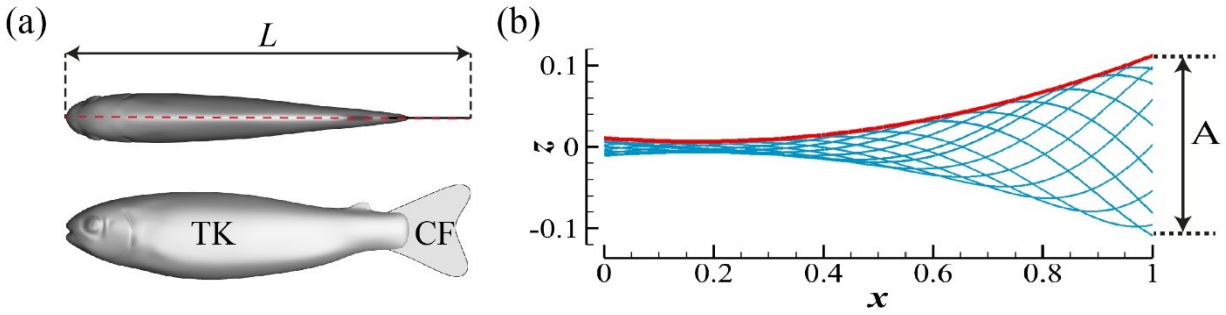

Figure 6-1. (a) Top and side views of the trout-like fish model, (b) traveling wave amplitude (red line) and midlines of the trout-like model during one tail-beat cycle (blue lines). A indicates the tip-to-tip amplitude of the undulating motion.

Instead of directly employing the kinematics recorded with the high-speed videos during the experiments, a traveling wave motion [96] is imposed on the body to capture the fundamental physics of hydrodynamic interactions, and some parameters are controlled to mimic the undulating motion of the live trout. The traveling equations are as follows

$$z(x,t) = A(x) \cdot sin\left(\frac{2\pi}{\lambda}x - \frac{2\pi}{T}t + \varphi\right), \tag{6-1}$$

$$A(x) = a_2x^2 + a_1x + a_0, \tag{6-2}$$

where x and z are the variables to denote the position of points on the trout body during the undulating motion and normalized by the body length L, λ and T indicate the wavelength and the period of the traveling wave, respectively, t is the time, and φ is the phase of the undulatory motion. The quadratic polynomial function $A(x)$ represents the amplitude of the lateral motion of the points. The coefficients of the quadratic polynomial function a_is are calculated based on the experimental data of a live trout [122], which is at steady swimming with local amplitudes of

$A(0) = 0.0097$, $A(0.4) = 0.0097$ and $A(1.0) = 0.1058$. Thus, by solving the quadratic polynomial functions, we can obtain $a_0 = 0.010$, $a_1 = -0.065$ and $a_2 = 0.161$. According to the relation between the wavelength and the total length measured for the rainbow trout [124], the wavelength is thus obtained $\lambda = 1.03$. In the experiments, the tail-beat frequency varies from 2.8 to 3.6 Hz [122]. In this work, the period of the traveling wave is normalized as $T = 1.0$. Several points on the body have been chosen to determine the phase to ensure that the prescribed kinematics match entirely with the experimental kinematics. After trial and error, the phase $\varphi = 131.8°$ is obtained. Figure 6-1(b) presents a sequence of midlines during one tail-beat cycle and the amplitude envelope of the traveling wave. Figure 6-2 compares the real kinematics for the experiments and prescribed kinematics with $\varphi = 131.8°$ through the motion of four points on the trunk and caudal fin over one tail-beat cycle. The points are chosen on the typical regions of the body, such as trunk point 1 with the smallest lateral displacement on the body, and caudal point 2 with the most flexible point on the body. Figure 6-2 demonstrates that the prescribed kinematics mimics the real kinematics very well.

Figure 6-3 shows the arrangements of the in-line, side-by-side and staggered schools from different views. The distance between the snouts of individual fish defines the arrangement. For instance, in Fig. 6-3(a), *S* is the distance between the snouts of the leading fish and the following fish and represents the streamwise distance of an in-line school. In this work, the streamwise distance *S* varies from 1.2*L* to 2.2*L*. *D* represents the lateral distance and is the distance between the fish snouts in a side-by-side fish school, as shown in Fig. 6-3(c). The lateral distance *D* of the side-by-side school changes from 0.25*L* to 0.85*L*. The streamwise and lateral distance of a staggered school have the same definitions as the in-line and side-by-side schools.

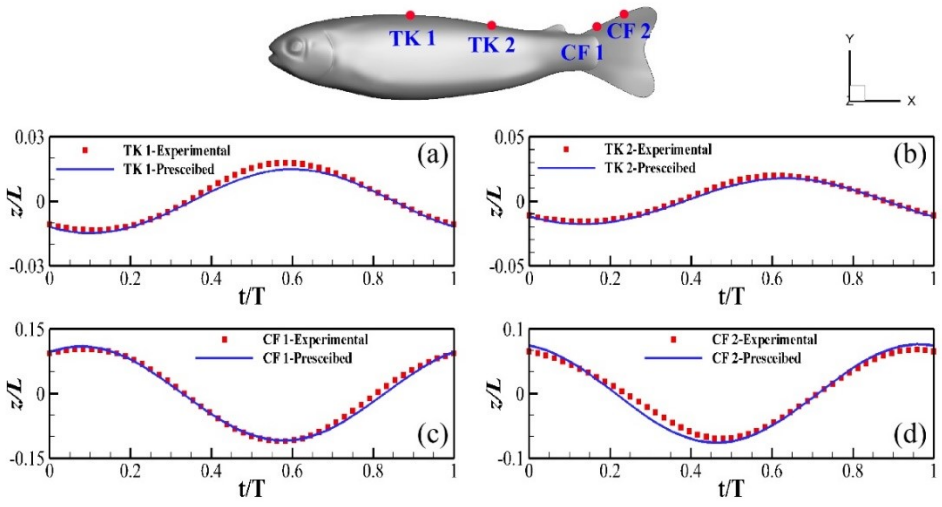

Figure 6-2. Comparison of the real kinematics from experiments and prescribed kinematics with $\lambda = 1.03$ and $\varphi = 131.8°$ through the motion of four points on the trunk and caudal fin over one period.

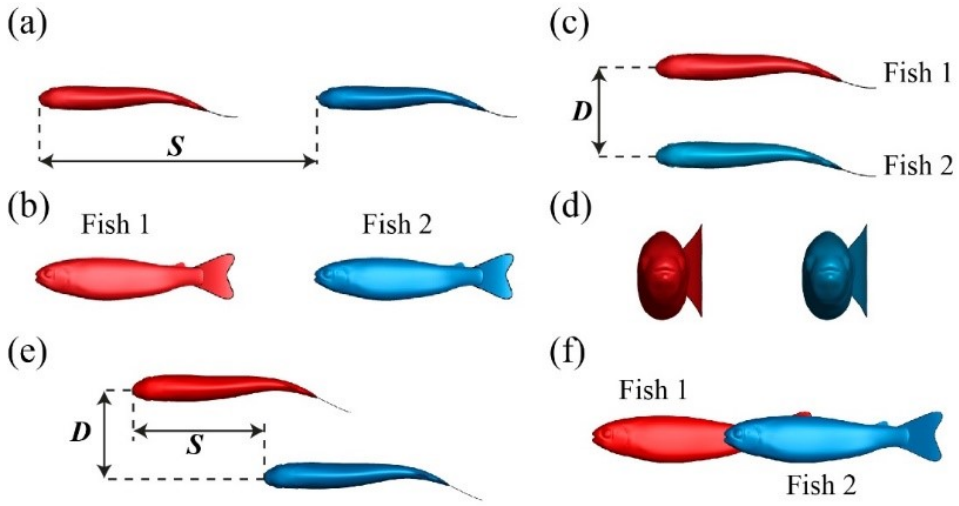

Figure 6-3. (a) Top view and (b) side view of an in-line school. (c) Top view and (d) front view of a side-by-side school. (e) Top view and (f) side view of a staggered school.

6.2 Computational Setup and Validation Study

Figure 6-4(a) shows a Cartesian computational grid and boundary conditions for the simulations, and Fig. 6-4(b) presents the local refinement meshes. The computational domain size of the base

layer of the mesh is $15L \times 6L \times 10L$ with grid points of $385 \times 113 \times 177$ (approximately 7.7 million). In this work, two levels of refinement mesh have been used, with three refined mesh blocks in total. With two-layer mesh refinement, the finest resolution is $\Delta_{min} = 3.13 \times 10^{-3}L$, which has been proven fine enough to obtain grid-independent results and resolve the fluid field [33]. The upstream boundary (left-hand) is set as the inflow boundary condition with a constant incoming flow velocity U_∞. At all the lateral boundaries, the zero-gradient boundary condition is applied. The right-hand boundary is the outflow boundary condition. A homogeneous Neumann boundary condition is used for the pressure at all boundaries.

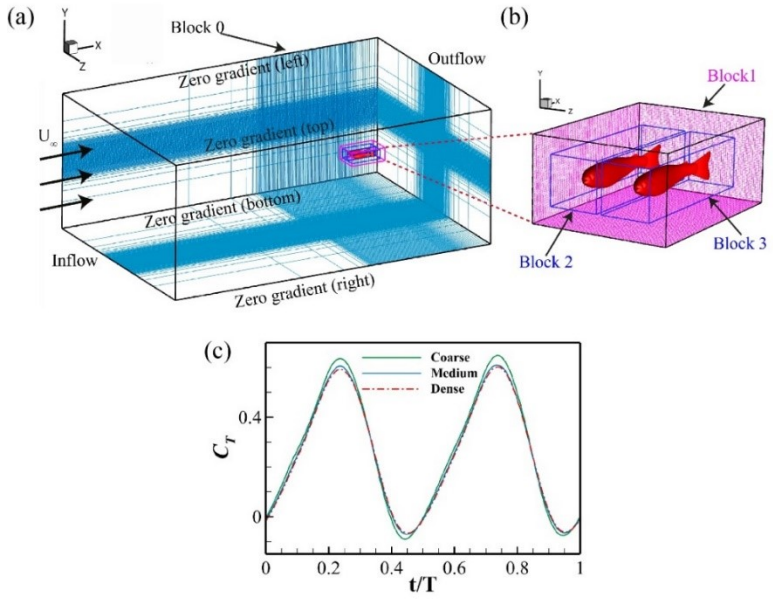

Figure 6-4. (a) Schematic of the computational mesh and boundary conditions, (b) local refinement blocks, and (c) comparison of the instantaneous thrust C_T on the caudal fin of a single fish between the coarse, medium and fine meshes.

A convergence study has been performed to demonstrate the grid independence of the simulations. Figure 6-4(c) compares the instantaneous caudal-fin thrust coefficients in three computational grids, i.e., coarse, medium and dense meshes. The finest resolutions of the three

meshes are $6.25 \times 10^{-3}L$, $3.13 \times 10^{-3}L$ and $2.23 \times 10^{-3}L$, respectively. The mean thrust difference between the medium and the dense mesh is around 1.8%, less than 2%. It demonstrates that the flow simulations performed on the medium mesh are grid-independent.

Two key non-dimensional parameters, the Reynolds number (Re) and the Strouhal number (St), are employed to describe the hydrodynamics and flow characteristics of fish-like swimming. The Re is defined as $Re = U_\infty L/\nu$, and the St is defined as $St = fA/U_\infty$, where f is the tail-beat frequency; A is the peak-to-peak amplitude of the tail-tip on the caudal fin. In the experiments, the Reynolds number for juvenile trout steady swimming ranges from 3000 to 7800, and the Strouhal number is from 0.46 to 0.73 [121, 122]. In this study, we perform the simulations at the *Re* and *St* of the same magnitude as the experiments. The forces acting on the fish model's trunk and caudal fin are computed by directly integrating the surface pressure and shear [33, 69]. The instantaneous thrust (F_T) and drag (F_D) are presented as non-dimensional coefficients, C_T and C_D, defined as $C_T = F_T/0.5\rho U_\infty^2 A_{CF}$ and $C_D = -F_D/0.5\rho U_\infty^2 A_{CF}$, where A_{CF} is the area of the caudal fin. The hydrodynamic power on the trunk and caudal is computed as $P = \oint -(\overline{\overline{\boldsymbol{\sigma}}} \cdot \boldsymbol{n}) \cdot \boldsymbol{V} dS$, where $\overline{\overline{\boldsymbol{\sigma}}}$ and $\boldsymbol{V}$ represent the stress tensor and the velocity tensor of the fluid, respectively, and *dS* denotes the surface area element on the trunk or the caudal fin. Hence, the hydrodynamic power on the trunk and caudal fin can be normalized as $C_{PW\_TK} = P_{TK}/0.5\rho U_\infty^3 A_{CF}$ and $C_{PW\_CF} = P_{CF}/0.5\rho U_\infty^3 A_{CF}$. The cycle-averaged force coefficients and power coefficients are represented by $\overline{C_T}$, $\overline{C_D}$, $\overline{C_{PW\_CF}}$ and $\overline{C_{PW\_TK}}$, respectively. Based on previous studies and the objective of the current study, two kinds of swimming efficiencies are defined. First, the modified Froude hydrodynamic efficiency η [35, 100], which measure the ratio of the useful power to the total power, is defined as the thrust-to-total power ratio, $\eta = \overline{C_T}/\overline{C_{PW\_Out}}$, where the total power $\overline{C_{PW\_Out}}$ is the summation of the power of the trunk and caudal fin, $\overline{C_{PW\_Out}} = \overline{C_{PW\_TK}} + \overline{C_{PW\_CF}}$. Second, the caudal fin propulsive

η_{CF} is utilized to examined the hydrodynamic interactions between caudal fins and is defined as $\eta_{CF} = \overline{C_T}/\overline{C_{PW\_CF}}$.

6.3 Results and Discussions

6.3.1 Performance and Wake Pattern of a Single Fish

The hydrodynamics of a single trout is simulated in this section as a reference for the following sections. To conveniently measure the variation of hydrodynamic performance in fish schools, the steady swimming condition at which the drag and thrust are balanced, i.e. $\overline{C_X} = \overline{C_T} - \overline{C_D} = 0$, is set as the initial condition for the schools. We keep the undulating kinematics of the fish and vary the incoming flow velocity from 0.46 to 0.6 to determine the steady swimming condition. Correspondingly, *St* is from 0.353 to 0.461. Figure 6-5(a) shows that the cycle-averaged net force in the swimming direction $\overline{C_X}$ monotonically increases with *St* and is zero when $St = 0.39$ at which the steady swimming condition has been reached [64] for a single trout.

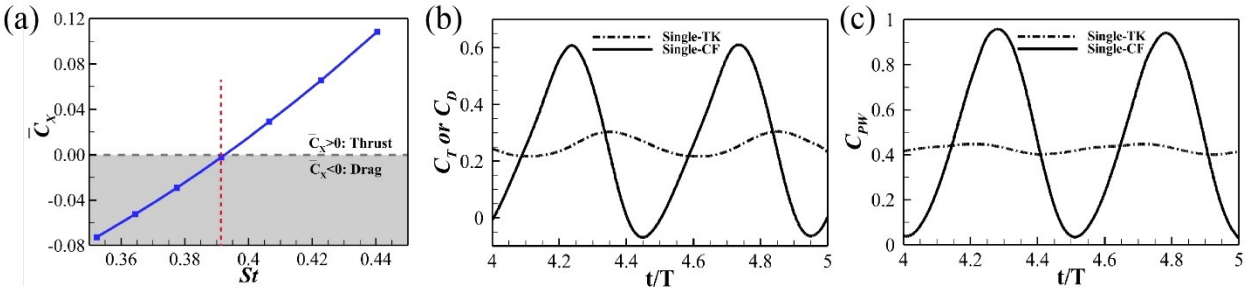

Figure 6-5. (a) Time-averaged net force coefficient $\overline{C_X}$ in the *x*-direction of an isolated fish at different St. The gray region indicates net drag. Time histories of (b) the thrust coefficient C_T of the caudal fin, the drag coefficient C_D of the trunk and (c) the associated power coefficients at $St = 0.393$.

Figures 6-5(b) and 6-5(c) show the time history of the hydrodynamic performance of a single trout at steady swimming, including the thrust coefficient C_T, drag coefficient C_D and the

associated power coefficients. The cycle-averaged hydrodynamic forces and swimming efficiency for the single trout are calculated and summarized in Table 6-1. From the results, the net force of the single fish in the swimming direction is close to zero, $\overline{C_X} = \overline{C_T} - \overline{C_D} = 0.0001$, verifying that the steady swimming condition has been achieved. The three-dimensional vortex structures of the single trout at $t = 5.0T$ are shown in Fig. 6-6 from a perspective and the top views. The wake structures are visualized by the Q-criterion [125] with an iso-surface of $Q = 5$. At steady swimming, a trout sheds two lines of linked vortex rings to the downstream, and the vortex rings are expanded laterally in the horizontal plane, as shown in Fig. 6-6(b). The vortex pattern is consistent with the wake structures reported in the experiments of carangiform fishes, such as trout [126], mullet [23] and mackerel [127].

TABLE 6-1. Summary of hydrodynamic performance of a single fish.

TK		CF		η	η_{CF}
$\overline{C_D}$	$\overline{C_{PW}}$	$\overline{C_T}$	$\overline{C_{PW}}$		
0.2441	0.4320	0.2442	0.4349	28.2%	56.2%

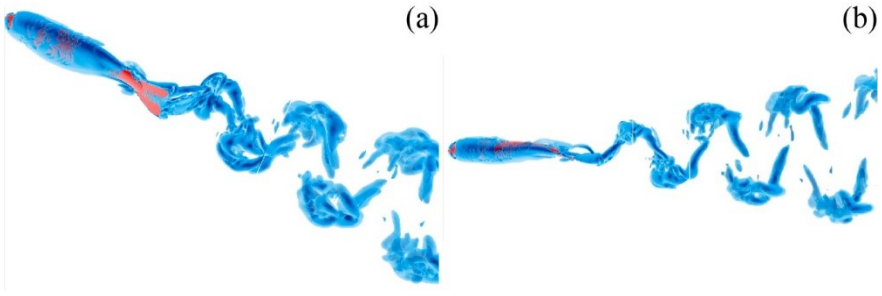

Figure 6-6. Three-dimensional wake structures of a single trout at steady swimming at $t = 5.0T$ from (a) a perspective view and (b) the top view.

6.3.2 Effect of Streamwise Distance in an In-Line Fish School

In the following sections, the performance of fish in a school is normalized by the corresponding values of the single steady-swimming trout to measure the effects of hydrodynamic interactions. For instance, $\Delta C_T = \left(C_T - C_{T,S}\right)/C_{T,S}$ represents the variation of the thrust coefficient for individuals in a fish school, where $C_{T,S}$ is the thrust of the single fish.

In this section, the streamwise spacing S varies from 1.2BL to 2.2BL. Figure 6-7 displays the variation of cycle-averaged performance of individuals in the in-line schools, including the normalized thrust coefficient ($\Delta\overline{C_T}$), drag coefficient ($\Delta\overline{C_D}$), power coefficient ($\Delta\overline{C_{PW}}$) and the efficiencies ($\Delta\eta$ and $\Delta\eta_{CF}$). Here, the gray shaded areas in Fig. 6-7, from -1% to 1%, are set based on the uncertainty of the numerical simulations, and the performance variation located in this range can be negligible.

Figure 6-7(a) shows that, for the leading fish (fish 1), the drag on the TK decreases and the thrust on the CF increases, compared to the single trout. The associated power coefficients of fish 1 are reduced. Hence, the leading fish benefits from the hydrodynamic interactions. For fish 1, When $S = 1.2L$, the thrust increases by 3.8%, the drag reduces by 2.8% and the power of the CF decreases by about 1.5%. And fish 1 achieves the maximum Froude efficiency, with an improvement of 5.3%. Besides, with the increasing *S*, the performance enhancements are monotonically reduced; when $S > 1.5L$, they are less than 1%, within the numerical uncertainty, and become independent of the streamwise distance. For fish 2, the hydrodynamic interactions are detrimental to the performance of the trunk, while the caudal fin is subject to limited influence from the interactions. At $S = 1.2L$, although the thrust on the CF is slightly improved, the drag on the TK increases by 9.1%, and it consumes 9.5% more power for undulating motion. Correspondingly, the Froude efficiency of fish 2 drops by 3.2%. This counterintuitive observation

agrees well with the in-line flapping flag experiments conducted by Ristroph and Zhang [128]. They found that the leader enjoys a significant drag reduction when the $S < 1.5L$, whereas the drag on the follower rises.

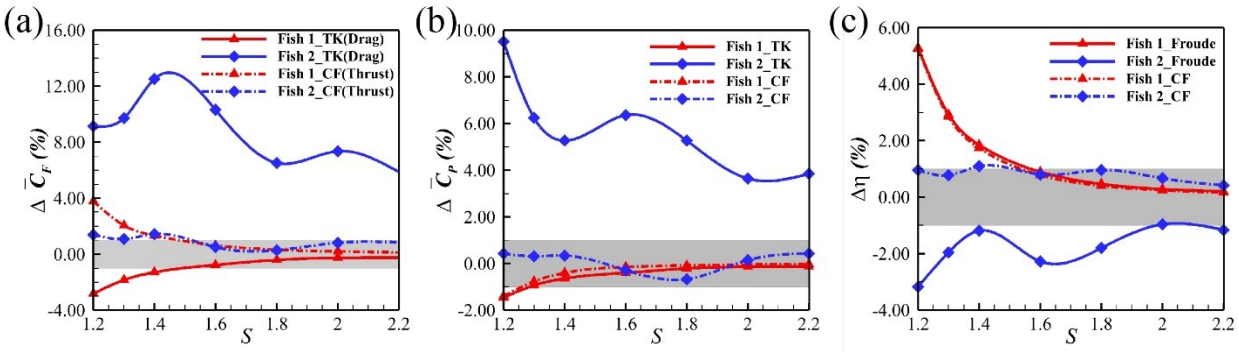

Figure 6-7. Hydrodynamic performance of individuals varying with the streamwise distance in the in-line schools: (a) normalized cycle-averaged thrust and drag coefficients, (b) normalized cycle-averaged power coefficients and (c) normalized Froude efficiency and caudal fin propulsive efficiency.

To understand the mechanisms behind the above performance variations, we present the instantaneous three-dimensional wake structures of the $S = 1.2L$ in-line school at $t = 0.08T$ [Figs. 6-8(a1-a2)], $t = 0.42T$ [Figs. 6-8(b1- (b2)], and $t = 0.75T$ [Figs. 6-8(c1-c2)], from a perspective view and the top view. The vortex structures in Fig. 6-8 are identified by the iso-surface of $Q = 5$. The corresponding horizontal flow field slices cutting through the frontal plane of the fish bodies are shown in Fig. 6-9 to assist the analysis. Figures 6-9(a1-c1) show the vorticity contours ω_y, and Figs. 6-9(a2-c2) present the contours of the normalized streamwise velocity u^*, where u^* is calculated by $u^* = (u - U_\infty)/U_\infty$. The pressure is normalized by $p^* = (p - p_\infty)/0.5\rho U^2$, where p_∞ is the pressure in the free stream, and displayed in Figs. 6-9(a3-c3). The red and blue arrows

indicate the moving direction of the tail tip at different times: red denotes moving upward and blue represents moving downward.

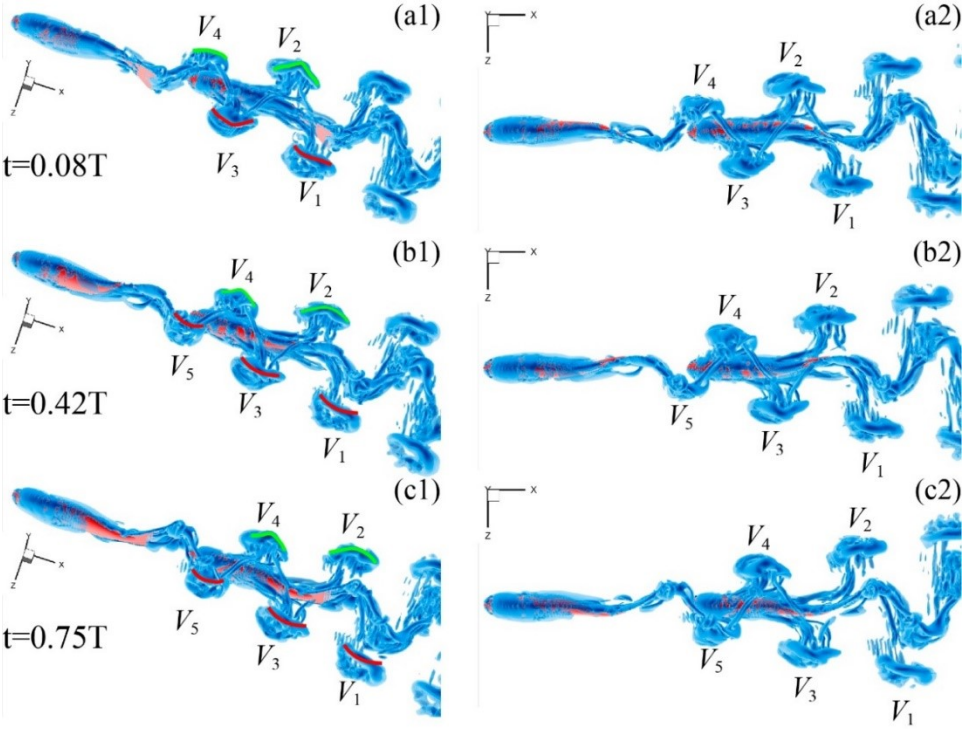

Figure 6-8. Three-dimensional wake structures from a perspective view (a1-c1) and the top view (a2-c2) at (a) $t = 0.08T$, (b) $t = 0.42T$ and (c) $t = 0.75T$. The wake structures are visualized by the iso-surface of $Q = 5$. The red and green solid lines denote the shapes of the vortex rings.

In Fig. 6-8, the linked vortex rings shed by fish 1 are interrupted by the trunk of fish 2, and double rows of discrete vortex rings are formed and transported downstream. In particular, when a vortex ring is shedding from the caudal fin of fish 1, the connection between this vortex ring and the next vortex ring will be interrupted by the snout of fish 2. For instance, the link between V_4 and V_5 is interrupted by fish 2, as shown in Figs. 6-8(b2) and 6-9(b1). Then, when the shedding vortex rings pass by the body of fish 2, they are also influenced. The shape of these vortex rings is thus changed. In Figs. 6-8(a1-c1), it can be found that the vortex ring V_2 become curved when it

passes by fish 2. In the meantime, the velocity field around fish 2 is also affected. In Figs. 6-8(a2) and 6-9(a1), the vortex ring V_2 contacts and merges with the boundary layer vortex sheet on the trunk of fish 2, decreasing the velocity around the corresponding position [see Fig. 6-9(a2)]. Also, the vortex ring V_4 is attached to the trunk of fish 2 and increases the velocity at the corresponding position. Consequently, the interactions finally increase the magnitude and area of the negative pressure zone on the upper surface of the trunk of fish 2, as shown in Fig. 6-9(a3). Similar phenomena can be observed at $t = 0.42T$ and $t = 0.75T$, which results in the increase of the drag and power on the TK of fish 2. To further validate the analysis, we present the difference in surface pressure between the individuals and the steady-swimming single fish in Fig. 6-10 at $t = 0.08T$, $t = 0.42T$, and $t = 0.75T$. The pressure difference is defined as $\Delta p = \left(p_{iFish} - p_{single}\right)/0.5\rho U_\infty^2$, where p_{iFish} indicates the surface pressure on the ith fish in the school and p_{single} denotes the pressure of the single fish. In comparison, the head of fish 2 experiences a much higher pressure difference than that of fish 1, which may explain the higher drag and power on the trunk of fish 2.

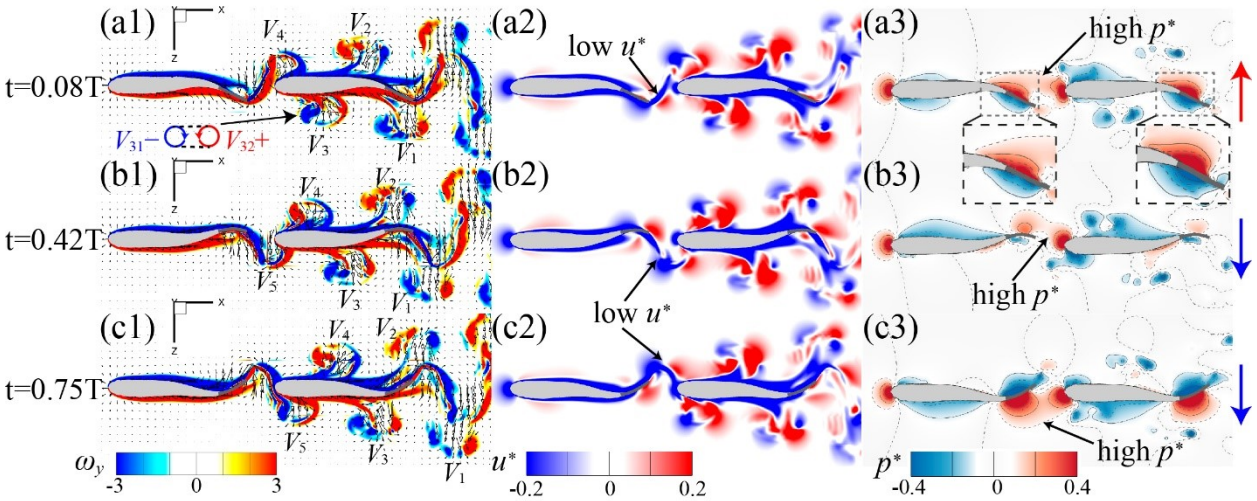

Figure 6-9. Contours of vorticity ω_y (a1-c1), normalized streamwise velocity u^* (a2-c2) and normalized pressure p^* (a3-c3) on a horizontal slice cutting through the frontal plane of the fish

body at (a) $t = 0.08T$, (b) $t = 0.42T$ and (c) $t = 0.75T$. The red arrow denotes the tail tip of the fish moving upward, and the blue arrows indicate moving downward.

In Figs. 6-9(a2-c2), low-velocity zones are observed in front of fish 2 at different times. It implies the flow drained by fish 1 is blocked by fish 2. Thus, high-pressure zones are generated behind fish 1 and connect the high-pressure zones on the caudal fin of fish 1 and the head of fish 2 [Figs. 6-9(a3-c3)]. At $t = 0.08T$, due to the variation of the flow fields, the area of the high positive pressure zone on the caudal fin of fish 1 is larger than that of fish 2, as shown in Fig. 6-9(a3). It finally results in a higher thrust produced by fish 1. Therefore, within a short streamwise distance, the blocked water with high pressure in front of trailing fish pushes the leading fish swimming forward and enhances the thrust production of the leading fish [129].

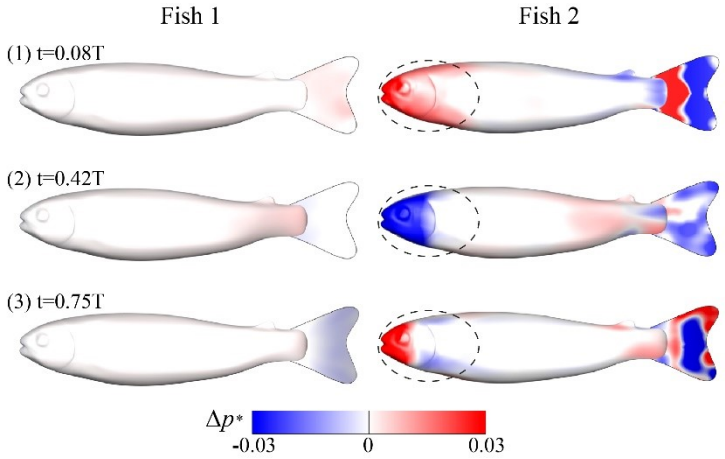

Figure 6-10. Surface pressure difference between the individuals in the in-line school and the single fish at (a) $t = 0.08T$, (b) $t = 0.42T$ and (c) $t = 0.75T$.

6.3.3 Effect of Phase Difference in an In-Line Fish School

In this section, the phase difference effects on the hydrodynamic interactions are explored in the in-line schools with a fixed streamwise distance S of 1.4BL. In these schools, the tail-beat phase of the leading fish is fixed at 0°, and the phase of the following fish changes from 0° to 360°. The

phase difference is thus defined as $\varphi = \varphi_2 - \varphi_1$. The normalized thrust, drag, powers and swimming efficiencies are shown in Fig. 6-11, varying with the phase difference. The performance of the leading fish, including the trunk and caudal fin, and the caudal fin of fish 2 is independent of the phase difference, whereas the performance of the trunk of fish 2 strongly depends on the phase. The drag of fish 2 first reduces when $\varphi \leq 120°$, then increases when $\varphi > 120°$. Compared with the in-phase school ($\varphi = 0°$), the drag of fish 2 in the school at $\varphi = 120°$ decreases by 4.4%. The curve of $\overline{C_{PW\_TK}}$ of fish 2 presents an opposite trend as the drag. It increases when $\varphi > 0°$ and then decreases when $\varphi > 180°$. The curve of Froude efficiency of fish 2 shows a similar trend as the drag.

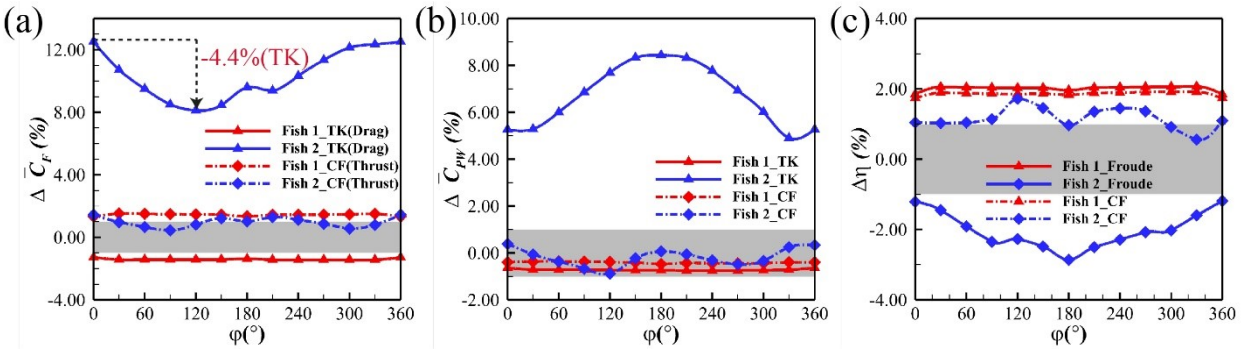

Figure 6-11. Hydrodynamic performance of individuals varying with the phase difference in the in-line schools: (a) normalized cycle-averaged thrust and drag coefficients, (b) normalized cycle-averaged power coefficients and (c) Froude and caudal fin propulsive efficiencies.

Because fish 2 suffers the lowest drag when $\varphi = 120°$, the wake of this school is presented and compared with that of the in-phase school to explore the potential drag reduction mechanisms. The performance difference for fish 2 in different schools is due to the flow environment variation caused by the phase difference. Thus, to measure the effects of varied flow environment on the performance of fish 2, the timeline of the out-of-phase school ($\varphi = 120°$) is shaft right by $1/3$.

Thus, fish 2 has the same undulating motion in these two schools. Figure 6-12 compares the three-dimensional vortex structures, the contour plots of the vorticity ω_y and normalized pressure p^* on a horizontal slice cutting through the frontal plane of the fish in the in-phase and out-of-phase schools at $t = 0.08T$. In Fig. 6-12(a1), the vortex ring V_5 is reaching the upper side of the head of fish 2 and the vortex ring V_4 is interacting with the lower side of fish 2. The velocity near V_4 and the fish body directs downwards, and a low-pressure zone is formed around the same position as V_4 [see Fig. 6-12(c1)]. Nevertheless, in the out-ot-phase school, the vortex ring V'_5 is passing by the upper surface of fish 2 at the anterior part. Meanwhile, the vortex ring V'_4 interacts with the lower surface of fish 2. Thus, low-pressure regions are formed both around the upper and lower surfaces of fish 2, as shown in Fig. 6-12(c2). Thus, the pressure difference between the lower and upper sides of fish 2 in the out-of-phase school is lower than that in the in-phase school, implying a smaller drag generated by fish 2 in the out-of-phase school.

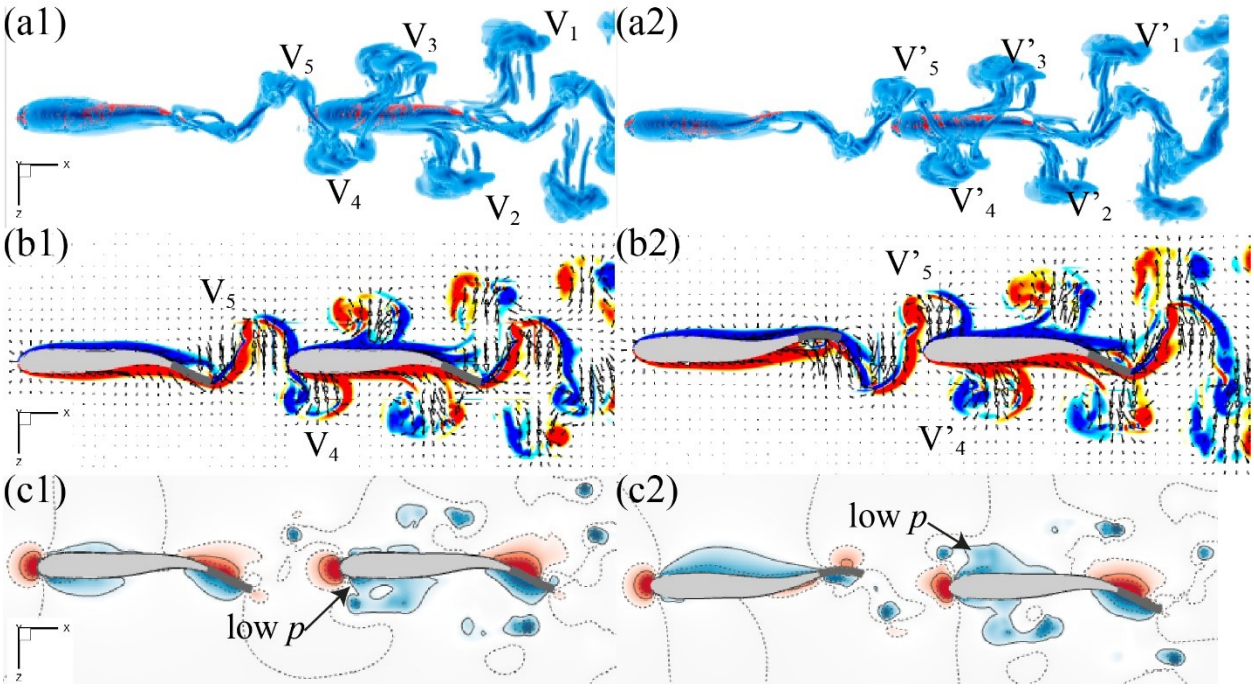

Figure 6-12. (a) Three-dimensional vortex structures, and (b) contours of vorticity ω_y and (c) normalized pressure p^* (a3-c3) on a horizontal slice cutting through the frontal plane of the fish bodies in the in-phase (a1-c1) and out-of-phase (a2-c2) schools at $t = 0.08T$.

Figure 6-13 shows the three-dimensional vortex structures, the contour plots of the vorticity ω_y and normalized pressure p^* of the two schools at $t = 0.33T$. In the in-phase school, the vortex ring V_5 is passing by the head of fish 2 at the upper side, and a low-pressure zone is formed at the same position [see Fig. 6-13(c1)]. In the out-of-phase school, the vortex ring V'_6 is arriving at the lower side of fish 2 and V'_5 is interacting with the upper side. Hence, the low-pressure zones are generated on both sides of fish 2. Similarly, the pressure difference between the upper and lower sides of fish 2 in the out-of-phase school is smaller, producing a lower drag.

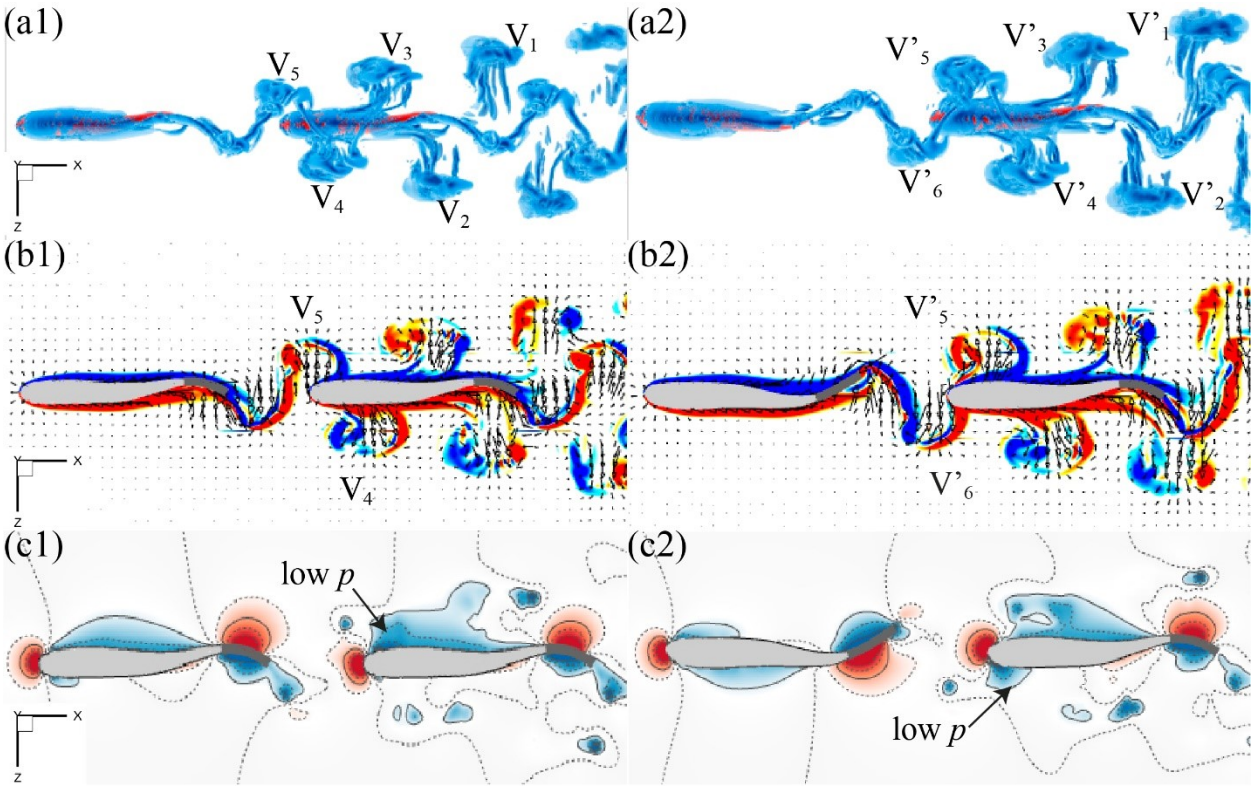

Figure 6-13. (a) Three-dimensional vortex structures, and (b) contours of vorticity ω_y and (c) normalized pressure p^* (a3-c3) on a horizontal slice cutting through the frontal plane of the fish bodies in the in-phase (a1-c1) and out-of-phase (a2-c2) schools at $t = 0.33T$.

6.3.4 Effect of Lateral Distance in a Side-by-Side Fish School

In this section, the lateral distance D has been changed to investigate its effects on the hydrodynamic interactions in a side-by-side school. By using the same definitions as the previous section, Fig. 6-14 presents the normalized performance of individual fish to measure the effects of hydrodynamic interactions in side-by-side fish schools. Within the numerical uncertainty, fish 2 has the same performance as fish 1 because of the symmetry of the side-by-side arrangement, as shown in Fig. 6-14. Thus, only the performance of one fish is discussed below unless otherwise specified.

The force and power coefficients are presented in Figs. 6-14(a) and 6-14(b), respectively, as a function of lateral spacing. As seen in Fig. 6-14, the general trends of the performance for both fish imply that the hydrodynamic interactions in the side-by-side schools weaken as the lateral spacing increases. Specifically, the hydrodynamic interactions in the side-by-side schools are detrimental to the performance of the trunk for both fish by increasing drag and power. In Fig. 6-14(a), the drag on the trunk of both fish in the schools increases with the decrease of D. When $D = 0.25L$, the drag on the trunk increases by 8.3%, and 3% more power is consumed at the same time. In comparison, the performance of the caudal fin is greatly enhanced when the lateral spacing is small. At $D = 0.25L$, the power consumed by the caudal fins is saved by 6.8% at the cost of a slight reduction in thrust production (reduced by 1.6%). Correspondingly, the caudal fin efficiency increases by 6%. When $D > 0.55L$, the variations of the power consumed by the trunk and caudal fin are less than 1%, implying the influence of the interactions is insignificant. Besides, the Froude efficiency of both fish is enhanced by more than 1% when $D < 0.45L$, as seen in Fig. 6-15(c), although the performance of the trunk is greatly diminished.

Figure 6-15 shows the three-dimensional vortex structures of the side-by-side school with $D = 0.25L$ at $t = 0.25T$[Figs. 6-15(a1- a2)], $t = 0.58T$ [Figs. 6-15(b1-b2)], and $t = 0.92T$ [Figs. 6-15(c1-c2)] from the top and lateral views to help examine the variation of hydrodynamic performance. As seen in Fig. 6-10, vortex rings are generated on the caudal fin, link with the neighboring vortex rings and move laterally in the horizontal plane when being advected downstream. However, with a small lateral distance, the shape of vortex rings shed by one fish changes due to the influence of the vortex wake of the other fish. Also, the vortex rings may collide and merge with vortex rings shed by the other fish and decay quickly. In Fig. 6-15(c2), the vortex rings V_3 and V_4 interact with vortex rings shed by fish 1 and break into smaller vortices.

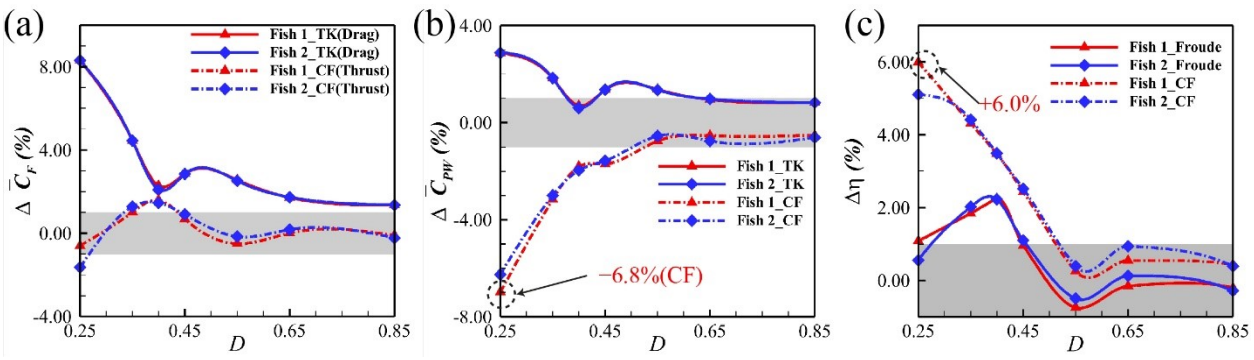

Figure 6-14. Hydrodynamic performance of individuals varying with the lateral distance in the side-by-side schools: (a) normalized cycle-averaged thrust and drag coefficients, (b) normalized cycle-averaged power coefficients and (c) normalized Froude efficiency and caudal fin propulsive efficiency.

To better illustrate the hydrodynamic interactions, Fig. 6-16 provides three snapshots of the contours of normalized streamwise velocity u^* (a1-c1), vorticity ω_y (a2-c2) and normalized p^* (a3-c3) on a horizontal slice cutting through the frontal plane of the fish body at the same times as in Fig. 6-15. The fish bodies form a channel in a side-by-side school, and the streamwise velocity between the trunks is high during the whole tail-beat cycle. It enhances and expands the negative pressure region in the channel. As a result, the surface of a fish body towards the channel maintains a larger area of negative pressure with a larger magnitude than the same side of the other fish, as indicated in Fig. 6-16(a3). It finally increases the drag and power of the trunk.

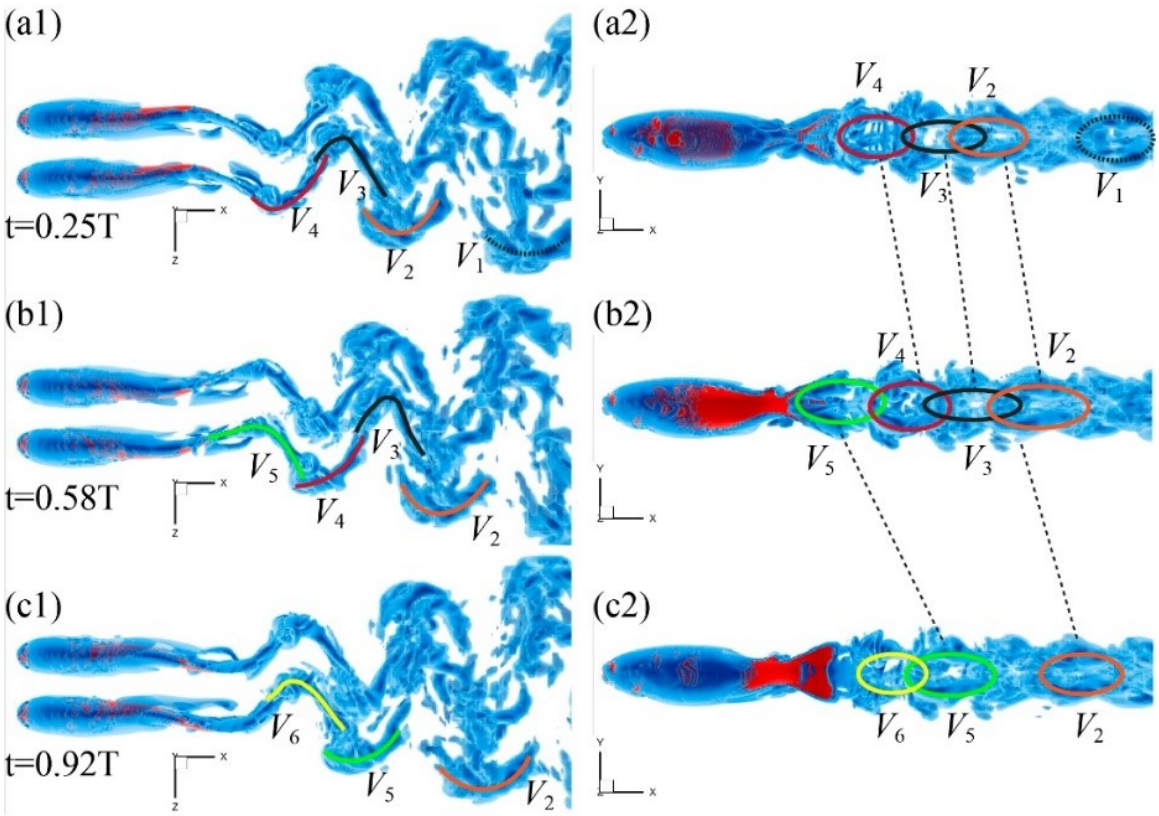

Figure 6-15. Three-dimensional wake structures from the top view (a1-c1) and the side view (a2-c2) at (a) $t = 0.25T$, (b) $t = 0.58T$ and (c) $t = 0.92T$. The wake structures are visualized via the iso-surface of $Q = 5$. The colored solid lines and ellipses denote the vortex rings.

Meanwhile, the streamwise velocity u^* around the caudal fins is lower in the channel than outside the channel. For example, Fig. 6-16(a3) shows that the pressure around the upper surface of fish 1's caudal fin is much larger than that of fish 2. The lower velocity induces an earlier and stronger flow separation. In Fig. 6-16(a2), the vortex flow around the upper surface of fish 2 separates earlier from the caudal fin than that of fish 1. Consequently, a higher-pressure zone is generated on the upper surface of fish 1's caudal fin, as shown in Fig. 6-16(a3). Considering the undulating direction of the caudal fin, it can derive that the caudal fin of fish 1 consumes more power to overcome the higher pressure force. It implies that the surfaces towards the channel save

energy in the undulating motion compared with those outside the channel. Hence, compared with a single trout, the fish swimming in a side-by-side school consumes less power on the caudal fin. A similar phenomenon happens at $t = 0.58T$ and $t = 0.92T$.

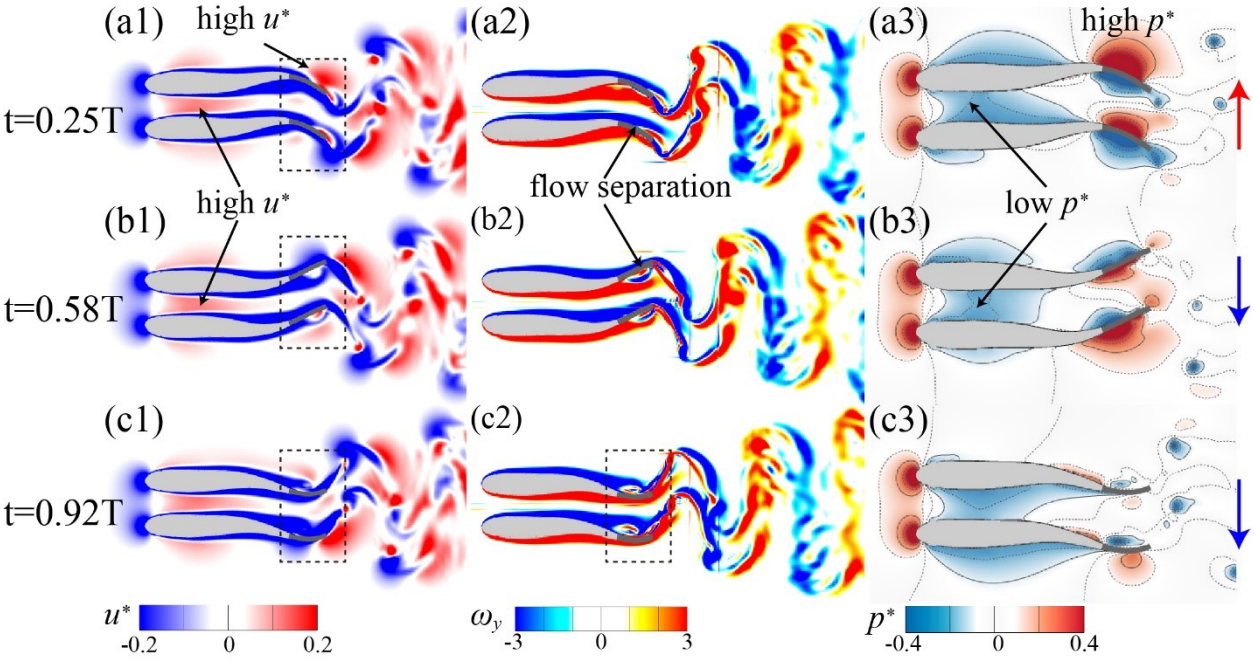

Figure 6-16. Contours of normalized streamwise velocity u^* (a1-c1), vorticity ω_y (a2-c2), and normalized pressure p^* (a3-c3) on a horizontal slice cutting through the frontal place of the fish body at (a1-a3) $t = 0.25T$, (b1-b3) $t = 0.58T$ and (c1-c3) $t = 0.92T$. The red arrow denotes the tail tip of the fish moving upward, and the blue arrows indicate moving downward.

6.3.5 Effect of Phase Difference in a Side-by-Side Fish School

We now consider the phase differences effects on the hydrodynamic interactions in the side-by-side schools. The lateral spacing of the schools is fixed at $D = 0.4L$. The phase of fish 1 is fixed at 0°, while the phase of fish 2 varies from 0° to 360°. Hence, the phase difference of a school is defined as $\varphi = \varphi_2 - \varphi_1$. The normalized thrust, drag, powers, Froude efficiency, and caudal fin propulsive efficiency are presented in Fig. 6-17 as a phase difference function. In Fig. 6-17, the

performance of the trunk, including drag and power, of each fish is barely influenced by the phase difference, while the thrust and power of the caudal fins depend strongly on the phase.

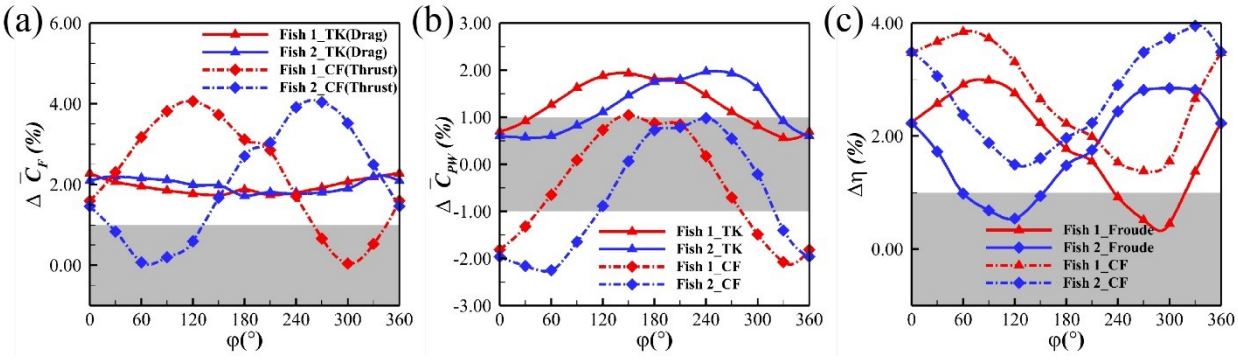

Figure 6-17. Hydrodynamic performance of individuals varying with the phase difference in the side-by-side schools: (a) normalized thrust and drag coefficients, (b) normalized power coefficients and (c) Froude efficiency and caudal fin propulsive efficiency.

As the fish swim in phase ($\varphi = 0°$), the power of the caudal fin is reduced, and the thrust increases slightly, which might be due to the constructive interaction of the trunk. Then, when the phase difference increases ($\varphi < 120°$), fish 1 yields an enhanced thrust at the cost of consuming more power, while fish 2 yields less thrust compared with the in-phase case. At $\varphi = 120°$, the thrust of fish 1 reaches the maximum, 4.1% higher than that of a single fish. As $\varphi \to 180°$, the thrust of fish 1 decreases while that of fish 2 increases, and the power of the caudal fin for each fish continues increasing. When $\varphi = 180°$, the total thrust enhancement of the two fish is 5.8%, with 1.6% more power consumed by the caudal fins, compared with a single fish. The Froude efficiency and caudal fin propulsive efficiency of each fish follow similar trends as the forces. Fish 1 achieves the maximum η_{CF} at $\varphi = 60°$, improved by 3.8% compared to a single fish, and fish 2 reaches the minimum η_{CF} at $\varphi = 120°$. The trends are reversed due to symmetry as the phase difference increases beyond 180°. The results suggest that the optimal swimming strategies can be

made for fish-like robots swimming in a side-by-side configuration by adjusting the flapping phase. If higher thrust is needed for fast acceleration, the robot fish should swim anti-phase, whereas when the robots are cruising, and energy saving is preferable, the fish-like robots should swim in phase.

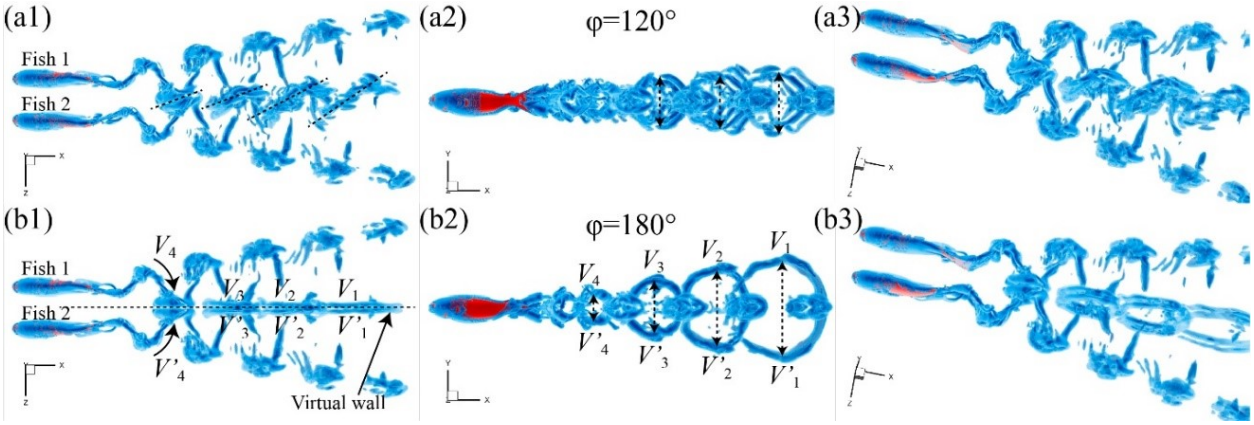

Figure 6-18. Three-dimensional vortex structures of the out-of-phase ($\varphi = 120°$) (a1-c1) and the anti-phase ($\varphi = 180°$) (a2-c2) side-by-side schools at $t = 5.0T$ from the top and side view and a perspective view. The wake structures are visualized via the iso-surface of $Q = 5$.

Figure 6-18 presents the three-dimensional vortex structures of the out-of-phase ($\varphi = 120°$) and anti-phase ($\varphi = 180°$) side-by-side schools at $t = 5.0T$ from the top and side views and a perspective view. The shedding vortex rings of fish 1 obliquely collide with those shed by fish 2 in the out-of-phase school ($\varphi = 120°$). In contrast, the vortex rings collide with other vortex rings at the center of the school, and the colliding interface is parallel to the median plane of the fish in the anti-phase school, as shown in Fig. 6-18(b1). The collided vortex rings thus are expanded in the vertical direction when being advected downstream, and a larger expansion rate exists in the anti-phase school [see Fig. 6-18(b2)].

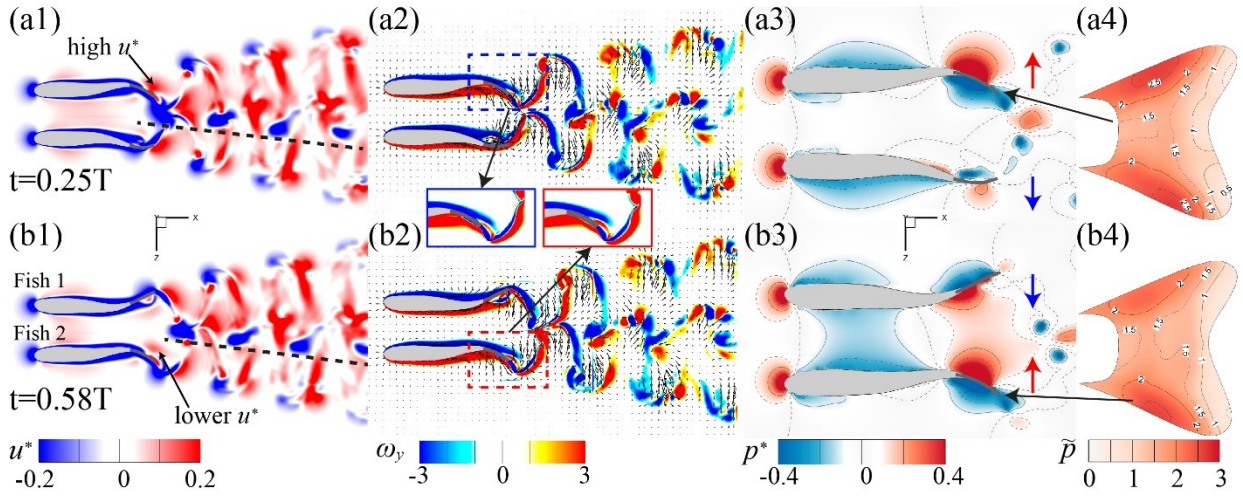

Figure 6-19. Contours of normalized streamwise velocity u^* (a1-b1), vorticity ω_y (a2-b2), and normalized pressure p^* (a3-b3) on a horizontal slice cutting through the frontal plane of fish bodies in the out-of-phase school of $\varphi = 120°$ at $t = 0.25T$ and $t = 0.58T$. Normalized surface pressure $\tilde{p}$ on the caudal fin of (a4) fish 1 at $t = 0.25T$ and (b4) fish 2 at $t = 0.58T$. The red arrow denotes the tail tip of the fish moving upward, and the blue arrows indicate moving downward.

The thrust enhancement mechanism in the out-of-phase school at $\varphi = 120°$ is explored by analyzing the flow fields in detail. Figure 6-19 shows the contour plots of the normalized streamwise velocity (u^*), vorticity (ω_y) and normalized pressure (p^*) on a slice in the horizontal plane cutting through the frontal plane of the fish in the out-of-phase school at $t = 0.25T$ and $t = 0.58T$. Besides, the normalized surface pressure $\tilde{p}$ on the caudal fin of fish1 at $t = 0.25T$ and of fish 2 at $t = 0.58T$ are shown in Figs. 6-19(a4) and 6-19(b4), respectively. The surface pressure is normalized by $\tilde{p} = p/0.5\rho U_\infty^2$. Due to the phase difference, the motion of fish 2 is behind that of fish 1 with a time interval of $\Delta t = 1/3$. Fish 2 at $t = 0.58T$ has the same kinematics as fish 1 at $t = 0.25T$, but experiences different flow environment. Thus, these two times are selected to illustrate the thrust enhancement mechanism for fish 1. In Figs. 6-19(a1) and 6-19(b1), the normalized streamwise velocity fields show that the wake at the center of the school inclines

downwards, which might be an indicator of high-thrust production of fish 1. In comparison, the streamwise velocity at the upper side of the caudal for fish 1 at $t = 0.25T$ is larger than that for fish 2 at $t = 0.58T$. The low velocity leads to earlier flow separation on the upper side of fish 2's caudal fin, as shown in the subplots in Figs. 6-19(a2) and 6-19(b2). Hence, the pressure on the caudal fin of fish 2 is less than that of fish 1 [see Figs. 6-19(a4) and (b4)]. Larger and stronger positive pressure regions are located on the caudal of fish 1, implying a higher thrust production. The above analysis unveils why fish 2 experiences thrust reduction in the side-by-side school. However, it cannot fully illustrate the mechanism of thrust enhancement for fish 1. Thus, we continue analyzing the flow fields of the anti-phase school to explore the thrust enhancement.

Figure 6-20 presents the contour plots of the normalized streamwise velocity (u^*), vorticity (ω_y) and normalized pressure (p^*) on a slice cutting through the anti-phase school at $t = 0.25T$, $t = 0.58T$ and $t = 0.92T$. A stable pattern of low-velocity zones, the blue regions at the center of the wake in Figs. 6-21(a1-c1), is generated behind the school. The low-velocity zones are backward relative to the incoming flow and push the school forward. For example, in Figs. 6-20(a1-a3), the backward flow will impede the flow coming from the channel, enhance the negative pressure on the fin surface and increase thrust generation. This mechanism is similar to the passive energy recapture in swimming medusae [130].

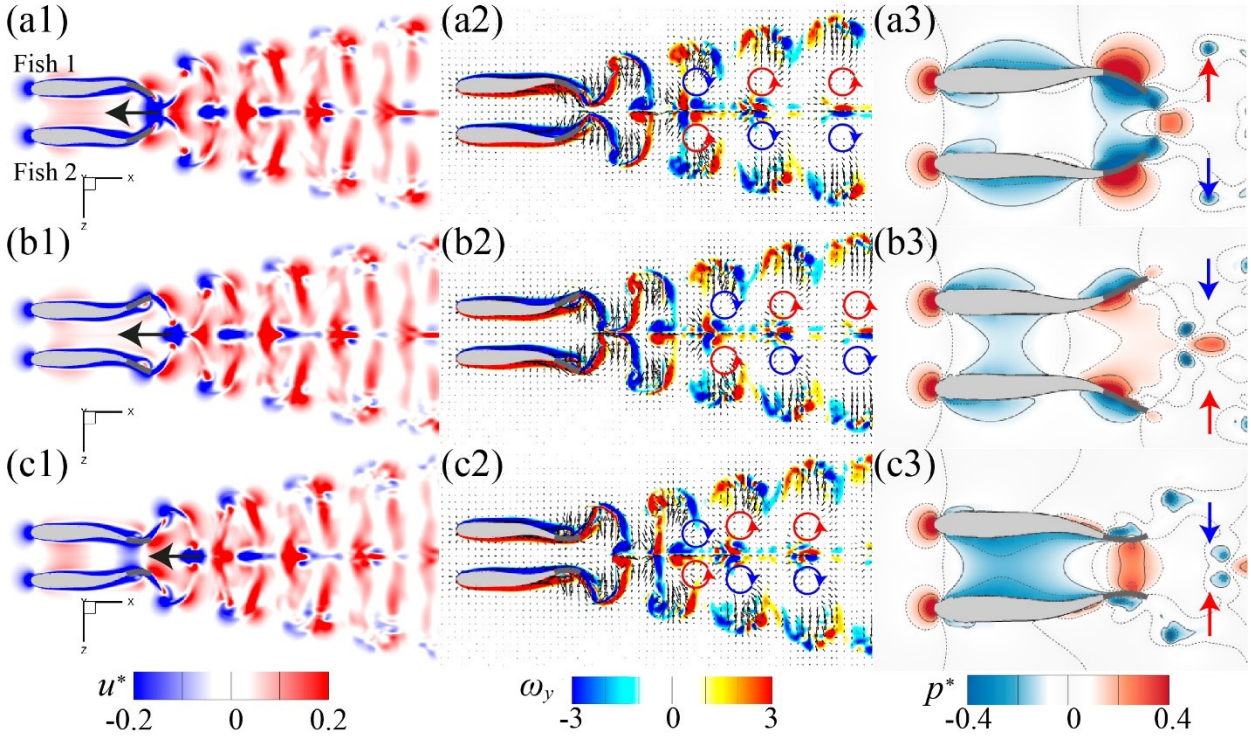

Figure 6-20. Contour of normalized streamwise velocity u^* (a1-b1), vorticity ω_y (a2-b2), and normalized pressure p^* (a3-b3) on a horizontal slice cutting through the frontal plane of fish bodies in the anti-phase school at $t = 0.25T$, $t = 0.58T$ and $t = 0.92T$.

Besides, fish 2 works like a virtual wall stopping the flow drained by fish 1 expanding in the lateral direction. The same scenario happens for fish 1. Wall effect or ground effect has been widely reported that can increase thrust and lift for swimming animals [131-134]. The effect is usually modeled as an interaction between a pair of vortices with opposite signs [42, 103]. In the contour plots of vorticity ω_y, the vortices generated by fish 1 are opposite to those shed by fish 2 and the vortices are symmetrical placed with respect to the centerline line of the school, which is exactly the same as the wall effect. Hence, the virtual wall effect can also be used to illustrate the thrust enhancement in the anti-phase side-by-side schools. The passive energy capture mechanism and virtual wall effect can also be employed to illustrate the thrust enhancement for fish 1 in the

out-of-phase school ($\varphi = 120°$). In Fig. 6-19(a1), the backward flow moves towards fish 1, indicating fish 1 benefits more from the backward flow. Fish 2 works like an inclined wall impeding the expansion of the vortex flow generated by fish 1 in the lateral direction, as shown in Figs. 6-18(a1) and 6-19(a2).

6.3.6 Effect of Streamwise Distance in a Staggered Fish School

In this and the following sections, we will consider a more prevalent planar fish school in nature, the staggered school, in which the following fish swim behind the leading fish with a streamwise distance of S and offset in the cross-stream direction with a lateral spacing of D. This section investigates the effects of streamwise distance on the performance of staggered schools by presenting the normalized performance and comparing the flow fields of schools. Besides, the surface pressure on the caudal fin is also presented connecting with the flow fields to examine the physical mechanisms. In these schools, the tail-beat phase of both fish is fixed at $\varphi = 0°$, the lateral spacing is $D = 0.4L$, and the streamwise distance S changes from $0.2L$ to $1.4L$. The normalized hydrodynamic performance of each fish in the schools is displayed in Fig. 6-21 as a function of streamwise distance S.

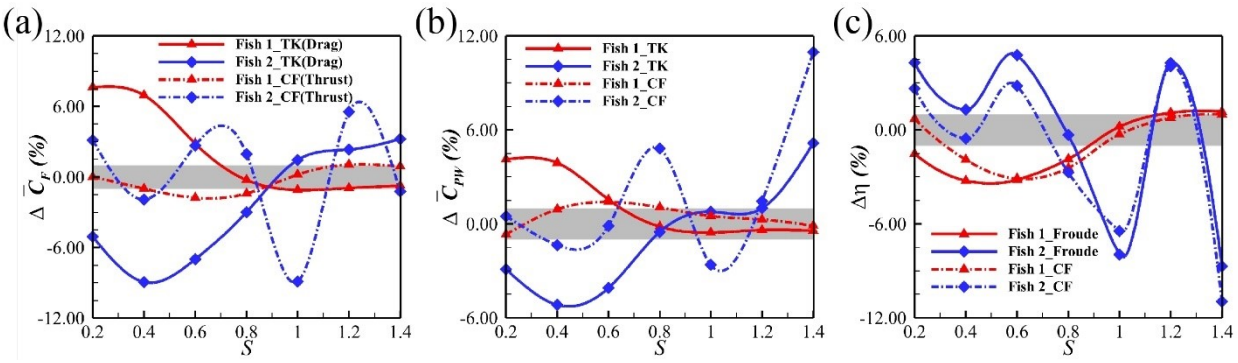

Figure 6-21. Hydrodynamic performance of individuals varying with the streamwise distance in the staggered schools: (a) normalized cycle-averaged thrust and drag coefficients, (b) normalized

cycle-averaged power coefficients and (c) normalized Froude efficiency and caudal fin propulsive efficiency.

As illustrated in Fig. 6-21(a), $\Delta\overline{C_{1D}} > 0$ indicates that fish 1 experiences drag increasing in the staggered schools, and with the increasing S, $\Delta\overline{C_{1D}}$ declines. When $D \geq 0.8L$, $\Delta\overline{C_{1D}}$ reaches a plateau and $\overline{C_{1D}}$ is close to $\overline{C_{D\_single}}$, the drag of a single fish, denoting that the drag of fish 1 is nearly independent of the hydrodynamic interactions in the fish schools. On the contrary, fish 2 benefits from the schools by reducing drag ($\Delta\overline{C_{2D}} < 0$) before $D = 0.95L$. When $D < 0.95L$, the $\Delta\overline{C_{2D}}$ curve presents a U-shape, and $\Delta\overline{C_{2D}}$ reaches the trough, $\Delta\overline{C_{2D}} = -9\%$, at $D = 0.4L$, representing fish 2 obtains the maximum drag reduction of 9% compared with a single fish. Beyond $D = 0.95L$, $\overline{C_{2D}}$ starts being larger than $\overline{C_{D\_single}}$ and increases as S increases. The normalized thrust of fish 1 $\Delta\overline{C_{1T}}$ varies at a range of $-1.8\%\sim1.0\%$, implying the thrust production of fish 1 is barely influenced by the school, whereas $\Delta\overline{C_{2T}}$ drastically varies at a range of $-9\%\sim5.5\%$ as S increases. The $\Delta\overline{C_{2T}}$ varying with S presents a traveling waveform, and the amplitude gradually increases. Local troughs of $\Delta\overline{C_{2T}}$ are at $S = 0.4L$ and $S = 1.0L$, whereas the local peaks are around $S = 0.7L$ and $S = 1.2L$. Fish 2 obtains the maximum thrust production at $S = 1.2L$ with the thrust increased by 5.5%.

The normalized power on the trunk $\Delta\overline{C_{PW\_TK}}$ shares similar trends as the drag for each fish. Fish 2 saves the maximum energy by 5.2% at $S = 0.4L$ compared to a single fish and consumes 5% more power at $S = 1.4L$. For the caudal fins, the normalized power on the caudal fin of fish 1, $\Delta\overline{C_{1PW\_CF}}$, shows an opposite trend to that of $\Delta\overline{C_{1T}}$, but also varies in a narrow range. However, $\Delta\overline{C_{2PW\_CF}}$ displays a similar curve as $\Delta\overline{C_{2T}}$, implying fish 2 can increase the thrust at the cost of consuming more power through the hydrodynamic interactions in a fish school. The Froude

efficiency and caudal fin efficiency curves are similar for each fish. It is because for fish 1, the performance of the caudal fin is independent of the streamwise distance and the efficiencies are thus mainly dependent on the trunk's performance. For fish 2, the traveling wave-like trend for efficiencies is due to the variation of the thrust. The efficiencies of fish 1 decrease compared to a single fish, while fish 2 achieves the highest Froude efficiency at $S = 0.6L$, improved by 4.8%, and obtains the highest caudal fin efficiency at $S = 1.2L$, increased by 4%.

Two main conclusions can be drawn from the performance results. First, the drag and power on the trunk of fish 2 strongly depend on the streamwise distance. According to the variation of $\Delta\overline{C_{2T}}$, the streamwise spacing can be divided into two regimes: drag reduction regime ($S < 0.95L$) and drag increasing regime ($S \geq 0.95L$). Second, the thrust production of fish 2 can be significantly enhanced by varying the streamwise distance. To elucidate the associated mechanisms, two cases are selected to perform detailed flow analysis: $S = 0.6L$ school in which $\overline{C_{2D}}$ and $\overline{C_{2PW\_TK}}$ decrease by up to 7%, and $S = 1.2L$ school in which $\overline{C_{2D}}$ and $\overline{C_{2PW\_TK}}$ both increases. Figure 6.22 compares the drag and thrust coefficients of fish in the $S = 0.6L$ school with those of a single fish during one cycle. The total drag on the trunk consists of a pressure drag and a friction drag, i.e. $F_D = F_{DP} + F_{DF}$. The pressure drag is calculated by integrating the surface pressure over the body surface, $F_{DP} = \int_S -pn_x dS$, where p is the surface pressure and the friction drag is computed by integrating the shear force, $F_{DF} = \int_S \tau_{xi} n_i dS$, where τ_{xi} is the x-component of viscous stress tensor and n_i represents the i-th component of the unit normal vector on a surface element dS.

In Fig. 6.22(a), although the friction drag of fish 2 takes the dominant part of the total drag , the difference in C_{DF} between fish 2 and the single fish is trivial. On the contrary, the difference

in C_{DP} is large. During the whole cycle, C_{DP_single} is close to C_{1DP} and larger than C_{2DP}. Thus, the difference between C_{DP_single} and C_{2DP} takes the major part in the drag reduction for fish 2. Additionally, in Fig. 6.22(b), the thrust coefficient of each fish reaches the first peak around $t = 0.25T$, and the peak of C_{2T} is greater than that of C_{T_single}.

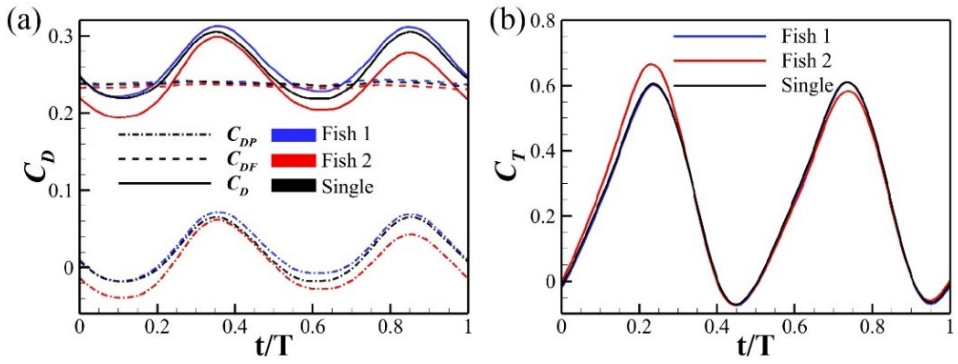

Figure 6-22. Time histories of hydrodynamic forces of fish in the $S = 0.6L$ staggered school: (a) pressure drag, friction drag and total drag coefficients of the trunk, (b) thrust coefficients.

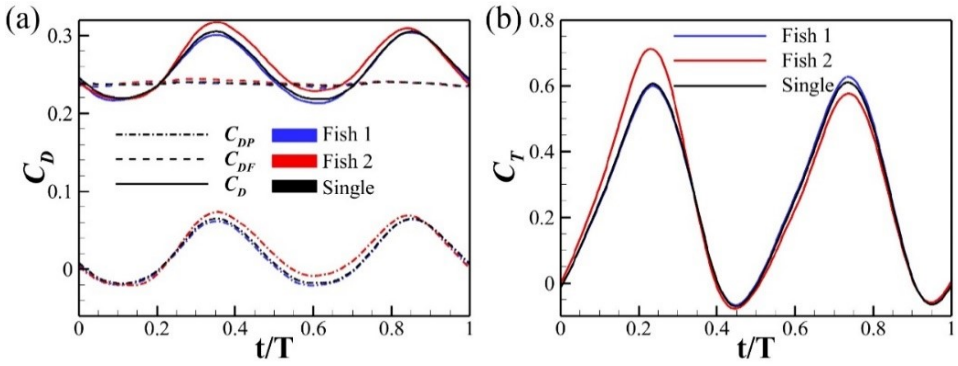

Figure 6-23. Time histories of hydrodynamic forces of fish in the $S = 1.2L$ staggered school: (a) pressure drag, friction drag and total drag coefficients of the trunk, (b) thrust coefficients.

Figure 6-23 displays the time histories of drag and thrust coefficients of each fish in the $S = 1.2L$ fish school and the single fish. In the $S = 1.2L$ school, fish 2 suffers a larger drag, which is also verified by the time history of drag coefficients in Fig. 6-23(a). In addition, the pressure

drag of fish 2 C_{2DP} takes the dominant role in the drag increasing of fish 2 because the difference between C_{2DF} and C_{DF_single} is trivial. Around $t = 0.6T$, the difference between C_{2DP} and C_{DP_single} is maximum. In Fig. 6-23(b), the thrust of each fish arrives the peak around $t = 0.25T$, and the peak of C_{2T} is much larger than that C_{T_single}. The exact quantities of the cycle-averaged force coefficients and their differences are summarized in Table 6-2. The reduction of pressure drag for fish 2 accounts for 80% of the total drag reduction in the $S = 0.6L$ school and takes 74.6% of the total drag increasing in the $S = 1.2L$ school.

TABLE 6-2. Summary of time-averaged force coefficients of individual fish in the schools.

		$\overline{C_{DP}}$	$\overline{C_{DF}}$	$\overline{C_D}$	$\overline{C_T}$	$\Delta\overline{C_{DP}}/\Delta\overline{C_D}$	$\Delta\overline{C_{DF}}/\Delta\overline{C_D}$
single		0.019	0.238	0.257	0.257		
$S = 0.6L$	Fish 1	0.025	0.240	0.264	0.252	77.3%	22.7%
	Fish 2	0.005	0.234	0.239	0.263	-80.0%	-20.0%
$S = 1.2L$	Fish 1	0.017	0.238	0.255	0.260	-84.7%	-15.2%
	Fish 2	0.023	0.240	0.263	0.266	74.6%	21.4%

Next, the drag reduction and thrust enhancement mechanisms are explored by analyzing and comparing the flow fields of $S = 0.6L$ and $S = 1.2L$ fish schools. According to the above time histories of forces, flow fields at two times are chosen to be analyzed: $t = 0.25T$ when the $\overline{C_T}$ of each fish is close to the peak, and $t = 0.58T$ when the differences between C_{2DP} and C_{DP_single} in

both schools are comparatively large. Figure 6-24 shows the three-dimensional vortex structures of both schools at $t = 0.25T$ and $t = 0.58T$ from a perspective view and the top view.

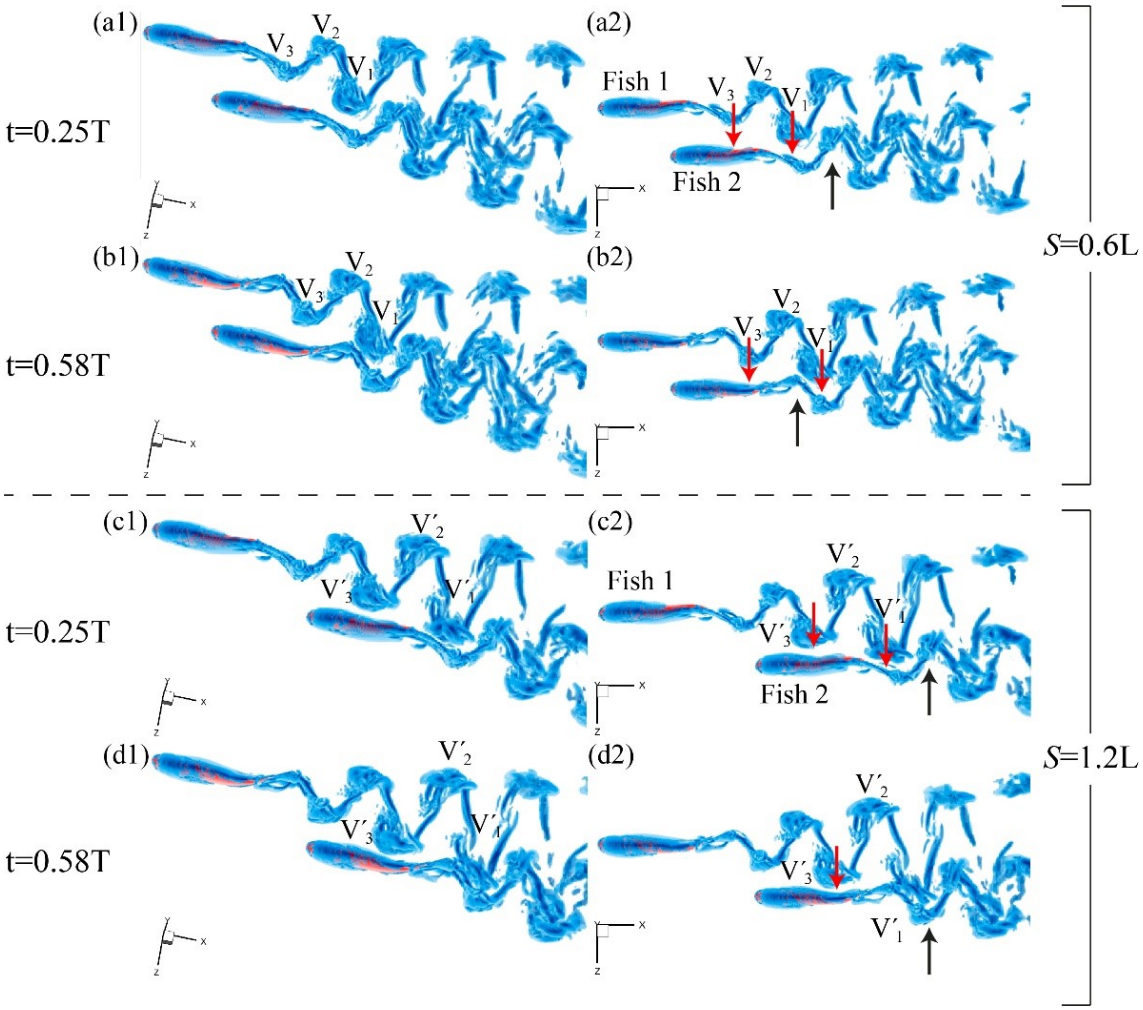

Figure 6-24. Three-dimensional vortex structures of $S = 0.6L$ (a1, a2, d1, d1) and $S = 1.2L$ (c1, c2, d1, d2) fish schools at $t = 0.25T$ and $t = 0.58T$ from a perspective view and the top view. The wake structures are visualized via the iso-surface of $Q = 5$.

Vortex rings are generated by tail motion carrying momentum jet into the fluid to produce thrust and lateral force [30, 135]. In Fig. 6-24(a2), at $t = 0.25T$, the tail of fish 2 moves upwards, and the vortex ring V_1 moves downwards when being advected downstream in the school of $S = 0.6L$. Because V_1 is in vicinity of the caudal fin of fish 2, the relative motion may contribute to the

thrust enhancement. A similar phenomenon happens in the school of $S = 1.2L$. In Fig. 6-24(c2), the vortex ring V'_1 is closer to the caudal fin of fish 2, and a stronger interaction exists, resulting in more significant thrust improvement, compared with the $S = 0.6L$ fish school. Comparing with V'_3 in Fig. 6-24(d2), the vortex wing V_3 is located at a similar position with respect to the trunk of fish 2 at $t = 0.58T$, as shown in Fig. 6-24(b2). However, at $t = 0.58T$, fish 2 benefits from the $S = 0.6L$ school by a drag reduction, while fish 2 in the $S = 1.2L$ school suffers a higher drag. It implies that different vortex-body interactions happen in these two schools. In the far wake, the vortex rings generated by fish 1 and 2 collide and merge, and more complex vortex structures are formed in both schools.

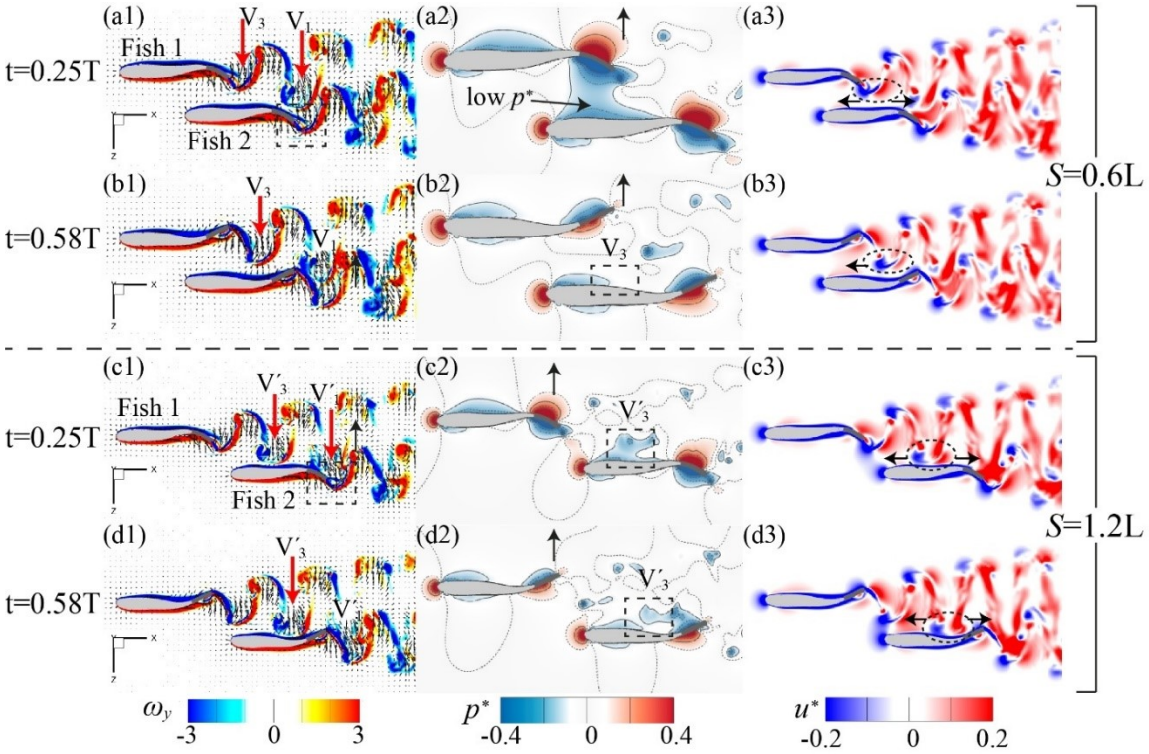

Figure 6-25. Contour plots of vorticity ω_y (a1-d1), normalized pressure p^* (a2-d2) and normalized streamwise velocity u^* (a3-d3) on a horizontal slice cutting through the frontal plane of fish bodies in the $S = 0.6L$ (a1-a3, b1-b3) and $S = 1.2L$ (c1-c3, d1-d3) schools at $t = 0.25T$ and $t = 0.58T$.

To further examine the thrust enhancement and drag reduction mechanisms, a more specific flow analysis is conducted by presenting the contour plots of vorticity ω_y, normalized pressure p^* and normalized streamwise velocity u^* on a slice cutting through the frontal plane of the fish bodies in the $S = 0.6L$ and $S = 1.2L$ schools at $t = 0.25T$ and $t = 0.58T$ in Fig. 6-25. At $t = 0.25T$, V_1 is directly above the caudal fin of fish 2 in the $S = 0.6L$ school, and a strong momentum jet carried by V_1 pushes against the caudal fin, increasing the surface pressure of the caudal fin for fish 2. It is validated by the surface pressure contour plots in Fig. 6-26. By comparing Fig. 6-26(a1) and 6-26(a2), it can be found that larger high-pressure areas are generated around the leading edges of the caudal fin of fish 2. Based on the moving direction of the fin, it can be derived that the thrust production is enhanced. In the $S = 1.2L$ school, V'_1 is the vicinity of the upper surface of the caudal fin and carrying a stronger momentum jet interacts with it. Accordingly, the surface pressure around the leading edges is higher on the caudal fin of fish 2 in the $S = 1.2L$ school than in the $S = 0.6L$ school. Thus, a higher thrust is generated by fish 2 in the $S = 1.2L$ school compared to that in the $S = 0.6L$ school.

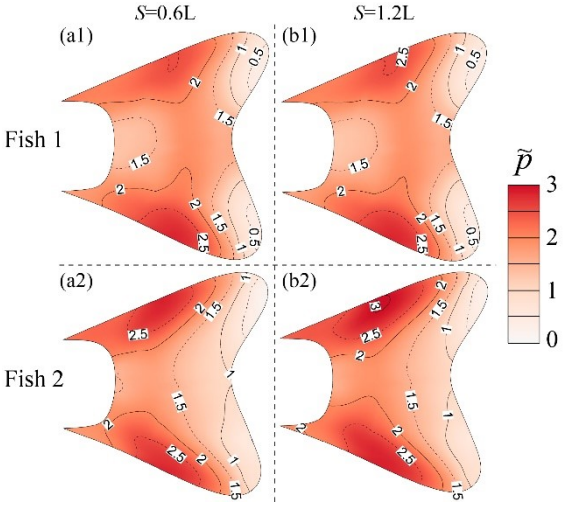

Figure 6-26. Normalized surface pressure $\tilde{p}$ on the caudal fin of fish 1 (a1, b1) and 2 (a2, b2) in the $S = 0.6L$ (a1, a2) and the $S = 1.2L$ (b1, b2) schools at $t = 0.25T$.

The interaction between the vortex ring and the caudal fin also suppresses the flow separation on the fin surface. Figure 6-27 zooms in the vortex flow contour around the caudal fin of each fish in both schools at $t = 0.25T$. In these two schools, the vortex flows around the caudal fin of fish 1 are similar, and the flow separation happens at the same position on the fin surface. In comparison, in the $S = 0.6L$ school, the flow separation on the caudal fin surface of fish 2, shown in Fig. 6-27(a2), is later than that of fish 1. In addition, flow separation does not happen for fish 2 in the $S = 1.2L$ school. By checking Figs. 6-25(a3) and 6-25(c3), the streamwise velocity around the tail-tip of fish 2 is larger than that of fish 1 in both schools. It contributes to the delay of the flow separation, which will finally enhance the thrust production.

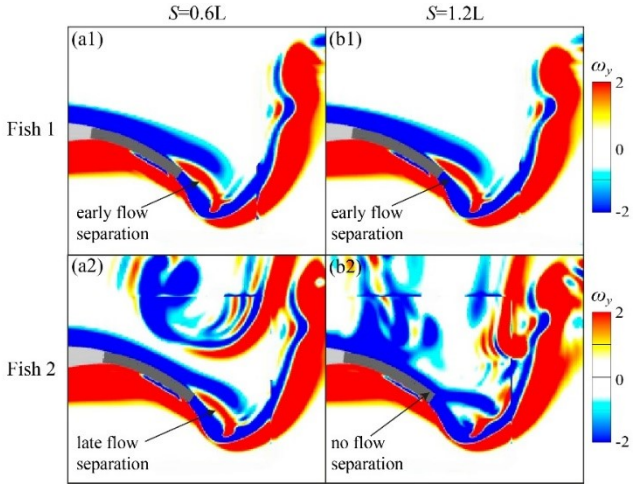

Figure 6-27. Contour plots of vorticity ω_y around the caudal fin of fish 1 (a1, b1) and 2 (a2, b2) in the $S = 0.6L$ (a1, a2) and the $S = 1.2L$ (b1, b2) schools at $t = 0.25T$.

At $t = 0.58T$, V_3 is closer to the trunk of fish 2 [see Fig. 6-25(b1)], affecting the velocity field around the body. Higher velocity at the center of V_3 directs downwards and decreases the negative pressure on the body surface, as shown in the area on the upper surface circled by a dashed square in Fig. 6-25(b2). More importantly, the low streamwise velocity zone generated by V_3 circled by the dashed oval in Fig. 6-25(b3) almost maintains the same compared to that in Fig. 6-

25(a3), whereas the associated high-velocity zone becomes wake. The difference results in V_3 reducing the streamwise velocity around the corresponding position on the trunk. Then, the body will experience a reduction in drag [5, 136]. However, in the $S = 1.2L$ school, even though V'_3 is closer to the trunk of fish 2 than V_3 in the $S = 0.6L$ school, the high velocity zone generated by V'_3 even becomes stronger when being advected downstream, as shown in Fig. 6-25(d3). This increases the streamwise velocity around the trunk and the drag at the associated position. The influence of V_3 and V'_3 on the streamwise velocity around the upper surface of fish 2 can also be verified by the time-averaged streamwise velocity fields shown in Fig. 6-28.

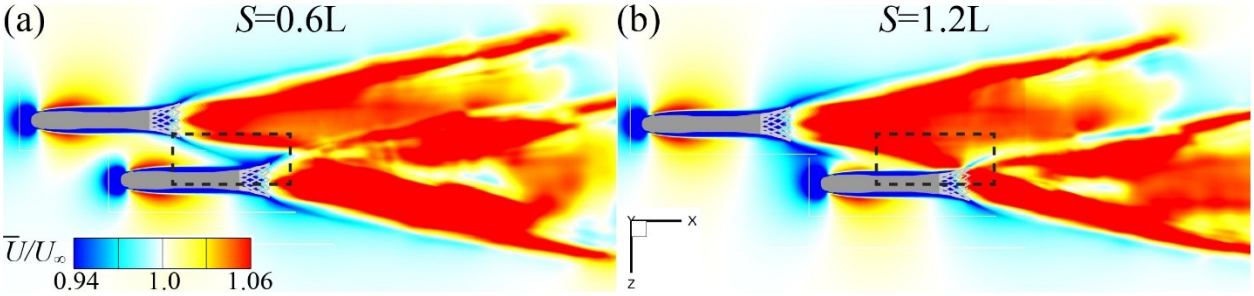

Figure 6-28. Time-averaged streamwise velocity fields of the (a) $S = 0.6L$ school and (b) the $S = 1.2L$ school.

The specific structures of V_3 and V'_3 at $t = 0.58T$ are zoomed in and presented in Fig. 6-29 from the top, front and perspective views. In the $S = 0.6L$ school, V_3 is inclined relative to the body of fish 2, and the left side of V_3 with clockwise vorticity is much closer to the body surface than the other side with counterclockwise vorticity. Nevertheless, in the $S = 1.2L$ school, V'_3 is almost parallel to the body of fish 2, as shown in Fig. 6-29(b1). Besides, the vorticity of the right side is stronger than that of the left side. Hence, the velocity induced by the right side of V'_3 directing to the swimming direction is larger than that induced by the left side. Thus, we can

conclude that the shape and position of the vortex rings determine the net induced velocity for the fish body, and increasing or reducing drag of the body.

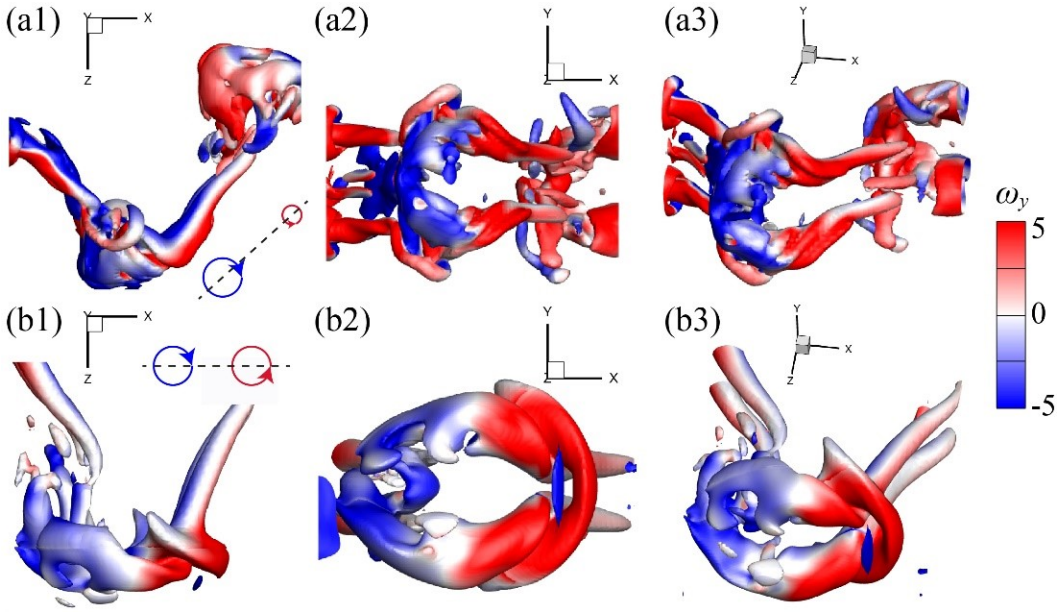

Figure 6-29. Three-dimensional structures of V_3 (a1-a3) and V'_3 (b1-b3) at $t = 0.58T$ from the top, front and perspective views.

Figure 6-30 presents the schematic of drag reduction (a) and drag increasing (b) mechanisms. Here we define the advection velocity in the swimming direction of vortex rings as the phase velocity U_{phase}, which borrows the definition in a two-dimensional study [14, 73]. We assume U_{phase} keeps constant when a vortex ring is advected downstream, and it is represented by the horizontal solid line in Fig. 6-30. Pervious two-dimensional study suggests that, for a thrust wake, $U_{phase} > U_\infty$, which is also verified by our measurement for three-dimensional cases. Hence, we use the dashed horizontal line whose position is lower than that of U_{phase} to represent the incoming velocity U_∞. The curved solid lines in Fig. 6-30 indicate the induced streamwise velocity $U_{induced}$ profiles of the negative (in blue) and positive (in red) side vortices of a vortex ring. In Fig. 6-30(a), due to $|\omega_+| < |\omega_-|$, the velocity induced by the negative vorticity is larger

than that induced by the positive vorticity, which may result in the net velocity is opposite to the streamwise direction. Then the streamwise velocity around the trunk decreases and the drag is thus reduced. In Fig. 6-30(b), even if the magnitude of vorticity of the two vortices is the same, the net velocity induced by the positive vortex is still larger than that induced by the negative velocity because $U_{phase} > U_{\infty}$ and the induced velocity of the positive vortex is in the streamwise direction. This results in the increase of the streamwise velocity around the trunk and drag.

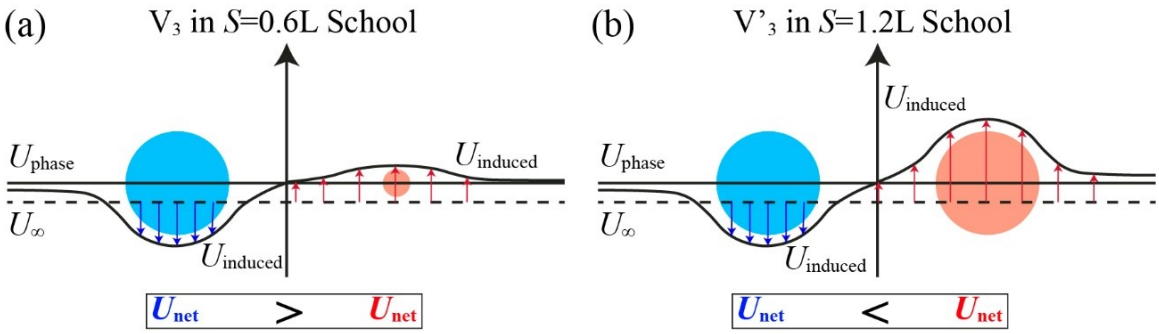

Figure 6-30. Schematics of (a) drag reduction mechanism in the $S = 0.6L$ school and (b) drag increasing mechanism in the $S = 1.2L$ school.

6.3.7 Effect of Phase Difference in a Staggered Fish School

In this section, two typical kinds of schools are chosen to be investigated the phase difference effects on hydrodynamic interactions: the $S = 0.6L$ schools in which the head of fish 2 is front of the tail of fish 1 and the $S = 1.2L$ schools in which the head of fish 2 is behind the tail of fish 1. In these two sets of schools, the phase of fish 1 is fixed at 0° and the phase of fish 2 changes from 0° to 360°. The lateral distance for all schools keeps at $D = 0.4L$. Here we define the $S = 0.6L$ schools as A-schools and the $S = 1.2L$ schools as B-schools. The effects of phase difference are studied by presenting the hydrodynamic performance and the associated flow analysis for each kind of schools.

Figure 6-31 shows the normalized hydrodynamic performance for each fish in the $S = 0.6L$ schools as a function of the phase difference φ. In Fig. 6-31(a), the normalized drag coefficients of both fish 1 and fish 2 present slight change with the increasing φ, i.e., fish 1 suffers 3% more drag over a single fish and fish 2 benefits by reducing around 7% no matter what the phase difference is. Also, the thrust of fish 1 is independent of the variation of φ. However, the thrust of fish 2 strongly depends on the phase difference. The curve of the normalized thrust for fish 2 $\Delta\overline{C_{2T\_A}}$ shows an approximate cosinusoidal waveform. Fish 2 receives the optimal benefit at $\varphi = 330°$ with the thrust increased by 4.3%, and reduces 4.7% thrust at $\varphi = 120°$. The power coefficients share similar trends as the force coefficients. The power consumed by the trunk and caudal fin of fish 1 seldom varies as the phase difference increases. Fish 2 consumes the minimum power at $\varphi = 120°$ and the maximum power at $\varphi = 330°$ both for the trunk and caudal fin. Correspondingly, the Froude efficiency and caudal fin efficiency of fish 1 change slightly with the increasing φ, whereas the efficiencies of fish 2 display a U-shape form when varying with the phase difference. When $\varphi = 330°$, fish 2 achieves its highest Froude efficiency $\Delta\eta_{max} = 5.5\%$, and the highest caudal fin efficiency $\Delta\eta_{CF\_max} = 3.2\%$. The performance results suggest: (1) the drag reduction for fish 2 is dependent on the phase difference, and (2) the thrust production can be improved by changing the phase difference and is determined by the vortex-fin interaction.

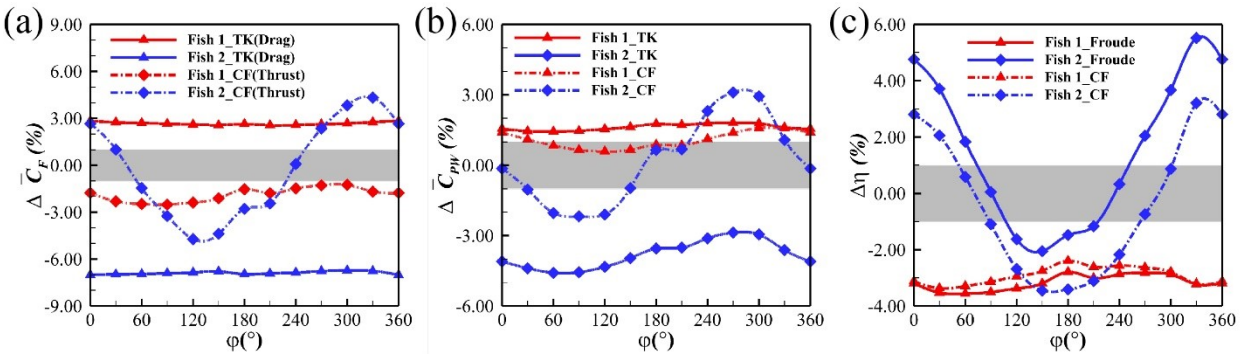

Figure 6-31. Hydrodynamic performance of individuals varying with the phase difference in the $S = 0.6L$ staggered schools: (a) normalized thrust and drag coefficients, (b) normalized power coefficients and (c) Froude efficiency and caudal fin propulsive efficiency.

The hydrodynamic performance of each fish varying with φ in the $S = 1.2L$ school is shown in Fig. 6-32. Similar to the $S = 0.6L$ school, the hydrodynamic performance of fish 1 in the $S = 1.2L$ school is unrelated to the phase difference, while the performance of fish 2 greatly relies on the phase difference. The normalized thrust and power of fish 2 $\Delta\overline{C_{2T\_B}}$ and $\Delta\overline{C_{2PW\_B}}$ both show a cosinsodial-wave-like relationship with the phase difference. Fish 2 receives the maximum thrust reduction at $\varphi = 180°$, 10.1% less than a single fish, and obtains the highest thrust enhancement of 8.8% over a single fish at $\varphi = 330°$ with a cost of 5% more power consumed. Correspondingly, fish 2 achieves the highest Froude efficiency at $\varphi = 330°$, $\eta_{max} = 5.1\%$. As for the drag of fish 2, it is higher than that of a single fish no matter what φ is and reaches the peak at $\varphi = 120°$, increasing by 8%. The results indicate: (1) the drag increasing always exits in the $S = 1.2L$ school, but the extent of the increase can be changed by varying φ, (2) φ is a significant factor influencing the vortex-fin interaction and thrust production for fish 2.

The drag reduction and drag increasing mechanisms have been thoroughly studied in the previous section and are confirmed to be independent of φ by the results in the current section.

Thus, we focus on the phase difference effects on the thrust enhancement in the staggered schools in the following.

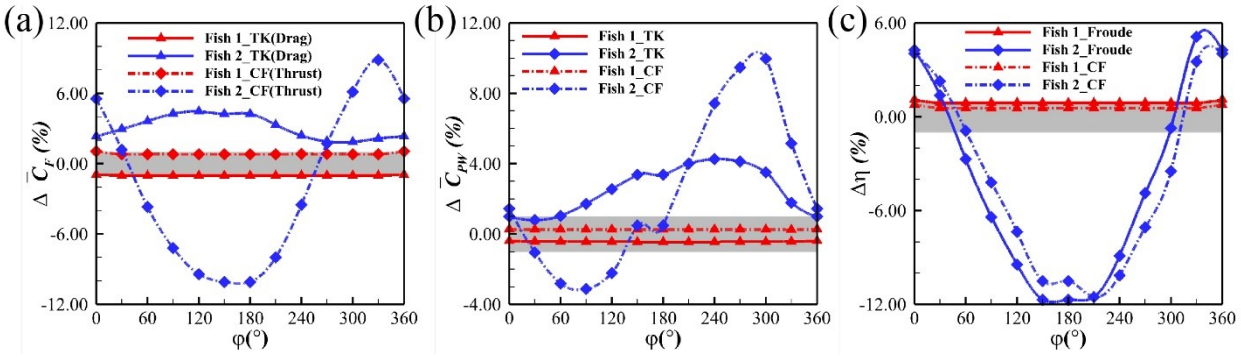

Figure 6-32. Hydrodynamic performance of individuals varying with the phase difference in the $S = 1.2L$ staggered schools: (a) normalized thrust and drag coefficients, (b) normalized power coefficients and (c) Froude efficiency and caudal fin propulsive efficiency.

Two A-schools ($S = 0.6L$) are chosen to be analyzed in detail: $\varphi = 120°$ A-school with the minimum $\overline{C_{2T\_B}}$ and $\varphi = 330°$ A-school with the maximum $\overline{C_{2T\_B}}$. Figure 6-33 shows the time histories of the force coefficients of fish 2 in the $\varphi = 120°$ and $\varphi = 330°$ A-schools and a single fish. Here it should be noted that for comparison, the timelines of the forces for fish 2 in both schools are shifted to have the same timeline as the single fish. In Figure 6-33(b), around $t = 0.25T$, fish 2 in the $\varphi = 330°$ school generates a much higher thrust than that in the $\varphi = 120°$ school, the variation of C_{2T} around the time determines that fish 2 has higher mean thrust in the $\varphi = 330°$ school. Thus, the vortex structures, vorticity and lateral velocity contours on a slice cutting through the frontal plane and surface pressure on the caudal fin are presented in Fig. 6-34 for both schools at $t = 0.25T$. In Figs. 6-34(b1) and 6-34(b2), a vortex ring is directly above the caudal fin of fish 2 and a high momentum jet pushes against the caudal fin in the $\varphi = 330°$ school, whereas in the $\varphi = 120°$ school, a vortex ring has passed by the caudal fin of fish 2. This results

in the water above the caudal fin of fish 2 with higher downward velocity in the $\varphi = 330°$ school and the caudal fin thus produces higher surface pressure, as shown in Fig. 6-34(b3) and 6-34(b4). The phase difference leads to the variation of the flow environment for fish 2 in different schools, and the vortex-fin interaction for fish 2 is thus changed, which affects the thrust production.

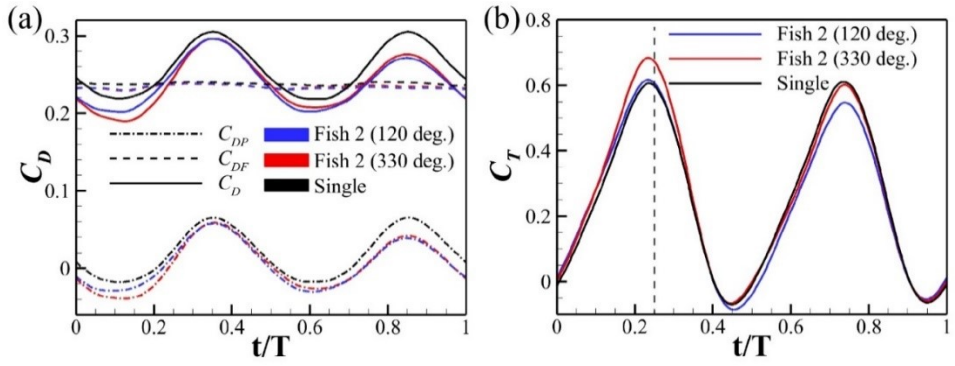

Figure 6-33. Time histories of the hydrodynamic forces of fish 2 in the $\varphi = 120°$ and $\varphi = 330°$ staggered schools at $S = 0.6L$: (a) pressure drag, friction drag and total drag coefficients of the trunk, (b) thrust coefficients.

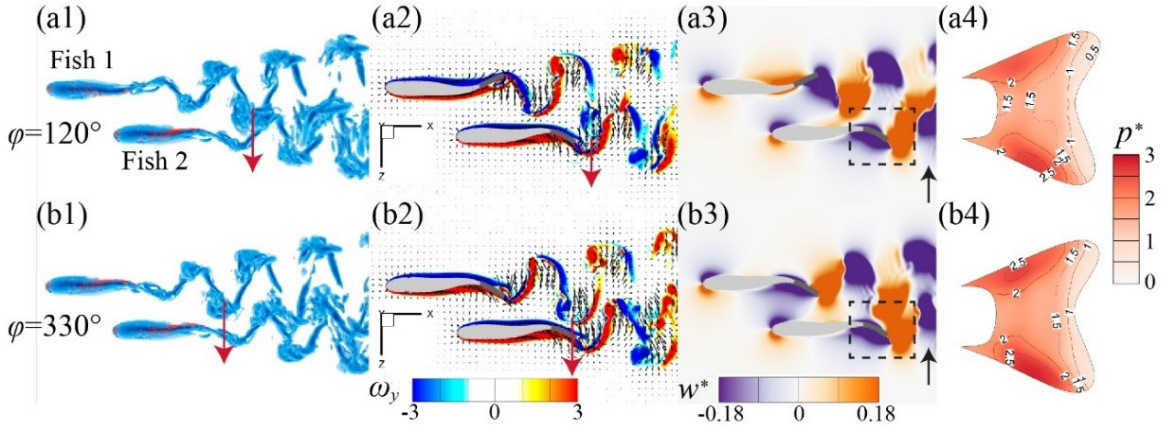

Figure 6-34. Three-dimensional vortex structures (a1, b1), contours of vorticity ω_y (a2-b2) and normalized cross-streamwise velocity w^* (a3-b3) on a horizontal slice cutting through the frontal plane of fish bodies in the $\varphi = 120°$ and $\varphi = 330°$ A-schoolsat $t = 0.25T$. Normalized surface

pressure $\tilde{p}$ on the caudal fin of fish 2 in the $\varphi = 120°$ (a4) and $\varphi = 330°$ (b4) A-schools at $t = 0.25T$.

We also perform a similar analysis for the thrust enhancement in the $S = 1.2L$ schools by providing the time histories of the force coefficients of fish 2 in Fig. 6-35 and the flow fields at $t = 0.25T$ in Fig. 6-36. Also, the timelines of the forces of fish 2 in the $\varphi = 120°$ B-school and $\varphi = 330°$ B-school are shifted. In Fig.6-36, due to the relative distance between the vortex rings and the caudal fin, the flow velocity above the fin surface may be increased [see Fig. 6-36(b3)] or decreased [see Fig. 6-36(a3)]. This difference results in a higher pressure on the caudal fin generated in the $\varphi = 330°$ B-school, as shown in Fig. 6-36(b4). It finally enhances the thrust production of the caudal fin or deteriorates it.

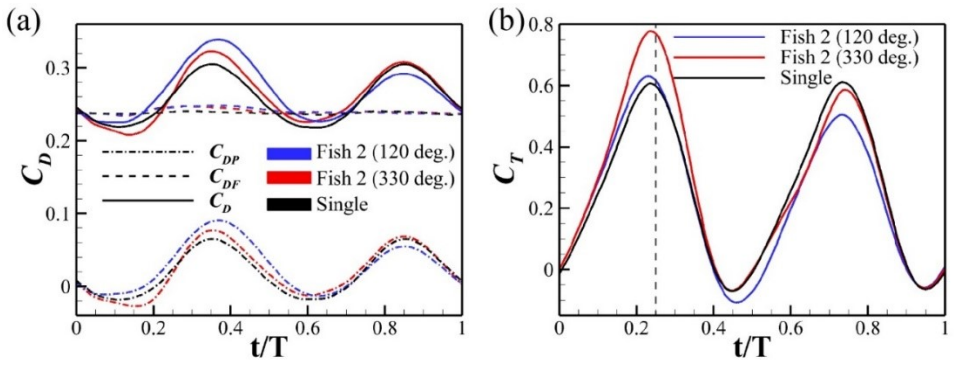

Figure 6-35. Time history of hydrodynamic forces of fish 2 in the $\varphi = 120°$ and $\varphi = 330°$ staggered schools at $S = 1.2L$: (a) pressure drag, friction drag and total drag on the trunk, (b) thrust production.

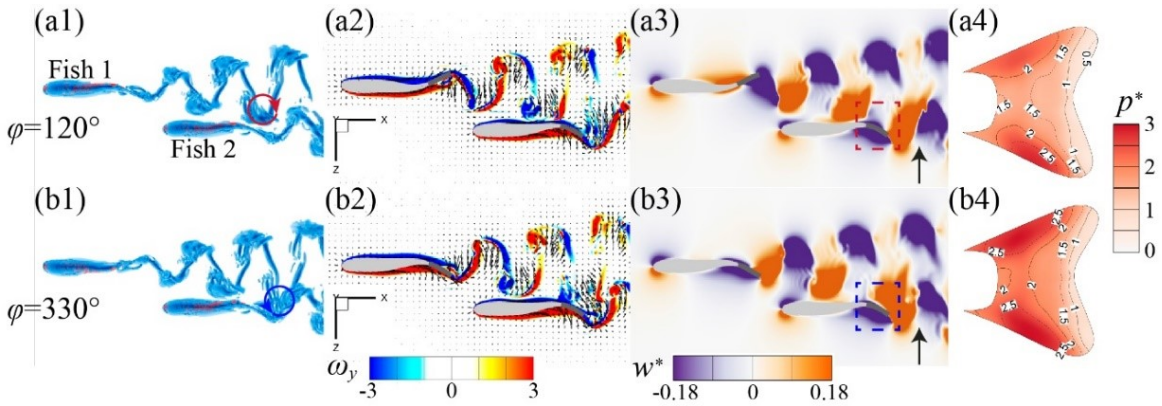

Figure 6-36. Three-dimensional vortex structures (a1, b1), contours of vorticity ω_y (a2-b2) and normalized cross-streamwise velocity w^* (a3-b3) on a horizontal slice cutting through the frontal plane of fish bodies in the $\varphi = 120°$ and $\varphi = 330°$ B-schools at $t = 0.25T$. Normalized surface pressure $\tilde{p}$ on the caudal fin of fish 2 in the $\varphi = 120°$ (a4) and $\varphi = 330°$ (b4) B-schools at $t = 0.25T$.

6.4 Chapter Summary

This section thoroughly investigates hydrodynamic interactions in the different planar schools, including in-line, side-by-side and staggered configurations, through three-dimensional simulations in an immersed-boundary-method-based incompressible Navier-Stokes flow solver. The realistic biological trout fish model is imposed on a traveling wave kinematics to mimic real fish swimming. The effects of spatial arrangements, such as the streamwise and lateral distances, and phase differences between swimmers, are examined over a wide range in these three kinds of schools. The hydrodynamic performance and flow fields of these schools are quantitatively characterized and well presented, which helps us identify various fundamental hydrodynamic interactions in the horizontal fish schools. Thrust enhancement exists in all kinds of schools, while drag reduction mainly appears in the staggered configuration. Drag increasing exists in most in-line and side-by-side schools and is little dependent on the phase difference. In addition, the

variation of the power is very correlated with drag and thrust. In general, for the trunk, the drag increasing is always accompanied by the increment of power, and the power decreases when the drag is reduced. For the caudal fin, the thrust can be improved with the cost of consuming more power, except for some special situations.

In the in-line school with a streamwise distance of 1.2BL, the thrust of the leading fish is enhanced by 3.8% and the drag decreases by 2.8% compared with a single fish. In the meantime, the power of the trunk and caudal fin both decreases by 1.5%. Correspondingly, the Froude efficiency of fish 1 is improved by more than 5%. These hydrodynamic benefits are obtained through the block effect of the trailing fish, by which a high-pressure zone is generated right behind the leading fish. And this constructive interaction will quickly dwindle as the streamwise increases. In comparison, the following fish suffers from the drag increasing. By changing the phase difference, this destructive interaction can be amended and less drag increasing can be obtained by reducing the pressure drag. It is because the phase difference alters the vortex-body interactions.

In the in-phase side-by-side schools, drag increasing happens and strongly depends on the lateral distance D. At $D = 0.25BL$, the drag for each fish increases by over 8%. It is because a narrow channel formed by the trunks of the fish speeds up the flow in it and increases the drag on the body surface facing the channel. With the increasing D, this detrimental interaction quickly weakens. However, it is found the caudal fins can achieve energy saving. At $D = 0.25BL$, 6.8% power can be saved for each caudal fin. It is because the channel decreases the flow speed around the surfaces of the caudal fins, resulting in an earlier flow separation on the fin surface. Thus, the pressure around the fin surface with the earlier flow separation is lower than the same side of the other caudal fin which is outside the channel, and the power consumption is thus reduced with a slight loss in thrust production. The existence of the channel can also enhance the thrust production

by adjusting the phase difference. At $\varphi = 120°$, the thrust of one fish (fish 1) is improved by 4% at $D = 0.4L$. Passive energy capture mechanisms and the virtual wall effect contribute to the thrust enhancement.

Surprisingly, drag reduction has been found in the staggered schools and strongly depends on the streamwise distance S. In particular, at $S = 0.4BL$, more than 9% drag and more than 5% of the power are reduced by the trunk of the following fish. Two regimes have been identified according to the variation of the drag: drag reduction regime ($S < 0.95L$) and drag increasing regime ($S \geq 0.95L$). By comparing the wakes of the two kinds of schools, we found that drag reduction and drag increasing are related to the evolution and advection of the vortex rings shed by the leading fish. In a school within the drag-reduction regime, due to the incline and stretching of the vortex rings, the vortex-body interaction results in the streamwise velocity around the fish body being reduced. In contrast, in a school of the drag-increasing regime, the advection velocity leads to the vortex rings inducing higher streamwise velocity around the body of the following fish. The streamwise velocity reduction results in the drag reduction on the trunk, and the velocity increasing results in the drag increasing. The streamwise distance and phase difference have the similar effect on the thrust enhancement. By setting the distance or phase difference at an appropriate value, the momentum carried by the vortex ring can enhance the leading-edge vortex and suppress the flow separation on the caudal fin, increasing the thrust production.

7 Hydrodynamic Interactions in Tip-to-Tip Schools

In the previous sections, two-dimensional (2D) and three-dimensional (3D) fish-like models are utilized to investigate the hydrodynamic interactions in fish schools. Those fish schools are arranged in a two-dimensional plane; however, fish usually place themselves at different depths, i.e., the structure of fish schools is highly three-dimensional in nature. The hydrodynamic interactions between swimmers in highly three-dimensional configurations received little attention. Thus, this section will explore the hydrodynamics of fish schools arranged in three-dimensional space. In particular, the tip-to-tip fish schools where swimmers are arranged in the vertical plane will be studied as a basis for this research field. A key goal of this section is to examine the effects of spatial arrangement and synchronization on the hydrodynamic interactions in a tip-to-tip fish school.

This section uses the same biological trout-like fish models imposed on a traveling wave to form the tip-to-tip schools. A high-fidelity immersed-boundary-based flow solver is employed to simulate the flow past the tip-to-tip schools. The effects of the vertical distance and phase distance on the hydrodynamic interactions in the schools are examined, respectively. The hydrodynamic performance is presented and compared with that of a single fish to quantitatively measure the effects of hydrodynamic interactions. Then detailed flow analyses are conducted to reveal the associated physical mechanisms. We aim to provide a thorough and systematic study of the hydrodynamic interactions in the tip-to-tip fish schools and improve the understanding of the hydrodynamics in fish schools. Finally, simulations of flow past two pitching-heaving panels arranged in the vertical plane are performed to examine the mechanisms unveiled in fish schools.

7.1 Models, Kinematics and Tip-to-Tip Configuration

The trout-like fish model here is the same as the model used in the previous section. The same traveling wave that resembles the carangifrom undulating motion is applied on the fish body. The two fish are arranged in the vertical plane to form a tip-to-tip school, as shown in Fig.7-1. In this work, H denotes the vertical distance of the tip-to-tip school and is defined as the distance between the snouts of the two fish. To investigate the spatial arrangement effects, H varies from 0.25 body length (BL) to 0.6BL.

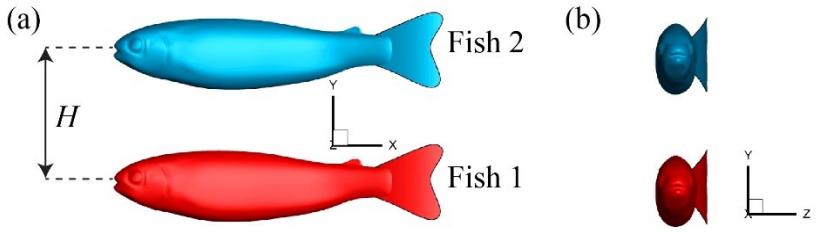

Figure 7-1. Schematic of a trout school arranged in the tip-to-tip configuration.

The geometry of the bio-inspired trapezoidal panel is shown in Fig. 7-2(a), and the associated parameters are listed in Table 7-1. c is the chord length of the panel, and all other dimensions are scaled based on the chord length. The aspect ratio (AR) of the trapezoidal panel is defined as the ratio of the square of the span (the longer base) to the area of the panel, i.e., $AR = b^2/A_{PL}$, where b is the span and A_{PL} is the area of the panel. In the current work, the panel is a low aspect ratio with $AR = 1.21$. The panel is pitched about the leading edge and undergoes a harmonic oscillating motion along the *y*-axis [see Fig. 7-2(b)]. The following equations describe the motions:

$$\theta(t) = \theta_0 sin(2\pi t + \varphi), \tag{7-1}$$

$$y(t) = \frac{A_y}{2} cos(2\pi t + \varphi) \tag{7-2}$$

where $\theta_0 = 15°$ denotes the amplitude of the pitching motion, $A_y = 0.4c$ is the peak-to-peak amplitude of the heaving motion, φ indicates the phase of the coupling motion, and t is time. Two panels are arranged in the vertical plane with a vertical distance of H', as shown in Fig. 7-2(3). When studying the spatial arrangement effects, the vertical distance H' varies from $0.1c$ to $1.0c$. The phase of panel 2 changes from 0° to 360° to investigate the phase difference effects on the hydrodynamic interactions.

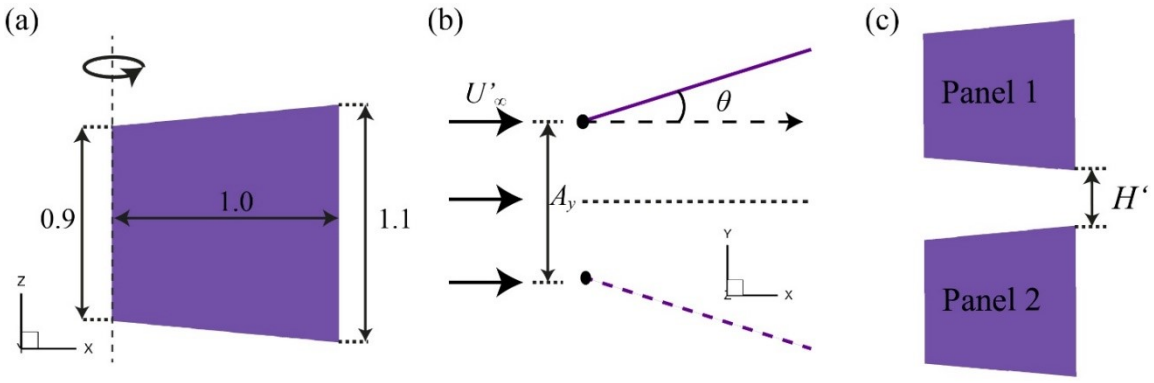

Figure 7-2. (1) Geometry of trapezoidal panel model, (2) top view of the pitching-heaving motion and definitions of heaving motion and pitching motion, and (3) schematic of panels in a tip-to-tip configuration.

7.2 Computational Setup and Validation Study

Similarly, the Reynolds number (*Re*) and the Strouhal number (*St*) are employed to describe the hydrodynamics and flow characteristics of fish-like swimming and the heaving-pitching panel propulsion. For trout-like swimming, following the setup in Chapter 6, $Re = 5384$, and $St = 0.39$. For the pitching-heaving panels, the Strouhal number is defined as the $St = f'A'/U'_\infty$, where $f' = 1.0$ is the driving frequency of the pitching motion, A' is the peak-to-peak trailing edge

amplitude of the pitching motion, and $U'_{\infty} = 1.5$ is the incoming flow velocity for the pitching-heaving panels, and the Reynolds number is calculated by $Re = U'_{\infty}c/\nu$. Here the Strouhal number $St = 0.35$ and the Reynolds number $Re = 600$ are chosen for the pitching-heaving motion.

For the trout-like fish bodies, all the performance parameters, including forces, powers and efficiencies, are calculated using the same definitions as Chapter 6. For the panels, the thrust coefficient is defined as $C_T = F_T/0.5\rho U_{\infty}^2 A_{PL}$, the power coefficient is computed as $C_{PW} = \mathrm{P}/0.5\rho U_{\infty}^3 A_{PL}$ and the associated propulsive efficiency is the ratio of the thrust to the power $\eta = \overline{C_T}/\overline{C_{PW}}$, where the overbars denote the time-averaged values.

Figure 7-3 illustrates the configuration of the Cartesian grid, boundary conditions and the local refinement meshes for the trout-like fish school simulations. The domain size of the base layer of mesh is $15L \times 10L \times 10L$ with grid points of $257 \times 177 \times 113$ (approximate 5.1 million). Two levels of refinement mesh have been used, and three refined mesh blocks are in total. With two-layer mesh refinement, the finest resolution is $\Delta_{min} = 3.47 \times 10^{-3}L$, which has been proven fine enough to obtain grid-independent results and to resolve the fluid fields in Chapter 6. The boundary conditions here are also set the same as in Chapter 6.

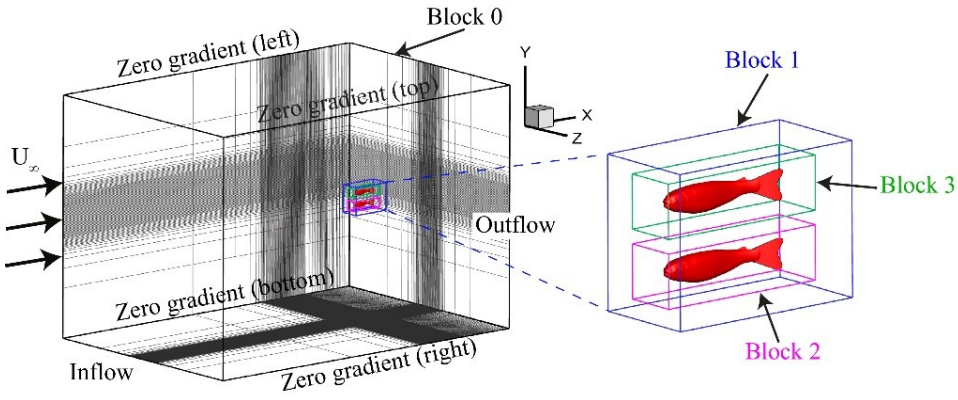

Figure 7-3. Schematic of computational mesh, boundary conditions and the local refinement blocks for tip-to-tip fish schools.

The Cartesian grid with the local refinement blocks and boundary conditions for the simulations of the pitching-heaving panels are shown in Fig. 7-4(a). The size of the computation domain is $16L \times 14L \times 14L$ with total grid points around 2.1 million ($145 \times 113 \times 129$). To resolve the flow near the panels, two layers of refined meshes, the red and blue blocks in Fig. 7-4(a), are employed, so the resolution near the panels is $\Delta_{min} = 0.011L$. The zero-gradient boundary condition is set at all the lateral boundaries, the inflow boundary condition with a constant velocity is imposed on the left-hand boundary, and the right-hand boundary is set as the outflow boundary condition. In addition, a convergence study on the grid density was conducted for the pitching-heaving panel simulations. Figure 7-4(b) displays the time histories of the thrust coefficient of a single panel at four different computational grids, including coarse, medium, fine and dense meshes. The finest resolutions of the four meshes are $0.035c$, $0.019c$, $0.011c$ and $0.009c$, respectively. The thrust coefficient converges when the resolution becomes finer. The difference in the mean value between the fine and the dense mesh is around 1.8%, less than 2%. It validates that the flow simulations performed on the mesh with $\Delta_{min} = 0.011L$ are grid-independent.

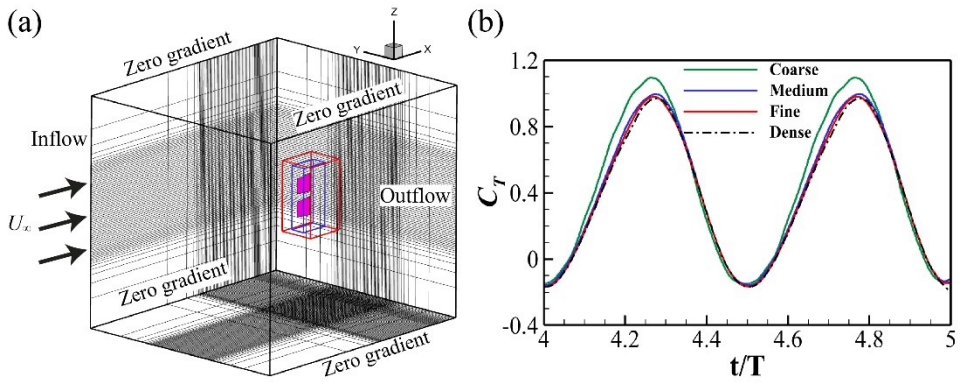

Figure 7-4. (a) Schematic of computational mesh and boundary conditions for the pitching-heaving trapezoidal panels in the tip-to-tip arrangement. (b) Comparison of the instantaneous thrust coefficients of a single pitching-heaving panel computed at the coarse ($\Delta_{min} = 0.035L$), medium ($\Delta_{min} = 0.019L$), fine ($\Delta_{min} = 0.011L$) and dense ($\Delta_{min} = 0.009L$) meshes.

7.3 Results and Discussions

7.3.1 Effect of Vertical Distance in a Tip-to-Tip Fish School

The effects of vertical spacing on the hydrodynamic interactions are investigated in this section. The vertical spacing H changes from 0.25L to 0.85L. The normalized hydrodynamic performance of each fish in the schools is shown in Fig. 7-5 as a function of the vertical spacing. Because the upper part and the bottom part of the body are not symmetrical, the performance of fish 1 differs from that of fish 2, although they share a similar trend.

In Fig.7-5, the force and power coefficients decline as the vertical spacing increases. At $H = 0.25L$, $\overline{C_T}$ of both fish are significantly enhanced. In particular, $\overline{C_T}$ of fish 1 and fish 2 in the tip-to-tip school increase by 12.7% and 8.8%, respectively, at the cost of consuming more power, 7.3% for fish 1 and 8.9% for fish 2. The thrust enhancement rapidly diminishes when increasing the vertical spacing H. When $H > 0.4L$, the performance of the caudal fin is nearly independent of the vertical distance. For the trunk, the hydrodynamic interactions are detrimental to its

performance. At $H = 0.25L$, the C_D and C_{PW_TK} of fish 1 and fish 2 increase by more than 10%, compared to a single trout. As for the hydrodynamic efficiencies, the caudal fin efficiency η_{CF} of fish 1 increases by 5.1% at $H = 0.25L$. The Froude and caudal fin efficiencies for both fish vary similarly, and present a U-shape form relationship with H.

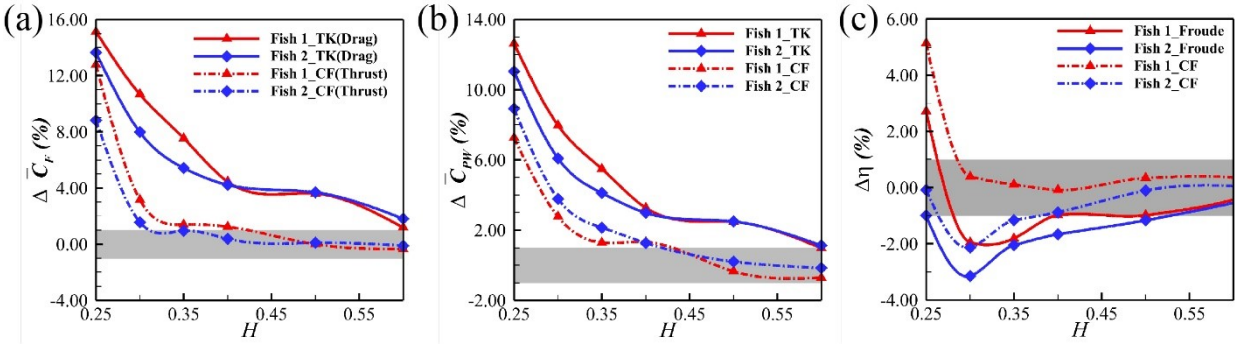

Figure 7-5. Hydrodynamic performance of individuals changing with the vertical distance in tip-to-tip schools: (a) normalized thrust and drag coefficients, (b) normalized power coefficients and (c) Froude efficiency and caudal fin propulsive efficiency.

Figure 7-6 shows three snapshots of the three-dimensional vortex structures (a1-c1) visualized by the iso-surface of $Q = 5$ and the normalized streamwise velocity u^* contours (a2-c2) on a vertical slice cutting through the sagittal plane of fish bodies in the $H = 0.25L$ vertical school at $t = 0.50T$, $t = 0.67T$ and $t = 0.92T$. Due to the symmetry of undulating motion in time, only half of the tail-beat cycle has been analyzed. For a single trout, the height of vortex rings approximately equals the caudal fin span [127], and due to the low aspect ratio, the size of the vortex rings maintains when being advected downstream. In comparison, a narrowing process in the vertical direction is observed for the downstream shedding vortex rings of the vertical school. Due to the mutual interaction between vortex wakes shed by fish 1 and 2, the vortex rings bend in the vertical direction when moving downstream. In Figs. 7-6(a1-c1), the vortex rings are gradually compressed in the vertical direction. In Figs. 7-6(a2-c2), the low-velocity zones (circled blue

regions) denote the cross-section of vortex rings. The corresponding labels of vortex rings are marked on the slices. The vertical distance between the cross-sections of a vortex ring becomes smaller, verifying that the narrowing process happens behind the fish school. The narrowing process results in higher momentum jet oriented to the center, resulting in a higher thrust production [137]. In addition, in Figs. 7-6(a2-c2), the streamwise velocity between the anterior part of the two fish increases, increasing the drag and power of the trunks.

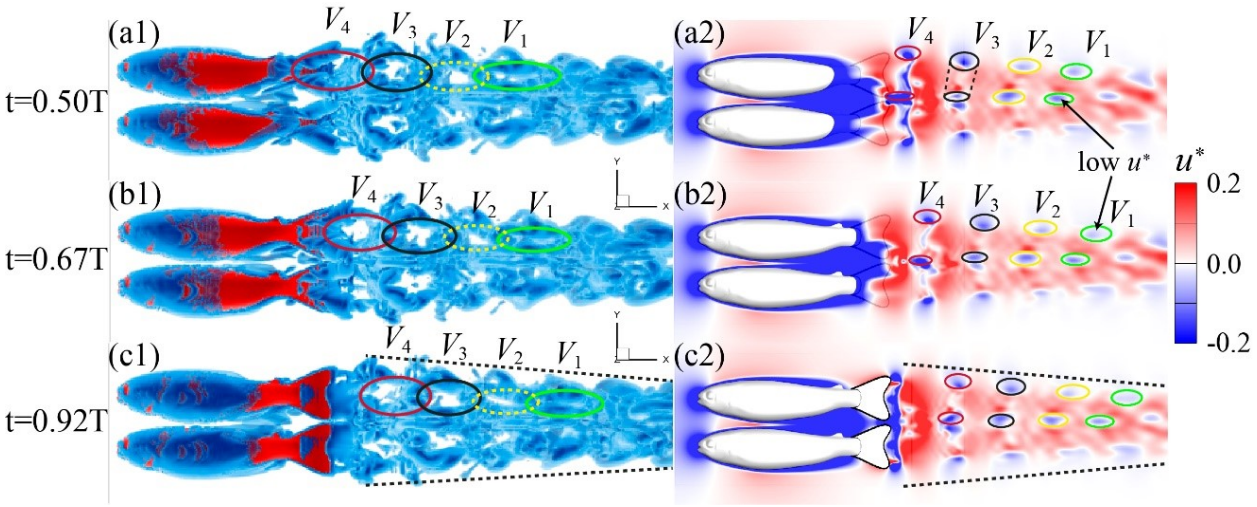

Figure 7-6. Three-dimensional wake structures from the side view (a1-c1) and normalized streamwise velocity u^* contours (a2-c2) on a vertical slice cutting through the sagittal plane of fish bodies at (a) t=0.50T, (b) t=0.67T and (c) t=0.92T. The wake structures are visualized by the iso-surface of $Q = 5$.

To further explain the thrust enhancement on the caudal fins, Fig. 7-7 presents the snapshots of the contours of normalized cross-streamwise velocity w^* (a1-a3), vorticity ω_x (b1-b3) and pressure p^* (c1-c3) on a vertical slice at $t = 0.50T$, $t = 0.67T$ and $t = 0.92T$. The slices cut through the caudal fins near the tail-tip, as shown in Fig. 7-7. The normalized cross-streamwise velocity is computed as $w^* = w/U_\infty$. The caudal fins move from the rightmost side (at $t = 0.50T$)

to the left. In Fig. 7-7(a1), when the caudal fins arrive at the rightmost side, a jet-like flow is left behind (the orange zone at the center). The velocity around the caudal fins at the center of the school is higher than that around the outter side of the caudal fins. Also, stronger leading-edge vortices are generated at the center of the school, as shown in Fig. 7-7(b1). Then, when the caudal fins move to the left, the jet-like flow can stabilize the enhanced leading-edge vortices generated on the adjacent caudal-fin leading edges of the two fish [138]. In Fig. 7-7(b2), the vortices at the center are more coherent and stronger than those on the lateral sides. Thus, a continuous higher-pressure zone is maintained at the center, which results in a larger thrust production on the lower side caudal fin of fish 2 and the upper side caudal fin of fish 1.

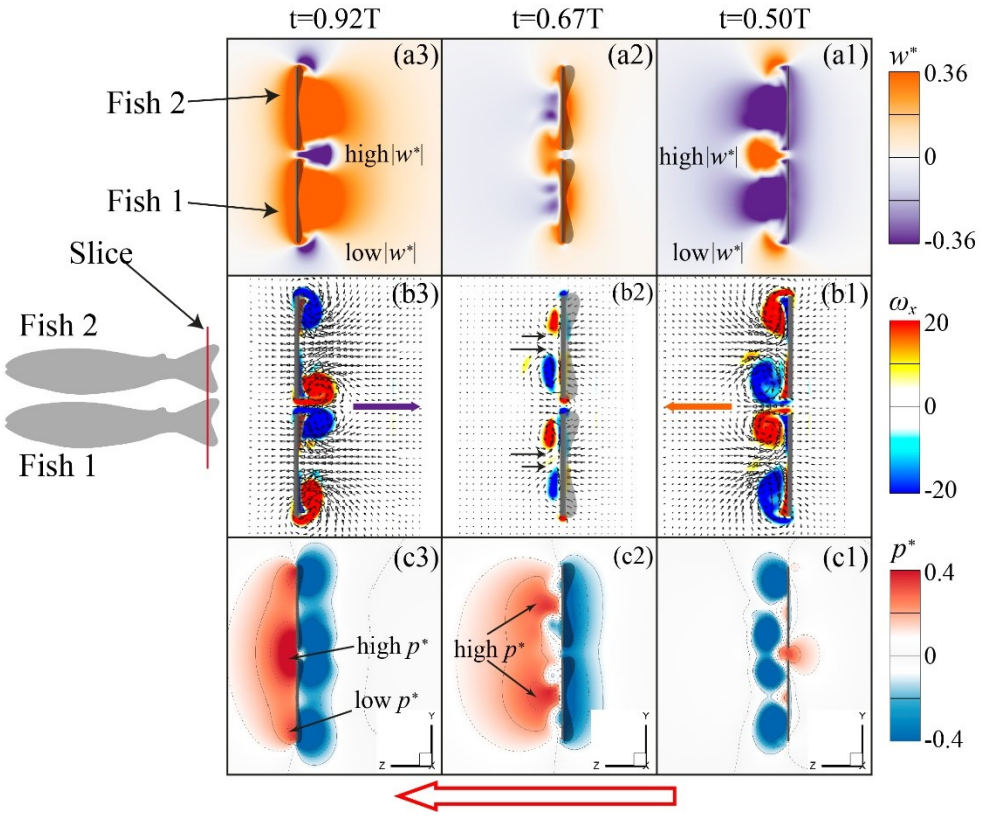

Figure 7-7. Contour plots of normalized lateral velocity w^* (a1-a3), vorticity ω_x (b1-b3), and pressure p^* (c1-c3) on a vertical slice cutting through the caudal fins at (a1, b1, c1) $t = 0.50T$, (a2,

b2, c2) $t = 0.67T$ and (a3, b3, c3) $t = 0.92T$. The red arrow denotes the moving direction of the tail tip of the fish.

Figure 7-8 shows the snapshots of surface pressure difference Δp on the fish bodies in the school (a) $t = 0.50T$ and (b) $t = 0.92T$. The pressure difference is defined as $\Delta p = (p_{iFish} - p_{single})/0.5\rho U_\infty^2$, where p_{iFish} indicates the surface pressure on the *i*th fish in the school and p_{single} denotes the pressure of the single fish. In Figs. 7-8(a) and 7-8(b), the ventral part of fish 1 and the abdomen part of fish 2 both experience negative surface pressure difference with higher magnitude, which is caused by the high velocity between the two fish. The high Δp on the fish trunk implies a higher drag generated.

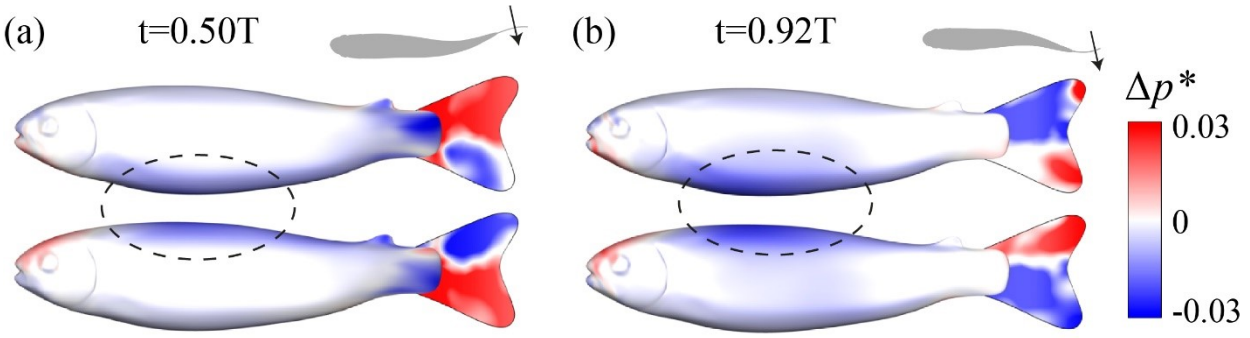

Figure 7-8. Surface pressure difference Δp_i of individual fish in the $H = 0.25L$ tip-to-tip school at (a) $t = 0.50T$ and (b) $t = 0.92T$.

7.3.2 Effect of Phase Difference in a Tip-to-Tip Fish School

The effects of phase difference on the hydrodynamic interactions in the tip-to-tip schools are investigated in this section. In this section, the vertical spacing between the two individuals is fixed at 0.25L, the phase of fish 1 keeps at 0° and the phase of fish 2 changes from 0° to 360°. The phase difference of the schools is thus defined as $\varphi = \varphi_2 - \varphi_1$. Figure 7-9 presents the normalized hydrodynamic performance of each fish in the schools as a function of the phase difference.

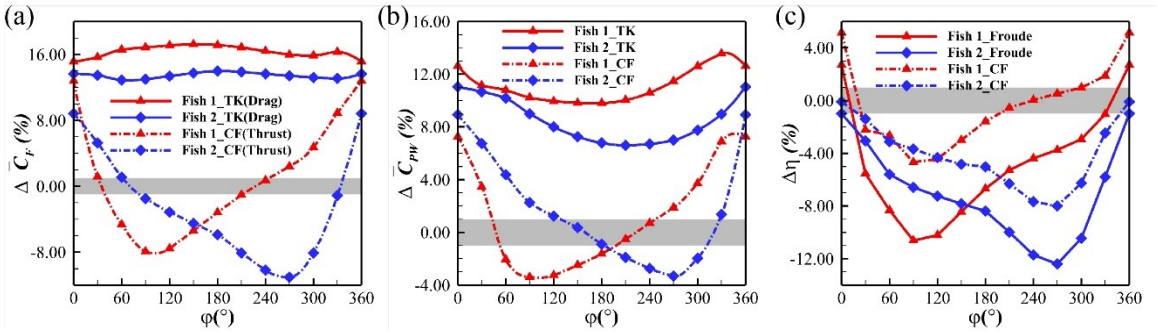

Figure 7-9. Hydrodynamic performance of individuals varying with the phase difference in the tip-to-tip schools: (a) normalized cycle-averaged thrust and drag coefficients, (b) normalized cycle-averaged power coefficients and (c) Froude and caudal fin propulsive efficiencies.

In Fig. 7-9(a), the drag on the trunk of fish 1 and 2 varies slightly as the phase difference increases. Comparing to a single fish, the drag of both fish increases by at least 13%, no matter what the phase difference is. In addition, the power consumed by the trunk increases by more than 6.5% for both fish as the phase difference varies, as shown in Fig. 7-9(b). It denotes that in a tip-to-tip school, varying the phase difference does not help reduce the drag and power on the trunks. However, the thrust production and power of the caudal fin are very sensitive to the variation of the phase difference. When fish 1 and 2 are in phase, the thrust production for fish 1 and 2 is improved by 12.8% and 8.8%, respectively, with a cost of consuming more power. As the phase difference increases, the thrust production and power consumption on the caudal fins of fish 1 and 2 present a U-shape curve, but with the troughs at varied phase differences. At $\varphi = 90°$, the thrust production of fish 1 reduces by 7.9% with consuming the smallest power, 3.4% less than a single fish, while for fish 2, the troughs of thrust production and power of the caudal fin reaches at $\varphi = 270°$ with thrust reduced by 11% and power decreased by 3.3%. The Froude efficiency and the caudal fin propulsive efficiency decrease and follow a similar trend as the thrust. In Fig. 7-9(c), the Froude efficiency and the caudal fin efficiency of fish 1 increase by up to 2.7% and 5.1%,

respectively, while the efficiencies of fish 2 show little change. When increasing the phase difference, η and η_{CF} of fish 1 and 2 both decrease. It can be concluded the synchronized tip-to-tip school ($\varphi = 0°$) obtains more hydrodynamic benefits than out-of-phase schools, although the phase difference might reduce the power consumption of caudal fin. It is because the thrust augmentation of the caudal fins in the synchronized tip-to-tip schools stems from the enhanced flow at the center of the school, while in the out-of-phase schools, the enhanced flow is jeopardized.

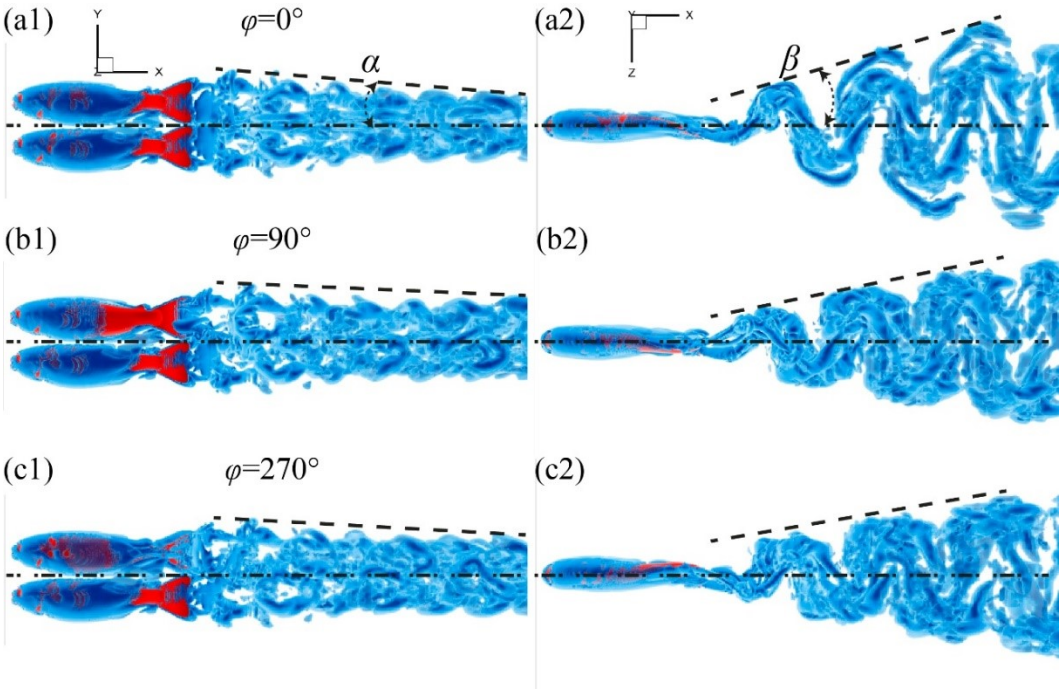

Figure 7-10. Three-dimensional vortex structures from the side view (a1-c1) and the top view (a2-c2) of schools at the phase difference of $\varphi = 0°$, $\varphi = 90°$ and $\varphi = 270°$ at $t = 5.0T$. The wake structures are visualized by the iso-surface of $Q = 5$.

Figure 7-10 compares the three-dimensional vortex structures of schools at varied phase differences, $\varphi = 0°$, $\varphi = 90°$ and $\varphi = 270°$, at $t = 5.0T$ from the side and top views. The interactions between shedding vortex rings in the out-of-phase schools become more complicated and chaotic. The vortex rings merge and tangle with their neighboring vortex rings and deform

complexly. To measure the differences in the vortex wakes, two angles are defined: narrowing angle α representing the extent of the downstream wake narrowing in the vertical direction, and expansion angle β indicating the extent of the wake expansion in the lateral direction. Larger narrowing angle and smaller extension angle denote that the flow is enhanced in the swimming direction and concentrates to the center, avoiding energy loss through wake expansion in the other directions. In Fig. 7-10, the narrowing angle and expansion angle of the in-phase school are both larger than those of the out-of-phase schools. According to performance results, we can conclude that the narrowing process significantly contributes to the thrust enhancement even though wake expansion in the undulating direction may be large.

Figure 7-11 compares the contour plots of vorticity ω_x and normalized lateral velocity w^* on the slices cutting through the caudal fins in the $\varphi = 0°$ and $\varphi = 90°$ fish schools. The position of the slices is close to the tail-tip of the caudal fins, as shown in Fig. 7-7. In the in-phase school ($\varphi = 0°$), the thrust peaks of the two fish are both around $t = 0.25T$, while in the $\varphi = 90°$ school, the thrust peak of fish 2 is shifted by $0.25T$ due to the phase difference, compared to fish 1. The contours plots at $t = 0.50T$ are thus also shown for the $\varphi = 90°$ school.

In both schools, fish 1 has the same undulating kinematics and achieves the thrust peak around $t = 0.25T$. In the in-phase school, the flow velocity between the two fins is enhanced by the narrow spacing. Because the flow between the fins directs the direction opposite to the moving direction of the fins, the effective flow velocity for the fins is improved, resulting in a stronger leading-edge vortex generated on the upper side of the caudal fin of fish 1. However, in the $\varphi = 90°$ school, the positive leading vortex generated on the caudal fin of fish 2 induces a flow that directs to the negative *z*-axis around the upper side leading edge of the caudal fin of fish 1, reducing

the effective velocity for the caudal fin, as shown in Fig. 7-11(b2). This diminishes the strength of the leading-edge vortex LEV_3 and reduce thrust production.

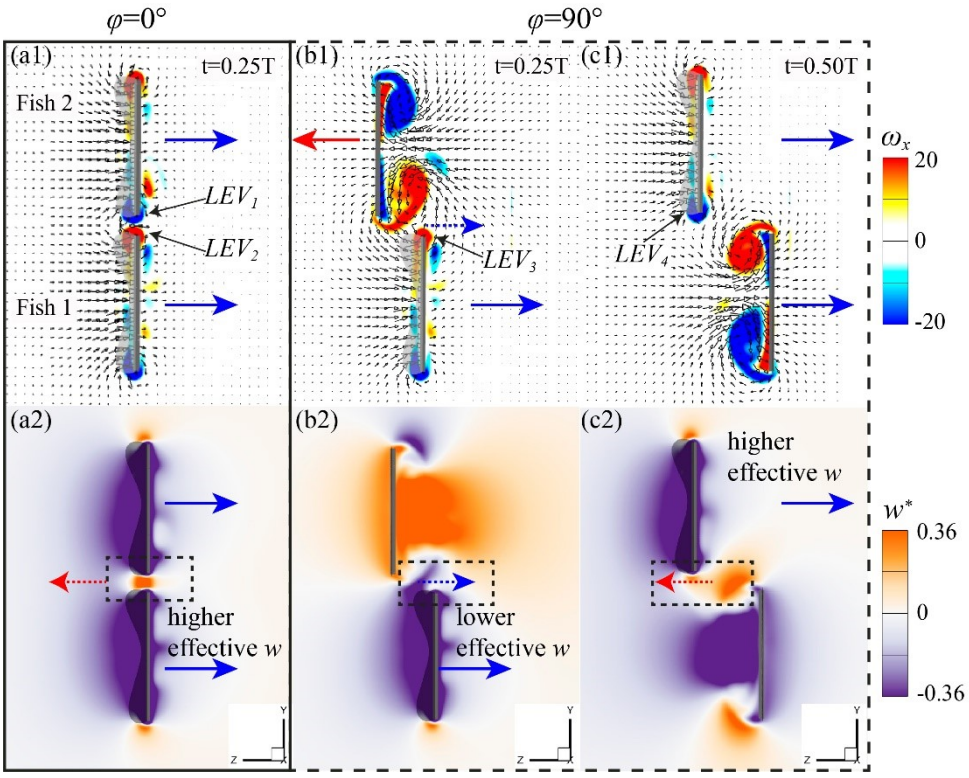

Figure 7-11. Contour plots of vorticity ω_x (a1-c1) and normalized cross-streamwise velocity w^* (a2-c2) on a slice cutting through the caudal fins near the tail-tip in the $\varphi = 0°$ school at $t = 0.25T$ and the $\varphi = 90°$ school at $t = 0.25T$ and $t = 0.50T$. The red and blue arrows with solid lines denote the moving direction of the caudal fin. The arrows with the dashed line indicate the direction of the flow between the caudal fins.

Due to the phase difference, the motion of fish 2 in the $\varphi = 90°$ school is behind that of fish 2 in the in-phase school for a time interval of $0.25T$. Hence, we compare the flow around the caudal fin of fish 2 in the $\varphi = 90°$ school at $t = 0.50T$ with that of fish 2 in the in-phase school at $t = 0.25T$. Although the positive vortex generated by the caudal fin of fish 1 induces a flow with a velocity that is opposite to the moving direction of the caudal fin of fish 2 in the $\varphi = 90°$

school, as shown in Fig. 7-11(c2), the amplitude of the induced flow velocity is lower than that in the in-phase school. Thus, the strength of the leading vortex LEV_4 is less than that of LEV_1, and a lower thrust is generated by fish 2 in the $\varphi = 90°$ school than in the in-phase school.

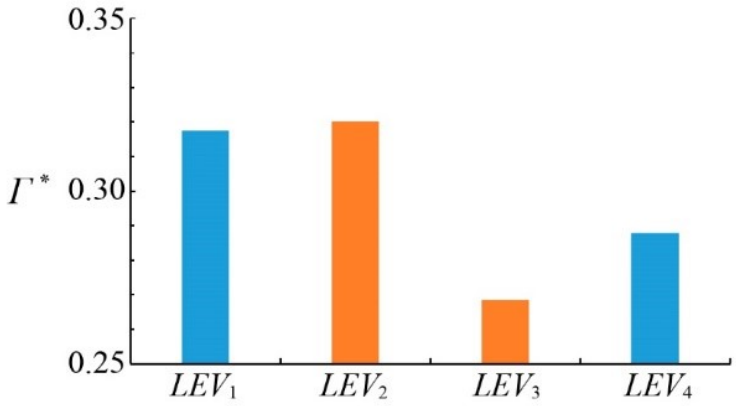

Figure 7-12. Normalized circulation of leading-edge vortices. The colors indicate the directions of these vortices, blue represents the clockwise vortex, and orange denotes the counterclockwise vortex.

The circulation of the leading-edge vortex is calculated and normalized as follows,

$$\Gamma^* = \left|\frac{\Gamma}{U_\infty c}\right| = \left|\iint_{A_\Gamma} \omega_z \cdot dA_\Gamma / U_\infty c\right|, \tag{7-3}$$

where A_Γ is region enclosing vorticity above or below the threshold value, c is chord length of the caudal fin. The quantitative results presented in Fig. 7-12 validate our flow analysis. The leading-edge vortices LEV_1 and LEV_2 are stronger than LEV_3 and LEV_4 due to the higher effective velocity. Additionally, LEV_4 has a larger circulation than LEV_3 because the vortex-induced flow increases the effect velocity for fish 2 in the school of $\varphi = 90°$. Thus, fish 2 obtains a higher thrust production than fish 1 in the $\varphi = 90°$ school, as shown in Fig. 7-9(a).

To further validate our analyses and conclusions, the surface pressure on the caudal fins of each fish is illustrated in Fig. 7-13. In comparison, the high-pressure zone on the bottom side of the caudal fin of fish 2 is larger in the $\varphi = 0°$ school than in the $\varphi = 90°$ school, which implies a higher thrust generated by fish 2 in the in-phase school ($\varphi = 0°$). Similarly, fish 1 has a larger high-pressure zone in the in-phase school than the out-of-phase school ($\varphi = 90°$). In addition, the high-pressure zone on the caudal fin of fish 2 is larger than that of fish 1 in the $\varphi = 90°$ school. Thus, according to the high-pressure distribution on the caudal fin surface, fish 2 generates a higher thrust than fish 1 in the out-of-phase school, and fish in the in-phase school has a higher thrust production than fish in the out-of-phase school.

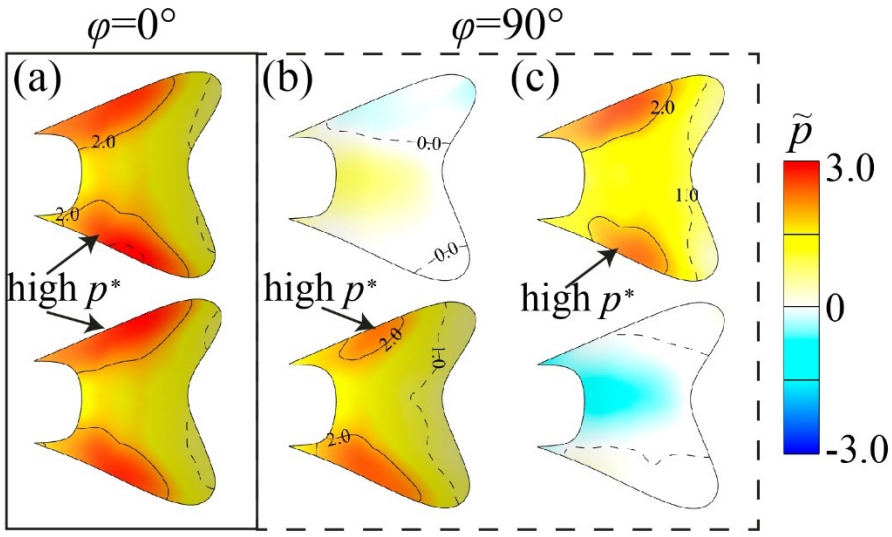

Figure 7-13. Surface pressure on the caudal fins in the $\varphi = 0°$ school at $t = 0.25T$ (a) and the $\varphi = 90°$ school at $t = 0.25T$ (b) and $t = 0.50T$ (c).

7.3.3 Effect of Vertical Distance between Oscillating Panels in a Tip-to-Tip Configuration

This section examines the thrust enhancement mechanism by using the trapezoidal panels arranged in the tip-to-tip configuration. The aspect ratio of the trapezoidal panels is $AR_{panel} = 1.21$, which is close to that of the trout model used in the previous sections, $AR_{trout} = 1.33$. To mimic the

propulsion of fish, the pitching-heaving motion is employed. The associated Strouhal number is 0.39, and the Reynolds number is chosen at $Re = 600$ at which the flow phenomena are similar to the real fish swimming and the vortex structures are more neat and coherent.

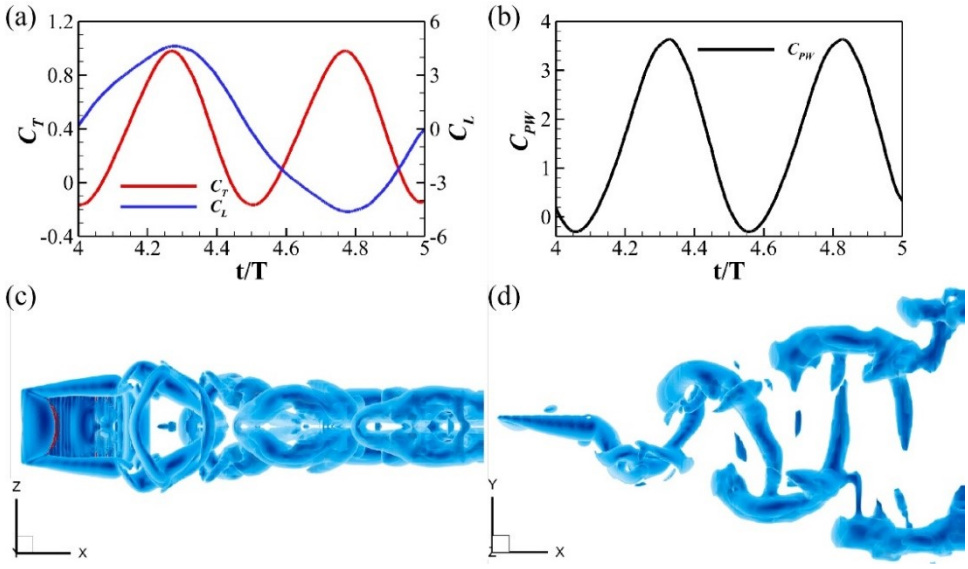

Figure 7-14. Time histories of (a) thrust and lift coefficients and (b) power coefficient of the single panel during one oscillating cycle. Three-dimensional vortex structures generated by the panel at $t = 5.0T$ from (c) the side and (d) top views. The wake structures are visualized by the iso-surface of $Q = 20$.

The time histories of thrust, lift power coefficients of a single pitching-heaving panel during one cycle are displayed in Figs. 7-14(a) and 7-14(b). The thrust and power curve show two peaks and two sinusoidal-form-like cycles, while the lift curve presents one peak and an approximate sinusoidal-form-like shape during one oscillating cycle. The time-averaged thrust $\overline{C_T}$ is 0.39, the mean power $\overline{C_{PW}}$ is 1.6 and the associated propulsive efficiency η is 0.246. The three-dimensional vortex structures at $t = 5.0T$ are shown in Figs. 7-14(c) and 7-14(d) from the side and top views, respectively. The two rows of linked vortex rings generated by the panel are similar to the wake produced by a single fish in Fig. 6-6.

Besides, the mean flow of the single panel is provided in Fig. 7-15. The mean flow is visualized by the normalized velocity iso-surfaces. The iso-surface of $\overline{U}/U_\infty = 0.94$ is in blue to denote low velocity and the iso-surface of $\overline{U}/U_\infty = 1.10$ is in orange representing high velocity. The mean flow iso-surfaces are presented from the top and side views. The mean flow contour plots on the horizontal and vertical slices are also shown in Fig. 7-15. In Figs. 7-15(a) and 7-15(b), the bifurcated jets are generated behind the panel, corresponding to the two rows of vortex rings. The low-velocity regions appear at the sides of bifurcated jets. In addition, the wake is narrowed in the vertical direction, as shown in Figs. 7-15(c) and 7-15(d).

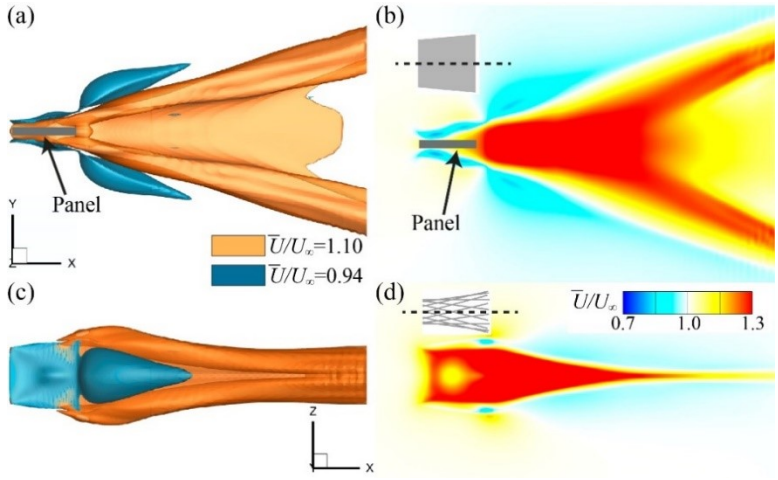

Figure 7-15. Mean flow iso-surfaces for a pitching-heaving single panel from (a) the top and (c) side views, and contour plots of mean flow on the (b) horizontal and (d) vertical slices.

Next, the effects of vertical distance H' on the hydrodynamic interactions between two pitching-heaving panels arranged in the tip-to-tip configurations are investigated. Figure 7-16 presents the normalized hydrodynamic performance of the panels, compared to a single panel, in the tip-to-tip configurations as functions of the vertical spacing. Because the two panels have the same performance, only the $\Delta\overline{C_T}$, $\Delta\overline{C_{PW}}$ and $\Delta\eta$ of one panel are presented. When $H' = 0.1$, the thrust production of the panels in the tip-to-tip arrangement increases by 14.2% compared to a

single panel. Meanwhile, 17.9% more power is needed by each panel in the configuration, which reduces the propulsive efficiency by 3.1%. Then, as the vertical distance H' increases, the thrust and power monotonically decrease. The normalized propulsive efficiency curve shows a V-shape and $\Delta\eta < 0$ at any vertical distance. The effects of the vertical distance on the performance of the panels are similar to those in the tip-to-tip fish schools.

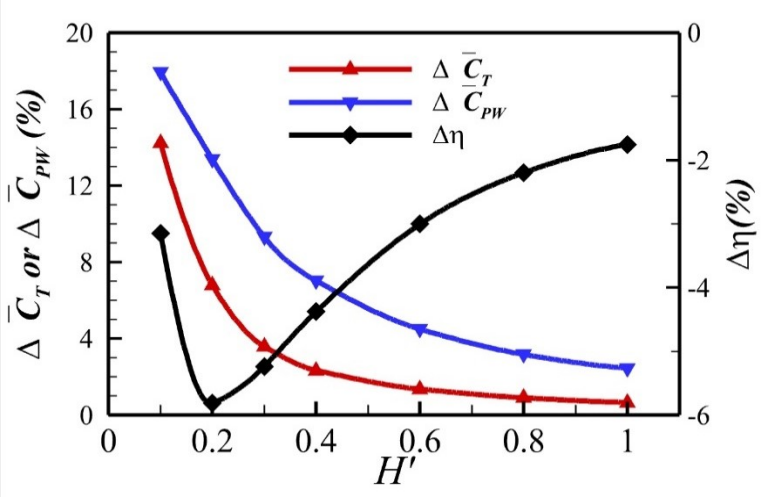

Figure 7-16. Propulsive performance of panels in a tip-to-tip configuration, including the normalized thrust coefficient $\Delta\overline{C_T}$, power coefficient $\Delta\overline{C_{PW}}$ and efficiency $\Delta\eta$.

Figure 7-17 shows the snapshots of three-dimensional vortex structures of the vertically arranged pitching-heaving panels with a distance of $H' = 0.1$ at $t = 0.08T$, $t = 0.33T$, $t = 0.58T$ and $t = 0.83T$ from the side (a1-d1) and top (a2-d2) views. The vortex rings shed by the panels are more coherent and neater than the wake of the tip-to-tip fish school. This helps illustrate the vortex wake's evolution in the tip-to-tip configuration. The vortex rings shed by the panels merge, and larger vortex rings are formed downstream, for instance, the formed vortex ring marked by a red circle in Fig. 7-17(a). In Figs. 7-17(a1-d1), the new vortex ring bends and shrinks in the vertical direction when being advected downstream. In the meantime, it gradually expands in the

streamwise direction, as shown in Figs. 7-17(a2)-(d2). The narrowing in the vertical direction contributes to the thrust enhancement.

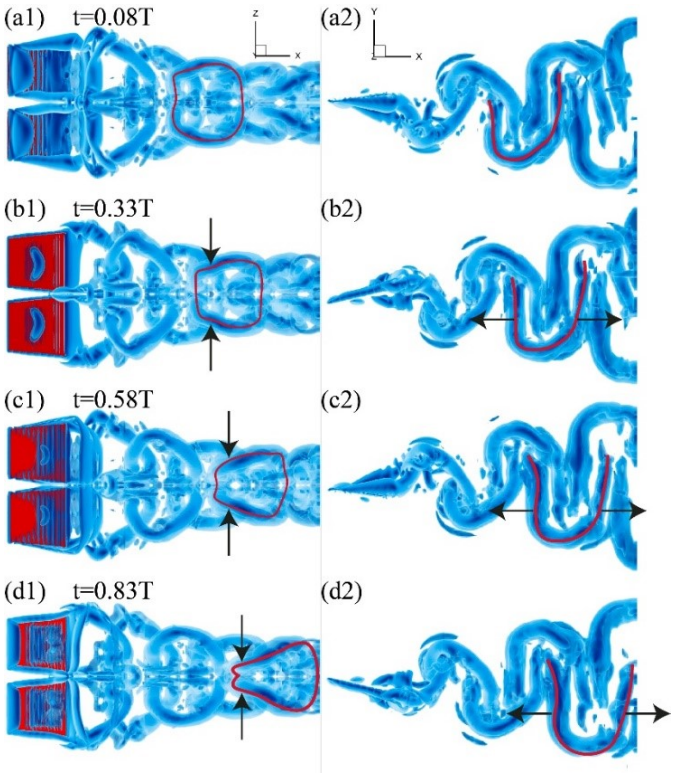

Figure 7-17. Three-dimensional wake structures of the panels in the tip-to-tip configuration panels at $t = 0.08T$, $t = 0.33T$, $t = 0.58T$ and $t = 0.83T$ from the side (a1-d1) and top (a2-d2) views.

The contour plots of the vorticity ω_x and normalized lateral velocity $v^* = v/U_\infty$ on a slice vertically cutting through the panels and the low-pressure iso-surfaces are plotted in Fig. 7-18 at $t = 0.08T$ and $t = 0.33T$. The red and blue arrows with solid lines denote the moving direction of the panels. The arrows with the dashed line indicate the direction of the flow between the panels. Due to the symmetry of the oscillating motion, only two times in a half cycle are shown here. The pressure coefficient is defined as $p^* = p/0.5\rho U_\infty^2$, where p is the gauge pressure. In Fig. 7-18(a3) and 7-18(b3), the transparent outer shell is visualized by the pressure iso-surface $p^* = -0.44$, and the inner core represents the pressure iso-surface of $p^* = -0.89$. At $t = 0.08T$, when the panel

moves to the right side, stronger leading-edge vortices generated at the center are shed at the left side of the panels. Correspondingly, a jet-like flow is left behind the panels. The low-pressure regions on the leading edges connect to the downstream low-pressure rings which are related to the vortex rings. When $t = 0.33T$, strong leading-edge vortices are at the center and the higher velocity opposite to the moving direction contributes to the higher thrust generation. In addition, a connected low-pressure region is generated on the trailing edges of the panels and a low-pressure ring is formed and advected downstream. The strong and coherent low-pressure rings are correlated to high thrust production.

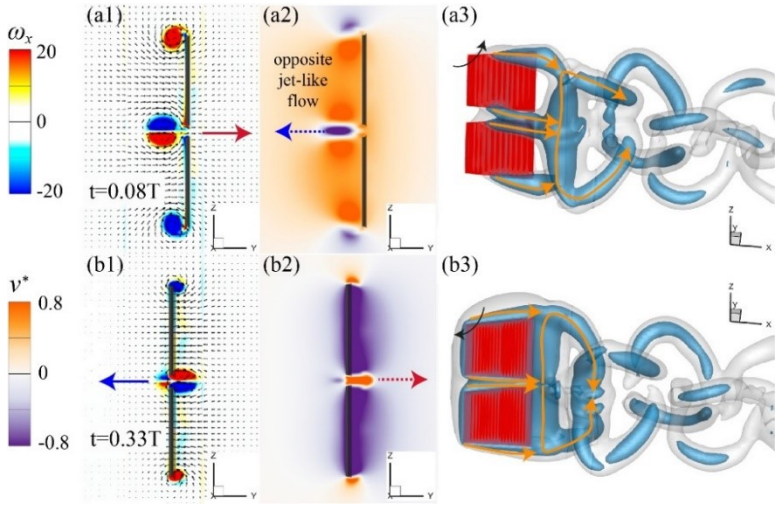

Figure 7-18. Contour plots of vorticity ω_x (a1-b1) and normalized lateral velocity v^* (a2-c2) on a slice cutting through the panels at $t = 0.08T$ and $t = 0.33T$. (c1-c2) Iso-surfaces of pressure coefficient p^*. The transparent outer shell is visualized by $p^* = -0.44$ and the inner core by $p^* = -0.89$.

The mean flow iso-surfaces are shown in Fig. 7-19 from the top (a1) and side view (b1). Also, the contour plots of mean flow are shown on the horizontal and vertical slices cutting through the center planes of the panels, as shown in Fig. 7-19(a2) and 7-19(b2). The mean flow of the

panels is similar to that of the single panel but with larger low-velocity regions. From the side view [Fig. 7-19(b1)] and the vertical slice [Fig. 7-19(b2)], the flow is compressed in the vertical direction, which is related to the high thrust production.

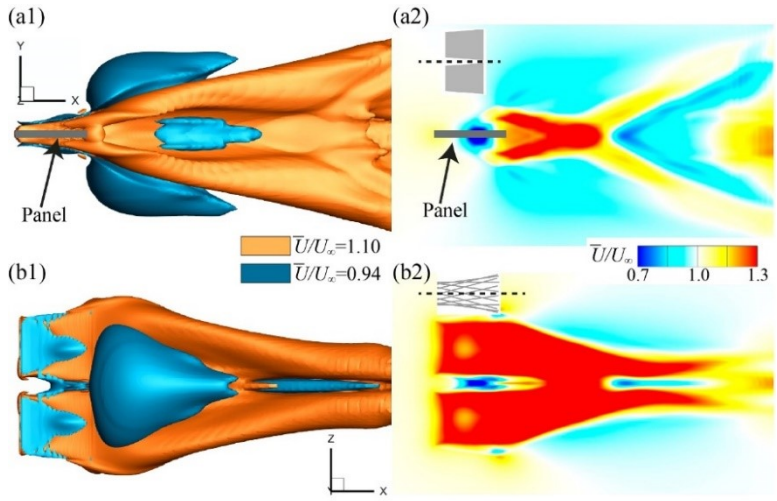

Figure 7-19. Mean flow iso-surfaces for the panels in the tip-to-tip configurations from (a) the top view and (c) the side view, and contour plots of mean streamwise velocity on (b) a horizontal slice and (d) a vertical slice.

7.3.4 Effect of Phase Difference between Oscillating Panels in a Tip-to-Tip Configuration

The phase difference effects on the hydrodynamic interactions between the panels are investigated in this section. The panels are arranged in a tip-to-tip configuration with a vertical distance of $H' = 0.1$, the phase of panel 1 maintains at 0°, and the phase of panel 2 changes from 0° to 360°. The normalized propulsive performance of the panels is illustrated in Fig. 7-20. In Fig. 7-20, the trust curves show a U-shape for panel 1, panel 2 and the averaged value of the configuration. The variation of the power presents a similar trend. It implies when there is a phase difference, the thrust production of the panels decreases with consuming less power. The variations of the thrust and power follow a U-shaped curve as the phase difference increases. In the meantime, the

propulsive efficiencies of the individuals display an approximate sinusoidal-form-like wave as the phase difference increases, while the averaged efficiency presents a U-shaped curve.

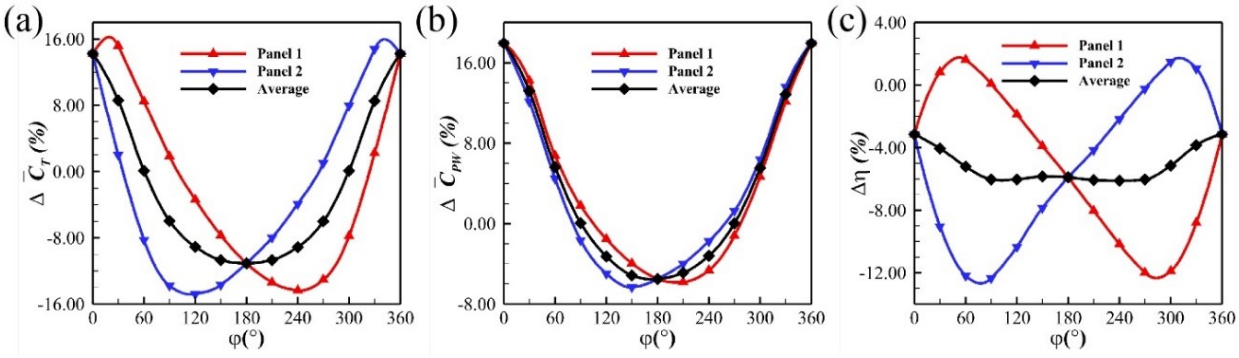

Figure 7-20. Performance of the panels in a tip-to-tip configuration varying with the phase difference.

In Fig. 7-20, the averaged thrust reached the trough at $\varphi = 180°$ and is 11.1% lower than a single panel. Also, the configuration has the lowest propulsive efficiency, 6% lower than a single panel. Thus, the configuration at a phase difference of $\varphi = 180°$ is chosen to compare with the synchronized configuration ($\varphi = 180°$). Figure 7-21 compares the three-dimensional vortex structures of the synchronized panels and the panels at a phase difference of $\varphi = 180°$ at $t = 5.0T$. The extension angle β and the narrowing angle α in the synchronized configuration are larger than those in the configuration of $\varphi = 180°$. It suggests that the wake of synchronized configuration is narrower in the vertical direction than that of the configuration of $\varphi = 180°$ but wider in the horizontal plane. This validates our conclusion in the previous section that the shape of the wake in the vertical plane contributes more to thrust production.

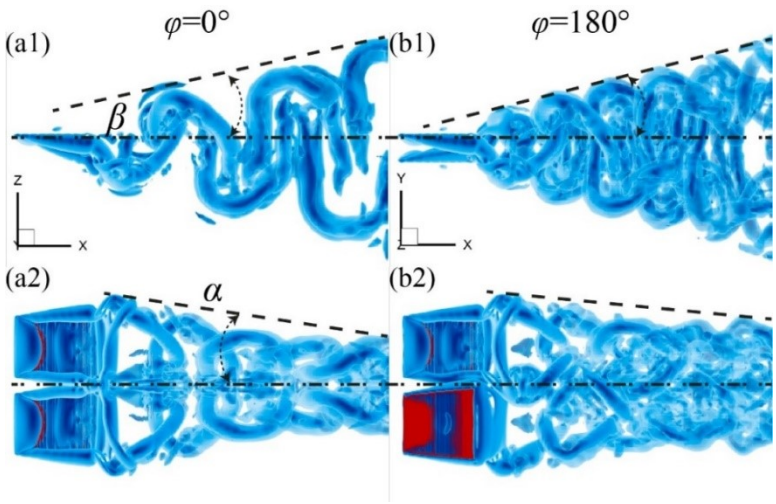

Figure 7-21. Vortex structures of the in-phase ($\varphi = 0°$) (a1-a2) and anti-phase ($\varphi = 180°$) configurations (b1-b2).

Figure 7-22 compares the contours plots of vorticity ω_x and normalized velocity v^* on a vertical slice and the low-pressure iso-surfaces of the in-phase ($\varphi = 0°$) and anti-phase ($\varphi = 180°$) configuration at $t = 0.25T$. The red and blue arrows with solid lines denote the moving direction of the panels, and the arrows with the dashed line indicate the direction of the flow between the panels. Stronger leading-edge vortices are generated at the center of the in-phase configuration, and the flow between the panels is enhanced. Also, the connected low-pressure is generated on the trailing edges of the panels, and a strong and coherent ring of low-pressure is formed, which benefits the flow advection. Thus, a higher thrust is generated by the in-phase configuration.

The mean flow of the anti-phase configuration ($\varphi = 180°$) is shown in Fig. 7-23 from the top and side views. Also, the contours of the streamwise mean velocity on slices in the horizontal and vertical planes are presented in Fig. 7-23. Compared with the mean flow of the in-phase school ($\varphi = 0°$), the flow in the vertical direction is wider, implying the thrust production in the anti-phase school is small.

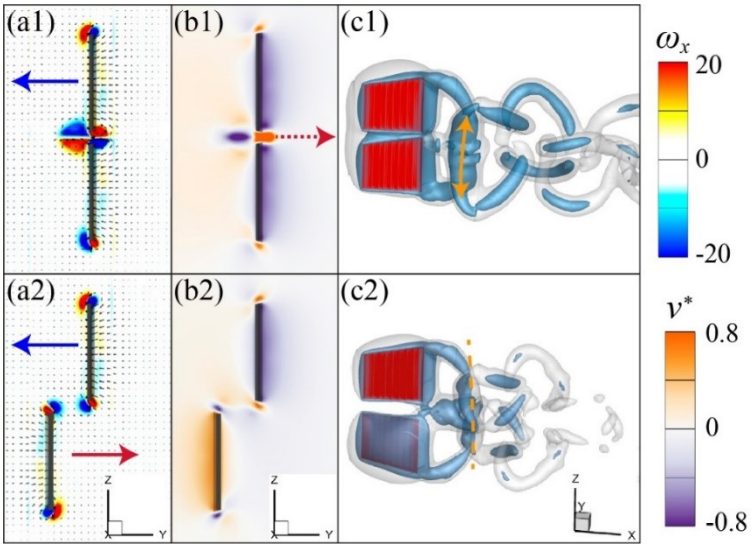

Figure 7-22. Contour plots of vorticity ω_x (a1-a2) and normalized lateral velocity v^* (b1-b2) on a vertical slice in the in-phase ($\varphi = 0°$) and anti-phase ($\varphi = 180°$) configuration at $t = 0.25T$. (c1-c2) Iso-surfaces of pressure coefficient p^*. The transparent outer shell is visualized by $p^* = -0.44$ and the inner core by $p^* = -0.89$.

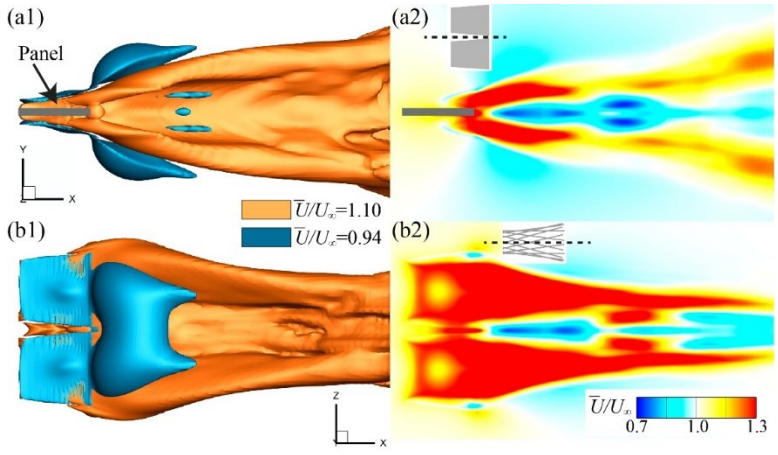

Figure 7-23. Mean flow iso-surfaces for the panels in the anti-phase configuration ($\varphi = 180°$) from (a1) the top view and (b1) the side view, and contour plots of mean streamwise velocity on (a2) a horizontal slice and (b2) a vertical slice.

7.4 Chapter Summary

Hydrodynamic interactions in the tip-to-tip fish schools have been comprehensively and systematically examined using an immersed-boundary-method-based in-house solver. The biological realistic fish model was reconstructed from live trout experiments and is imposed on a traveling wave kinematics to mimic fish swimming. The high-fidelity simulations of flow past the two-fish schools provide hydrodynamic performance and detailed flow information for quantitative analysis. In this section, the vertical distance is first changed from 0.25BL to 0.65BL to explore its effects on the hydrodynamic interactions. Results show that at a small vertical distance, the thrust production of both fish is significantly enhanced with the cost of consuming more power. In particular, at $H = 0.25L$, $\overline{C_{1T}}$ and $\overline{C_{2T}}$ increases by 12.8% and 8.8%, respectively. When $H \leq 0.4L$, the thrust and drag of individuals increase rapidly with the decreasing vertical distance. In the meantime, the power on the trunk and caudal fin for each fish also rises with a large growth rate as the vertical distance decreases. The Froude efficiency and caudal fin efficiency of both fish are lower than that of a single fish except for $H = 0.25L$ at which the caudal fin efficiency of fish 1 η_{1CF} increased by 5.1%.

The phase difference of the schools at $H = 0.25L$ varies from 0° to 360° to examine its effects on the hydrodynamic interactions. Results suggest that the performance of the trunk for both fish is independent of the phase difference and is penalized by the destructive interactions at a close distance. It is because, with a small distance, the flow between the trunks is speeded up, increasing the drag and power. Nevertheless, the caudal fin's performance strongly depends on the phase difference. The results indicate that the out-of-phase schools have lower thrust production than the in-phase school, while they can save more energy. Flow analyses show that the thrust enhancement in the in-phase school stems from the high momentum flow in the cross-streamwise

direction between the caudal fins. It enhances and stabilizes the leading-edge vortices at the center of the school, resulting in higher thrust production. However, in out-of-phase schools, the mutually beneficial scenario is destroyed, and the relative motion between the two caudal fins results in that one experiencing a higher effective cross-streamwise velocity and the other with a lower effective velocity for a certain period during one cycle. This leads to the difference in the thrust production between fish in out-of-phase schools. Besides, the higher effective velocity in the out-of-phase school is lower than the effective velocity of the flow between the caudal fins in the in-phase school, which illustrates why fish have lower thrust production in out-of-phase schools than in the in-phase school. In addition, the thrust enhancement is related to a narrowing process of the wake in the vertical direction in in-phase schools. By comparison, we conclude that the thrust production is more sensitive to the wake variation in the vertical direction than in the lateral direction.

Finally, we tested the tip-to-tip schools' thrust enhancement mechanism using two heaving-pitching panels. The simulation results confirm our conclusions made for the tip-to-tip fish schools. Additionally, with a lower Reynolds number, cleaner vortex structures, pressure contours, and mean flow structures are provided to support the analyses.

8 Concluding Remarks

The works presented in the current dissertation have investigated hydrodynamic performance, wake dynamics and the associated hydrodynamic interactions in two-dimensional and three-dimensional fish schools using high-fidelity direct numerical simulations. In the current studies, we ought to identify performance enhancement mechanisms, clarify the effects of formation and synchronization on hydrodynamic interactions in a fish school, advance the understanding of the role of hydrodynamics in fish schooling, offer new insight into the design and control of efficient bio-inspired underwater robotic swarms.

8.1 Summary of Contribution

In Chapter 2, a narrow-band level-set-based immersed boundary method (NBLS-IBM) has been developed for boundary reconstructions by calculating the level-set value of points in the immediate vicinity of the solid boundary and propagating these level-set values in a narrow band. Compared with the direct searching method, the NBLS-IBM reduces the computational cost for reconstruction from $O((L_D/\Delta x)^5)$ to $O(k(L_D/\Delta x)^2)$, where L_D is the characteristic length and Δx is the minimum mesh size. Besides, we also develop a tree-topological local mesh refinement (TLMR) method coupling with parallel computing on Cartesian grids. These advanced numerical methods enable a fast and high-fidelity simulation of an incompressible flow past multiple moving objects with complex geometry.

In Chapter 3, the effects of spatial arrangement on the hydrodynamic performance and wake structures of a diamond-shaped fish school were numerically studied at an intermediate Reynolds number ($Re = 1000$). The fish is modeled by a NACA foil imposed on a traveling wave kinematics. Compared with a sparse school, lateral fish diagonally located in a dense school can

obtain much higher thrust and swimming efficiency than a solitary fish. In particular, the thrust production can be enhanced by up to 77%, and the swimming efficiency is improved by up to 30%. The enhancement stems from the trailing fish that works like a wavy wall to the lateral fish in a dense school, and this wall effect is enhanced when the lateral fish approach the trailing fish. The vortices shed by lateral fish start pairing, and the vortex wake transfers from 2S to 2P pattern when the lateral spacing is less than 0.6BL. Correspondingly, angled momentum jets are formed behind the lateral fish. The leading produces 30% more thrust fish in a diamond-shaped dense school than in the triangular school when the lateral spacing is 0.4BL. The improvement identifies the block effect of the trailing fish in a dense school. Flow analyses show that the trailing fish blocks the flow drained by the leading fish, generating a high-pressure zone right behind the leading fish. Then the thrust production of the leading fish is enhanced. This work is the first to quantitatively defined the dense fish school based on the variation of performance and flow phenomena and reveals the wall effect and block effect in a dense school, which will provide new insights into the physical mechanisms of fish schooling.

Chapter 4 and Chapter 5 investigate the synchronization effect on the hydrodynamic performance and wake dynamics of high-density fish schools from the phase difference and tail-beat frequency, respectively, based on the work in Chapter 3. In Chapter 4, the tail-beat phase difference between the trailing fish and other individuals changes from 0° to 360°. Simulation results show that the thrust of the trailing fish increases by 108% in the in-phase school, and the efficiency is improved by 58% when the phase difference is 90°. Detailed quantitative analyses accurately linked the performance and flow of the trailing fish. It shows that the posterior part of the trialing fish, which is outside of the channel formed by the lateral fish, captures the energy from the vortex flow generated by the lateral fish to increase thurst or reduce the power by setting

the approximate phase difference. Also, the secondary induced vortex is observed on the body of trailing fish when the vortex-body interaction happens. The anterior part can generate a high suction thrust through body-body interaction with the channel, and the interaction is controlled by the phase difference. In Chapter 5, results show that a synchronized school, where all individual fish have the same frequency, achieves optimal swimming efficiency, improved by 32% over a single fish, at $f = 0.83$. And in the asynchronized schools, where only the frequency of the tailing fish changes, the trialing obtains the optimal swimming efficiency, 74% higher than a single fish, at $f = 0.71$. The results support that fish in a school can use less energy, i.e., swim at a lower frequency to reach steady swimming and high swimming efficiency. Finally, the wake patterns of the density fish schools have been quantitatively analyzed both in Chapter 4 and Chater 5. The results show that the wake pattern strongly depends on the phase difference and tail-beat frequency. The vortex wake of the trailing fish varies from the rBvK pattern to the rBvK pattern as the phase difference increases, and some parameters characterizing 2P wakes of the lateral fish, such as rotation angle and advection velocity, vary with phase difference due to the interactions with the trailing fish and its wake. When varying the tail-beat frequency, according to the value of net streamwise momentum Δp_x relative to the incoming flow, the mean flow patterns are categorized as the drag wake ($\Delta p_x < 0$), the momentum less wake (($\Delta p_x = 0$), and the jet wake (($\Delta p_x > 0$). Besides, the variation of the momentum entrainment ratio γ implies the strong correlation between the efficiency of fish school swimming and the wake-wake interaction. Both in the synchronized and asynchronized schools, the optimal efficiency is accompanied by stable 2P wakes behind the lateral fish and a 2S wake behind the trailing fish. To our knowledge, the works are the first to categorize the wake patterns of fish schools and bridge the gap between performance and wake patterns.

Chapter 6 investigated the effects of the spatial arrangement and phase difference on the hydrodynamic performance and wake structures of two-fish horizontal schools, including the in-line, side-by-side and staggered configurations, using high-fidelity three-dimensional numerical simulations. The biological fish model is reconstructed based on a real trout and is controlled by a traveling wave kinematics. In the in-line schools, results show that the thrust of the leading fish can be enhanced at a small streamwise distance S, and the Froude efficiency can be improved by up to 5%. The thrust enhancement originates from the blockage of the trailing fish, which generates a high-pressure region right behind the leading fish. Nevertheless, the following fish experiences an increased drag because the interaction with vortex rings shed by the leading fish increases the streamwise velocity around the body of the following fish. The destructive interaction can be weakened by adjusting the tail-beat phase of the following fish. In the side-by-side schools, around 6.8% power is saved for each fish when the lateral spacing is 0.25BL. Flow analyses illustrate the streamwise velocity of flow between the two caudal fins is reduced, inducing an earlier flow separation on the fin surfaces. Hence, the pressure around the surfaces is reduced, and less power is thus required for the prescribed motion of the caudal fin. In the case of out-of-phase side-by-side schools, the thrust of one fish can be enhanced through the passive energy capture mechanism and virtual wall effect, similar to the mechanisms in jellyfish swimming. Both in the in-line and side-by-side schools, the drag and power on the trunk of individual fish increase compared with a single fish, which, to some extent, counteracts the performance improvement of the caudal fins. In contrast, a drag reduction mechanism has been found in staggered schools. Performance results suggest that the drag of the following fish in a staggered school strongly depends on the streamwise distance S and is independent of the phase difference. The streamwise distance can be divided into two regimes: the drag reduction regime ($S \leq 0.95BL$) and the drag increasing regime ($S >$

$0.95BL$). When $S \leq 0.95BL$, the vortex rings located around the body of the following fish are inclined, and the clockwise rotating part of these vortex rings is closer to the following fish, reducing the streamwise velocity around the fish body. The drag of the following fish is thus reduced. When $S > 0.95BL$, the vortex rings are approximately parallel to the following fish and increase the streamwise velocity because these vortex rings move faster than the incoming flow. The drag of the following fish thus increases. In addition, the vortex rings can enhance the leading-edge vortex on the caudal fin of the following fish by increasing the effective cross-streamwise velocity and suppressing flow separation on the fin to improve thrust production. Changing distance and phase differences have the same effect on thrust enhancement. This chapter systematically studied hydrodynamic interactions in the horizontal schools and is the first to reveal the vortex-ring-induced drag reduction mechanism and point out the role of flow separation in power-saving and thrust enhancement mechanisms in fish schools by conducting detailed flow analyses.

Chapter 7 explored the effects of the vertical distance and phase difference on the hydrodynamic performance and vortex dynamics in a tip-to-tip two-fish school using three-dimensional numerical simulations. The fish model and undulating kinematics are the same as in Chapter 6. Performance results show that the thrust enhancement is significant, up to 12.8%, compared with a single fish, when the vertical distance H is small. As the vertical distance increases, the thrust enhancement rapidly weakens. In the meantime, the performance of the trunk is penalized for close vertical distance, i.e., the drag and power on the trunk increase at a small vertical distance, and this deconstructive interaction between the trunks is independent of the phase difference. Also, the study on the effects of phase difference confirms that the thrust enhancement in the in-phase schools stems from the high momentum flow in the cross-stream direction between

the caudal fins. Stronger leading-edge vortices are thus generated and stabilized at the center of the in-phase schools, increasing the thrust production. However, the enhancement will be diminished in out-of-phase schools. Besides, the vortex structures suggest that the thrust enhancement is related to a narrowing process of vortex wake in the vertical direction. The thrust enhancement mechanism is tested by simulating the flow past two heaving-pitching trapezoidal panels in a tip-to-tip configuration at a lower Reynolds number. Cleaner vortex structures, pressure contours and mean flows are provided to support the thrust enhancement mechanism. This study is the first to present the thrust enhancement mechanism in a tip-to-tip fish school.

8.2 Future Work

The works presented in this dissertation advance our understanding of hydrodynamic interactions in fish schools using 2D and 3D direct numerical simulations. Nevertheless, there is room for improvement and future work. The number of fish both in 2D and 3D schools is limited, but more is different. The hydrodynamic interactions in more complex school configurations involving more fish might offer new physical insights into this study. The investigation might help researchers determine the maximum range in which hydrodynamic interactions take effect and decide the school size that should be studied. Additionally, the effects of other parameters controlling the undulating kinematics on hydrodynamic interactions, such as wavelength and tail-tip undulating amplitude, should be examined.

In the current works, the swimming kinematics of fish is prescribed, and the fish are fixed in an oncoming flow. However, in nature, fish schooling is a dynamic process. To better present real-world fish schooling, two methods are proposed to extend the current research. First, the self-propelled fish model combined with closed-loop control or reinforcement learning methods can be used to investigate the dynamic response of individuals to hydrodynamic interactions. However,

the actuations and objectives set for the self-propelled model strongly depend on the existing knowledge. Also, the computational load for this method is heavy when involving more swimmers, especially for three-dimensional flows. Second, by using an integrated study combining high-speed photogrammetry of live fish experiments, high-fidelity 3D surface reconstruction, and direct numerical simulations, we ought to examine hydrodynamic interactions and identify fundamental physical mechanisms in a real-world fish school. In particular, high-fidelity computational fish models with swimming kinematics are reconstructed based on high-speed videos of live fish experiments. Simulations are then performed in the current immersed boundary-based flow solver to obtain hydrodynamic performance and flow information of the schools. Because of the randomness of swimming in a real fish school, massive experiments are required to be investigated. Hence, an integrated reconstruction platform can be developed by combining deep learning methods with the traditional image-guided reconstruction method to realize automatic, fast and accurate reconstruction.

Bibliography

[1] E. Shaw, Schooling fishes: the school, a truly egalitarian form of organization in which all members of the group are alike in influence, offers substantial benefits to its participants, American Scientist, 66 (1978) 166-175.

[2] V.E. Brock, R.H. Riffenburgh, Fish schooling: a possible factor in reducing predation, ICES Journal of Marine Science, 25 (1960) 307-317.

[3] J.J. Cech, P.B. Moyle, Fishes: an introduction to ichthyology, Pearson/B. Cummings2004.

[4] T.J. Pitcher, Functions of shoaling behaviour in teleosts, The behaviour of teleost fishes, Springer1986, pp. 294-337.

[5] D. Weihs, Hydromechanics of fish schooling, Nature, 241 (1973) 290-291.

[6] J. Zhu, C. White, D.K. Wainwright, V. Di Santo, G.V. Lauder, H. Bart-Smith, Tuna robotics: A high-frequency experimental platform exploring the performance space of swimming fishes, Science Robotics, 4 (2019) 2470-9476.

[7] C.H. White, G.V. Lauder, H. Bart-Smith, Tunabot flex: a tuna-inspired robot with body flexibility improves high-performance swimming, Bioinspiration & Biomimetics, 16 (2021) 026019.

[8] Q. Zhong, J. Zhu, F.E. Fish, S.J. Kerr, A.M. Downs, H. Bart-Smith, D.B. Quinn, Tunable stiffness enables fast and efficient swimming in fish-like robots, Science Robotics, 6 (2021) 2470-9476.

[9] T. Schmickl, R. Thenius, C. Moslinger, J. Timmis, A. Tyrrell, M. Read, J. Hilder, J. Halloy, A. Campo, C. Stefanini, CoCoRo--The self-aware underwater swarm, IEEE, 2011, pp. 120-126.

[10] N.E. Leonard, D.A. Paley, R.E. Davis, D.M. Fratantoni, F. Lekien, F. Zhang, Coordinated control of an underwater glider fleet in an adaptive ocean sampling field experiment in Monterey Bay, Journal of Field Robotics, 27 (2010) 718-740.

[11] J.S. Jaffe, P.J.S. Franks, P.L.D. Roberts, D. Mirza, C. Schurgers, R. Kastner, A. Boch, A swarm of autonomous miniature underwater robot drifters for exploring submesoscale ocean dynamics, Nature communications, 8 (2017) 1-8.

[12] F. Berlinger, M. Gauci, R. Nagpal, Implicit coordination for 3D underwater collective behaviors in a fish-inspired robot swarm, Science Robotics, 6 (2021) 2470-9476.

[13] J.M. Anderson, K. Streitlien, D.S. Barrett, M.S. Triantafyllou, Oscillating foils of high propulsive efficiency, Journal of Fluid mechanics, 360 (1998) 41-72.

[14] R. Godoy-Diana, C. Marais, J.-L. Aider, J.E. Wesfreid, A model for the symmetry breaking of the reverse Bénard–von Kármán vortex street produced by a flapping foil, Journal of Fluid Mechanics, 622 (2009) 23-32.

[15] D. Floryan, T. Van Buren, C.W. Rowley, A.J. Smits, Scaling the propulsive performance of heaving and pitching foils, Journal of Fluid Mechanics, 822 (2017) 386-397.

[16] D.J. Cleaver, Z. Wang, I. Gursul, Bifurcating flows of plunging aerofoils at high Strouhal numbers, Journal of Fluid Mechanics, 708 (2012) 349-376.

[17] T. Van Buren, D. Floryan, N. Wei, A.J. Smits, Flow speed has little impact on propulsive characteristics of oscillating foils, Physical Review Fluids, 3 (2018).

[18] G.S. Triantafyllou, M.S. Triantafyllou, M.A. Grosenbaugh, Optimal thrust development in oscillating foils with application to fish propulsion, Journal of Fluids and Structures, 7 (1993) 205-224.

[19] D.A. Read, F.S. Hover, M.S. Triantafyllou, Forces on oscillating foils for propulsion and maneuvering, Journal of Fluids and Structures, 17 (2003) 163-183.

[20] R. Godoy-Diana, J.-L. Aider, J.E. Wesfreid, Transitions in the wake of a flapping foil, Physical Review E, 77 (2008) 016308.

[21] T. Schnipper, A. Andersen, T. Bohr, Vortex wakes of a flapping foil, Journal of Fluid Mechanics, 633 (2009) 411-423.

[22] G.V. Lauder, E.D. Tytell, Hydrodynamics of undulatory propulsion, Fish physiology, 23 (2005) 425-468.

[23] U.K. Müller, B.L.E. Van Den Heuvel, E.J. Stamhuis, J.J. Videler, Fish foot prints: morphology and energetics of the wake behind a continuously swimming mullet (Chelon labrosus Risso), The Journal of experimental biology, 200 (1997) 2893-2906.

[24] C. Eloy, Optimal Strouhal number for swimming animals, Journal of Fluids and Structures, 30 (2012) 205-218.

[25] M. Sfakiotakis, D.M. Lane, J.B.C. Davies, Review of fish swimming modes for aquatic locomotion, IEEE Journal of oceanic engineering, 24 (1999) 237-252.

[26] A.J. Smits, Undulatory and oscillatory swimming, Journal of Fluid Mechanics, 874 (2019).

[27] V. Di Santo, E. Goerig, D.K. Wainwright, O. Akanyeti, J.C. Liao, T. Castro-Santos, G.V. Lauder, Convergence of undulatory swimming kinematics across a diversity of fishes, Proceedings of the National Academy of Sciences, 118 (2021) e2113206118.

[28] L.P. Hansen, B.J.A. Jonsson, Downstream migration of hatchery-reared smolts of Atlantic salmon (Salmo salar L.) in the River Imsa, Norway, Aquaculture, 45 (1985) 237-248.

[29] B.L. Partridge, J. Johansson, J. Kalish, The structure of schools of giant bluefin tuna in Cape Cod Bay, Environmental Biology of Fishes, 9 (1983) 253-262.

[30] G.V. Lauder, E.G. Drucker, Forces, fishes, and fluids: hydrodynamic mechanisms of aquatic locomotion, Physiology, 17 (2002) 235-240.

[31] P. Han, G.V. Lauder, H. Dong, Hydrodynamics of median-fin interactions in fish-like locomotion: Effects of fin shape and movement, Physics of Fluids, 32 (2020) 011902.

[32] D.S. Barrett, M.S. Triantafyllou, D.K.P. Yue, M.A. Grosenbaugh, M.J. Wolfgang, Drag reduction in fish-like locomotion, Journal of Fluid Mechanics, 392 (1999) 183-212.

[33] G. Liu, Y. Ren, H. Dong, O. Akanyeti, J.C. Liao, G.V. Lauder, Computational analysis of vortex dynamics and performance enhancement due to body–fin and fin–fin interactions in fish-like locomotion, Journal of Fluid Mechanics, 829 (2017) 65-88.

[34] C.K. Hemelrijk, D.A.P. Reid, H. Hildenbrandt, J.T. Padding, The increased efficiency of fish swimming in a school, Fish and Fisheries, 16 (2015) 511-521.

[35] M. Daghooghi, I. Borazjani, The hydrodynamic advantages of synchronized swimming in a rectangular pattern, Bioinspir Biomim, 10 (2015) 056018.

[36] B.L. Partridge, The structure and function of fish schools, Scientific american, 246 (1982) 114-123.

[37] B.M. Boschitsch, P.A. Dewey, A.J. Smits, Propulsive performance of unsteady tandem hydrofoils in an in-line configuration, Physics of Fluids, 26 (2014).

[38] I. Akhtar, R. Mittal, G.V. Lauder, E. Drucker, Hydrodynamics of a biologically inspired tandem flapping foil configuration, Theoretical and Computational Fluid Dynamics, 21 (2007) 155-170.

[39] G. Novati, S. Verma, D. Alexeev, D. Rossinelli, W.M. van Rees, P. Koumoutsakos, Synchronisation through learning for two self-propelled swimmers, Bioinspir Biomim, 12 (2017) 036001.

[40] G. Xu, W. Duan, W.J.P.o.F. Xu, The propulsion of two flapping foils with tandem configuration and vortex interactions, 29 (2017) 097102.

[41] G.-J. Dong, X.-Y. Lu, Characteristics of flow over traveling wavy foils in a side-by-side arrangement, Physics of Fluids, 19 (2007).

[42] P.A. Dewey, D.B. Quinn, B.M. Boschitsch, A.J. Smits, Propulsive performance of unsteady tandem hydrofoils in a side-by-side configuration, Physics of Fluids, 26 (2014).

[43] Y. Bao, D. Zhou, J. Tao, Z. Peng, H. Zhu, Z. Sun, H. Tong, Dynamic interference of two anti-phase flapping foils in side-by-side arrangement in an incompressible flow, Physics of Fluids, 29 (2017) 033601.

[44] G. Li, D. Kolomenskiy, H. Liu, B. Thiria, R. Godoy-Diana, On the energetics and stability of a minimal fish school, PLoS One, 14 (2019) e0215265.

[45] M. Kurt, A. Eslam Panah, K.W. Moored, Flow Interactions Between Low Aspect Ratio Hydrofoils in In-line and Staggered Arrangements, Biomimetics, 5 (2020) 13.

[46] Z.-R. Peng, H. Huang, X.-Y. Lu, Collective locomotion of two self-propelled flapping plates with different propulsive capacities, Physics of Fluids, 30 (2018).

[47] D. Jian, X.-m. Shao, Hydrodynamics in a diamond-shaped fish school, Journal of Hydrodynamics, Ser. B, 18 (2006) 438-442.

[48] S.-Y. Chen, Y.-H.J. Fei, Y.-C. Chen, K.-J. Chi, J.-T. Yang, The swimming patterns and energy-saving mechanism revealed from three fish in a school, Ocean Engineering, 122 (2016) 22-31.

[49] J.C. Liao, A review of fish swimming mechanics and behaviour in altered flows, Philos Trans R Soc Lond B Biol Sci, 362 (2007) 1973-1993.

[50] J.C. Liao, D.N. Beal, G.V. Lauder, M.S. Triantafyllou, Fish exploiting vortices decrease muscle activity, Science, 302 (2003) 1566-1569.

[51] J.C. Liao, D.N. Beal, G.V. Lauder, M.S. Triantafyllou, The Karman gait: novel body kinematics of rainbow trout swimming in a vortex street, J Exp Biol, 206 (2003) 1059-1073.

[52] T.M. Broering, Y. Lian, W. Henshaw, Numerical investigation of energy extraction in a tandem flapping wing configuration, AIAA journal, 50 (2012) 2295-2307.

[53] M. Kurt, K.W. Moored, Flow interactions of two-and three-dimensional networked bio-inspired control elements in an in-line arrangement, Bioinspiration & biomimetics, 13 (2018) 045002.

[54] R. Godoy-Diana, J. Vacher, V. Raspa, B. Thiria, On the Fluid Dynamical Effects of Synchronization in Side-by-Side Swimmers, Biomimetics (Basel), 4 (2019).

[55] L. Li, M. Nagy, J.M. Graving, J. Bak-Coleman, G. Xie, I.D. Couzin, Vortex phase matching as a strategy for schooling in robots and in fish, Nat Commun, 11 (2020) 5408.

[56] J.J. Rohr, F.E. Fish, Strouhal numbers and optimization of swimming by odontocete cetaceans, Journal of Experimental Biology, 207 (2004) 1633-1642.

[57] J. Herskin, J.F. Steffensen, Energy savings in sea bass swimming in a school: measurements of tail beat frequency and oxygen consumption at different swimming speeds, Journal of Fish Biology, 53 (1998) 366-376.

[58] S.S. Killen, S. Marras, J.F. Steffensen, D.J. McKenzie, Aerobic capacity influences the spatial position of individuals within fish schools, Proc Biol Sci, 279 (2012) 357-364.

[59] A.U. Oza, L. Ristroph, M.J. Shelley, Lattices of Hydrodynamically Interacting Flapping Swimmers, Physical Review X, 9 (2019).

[60] M. Gazzola, A.A. Tchieu, D. Alexeev, A. de Brauer, P. Koumoutsakos, Learning to school in the presence of hydrodynamic interactions, Journal of Fluid Mechanics, 789 (2016) 726-749.

[61] S. Verma, G. Novati, P. Koumoutsakos, Efficient collective swimming by harnessing vortices through deep reinforcement learning, Proc Natl Acad Sci U S A, 115 (2018) 5849-5854.

[62] S. Alben, Collective locomotion of two-dimensional lattices of flapping plates. Part 2. Lattice flows and propulsive efficiency, Journal of Fluid Mechanics, 915 (2021).

[63] A. Filella, F. Nadal, C. Sire, E. Kanso, C. Eloy, Model of Collective Fish Behavior with Hydrodynamic Interactions, Phys Rev Lett, 120 (2018) 198101.

[64] Y. Pan, H. Dong, Computational analysis of hydrodynamic interactions in a high-density fish school, Physics of Fluids, 32 (2020) 121901.

[65] P. Han, Y. Pan, G. Liu, H. Dong, Propulsive performance and vortex wakes of multiple tandem foils pitching in-line, Journal of Fluids and Structures, 108 (2022) 103422.

[66] J.-H. Seo, R. Mittal, Improved swimming performance in schooling fish via leading-edge vortex enhancement, Bioinspiration & Biomimetics, (2022).

[67] B.L. Partridge, T. Pitcher, J.M. Cullen, J. Wilson, The three-dimensional structure of fish schools, Behavioral Ecology and Sociobiology, 6 (1980) 277-288.

[68] T.J. Pitcher, The three-dimensional structure of schools in the minnow, Phoxinus phoxinus (L.), Animal Behaviour, 21 (1973) 673-686.

[69] R. Mittal, H. Dong, M. Bozkurttas, F. Najjar, A. Vargas, A. Von Loebbecke, A versatile sharp interface immersed boundary method for incompressible flows with complex boundaries, Journal of computational physics, 227 (2008) 4825-4852.

[70] J. Kim, P. Moin, Application of a fractional-step method to incompressible Navier-Stokes equations, Journal of computational physics, 59 (1985) 308-323.

[71] D.L. Brown, R. Cortez, M.L. Minion, Accurate projection methods for the incompressible Navier–Stokes equations, Journal of computational physics, 168 (2001) 464-499.

[72] J. Wang, D.K. Wainwright, R.E. Lindengren, G.V. Lauder, H. Dong, Tuna locomotion: a computational hydrodynamic analysis of finlet function, Journal of the Royal Society Interface, 17 (2020) 20190590.

[73] M.S.U. Khalid, J. Wang, H. Dong, M. Liu, Flow transitions and mapping for undulating swimmers, Physical Review Fluids, 5 (2020) 063104.

[74] Y. Pan, P. Han, J. Huang, H. Dong, Effect of Formation Pattern on Schooling Energetics in Fish-Like Swimming, Fluids Engineering Division Summer Meeting, American Society of Mechanical Engineers, 2020, pp. 003T005A046.

[75] Y. Pan, H. Dong, Effects of phase difference on hydrodynamic interactions and wake patterns in high-density fish schools, Physics of Fluids, 34 (2022) 111902.

[76] C. Li, H. Dong, Three-dimensional wake topology and propulsive performance of low-aspect-ratio pitching-rolling plates, Physics of Fluids, 28 (2016).

[77] H. Dong, Z. Liang, M. Harff, Optimal settings of aerodynamic performance parameters in hovering flight, International Journal of Micro Air Vehicles, 1 (2009) 173-181 %@ 1756-8293.

[78] Y. Pan, J. Wang, H. Dong, Study on the passive pitching mechanism of different forms of flapping motion in turning flight, AIAA Aviation 2019 Forum, 2019, pp. 3435.

[79] J. Wang, J. Xi, P. Han, N. Wongwiset, J. Pontius, H. Dong, Computational analysis of a flapping uvula on aerodynamics and pharyngeal wall collapsibility in sleep apnea, Journal of Biomechanics, 94 (2019) 88-98.

[80] A.T. Bode-Oke, S. Zeyghami, H. Dong, Flying in reverse: kinematics and aerodynamics of a dragonfly in backward free flight, J R Soc Interface, 15 (2018).

[81] X. Deng, P. Han, J. Wang, H. Dong, A level set based boundary reconstruction method for 3-D bio-inspired flow simulations with sharp-interface immersed boundary method, 2018 Fluid Dynamics Conference, 2018, pp. 4163.

[82] I. Senocak, M. Sandusky, R. DeLeon, D. Wade, K. Felzien, M. Budnikova, An Immersed Boundary Geometric Preprocessor for Arbitrarily Complex Terrain and Geometry, Journal of Atmospheric and Oceanic Technology, 32 (2015) 2075-2087.

[83] D. Adalsteinsson, J.A. Sethian, A fast level set method for propagating interfaces, Journal of computational physics, 118 (1995) 269-277 0021-9991.

[84] J.A. Sethian, Level set methods and fast marching methods: evolving interfaces in computational geometry, fluid mechanics, computer vision, and materials science, Cambridge university press1999.

[85] M. Sussman, P. Smereka, S. Osher, A level set approach for computing solutions to incompressible two-phase flow, Journal of Computational physics, 114 (1994) 146-159.

[86] Y. Saad, M.H. Schultz, GMRES: A generalized minimal residual algorithm for solving nonsymmetric linear systems, SIAM Journal on scientific and statistical computing, 7 (1986) 856-869.

[87] H.A. Van der Vorst, Bi-CGSTAB: A fast and smoothly converging variant of Bi-CG for the solution of nonsymmetric linear systems, SIAM Journal on scientific and Statistical Computing, 13 (1992) 631-644.

[88] G.E. Schneider, M. Zedan, A Modified Strongly Implicit Procedure for the Numerical Solution of Field Problems, Numerical Heat Transfer, 4 (1981) 1-19.

[89] H.L. Stone, Iterative solution of implicit approximations of multidimensional partial differential equations, SIAM Journal on Numerical Analysis, 5 (1968) 530-558.

[90] M. Zedan, G.E. Schneider, A three-dimensional modified strongly implicit procedure for heat conduction, AIAA Journal, 21 (1983) 295-303.

[91] S.R. Fulton, P.E. Ciesielski, W.H. Schubert, Multigrid methods for elliptic problems: A review, Monthly Weather Review, 114 (1986) 943-959.

[92] J.H. Bramble, Multigrid methods, Chapman and Hall/CRC2019.

[93] H.A. Schwarz, Ueber einige Abbildungsaufgaben, (1869).

[94] J.T. King, R. Kumar, M.A. Green, Experimental observations of the three-dimensional wake structures and dynamics generated by a rigid, bioinspired pitching panel, Physical Review Fluids, 3 (2018) 034701.

[95] J.C.R. Hunt, A.A. Wray, P. Moin, Eddies, streams, and convergence zones in turbulent flows, Studying turbulence using numerical simulation databases, 2. Proceedings of the 1988 summer program, (1988).

[96] J. Videler, F. Hess, Fast continuous swimming of two pelagic predators, saithe (Pollachius virens) and mackerel (Scomber scombrus): a kinematic analysis, Journal of experimental biology, 109 (1984) 209-228.

[97] I. Borazjani, F. Sotiropoulos, Numerical investigation of the hydrodynamics of carangiform swimming in the transitional and inertial flow regimes, J Exp Biol, 211 (2008) 1541-1558.

[98] A.P. Maertens, M.S. Triantafyllou, D.K. Yue, Efficiency of fish propulsion, Bioinspir Biomim, 10 (2015) 046013.

[99] W.W. Schultz, P.W. Webb, Power Requirements of Swimming: Do New Methods Resolve Old Questions?1, Integrative and Comparative Biology, 42 (2002) 1018-1025.

[100] E.D. Tytell, G.V. Lauder, The hydrodynamics of eel swimming: I. Wake structure, J Exp Biol, 207 (2004) 1825-1841.

[101] M.S.U. Khalid, I. Akhtar, H. Dong, Hydrodynamics of a tandem fish school with asynchronous undulation of individuals, Journal of Fluids and Structures, 66 (2016) 19-35.

[102] I. Borazjani, F. Sotiropoulos, Numerical investigation of the hydrodynamics of anguilliform swimming in the transitional and inertial flow regimes, J Exp Biol, 212 (2009) 576-592.

[103] D.B. Quinn, K.W. Moored, P.A. Dewey, A.J. Smits, Unsteady propulsion near a solid boundary, Journal of Fluid Mechanics, 742 (2014) 152-170.

[104] D.B. Quinn, G.V. Lauder, A.J. Smits, Flexible propulsors in ground effect, Bioinspir Biomim, 9 (2014) 036008.

[105] P.A. Dewey, A. Carriou, A.J. Smits, On the relationship between efficiency and wake structure of a batoid-inspired oscillating fin, Journal of Fluid Mechanics, 691 (2011) 245-266.

[106] T. Ming, B. Jin, J. Song, H. Luo, R. Du, Y. Ding, 3D computational models explain muscle activation patterns and energetic functions of internal structures in fish swimming, PLoS computational biology, 15 (2019) e1006883.

[107] O.R. Burggraf, Analytical and numerical studies of the structure of steady separated flows, Journal of Fluid Mechanics, 24 (1966) 113-151.

[108] R. Gopalkrishnan, M.S. Triantafyllou, G.S. Triantafyllou, D. Barrett, Active vorticity control in a shear flow using a flapping foil, Journal of Fluid Mechanics, 274 (1994) 1-21.

[109] L. Kang, Z.-R. Peng, H. Huang, X.-Y. Lu, W. Cui, Active external control effect on the collective locomotion of two tandem self-propelled flapping plates, Physics of Fluids, 33 (2021) 101901.

[110] L. Kang, W. Cui, X.-Y. Lu, H. Huang, Hydrodynamic force induced by vortex–body interactions in orderly formations of flapping tandem flexible plates, Physics of Fluids, 34 (2022) 021901.

[111] J.O. Dabiri, On the estimation of swimming and flying forces from wake measurements, Journal of experimental biology, 208 (2005) 3519-3532.

[112] M.S.U. Khalid, J. Wang, I. Akhtar, H. Dong, M. Liu, A. Hemmati, Why do anguilliform swimmers perform undulation with wavelengths shorter than their bodylengths?, Physics of Fluids, 33 (2021) 031911.

[113] H. Ben-Gida, A. Kirchhefer, Z.J. Taylor, W. Bezner-Kerr, C.G. Guglielmo, G.A. Kopp, R. Gurka, Estimation of unsteady aerodynamics in the wake of a freely flying European starling (Sturnus vulgaris), PLoS One, 8 (2013) e80086.

[114] G.C. Lewin, H. Haj-Hariri, Modelling thrust generation of a two-dimensional heaving airfoil in a viscous flow, Journal of Fluid Mechanics, 492 (2003) 339-362.

[115] P.F. Linden, J.S. Turner, The formation of 'optimal'vortex rings, and the efficiency of propulsion devices, Journal of Fluid Mechanics, 427 (2001) 61-72.

[116] K.W. Moored, P.A. Dewey, A.J. Smits, H. Haj-Hariri, Hydrodynamic wake resonance as an underlying principle of efficient unsteady propulsion, Journal of Fluid Mechanics, 708 (2012) 329-348.

[117] K.W. Moored, P.A. Dewey, B.M. Boschitsch, A.J. Smits, H. Haj-Hariri, Linear instability mechanisms leading to optimally efficient locomotion with flexible propulsors, Physics of Fluids, 26 (2014) 041905.

[118] M.L. Finson, Similarity behaviour of momentumless turbulent wakes, Journal of Fluid Mechanics, 71 (1975) 465-479.

[119] M.R. Arbie, U. Ehrenstein, C. Eloy, Stability of momentumless wakes, Journal of Fluid Mechanics, 808 (2016) 316-336.

[120] D.N.B. James C. Liao, George V. Lauder, Michael S. Triantafyllou, fish exploiting vortices decrease muscle activity.pdf, (2003).

[121] W. Zhang, Y. Pan, J. Wang, V. Di Santo, G.V. Lauder, H. Dong, An Efficient Tree-Topological Local Mesh Refinement on Cartesian Grids for Multiple Moving Objects in Incompressible Flow, Available at SSRN 4169528.

[122] J. Wang, Body-Involved Fluid Dynamic Interactions and Performance Enhancement Mechanisms in Biological Propulsion, University of Virginia, Mechanical and Aerospace Engineering - School of Engineering and Applied Science, PHD (Doctor of Philosophy), 2021, Charlottesville, VA, 2021.

[123] C. Koehler, Z. Liang, Z. Gaston, H. Wan, H. Dong, 3D reconstruction and analysis of wing deformation in free-flying dragonflies, Journal of Experimental Biology, 215 (2012) 3018-3027.

[124] P.W. Webb, P.T. Kostecki, E.D. Stevens, The effect of size and swimming speed on locomotor kinematics of rainbow trout, Journal of Experimental Biology, 109 (1984) 77-95.

[125] C. Koehler, T. Wischgoll, H. Dong, Z. Gaston, Vortex visualization in ultra low Reynolds number insect flight, IEEE transactions on visualization and computer graphics, 17 (2011) 2071-2079

[126] R. Blickhan, C. Krick, D. Zehren, W. Nachtigall, T. Breithaupt, Generation of a vortex chain in the wake of a subundulatory swimmer, Naturwissenschaften, 79 (1992) 220-221.

[127] J.C. Nauen, G.V. Lauder, Hydrodynamics of caudal fin locomotion by chub mackerel, Scomber japonicus (Scombridae), Journal of Experimental Biology, 205 (2002) 1709-1724.

[128] L. Ristroph, J. Zhang, Anomalous hydrodynamic drafting of interacting flapping flags, Phys Rev Lett, 101 (2008) 194502.

[129] R. Thandiackal, G. Lauder, In-line swimming dynamics revealed by fish interacting with a robotic mechanism, bioRxiv, (2022).

[130] B.J. Gemmell, S.P. Colin, J.H. Costello, Widespread utilization of passive energy recapture in swimming medusae, Journal of Experimental Biology, 221 (2018) jeb168575.

[131] B.N. Nowroozi, J.A. Strother, J.M. Horton, A.P. Summers, E.L. Brainerd, Whole-body lift and ground effect during pectoral fin locomotion in the northern spearnose poacher (Agonopsis vulsa), Zoology, 112 (2009) 393-402.

[132] R.W. Blake, The energetics of hovering in the mandarin fish (Synchropus picturatus), Journal of Experimental Biology, 82 (1979) 25-33.

[133] E. Blevins, G.V. Lauder, Swimming near the substrate: a simple robotic model of stingray locomotion, Bioinspiration & biomimetics, 8 (2013) 016005.

[134] P.W. Webb, The effect of solid and porous channel walls on steady swimming of steelhead trout Oncorhynchus mykiss, Journal of Experimental Biology, 178 (1993) 97-108.

[135] P.F. Linden, J.S. Turner, 'Optimal'vortex rings and aquatic propulsion mechanisms, Proceedings of the Royal Society of London. Series B: Biological Sciences, 271 (2004) 647-653.

[136] F.E. Fish, Imaginative solutions by marine organisms for drag reduction, Newport, Rhode Island, 1998, pp. 443-450.

[137] G.V.L. Fish, Passive and Active Flow Control by Swimming Fishes and Mammals, (2006).

[138] R.R. Harbig, J. Sheridan, M.C. Thompson, The role of advance ratio and aspect ratio in determining leading-edge vortex stability for flapping flight, Journal of Fluid Mechanics, 751 (2014) 71-105.